MEASUREMENTS OF SMALL-SCALE PROPELLERS OPERATING IN THE VORTEX RING STATE

BY

OMKAR RAVINDRA SHETTY

THESIS

Submitted in partial fulfillment of the requirements
for the degree of Master of Science in Aerospace Engineering
in the Graduate College of the
University of Illinois at Urbana-Champaign, 2010

Urbana, Illinois

Adviser:

Professor Michael S. Selig

Abstract

The behavior of small-scale propellers operating in vertical descent and through the vortex ring state (VRS) was measured. In particular, a total of 26 propellers with varying diameters (9 to 11-in) were tested in the UIUC 2.8×4 ft wind tunnel at low Reynolds numbers to measure the propeller thrust over a range of advance ratios from -0.8 to 0. Also, time histories of the measured thrust for different propellers were recorded to characterize the unsteady thrust fluctuations for advance ratios through the vortex ring state. The effects of propeller geometry, e.g. pitch and planform effects, on the thrust characteristics of these propellers in the VRS are discussed. The motivation of this research is to understand better, the phenomenon of VRS observed in helicopter rotors in descent.

Acknowledgments

There are many people who are responsible for the success of this project. First and foremost, I would like to thank my adviser, Prof. Michael Selig for giving me the opportunity and the motivation to undertake this endeavor. It would have been impossible to complete this research successfully without his guidance and for that I would like to express my sincere and heartfelt gratitude. I thank all my colleagues in the UIUC Applied Aerodynamics Research Group for their constant support. I am deeply grateful to Rob Deters for his advice, assistance and support and for being there to answer my numerous questions and helping me out on the numerous difficulties encountered in the way. I would also like to thank Pritam Sukumar for being my TEX support. Lastly and most importantly, I would like to express my deepest appreciation for my parents and my friends for their unswerving faith and for being my strongest support system for the many years I have known them.

Table of Contents

List of Tables

List of Figures

Nomenclature

Symbols

a	lift-curve slope ($= 2\pi$)
A	disk area of propeller
A_b	blade area of propeller
AF	activity factor
B	tip loss factor
c	propeller chord length
C	cross-sectional area of wind tunnel
C_t	rotor thrust coefficient ($= T/\rho\ A\ \pi^2\ n^2\ D^2$)
C_{th}	rotor thrust coefficient at hover ($= T_h/\rho\ A\ \pi^2\ n^2\ D^2$)
C_T	thrust coefficient ($= T/\rho\ n^2\ D^4$)
D	propeller diameter
J	advance ratio ($= V/n\ D$)
n	rotational speed (revs/sec)
P_{atm}	atmospheric pressure
q	dynamic pressure ($= (1/2)\ \rho\ V^2$)
R	propeller radius, ideal gas constant for air
r_c	blade root cutout
T	thrust
T_{air}	air temperature
T_h	thrust at hover

V	freestream velocity
w	induced velocity
w_h	induced velocity at hover
x	radial station
β	propeller twist angle at the 75% radial station
Δq	effective increase in dynamic pressure
ϵ	blockage factor ($= 5/2$)
ρ	air density
σ	propeller solidity ($= A_b/A$), standard deviation
λ	rotor inflow ratio ($= w/\pi\ n\ D$)
λ_h	rotor inflow ratio at hover ($= w_h/\pi\ n\ D$)
μ	rotor advance ratio ($= V/\pi\ n\ D$)

Abbreviations

AF	Activity Factor
GUI	Graphical User Interface
UIUC	University of Illinois at Urbana-Champaign
VRS	Vortex Ring State

Chapter 1

Introduction

The interaction between the induced flow from a propeller in descent and the freestream velocity acting upwards results in the formation of large vortices, leading to the vortex ring state (VRS). The VRS is observed when the descent velocity is of a similar magnitude as the induced velocity,[1] thereby preventing the vortex rings from convecting away. It is an unsteady, turbulent condition characterized by a loss of collective control and thrust fluctuations. Beyond the VRS, as the descent velocity is increased, the vortices get convected away from the rotor and a definite slipstream is developed. Since the absence of a defined slipstream makes it impractical to apply models such as the momentum theory, a considerable amount of research has been conducted to understand VRS.

One of the earliest attempts to define the behavior of propellers in descent was undertaken by Glauert[2] who proposed an empirical form of the characteristic curve based on experimental investigation. Castles and Gray[3] later specified an empirical relation between the induced velocity, thrust and vertical descent velocity for rotors in axial descent. They noted the difference in behavior of linearly tapered planforms and rotors with twist as compared to constant chord, untwisted blades. They also observed fluctuations in the force and moment data for the rotors in the VRS. Washizu[4] investigated and quantified these unsteady aerodynamic characteristics of rotors in the VRS under both axial and inclined descent conditions. They observed the presence of extensive thrust fluctuations in the VRS with a certain periodicity exhibited in some regions. Similarly, Yaggy and Mort[5] too examined the fluctuations in thrust under axial and inclined descent for a rigid and flapping propeller, establishing a relation between the extent of these fluctuations and the disk loading. More recently, Betzina[6] studied these phenomena experimentally, noting significant differences in the VRS characteristics of a single rotor and tandem rotor configuration. The

possibility of low frequency roll oscillations in tiltrotor aircraft was also suggested.

Apart from the experimental research, there have been considerable efforts to study the phenomenon computationally as well. Leishman[7] carried out a computational study on the onset of the VRS for single and multi-rotor configurations and the flow and rotor geometric factors that affect it. Chen and Prasad[8] developed the ring vortex model to predict the inflow characteristics for rotors in descent.

Most of the research carried out previously deals exclusively with the effects of the VRS on the main helicopter rotors. However, in a general helicopter configuration, along with the main rotor, the tail rotor too is susceptible to the VRS. This condition known as the tail rotor VRS can lead to a loss of tail rotor effectiveness (LTE).[9] This phenomenon is experienced usually in the presence of a left crosswind and results in yaw deviations because of the thrust fluctuations. Considering the relatively smaller sizes of the tail rotors as compared to the main rotor and the lack of cyclic pitch, the propellers tested in this study resemble tail rotors to a great extent and it is believed that the results of this research would be applicable in the design considerations for the same.

The current study tests a wide range of propellers in the VRS and analyzes the results to understand better the effect of propeller parameters such as the pitch, diameter, solidity and the activity factor on the thrust characteristics of propellers in the VRS. For the wind tunnel experiments, a total of 26 propellers have been tested and the data analyzed in further sections. The tests were essentially carried out in two stages. The first stage consisted of test runs where steady state thrust coefficient data was acquired as a function of propeller advance ratio. For the second stage of tests, thrust time history data was recorded for a given advance ratio, and the data is analyzed to measure the nature and the extent of thrust fluctuations. This thesis discusses the results obtained from these tests.

Testing of small scale propellers in the normal working state has been carried out for several years at the University of Illinois at Urbana-Champaign.[10–12] The existing wind tunnel setup has been modified to enable testing of propellers in axial vertical descent. For the present work, the diameters of the propellers tested range between 9 in and 11 in. Figure 1.1 shows the three types of propellers tested for this study, namely APC Slow Flyer, APC Sport and APC Thin Electric.[13] The propellers are denoted as $D \times p$ where D is the

propeller diameter (in) and p represents the pitch (in/rev).

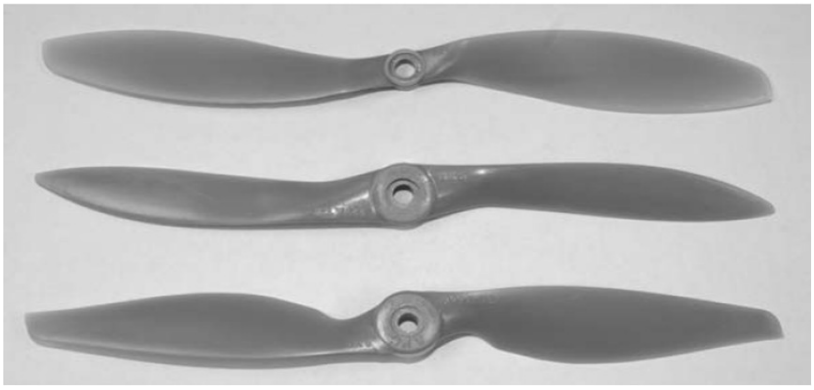

Fig. 1.1: APC Slow Flyer, Sport and Thin Electric Propellers.[13]

Chapter 2

Experimental Setup

The experimental setup for testing propellers in the normal working state was developed by Brandt[10] and Tehrani.[11] A few modifications were incorporated in order to test propellers in descent.

2.1 Wind Tunnel Facility

The tests were conducted in the UIUC subsonic wind tunnel, illustrated in Fig. 2.1. The wind tunnel is an open return type with a contraction ratio of 7.5:1. The test section measured 2.8 ft (height) by 4.0 ft (width) by 8.0 ft (length). The tunnel was powered by a 125 hp motor achieving maximum flow speeds of up to 235 ft/sec. However, for the current set of propeller tests the maximum freestream velocity was limited to 40 ft/sec. The wind tunnel settling chamber consisted of a 4 in thick honeycomb structure in addition to four anti-turbulence screens. The turbulence intensity in the subsonic wind tunnel was measured to be less than 0.1%.[10]

2.2 Setup

In order to observe the performance of the propellers in the VRS, the thrust generated by the propeller was measured along with the rotational speed of the propeller and the freestream velocity. The following sections provide the details of the experimental setup used to measure these parameters.

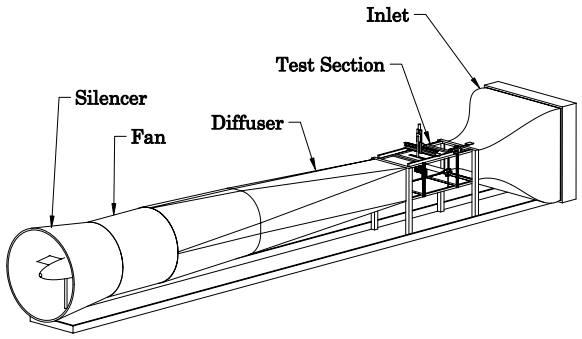

Fig. 2.1: UIUC subsonic wind tunnel.

2.2.1 Thrust Measurement

The thrust generated by the propeller was transferred to a rectangular post that served to hold the propeller, the motor and the motor housing at the center of the wind tunnel test section. The post then transferred the thrust to the pivot arm of the experimental rig. The pivot arm of the rig consisted of 10 holes wherein a load cell could be mounted depending upon the expected thrust of the propeller and consequently, the moment arm required. The holes were located from a distance of 3.75 in (9.53 cm) from the pivot to a distance of 12.75 in (32.39 cm) in increments of 1 in. Thus, the apparatus converted the thrust generated by the propeller to tension acting on the load cell when the propeller is in the normal working state. In order to test propellers in descent, the propellers were mounted facing downstream as is shown in Fig 2.2. This caused the thrust to be generated in the opposite direction thereby exerting a compressive force on the load cell. Since the load cell used was designed to withstand only tensile forces, it was decided that the load cell would be subjected to a constant preloading by means of counterweights, so that at any given time the net force acting on the load cell would be tensile in nature. The load cell setup with the counterweights is illustrated in Fig 2.3. The load cell used for these tests was an Interface SM-10 load cell with a maximum capacity of 10 lb.

The portion of the rectangular post present in the test section was enclosed in a symmetric fairing to ensure that the thrust measurements were not affected by drag.

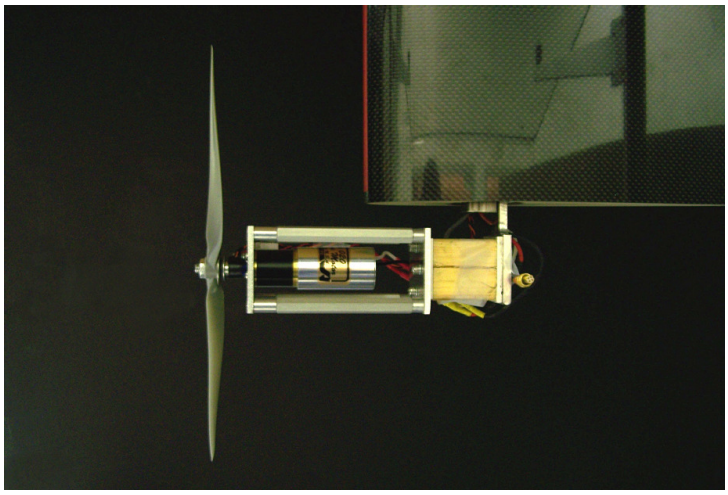

Fig. 2.2: Modified test apparatus for propellers in descent (freestream flow from left-to-right while thrust is directed downstream).

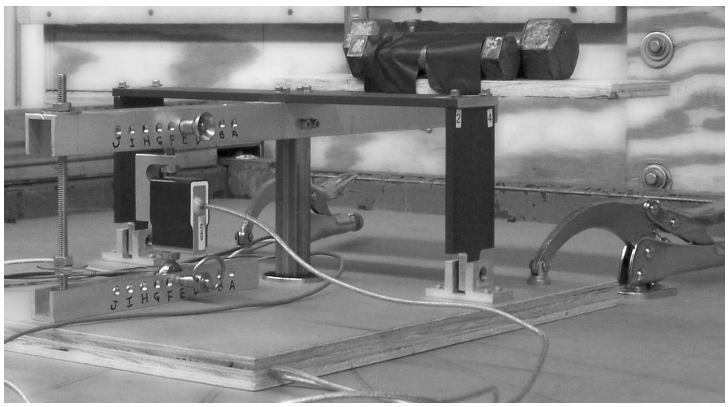

Fig. 2.3: Load cell setup with the counterweights.

2.2.2 Propeller Speed Measurement

The propeller rotational speed was measured in terms of revolutions per minute (RPM) using a reflective sensor manufactured by Honeywell (Part HOA1180-002). The sensor consisted of an infrared emitting diode placed next to a silicon photo transistor. When connected, the diode continuously emitted an infrared signal and this signal would get reflected to the photo transistor only when a reflective surface was placed in front of the sensor. In order to obtain a reflective surface, the stainless metal portion of the propeller hub was covered with black electrical tape such that only a small portion of the hub was uncovered. This portion of the hub essentially acted as the reflective surface which appeared in front of the sensor once every revolution of the propeller.

The revolution speed of the propeller was measured at a frequency of 20,000 Hz over a time period of 0.75 sec.

2.2.3 Freestream Flow Measurement

The wind tunnel has pressure taps mounted on each of its four walls at the settling chamber and at a location just upstream of the test section. The freestream velocity is determined by calculating the pressure difference between the total pressure head and the static pressure. This system was chosen over a pitot tube for measuring the freestream velocity, as it was observed that using the pitot probe led to an unsteadiness in the measured velocity. This variation was attributed to the unsteadiness in the flow within and near the test section observed while testing propellers in the VRS.

The freestream velocity correction schemes used in the data acquisition software are discussed in greater detail by Brandt[10] and Tehrani.[11] In order to account for the wake blockage and the boundary corrections for propellers in descent, the following equation[14,15] was used:

$$\frac{\Delta q}{q} = \epsilon C_T \frac{A}{C} \tag{2.1}$$

2.2.4 Additional Experimental Equipment

Apart from the equipment discussed in the previous sections, a few other components were required in order to test the propellers. The propellers were driven by an AstroFlight 020 Brushless motor. The motor was rated to a maximum RPM limit of 40,000 with a power limit of 200 W. However, in practice when used to drive a propeller, the maximum achievable RPM ranged between 4,000 – 7,000 RPM depending on the size of the propeller.

The rotational speed of the motor was regulated by a 25 amp Castle Creations Speed Controller. The speed controller was supplied power from a BK Precision ® Model BK1692 power supply. The speed controller was regulated using a ServoXciter, manufactured by Vexa Control. The ServoXciter was connected to a computer through a digital to analog converter and it controlled the propeller RPM by generating servo pulse widths that were used by the speed controller.

2.3 Data Acquisition System

The Data acquisition hardware consisted of a National Instruments ^{TM} 16-bit PCI-6031E analog-to-digital board connected to a 1.4-GHz, Precision-330 Dell ^{TM} personal computer. The analog-to-digital board included 32 input channels and two 16-bit digital-to-analog outputs. This board had a high accuracy of $\pm$ 0.305 mV for a full scale range of $\pm$ 10.0 V. The National Instruments LabWindows ^{TM} /CVI software was used to construct the graphical user interface (GUIs) along with the underlying C code which facilitated data acquisition and recording. The GUI displayed parameters such as the thrust, RPM, ambient pressure and temperature in a real time format enabling complete control on the test at all times. The operator also had the option of aborting a test in case of a problem.

As mentioned earlier, the propeller RPM was measured at a sampling frequency of 20,000 Hz on account of its high speed. The other parameters such as the thrust, temperature and pressure were measured at a lower sampling frequency of 3,000 Hz.

2.4 Experimental Procedure

Based on prior tests, a set procedure had been established for propeller testing outlining the setup for hardware and software components and calibration techniques. A similar procedure had been followed for the current set of tests as well. Before the tests, weights were used to calibrate the load cell. The pressure transducers had been factory calibrated owing to the difficulty in generating sufficiently low pressures required for in house calibration.

2.4.1 Experimental Setup

A specialized ceiling used specifically with the propeller setup was added to the wind tunnel test section. The ceiling was designed to hold the test rig which consisted of the load cell on top of the test section and the post that held the propeller and motor at the center of the test section as discussed in the previous section. A fairing surrounding the vertical post was mounted using two bolts. The wires connected to the motor and the reflective sensor were carried inside the fairing to the roof of the tunnel. The drag forces generated by the flow on the fairing did not affect the thrust measurement. Once the rig was installed, any gaps

or openings in the test section walls or the ceiling were sealed with tape. The vertical test section walls that opened outwards were clamped shut to prevent ambient air from leaking into the test section.

The load cell was connected to a signal conditioner through a patch board. The signal conditioner filtered and amplified the signal and provides an excitation voltage to the load cell. For the current tests, the load cell signal was amplified with a gain of 100 and the excitation voltage was supplied at 10 V. The thermocouple used to measure the ambient temperature was amplified with a gain of 1,000 and had no excitation voltage.

Once the motor housing was connected to the lower end of the support, the load cell was mounted to the appropriate hole in the pivot arm. As mentioned in the previous section, a constant load is exerted on the load cell to ensure that the net load acting on the load cell remains tensile in nature. However, the load cell is zeroed before each run to ensure that the offset is accounted for.

1 torr pressure transducers were used to measure the dynamic pressure for the current set of tests. The transducer needed to be warmed up for at least four hours before a run to ensure accurate readings.

The data acquisition board was connected to the required components and the computer. The software was used to test the connections and run checks on the inputs and outputs.

2.4.2 Calibration

The instruments used were calibrated regularly to ensure that the data recorded was accurate and consistent. The load cell used to measure the propeller thrust was calibrated at least every 48 hours.

To calibrate the load cell, a known load was exerted on the system and the load cell signal was measured in volts, thus yielding a correlation between the load in terms of pounds and volts. A string was tied to an adapter mounted on the motor shaft. The string then passed over a frictionless pulley and was connected to a load hanger on the other side. Precision weights were loaded on the hanger one by one and the corresponding load cell signal was recorded by the data acquisition software. When the value of the total load was close to the maximum range of the load cell, the weights were unloaded in steps and the

corresponding load cell signal was recorded. This was done to account for hysteresis in the process. Based on the data points recorded a calibration curve was calculated for the load cell.

2.4.3 Testing Procedure

Before starting each test, a number of input variables were set in the data acquisition software corresponding to the propeller being tested and the specifications of the test run. The parameters included the propeller pitch and diameter, the range of freestream velocities over which the test was to be carried out, the propeller RPM, the number of data acquisition points and the load cell location. For these tests, the propeller was maintained at a rotational speed of 4,000 RPM. The descent velocity was varied from 8 ft/sec to 40 ft/sec in increments of 2 ft/sec and three data points were recorded at each velocity step thereby corresponding to 51 points for the entire run. On occasion, it was observed that the motor torque was insufficient to maintain the propeller RPM. This was noted especially at higher descent velocities where the propeller starts driving the motor. The test was aborted when such conditions were achieved.

2.5 Data Reduction

The data acquisition software recorded the signals from the sensors in terms of voltages. The reduction process converted these raw voltages to physical units. The calibration curves were used to convert the thrust, pressure and temperature raw data to the corresponding physical units. As discussed in Section 2.2.2, the rotational speed was measured by means of the reflective sensor. The number of voltage spikes corresponding to the reflective surface were measured for a corresponding sampling period which yielded the propeller RPM. The atmospheric density and the freestream velocity are used to reduce the propeller thrust data. The data acquisition software uses the following formulas:

$$\rho = \frac{P_{atm}}{R\, T_{air}} \tag{2.2}$$

$$V = \sqrt{\frac{2q}{\rho}} \tag{2.3}$$

Finally, the above measured and derived quantities were non-dimensionalized to obtain the propeller performance data. The thrust coefficient was plotted against the advance ratio. The definitions for the advance ratio and thrust are given by the following equations:[16]

$$J = \frac{V}{nD} \tag{2.4}$$

$$C_T = \frac{T}{\rho\, n^2 D^4} \tag{2.5}$$

Based on propeller geometry and the thrust, the induced velocity and the net inflow were calculated using the Eq 2.6–2.10. From Johnson,[17] the values for the tip loss factor (B) and the blade root cutout (r_c) were taken as 0.97 and 0.15 respectively. The thrust coefficent and the freestream velocity data were obtained from the wind tunnel experiments, while the pitch angle at the 75% station (β) and the propeller solidity (σ) was taken from the propeller geometry measurements. The freestream velocity was used to calculate the rotor advance ratio (μ) using Eq 2.6. Using the advance ratio and the other parameters as described earlier, the rotor inflow ratio (λ) was calculated using Eq 2.7. Finally, the induced velocity (w) was calculated from Eq 2.10. Similarly, using Eq 2.9–2.10, the induced velocity at hover (w_h) was calculated using previously conducted static tests.[10] The only difference here was that the value of μ was zero since the freestream velocity was zero. From these set of equations, the non-dimensionalized induced velocity (w/w_h) and the net inflow ($(V + w)/w_h$) were calculated. These parameters are plotted in Chapter 4 for the tested propellers.

$$\mu = \frac{V}{(\pi n)D} \tag{2.6}$$

$$\frac{3}{2}(B^2 - r_c^2)\lambda = -\frac{6C_t}{\sigma a} + \beta(B^3 - r_c^3)\left(1 + \frac{3}{2}\mu^2\right) \tag{2.7}$$

$$w = \lambda(2\pi n)\frac{D}{2} \tag{2.8}$$

$$\frac{3}{2}(B^2 - r_c^2)\lambda_h = -\frac{6C_{th}}{\sigma a} + \beta(B^3 - r_c^3) \tag{2.9}$$

$$w_h = \lambda_h(2\pi n)\frac{D}{2} \tag{2.10}$$

2.6 Thrust Time History Measurement

In order to observe the flow instability and the thrust fluctuations experienced by a propeller in the VRS, it was decided to record the thrust time history. The existing data acquisition code was altered such that the time history would be recorded on a file for a constant advance ratio. The initial time history data revealed the presence of noise along with the useful data. The thrust time history recorded under static tests showed large fluctuations which would not be expected from such a test.

The next step was to identify and eliminate the noise content from the data. The possibility of the fluctuations being aerodynamic in nature or as a result of vibrations induced by the propeller was eliminated. Figure 2.4 shows the energy density spectrum that was created based on the time history data which showed the presence of high frequency noise in the signal. Also some lower frequency content was observed at a frequency of around 10 Hz. The possibility that the rig was the source of this data content was discussed. To verify this possibility, an excitation was imparted to the experimental rig and the vibrations were allowed to be damped out. The load cell signal was recorded for this duration and the energy/spectral density spectra were created which is shown in Fig 2.6. These spectra contained a distinctive spike around 10 Hz indicating that during tests the vibrations induced by the propeller were causing the rig to vibrate at its natural frequency leading to the fluctuations in the load cell measurements.

It was decided to filter out the higher frequency content of the signal as it was highly unlikely that the higher frequency data could be aerodynamic in nature. As discussed in Section 2.4.1, the signal conditioner is also used to filter the load cell signal. Based on the current analysis, it was decided to set the cut-off frequency of the low pass filter at 10 Hz instead of the 100 Hz which had been used previously for the other tests. However, since a

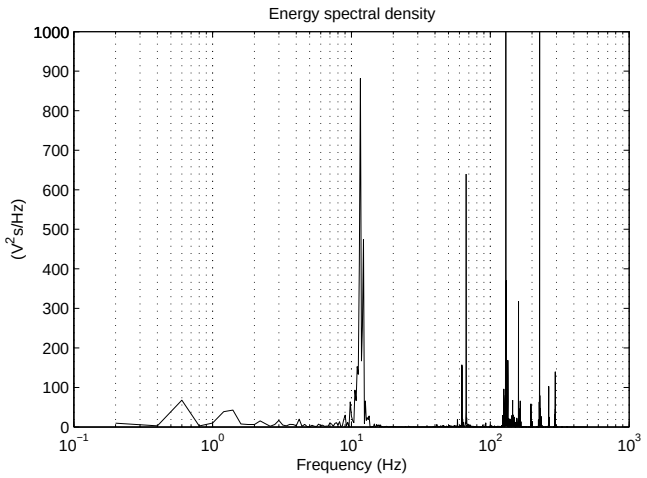

Fig. 2.4: Energy spectral density for the APC Thin Electric 9×7.5 at 4,000 RPM filtered at 100 Hz.

number of the tests for the current study had been conducted at 100 Hz, it was necessary to verify if these tests yielded consistent results with the tests carried out at a filter setting of 10 Hz. In order to do that, a MATLAB ® code was written which would simulate the data acquisition code. Based on a time history sampled at 3,000 Hz, the code outputs three data points over a time history of 5 sec. Each data point was the average of 3,000 points. Each such data point was compared to the mean of the time history and in each case, the difference was less than 1%. Hence it was concluded that the test reults at both 10 Hz and 100 Hz filter cut off were consistent.

The thrust time history was then recorded at specific advance ratios at a sampling frequency of 120 Hz over a period of 100 sec. The data is then further filtered at 10 Hz using the signal processing toolbox in MATLAB ®. The filter used is a Butterworth 6 pole filter with a cut off at 10 Hz.

2.7 Propeller Geometry

In order to analyze the performance data, it was necessary to measure some of the geometric parameters of the propellers including the chord distribution and the twist. This measurement was done using the software PropellerScanner.[18] Scans were taken of the front and side views of the propeller and processed by the program to give the geometric data as the

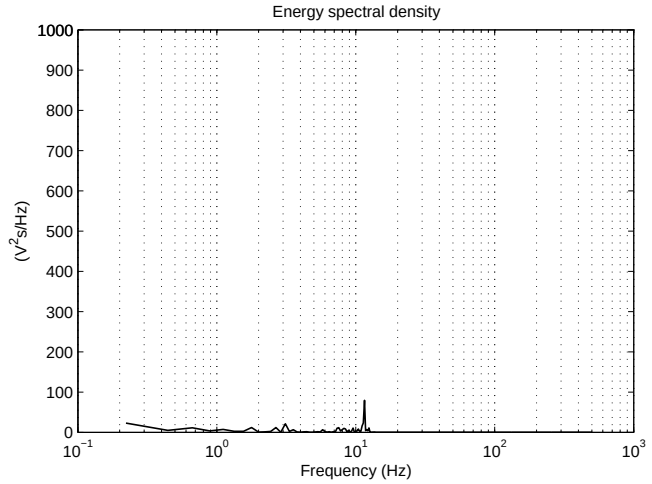

Fig. 2.5: Energy spectral density for the APC Thin Electric 9×7.5 at 4,000 RPM filtered at 10 Hz.

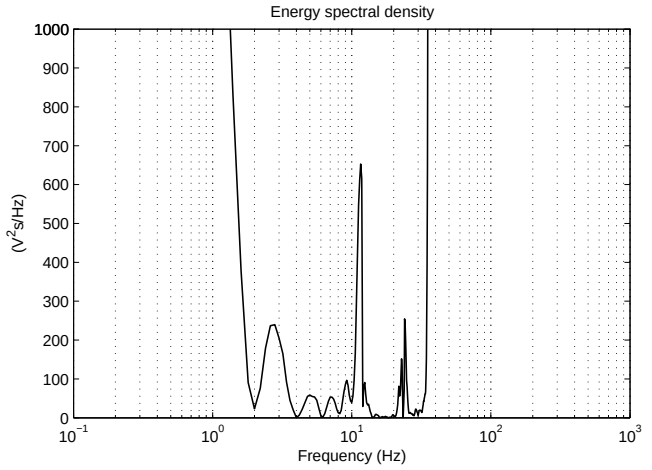

Fig. 2.6: Energy spectral density by imparting a vibration to the propeller test set-up.

output. A more detailed explanation of the software and its usage was provided by Uhlig.[12] Along with the twist and chord distribution, it was also necessary to measure the zero lift angle of attack for the airfoil at the 75% radial station to calculate the induced velocity and net inflow. To do this, one propeller of each style was sliced at the 75% station such that the airfoil shape was exposed. The airfoil coordinates were acquired by importing scans of these slices in a CAD program. These coordinates were then imported in XFOIL,[19] and the zero lift angle of attack was calculated. For the purpose of this project, it was assumed that all propellers belonging to a particular style had a similar zero lift angle of attack at the 75% station.

Chapter 3

Data Validation

To ensure that the test results remain consistent, test runs were carried out using known propellers and the results verified with prior test results. Since the set up had not been used to test propellers in descent so far, the only comparisons that could have been made were with earlier tests with the same propeller. These check runs showed that the test results were within acceptable limits. To ensure reliability, the control tests were carried out on two different propellers rather than on a single propeller as was done in prior research. A detailed analysis of data repeatability for the propeller setup applicable for propellers operating in the normal working state had been carried out by Brandt[10] and Tehrani.[11]

3.1 Repeatability of Measurements

For the current set of tests, the APC 9×4.7 Slow Flyer and the APC 9×7.5 Thin Electric were used as the control test. Figures 3.1 and 3.2 show the comparison of the thrust coefficient data plotted as a function of the advance ratio. As can be seen, the data shows sufficient repeatability overall. For the APC Slow Flyer, the thrust coefficient data exhibits some unsteadiness until an advance ratio of about -0.4. However, as the descent velocity increases beyond that point, the thrust coefficient exhibits excellent repeatability for the rest of the test. This instability in the data is a direct result of the flow unsteadiness observed in the VRS. A similar behavior of unsteadiness in the thrust coefficient data until an advance ration of -0.4 is is observed for the second set of control tests conducted on the APC Thin Electric 9×7.5.

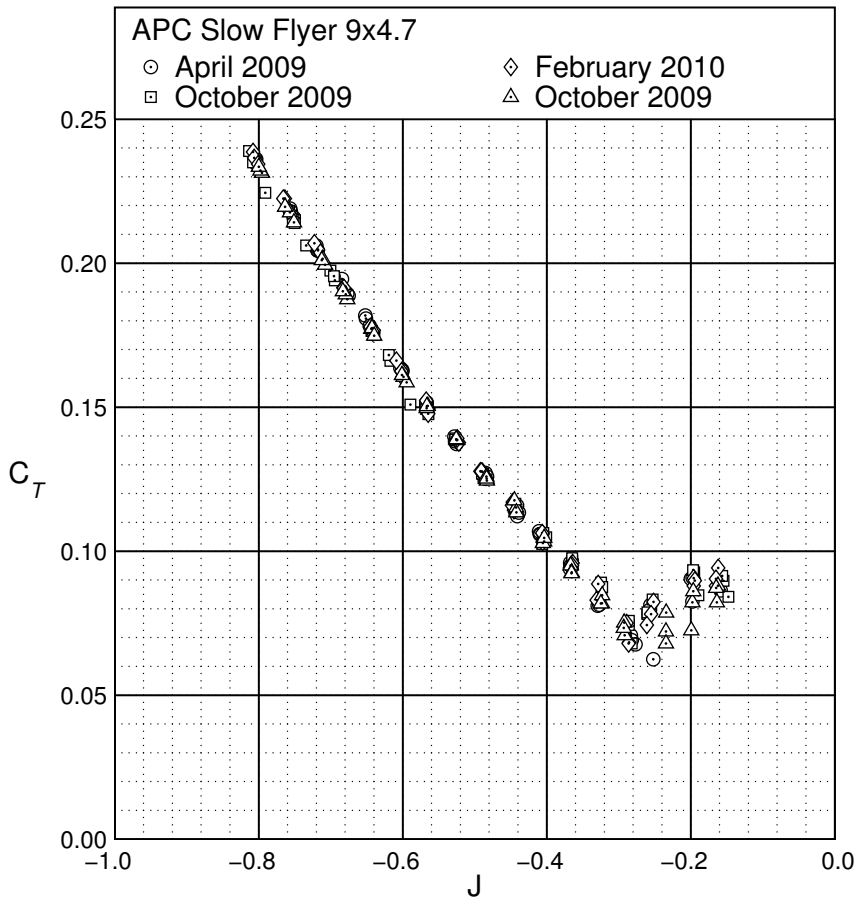

Fig. 3.1: Thrust coefficient data comparison for the APC Slow Flyer 9×4.7.

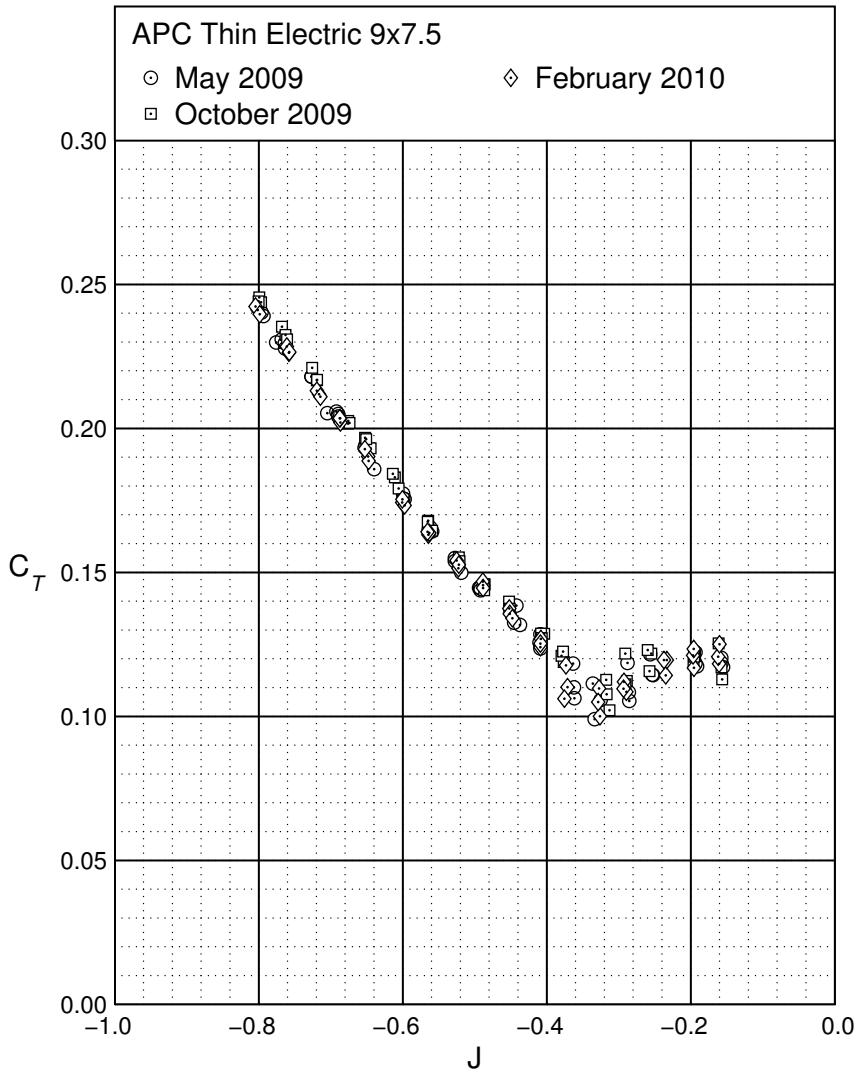

Fig. 3.2: Thrust coefficient data comparison for the APC Thin Electric 9×7.5.

Chapter 4

Experimental Results

4.1 Steady State Performance Data

This section includes the steady state data for the tested propellers. Table 4.1 gives the list of the propellers along with the solidity, activity factor and the pitch angle at the 75% radial station. The performance data includes the steady state thrust coefficient as a function of the advance ratio, induced velocity and the net inflow plotted as a function of the non-dimensionalized descent velocity. As mentioned in Section 2.4.3, three data points are recorded at each value of the advance ratio. Each of these points is the average of the data collected over 1 sec, i.e. at a sampling frequency of 3,000 Hz, each recorded point represents the average of 3,000 data points. The flow unsteadiness causes a variation in the data recorded even at the same advance ratio. This variation is maximum at the point where the minimum thrust is generated. A more detailed explanation of this behavior is provided in the subsequent chapter. Based on the measured thrust data and the propeller geometry, the ratio of the induced velocity to the induced velocity at hover (w/w_h) and the ratio of the net inflow to the induced velocity at hover ($(V + w)/w_h$) are calculated using Eq 2.6–2.10.

Figures 4.1–4.24 show the thrust, induced velocity and net inflow data plots for the APC Slow Flyer propellers, Fig. 4.25–4.45 represent the data for the APC Sport propeller and the data for the APC Thin Electric propellers is given in Fig 4.46–4.63. The diameter of these propellers ranged from 9 in to 11 in.

Table 4.1: List of Propellers Tested

Brand	Style	Designation	$\theta_{(0.75R)}$(deg)	Solidity	Activity Factor
APC	Slow Flyer	9×3.8	10.80	0.0978	120.43
		9×4.7	11.56	0.0978	122.65
		9×6	14.54	0.0976	123.04
		9×7.5	16.71	0.0924	115.62
		10×3.8	9.24	0.0978	123.62
		10×4.7	10.27	0.0957	118.34
		11×3.8	7.43	0.0981	124.77
		11×4.7	9.53	0.0973	118.77
APC	Sport	9×5	14.87	0.0729	83.97
		9×7	18.87	0.0759	85.50
		9×8	23.80	0.0765	87.27
		9×9	26.00	0.0767	88.38
		10×4	9.93	0.0737	82.81
		10×5	16.60	0.0774	90.37
		10×10	23.97	0.0746	88.12
		11×4	10.69	0.0762	82.13
		11×5	12.44	0.0755	81.42
APC	Thin Electric	9×4.5	12.56	0.0912	98.21
		9×6	16.37	0.0903	98.09
		9×7.5	20.40	0.0897	93.44
		10×5	13.39	0.0806	83.96
		10×7	16.74	0.0811	84.05
		10×10	24.80	0.0799	81.93
		11×7	16.28	0.0773	82.18

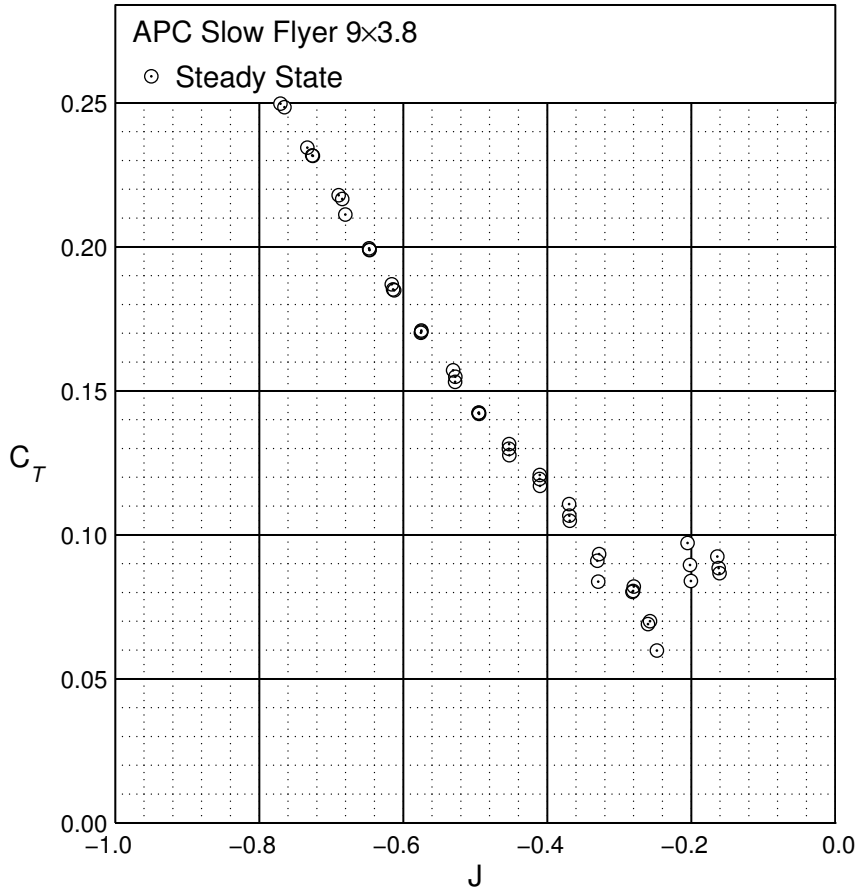

Fig. 4.1: Steady state thrust coefficient data for the APC Slow Flyer 9×3.8.

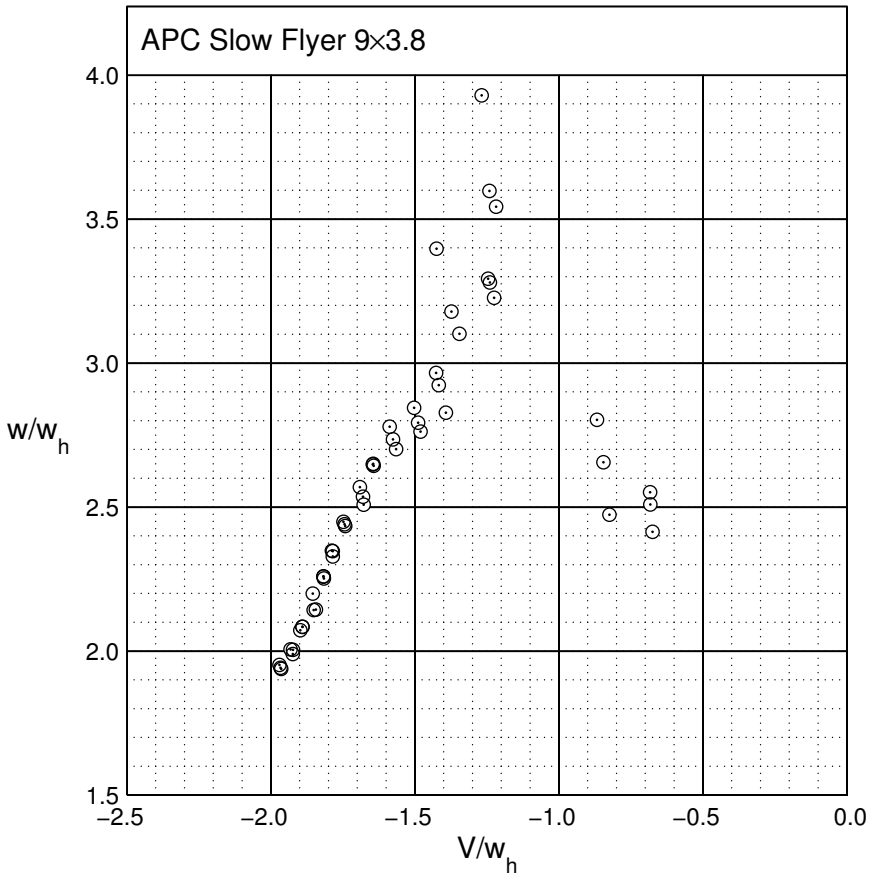

Fig. 4.2: Induced velocity data for the APC Slow Flyer 9×3.8.

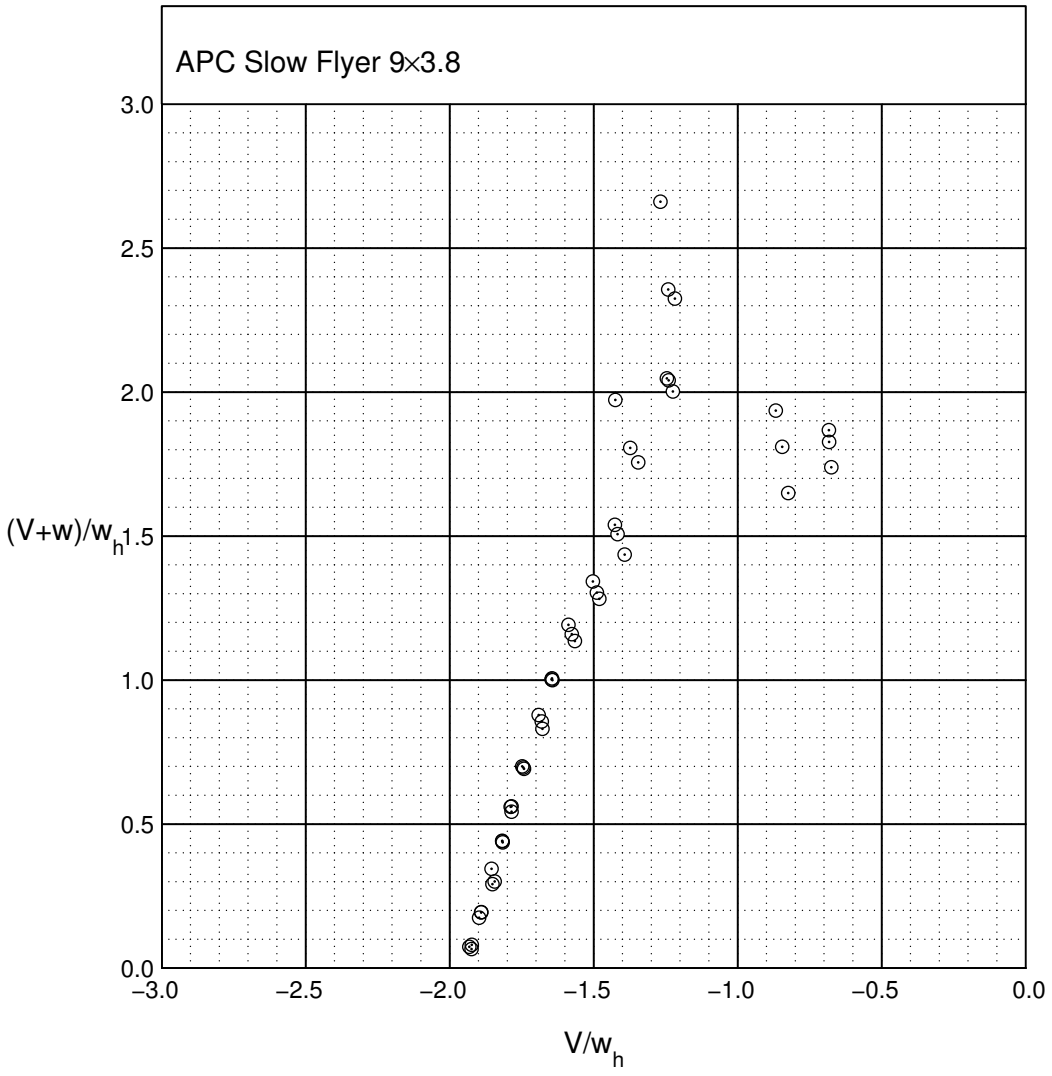

Fig. 4.3: Net inflow data for the APC Slow Flyer 9×3.8.

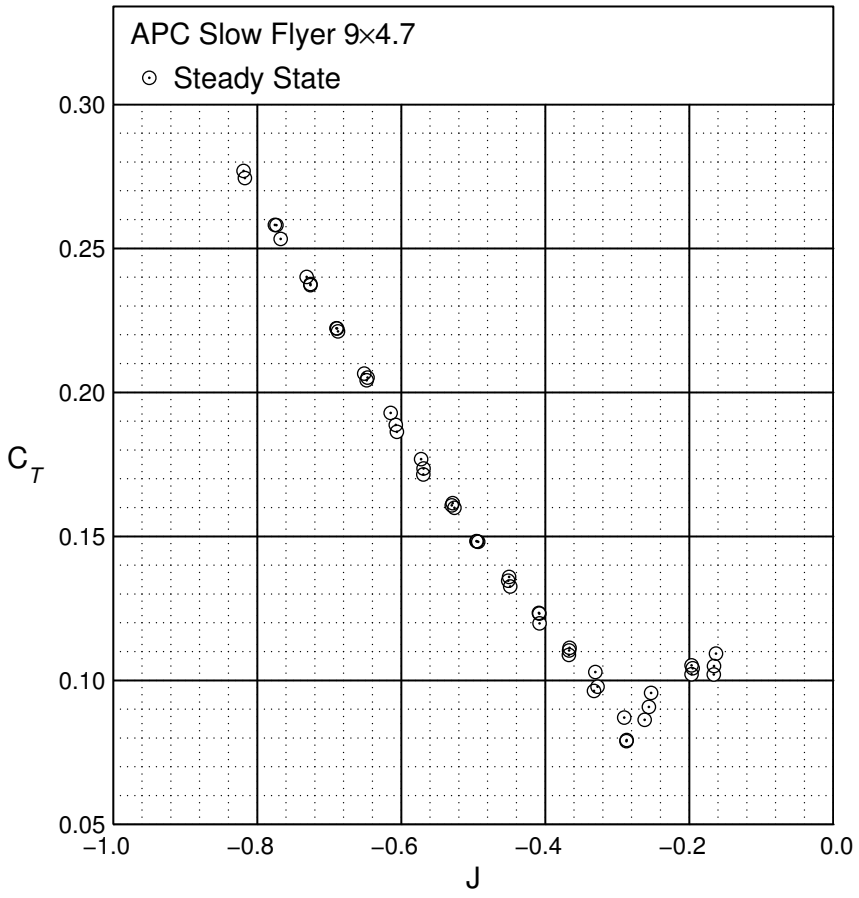

Fig. 4.4: Steady state thrust coefficient data for the APC Slow Flyer 9×4.7.

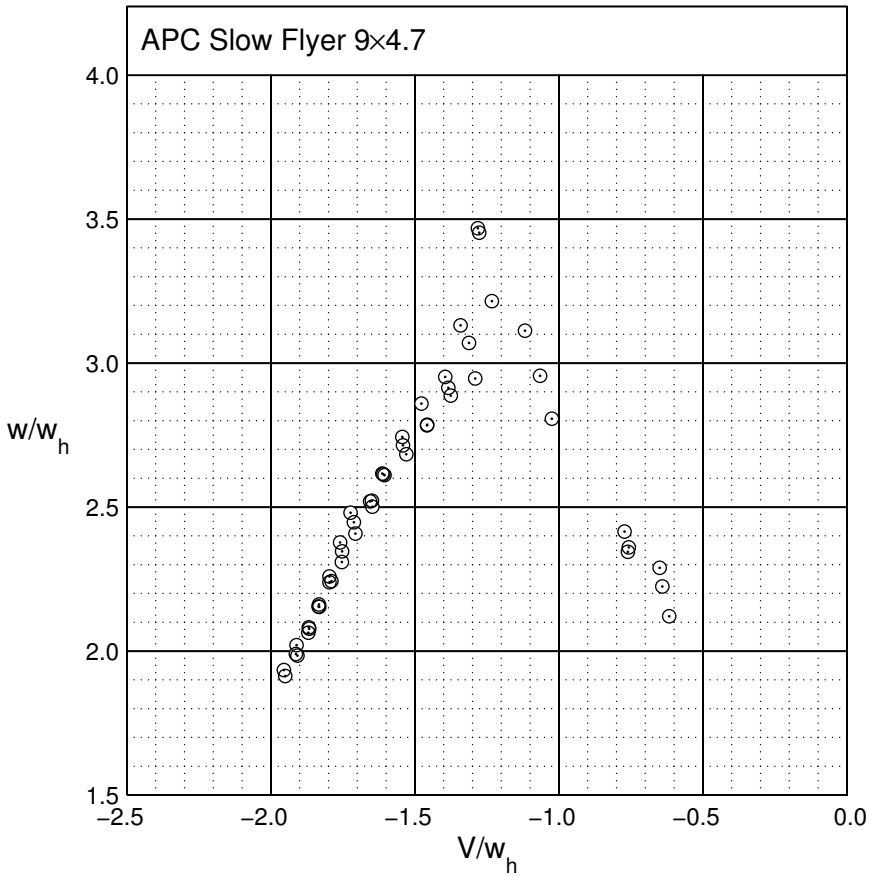

Fig. 4.5: Induced velocity data for the APC Slow Flyer 9×4.7.

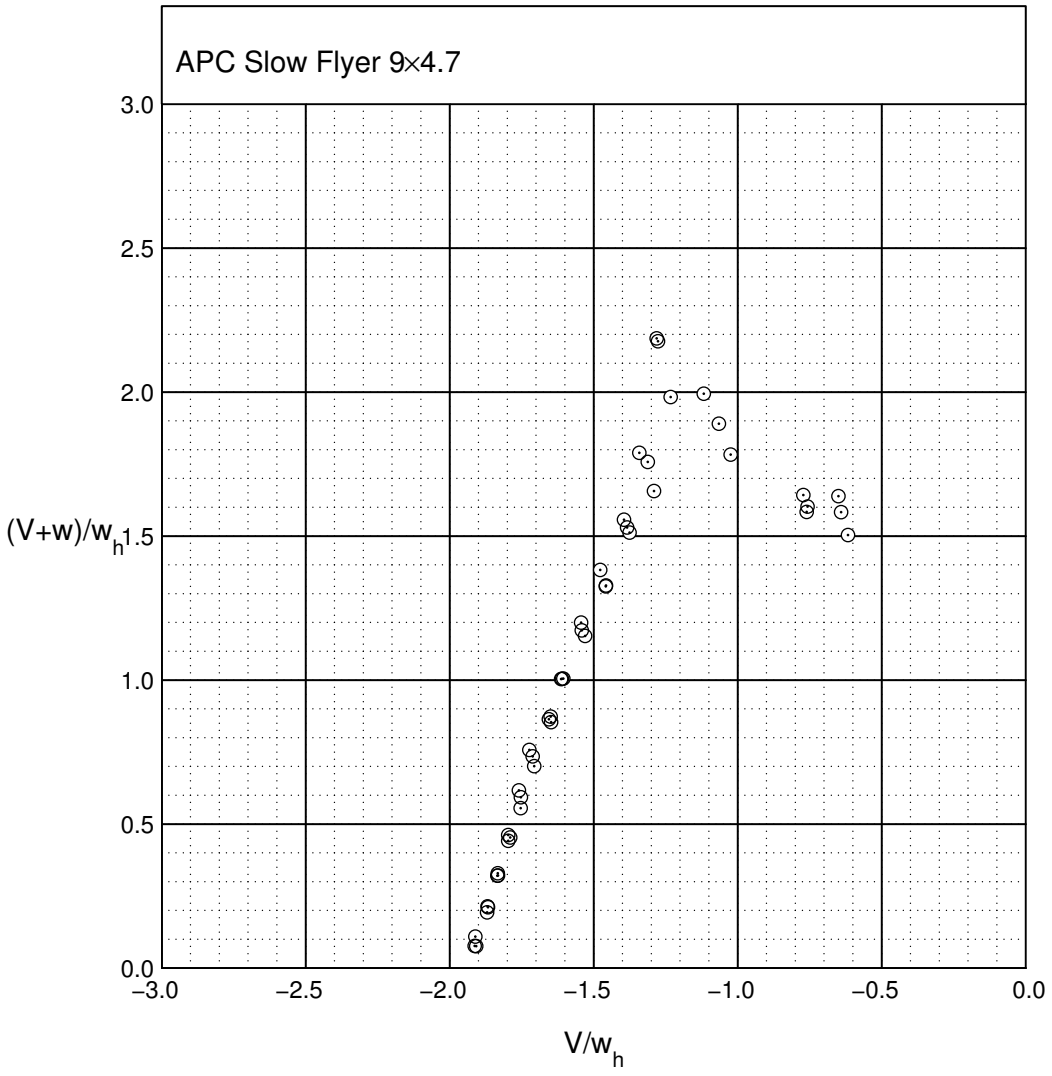

Fig. 4.6: Net inflow data for the APC Slow Flyer 9×4.7.

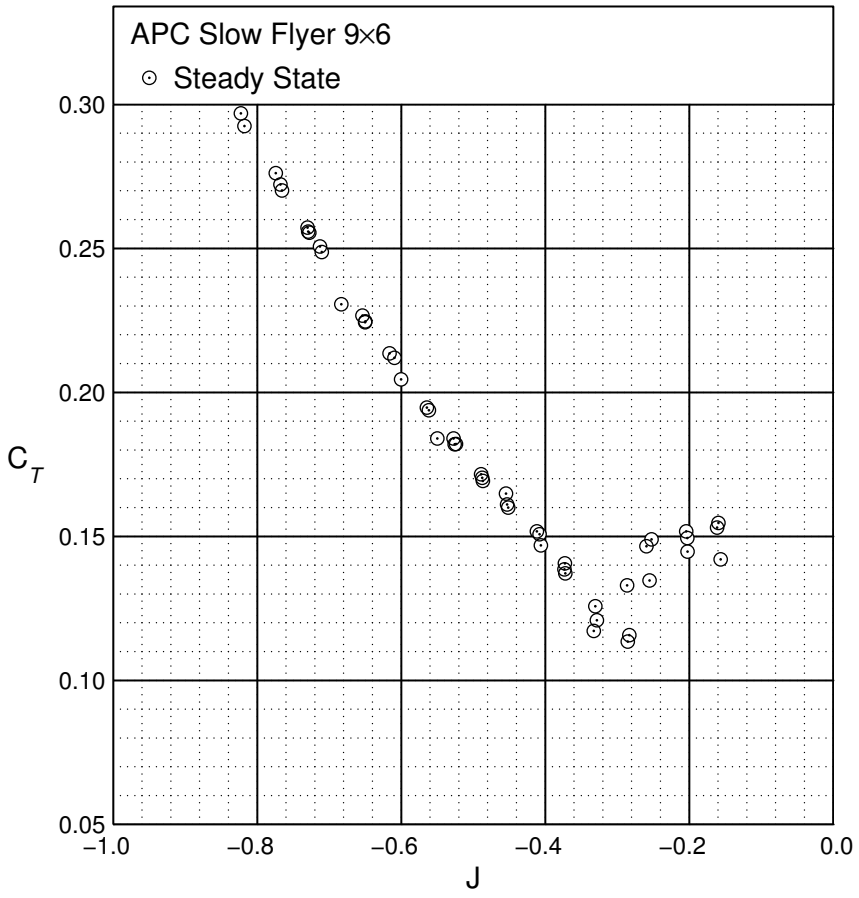

Fig. 4.7: Steady state thrust coefficient data for the APC Slow Flyer 9×6.

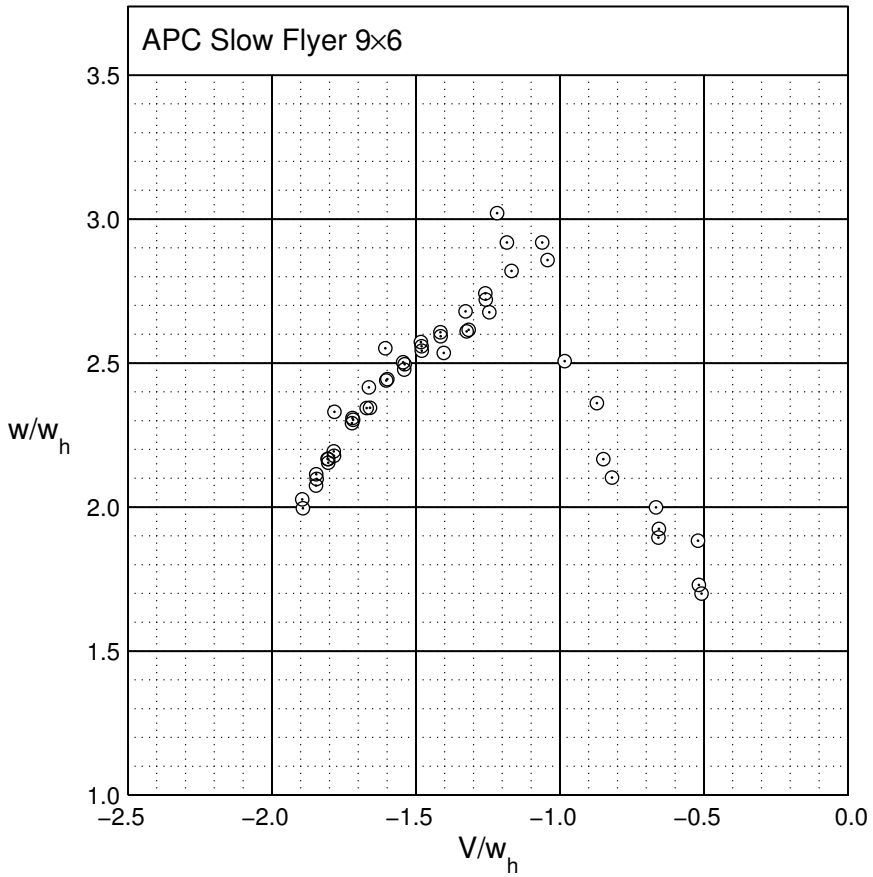

Fig. 4.8: Induced velocity data for the APC Slow Flyer 9×6.

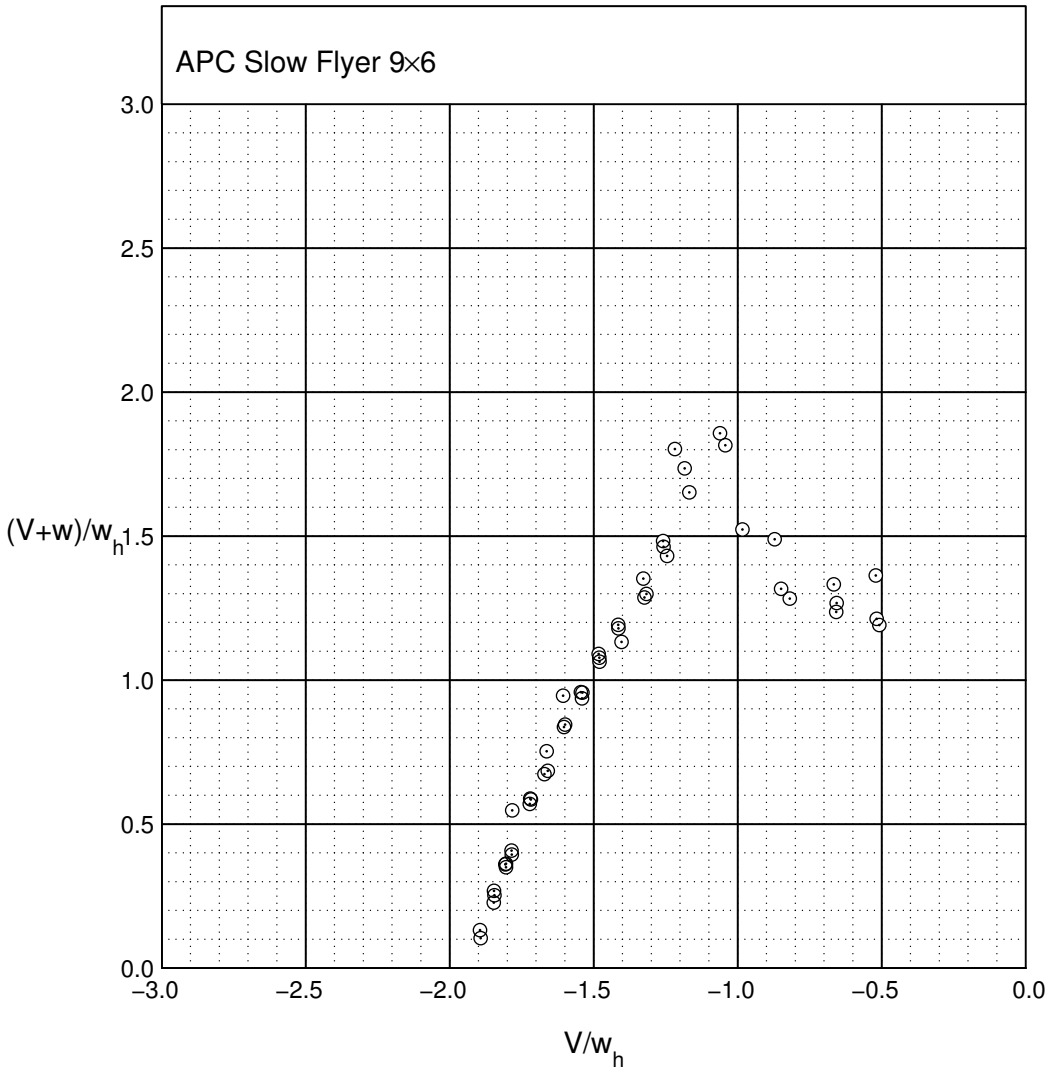

Fig. 4.9: Net inflow data for the APC Slow Flyer 9×6.

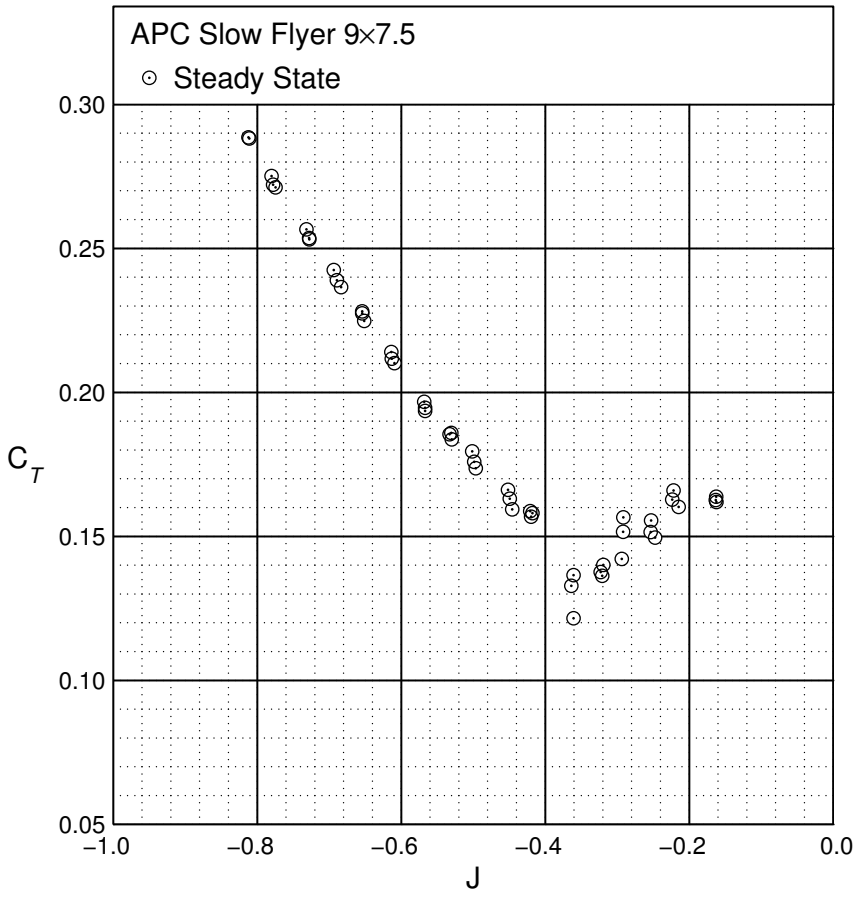

Fig. 4.10: Steady state thrust coefficient data for the APC Slow Flyer 9×7.5.

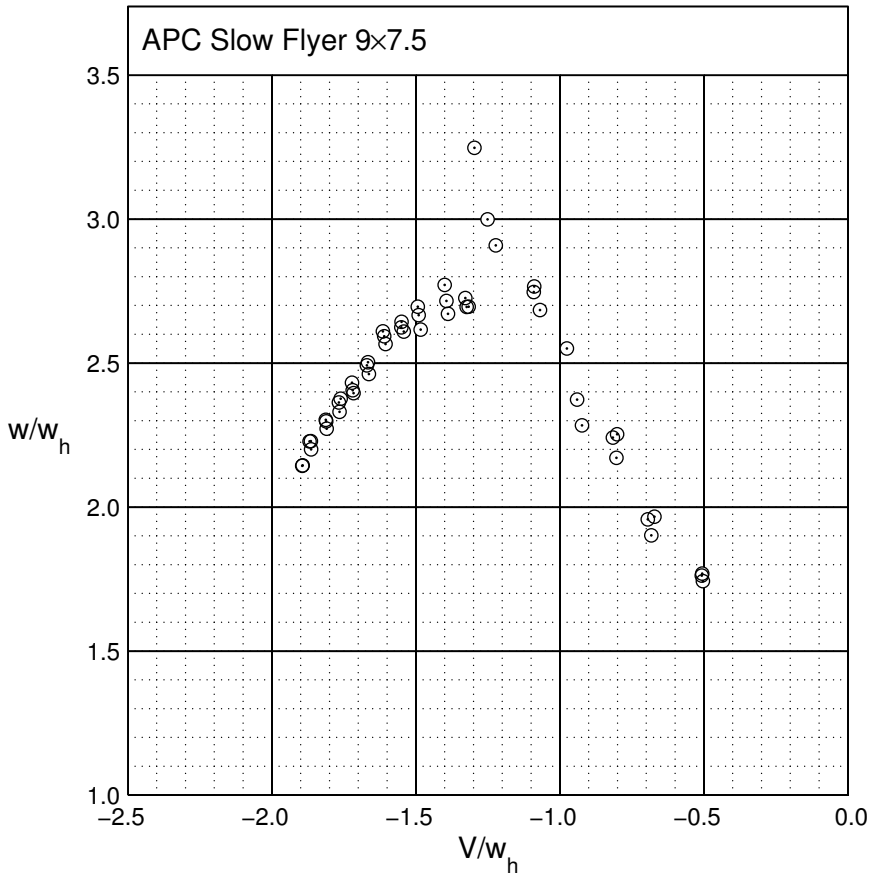

Fig. 4.11: Induced velocity data for the APC Slow Flyer 9×7.5.

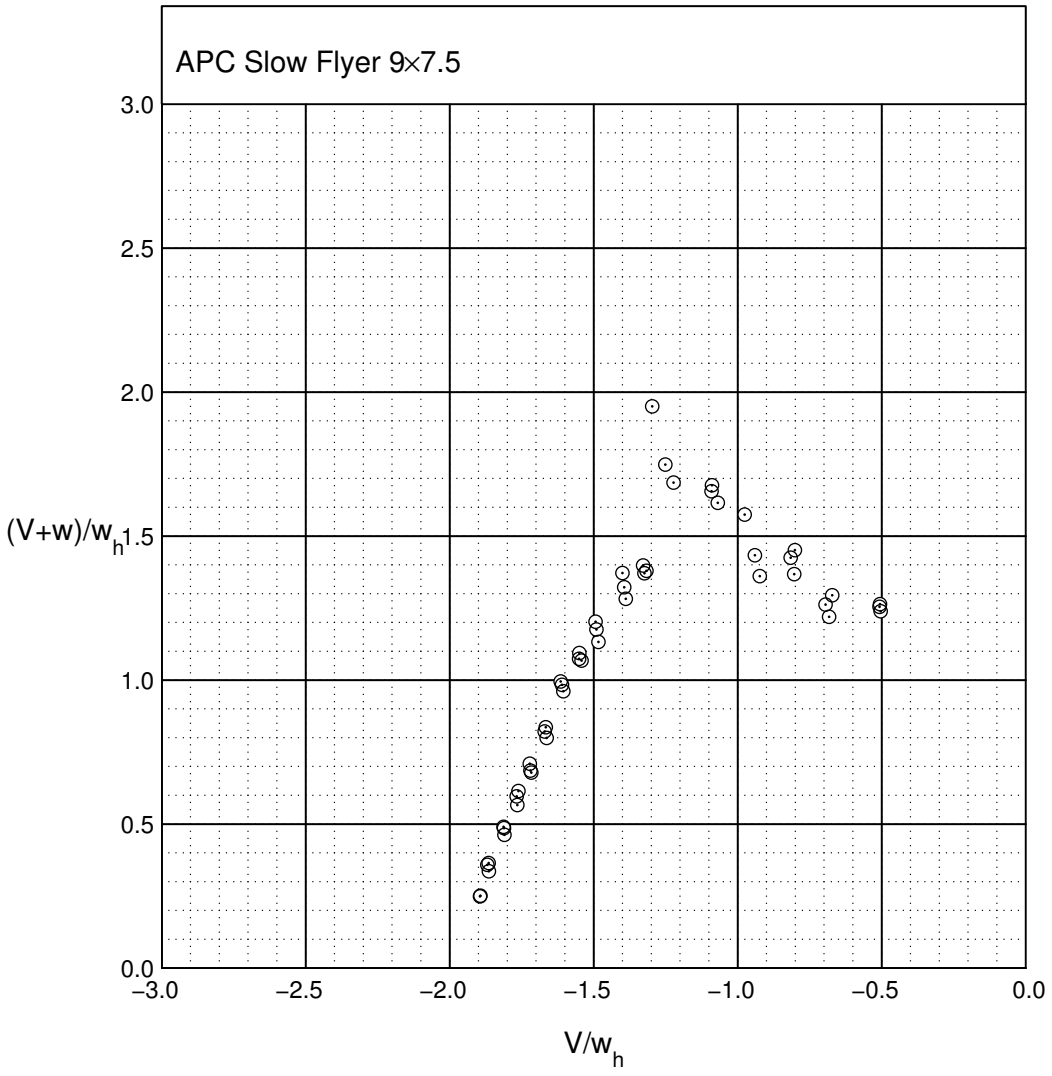

Fig. 4.12: Net inflow data for the APC Slow Flyer 9×7.5.

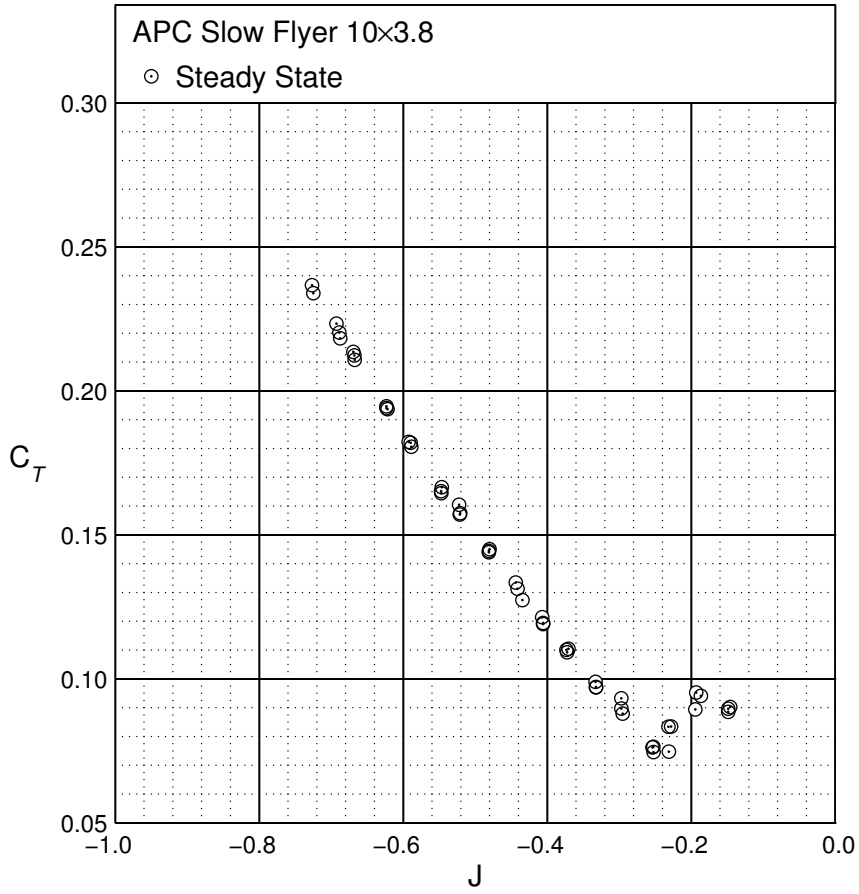

Fig. 4.13: Steady state thrust coefficient data for the APC Slow Flyer 10×3.8.

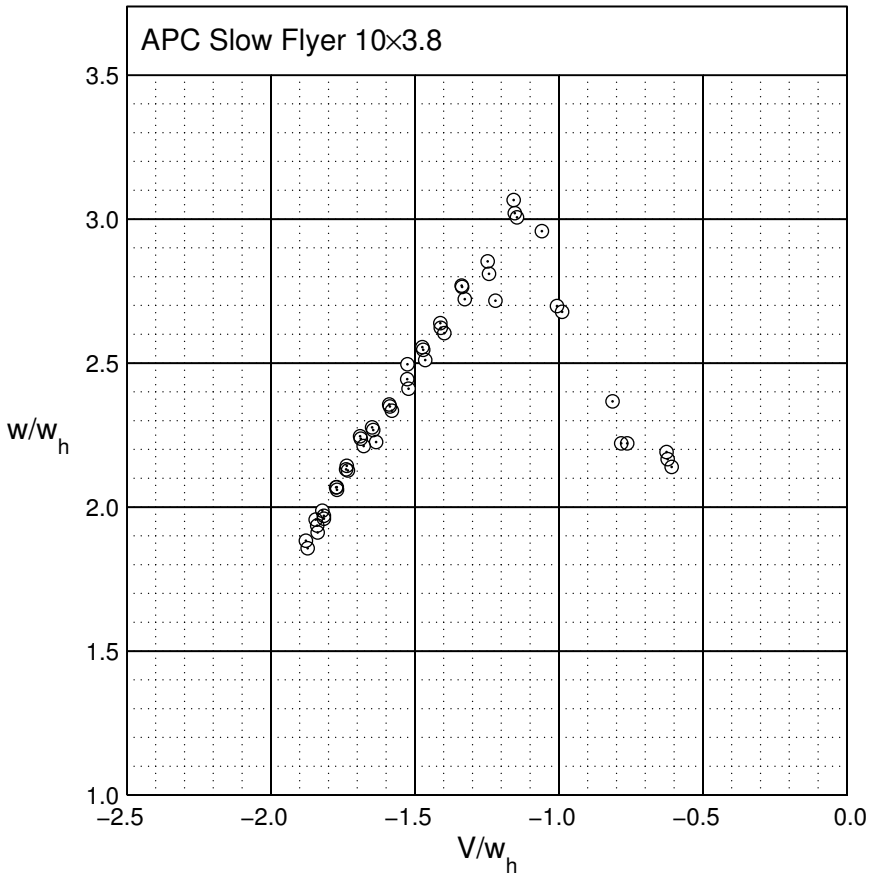

Fig. 4.14: Induced velocity data for the APC Slow Flyer 10×3.8.

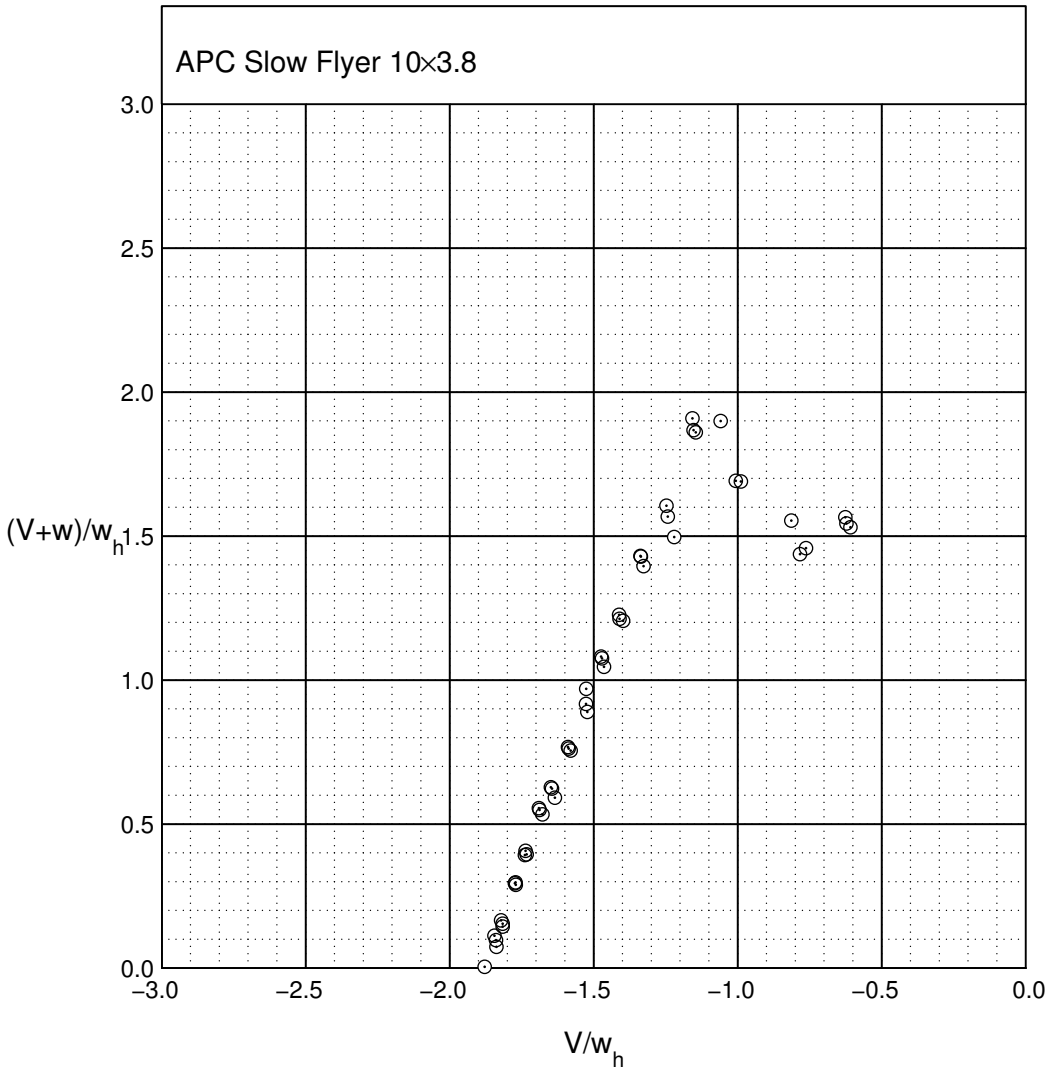

Fig. 4.15: Net inflow data for the APC Slow Flyer 10×3.8.

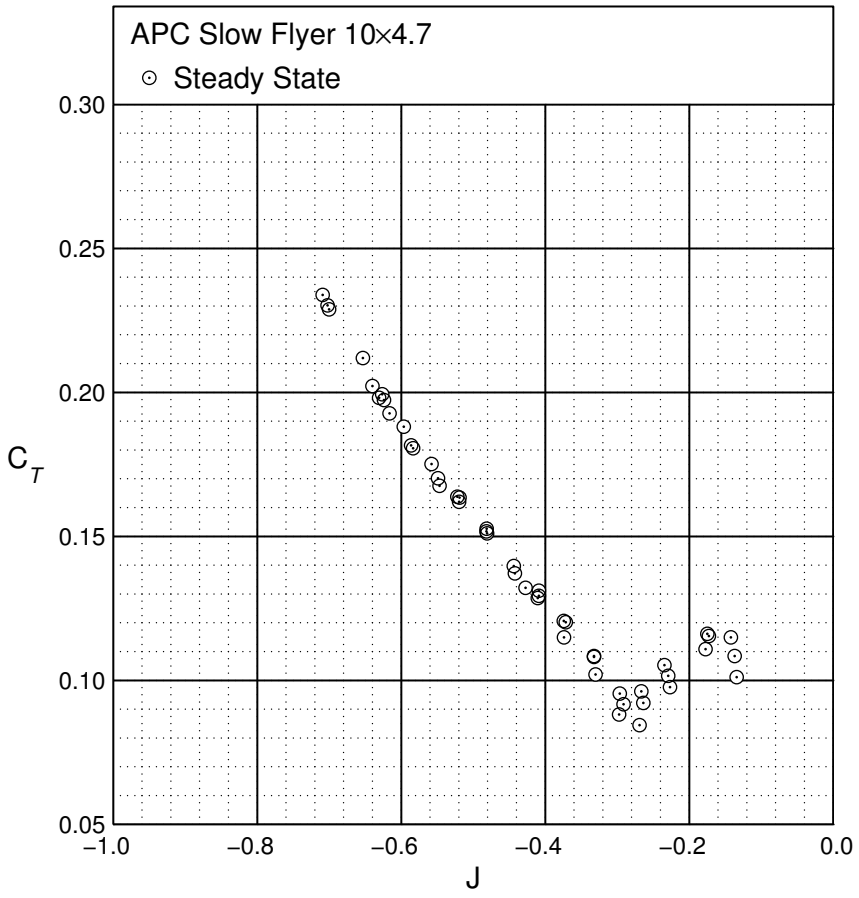

Fig. 4.16: Steady state thrust coefficient data for the APC Slow Flyer 10×4.7.

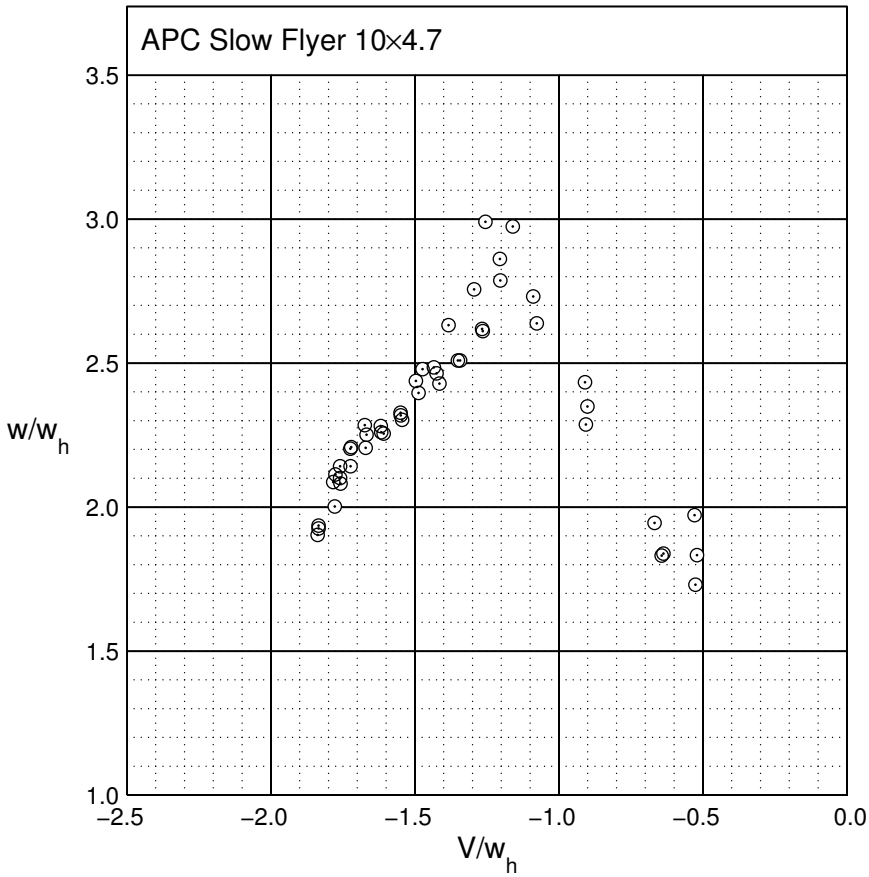

Fig. 4.17: Induced velocity data for the APC Slow Flyer 10×4.7.

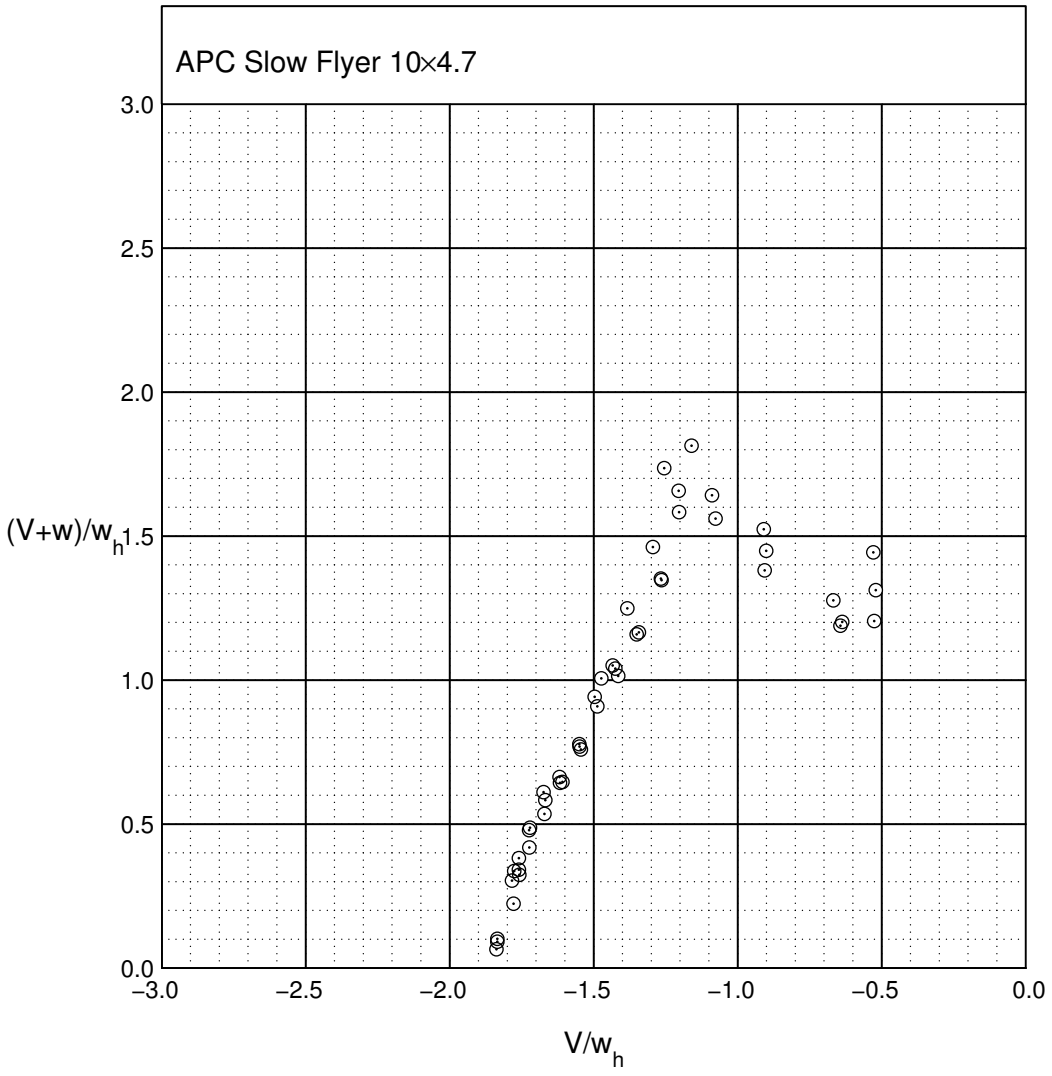

Fig. 4.18: Net inflow data for the APC Slow Flyer 10×4.7.

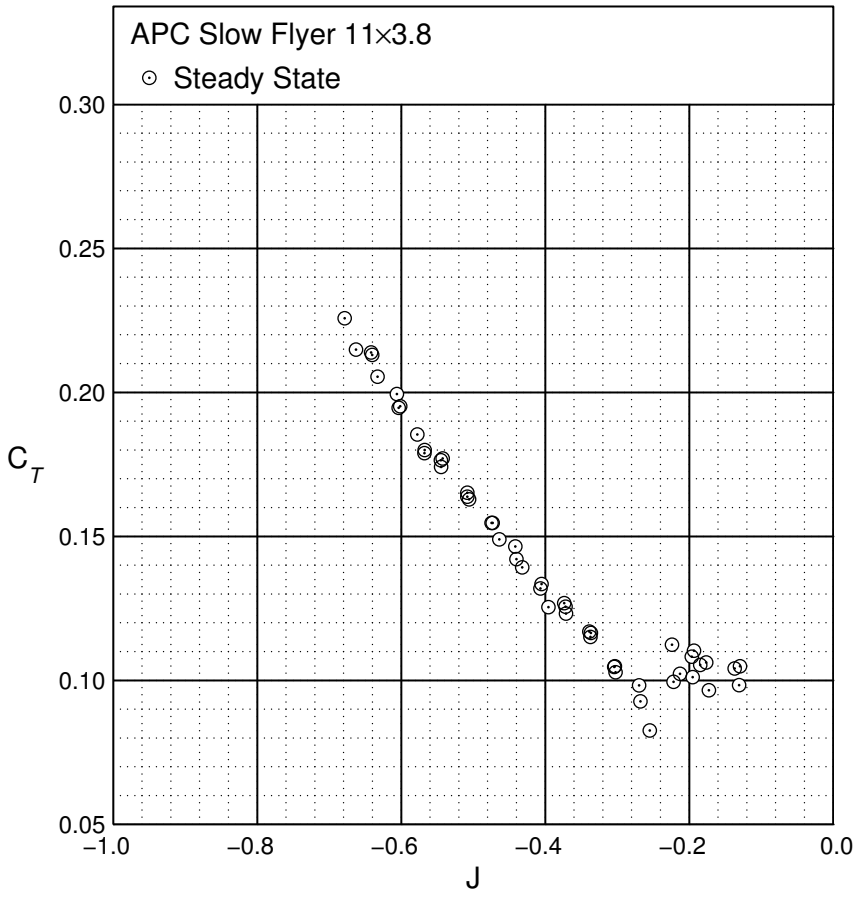

Fig. 4.19: Steady state thrust coefficient data for the APC Slow Flyer 11×3.8.

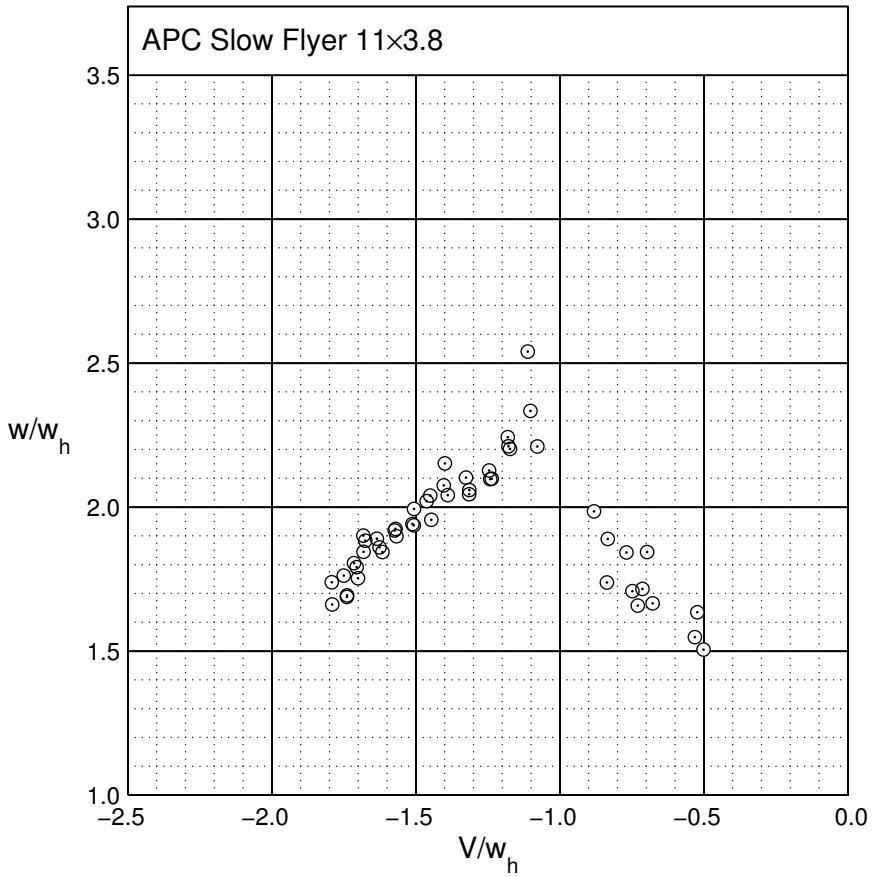

Fig. 4.20: Induced velocity data for the APC Slow Flyer 11×3.8.

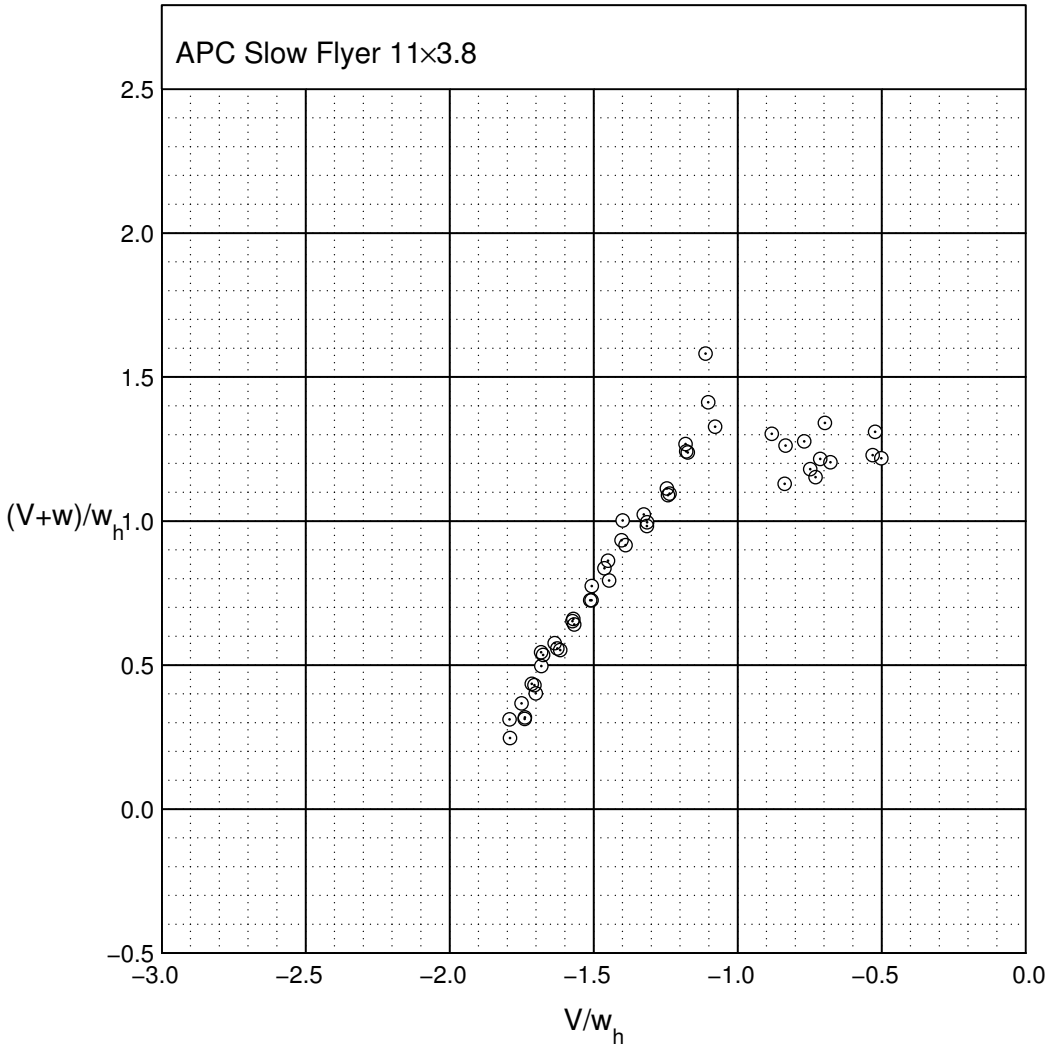

Fig. 4.21: Net inflow data for the APC Slow Flyer 11×3.8.

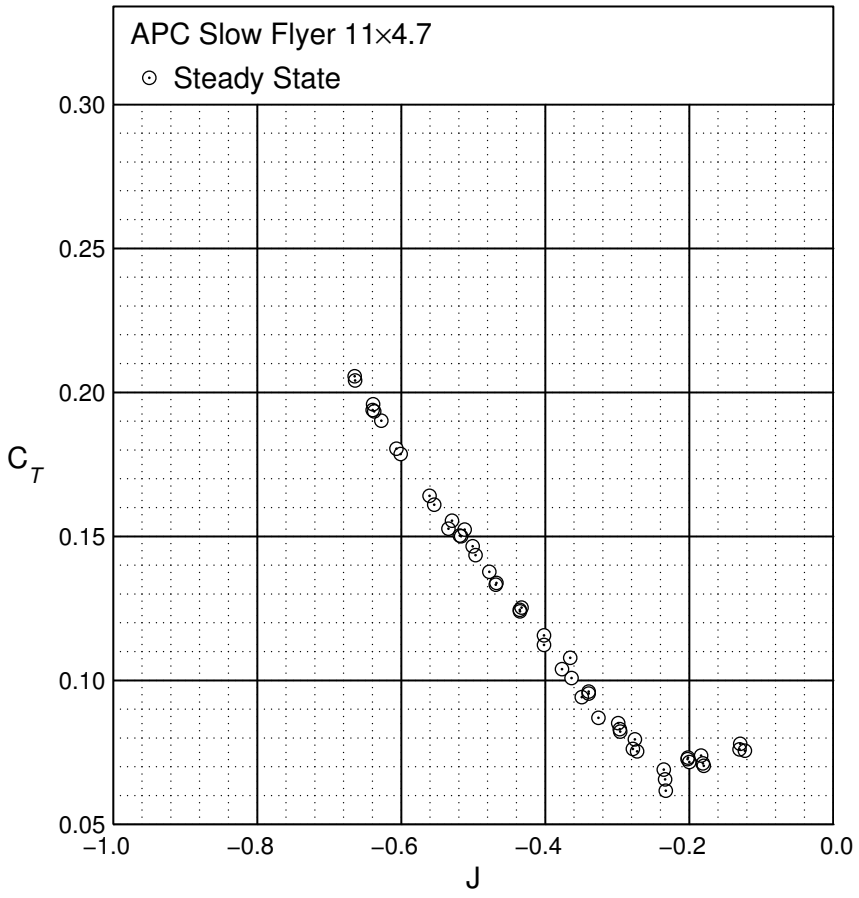

Fig. 4.22: Steady state thrust coefficient data for the APC Slow Flyer 11×4.7.

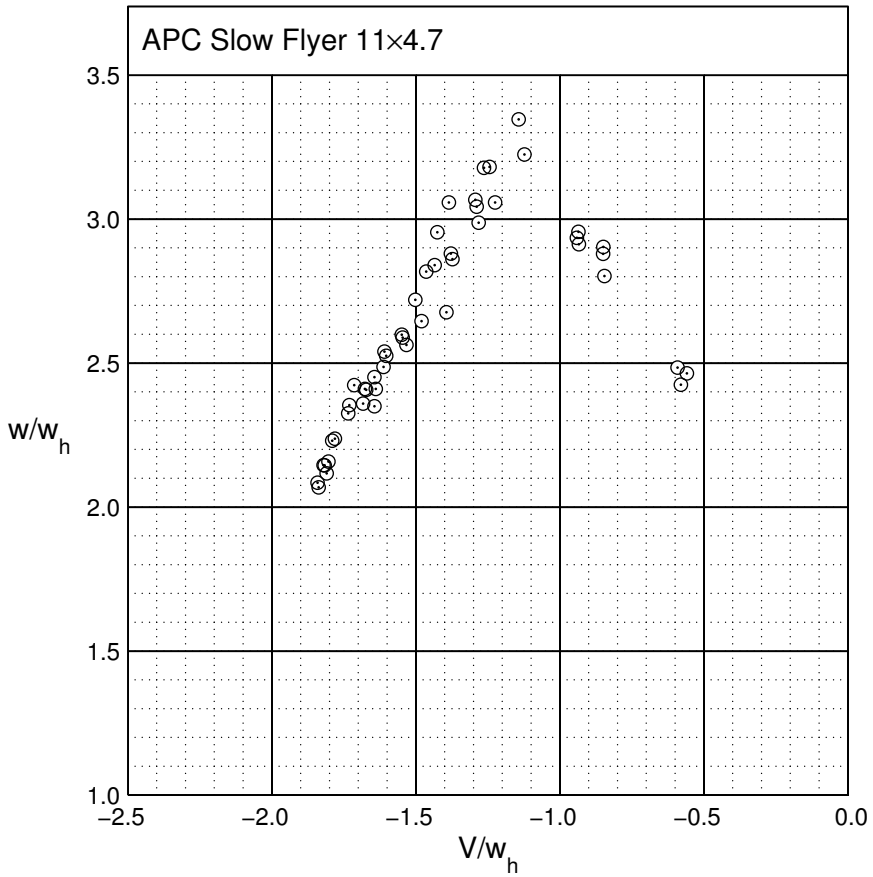

Fig. 4.23: Induced velocity data for the APC Slow Flyer 11×4.7.

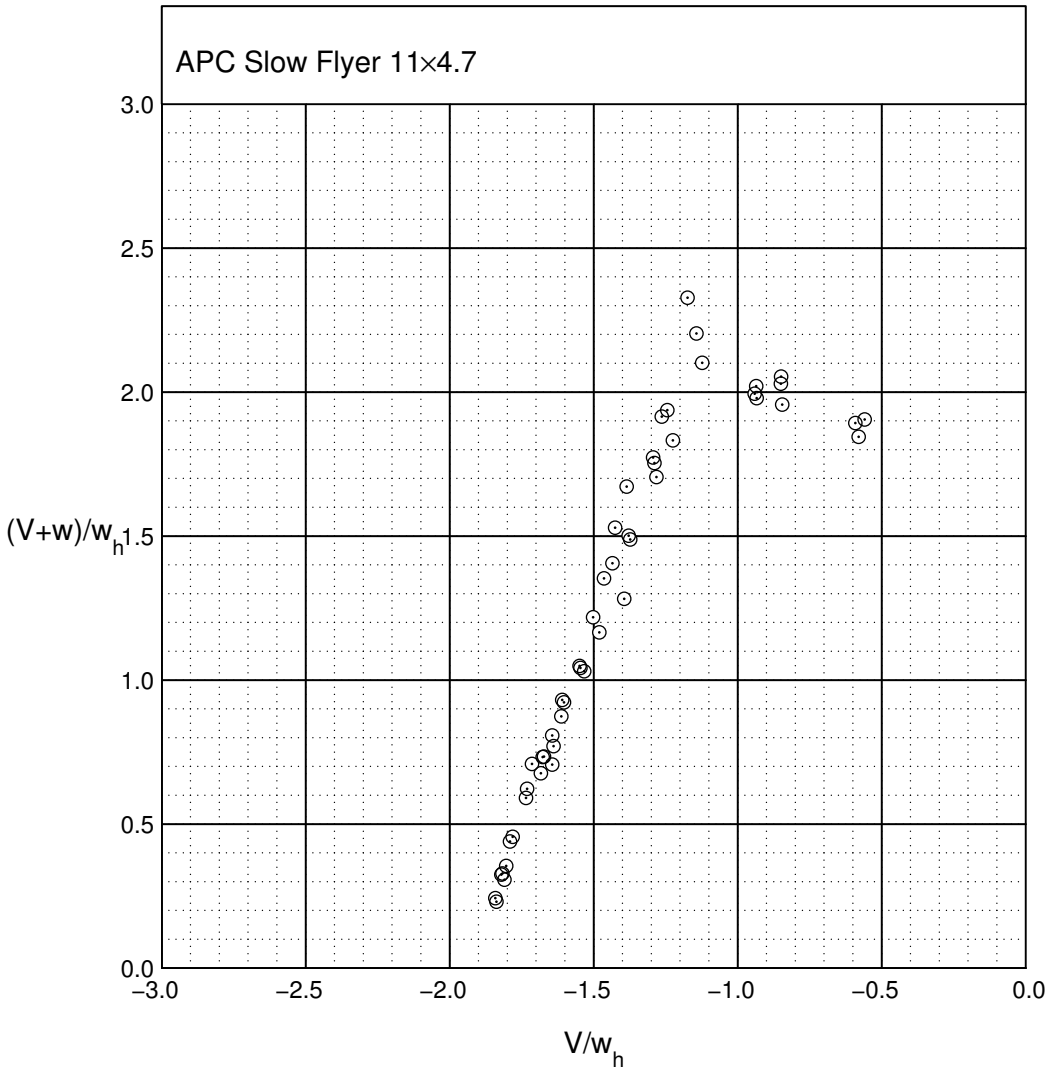

Fig. 4.24: Net inflow data for the APC Slow Flyer 11×4.7.

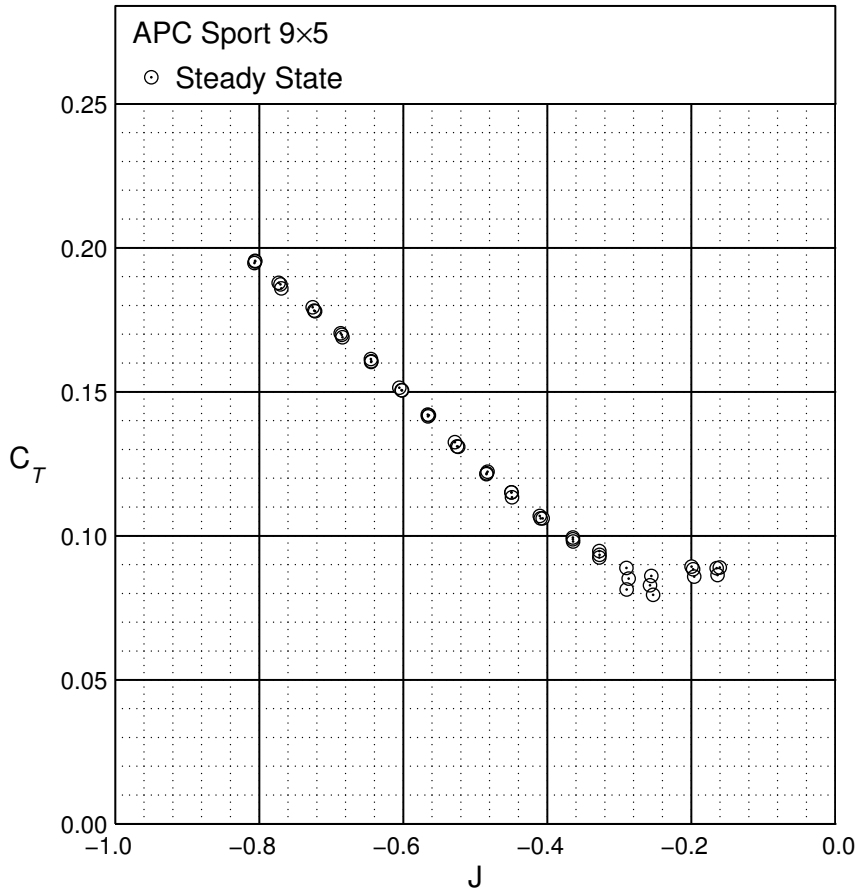

Fig. 4.25: Steady state thrust coefficient data for the APC Sport 9×5.

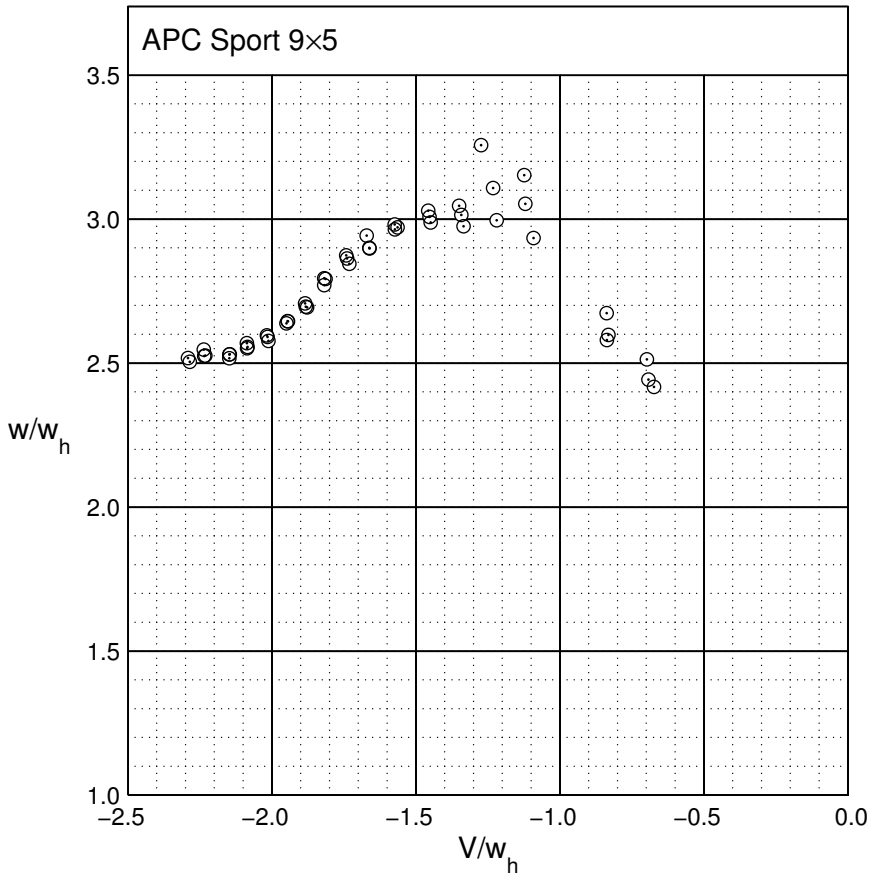

Fig. 4.26: Induced velocity data for the APC Sport 9×5.

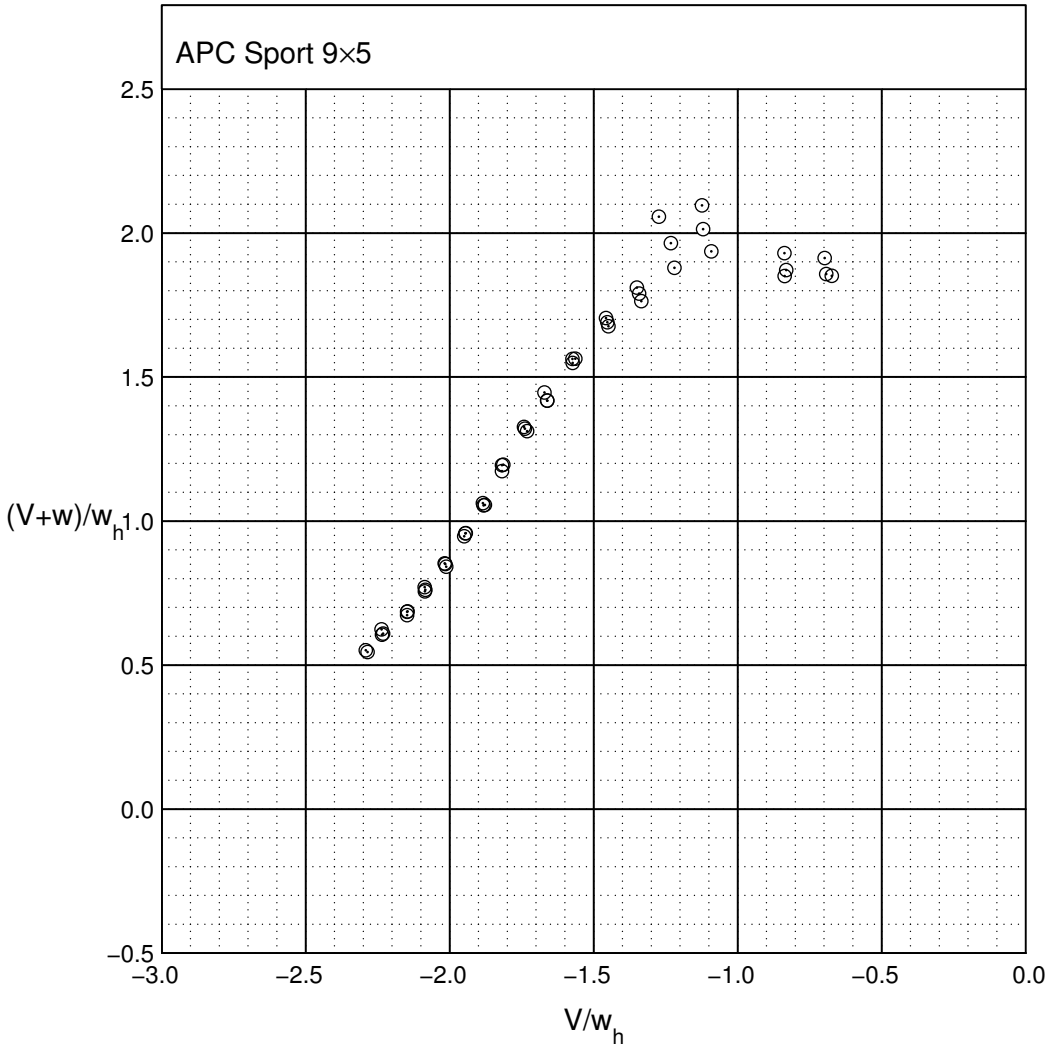

Fig. 4.27: Net inflow data for the APC Sport 9×5.

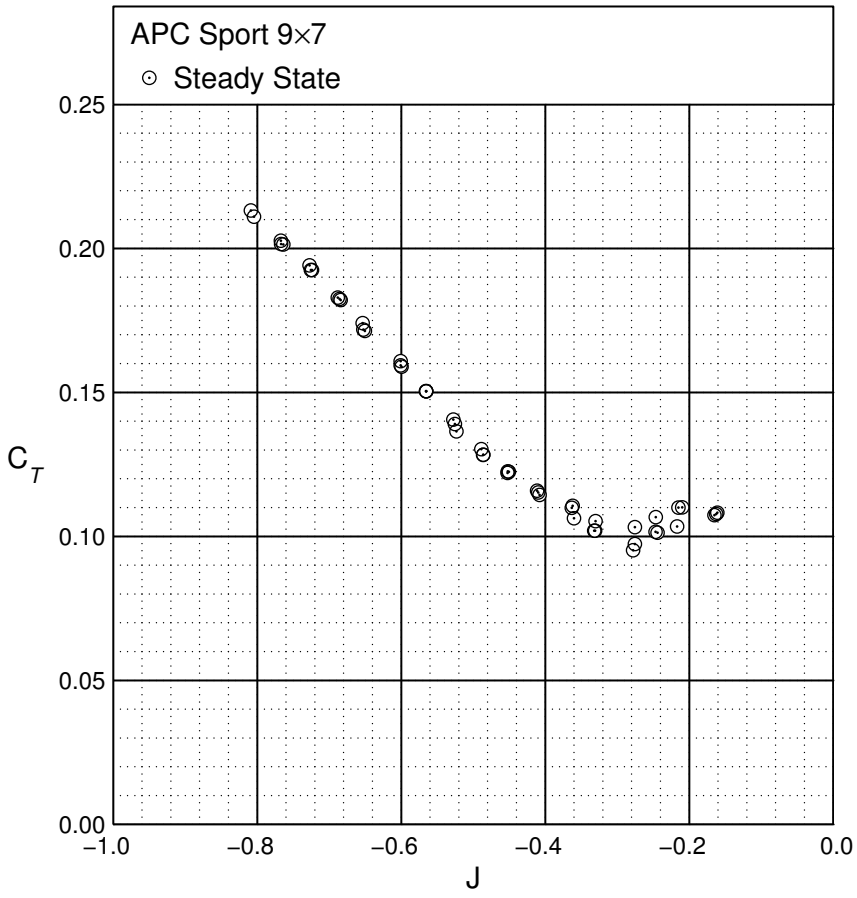

Fig. 4.28: Steady state thrust coefficient data for the APC Sport 9×7.

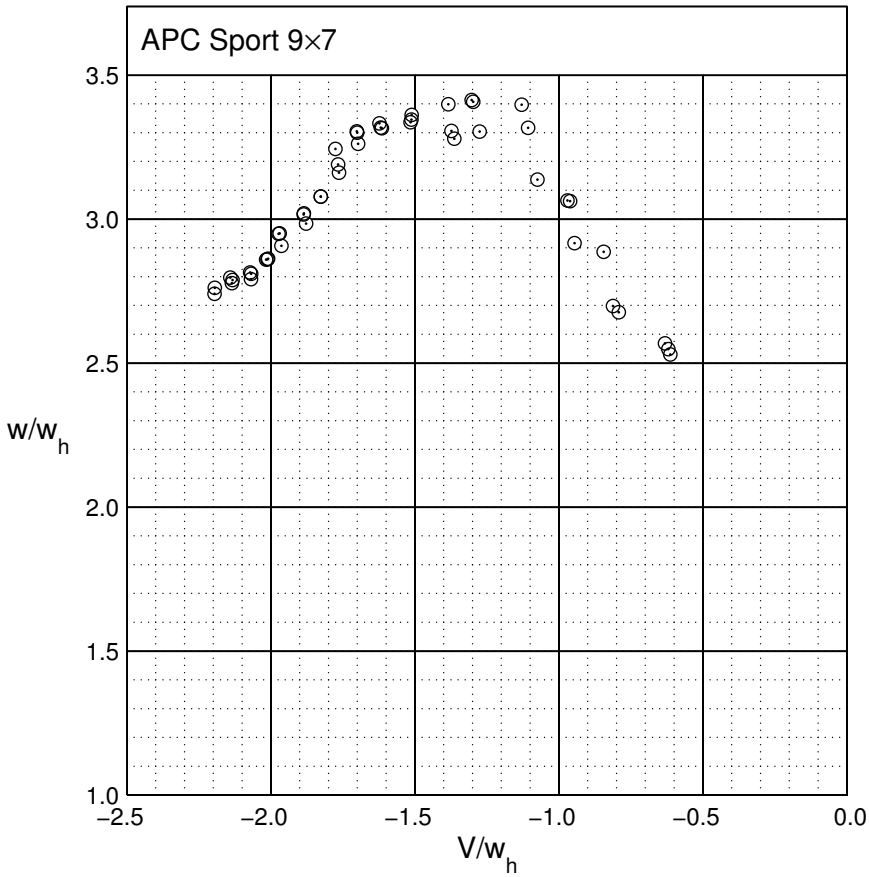

Fig. 4.29: Induced velocity data for the APC Sport 9×7.

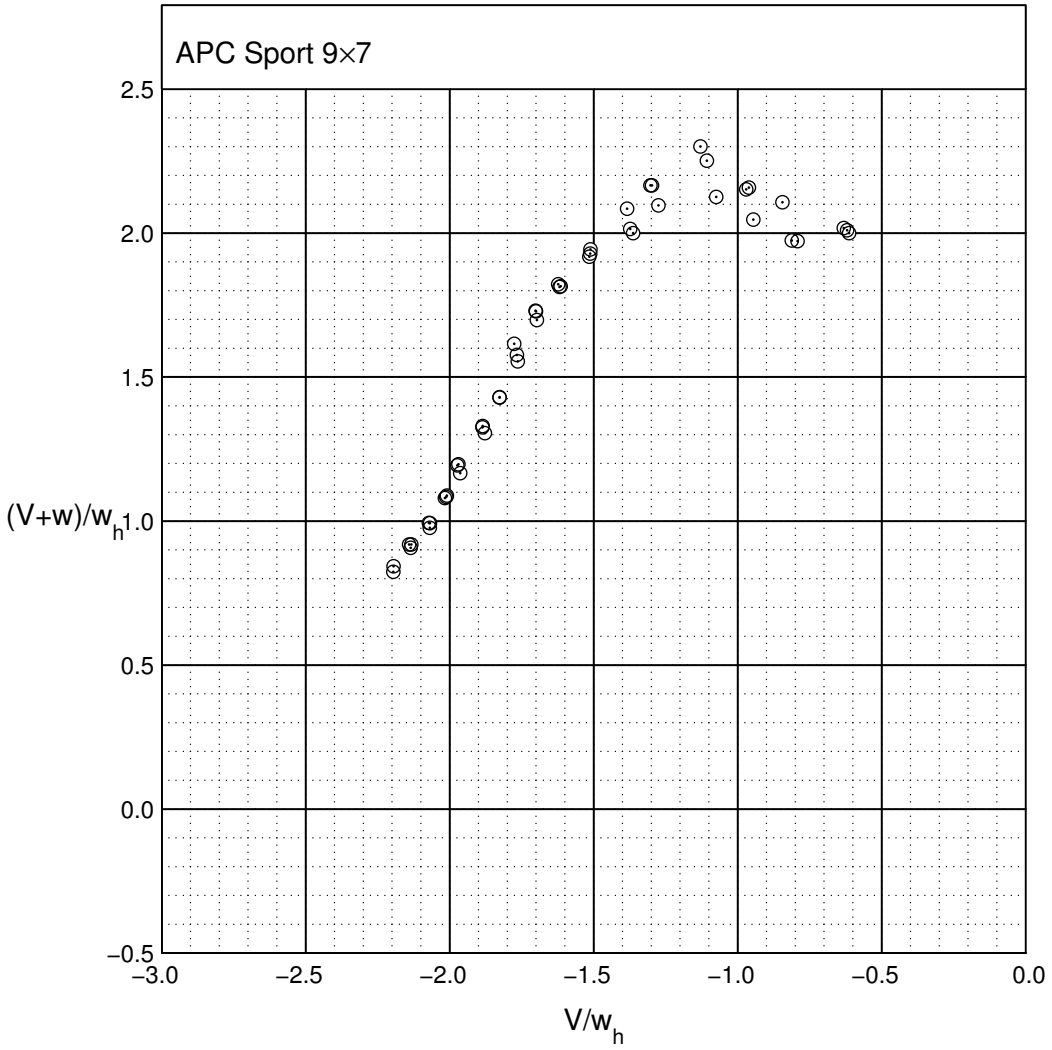

Fig. 4.30: Net inflow data for the APC Sport 9×7.

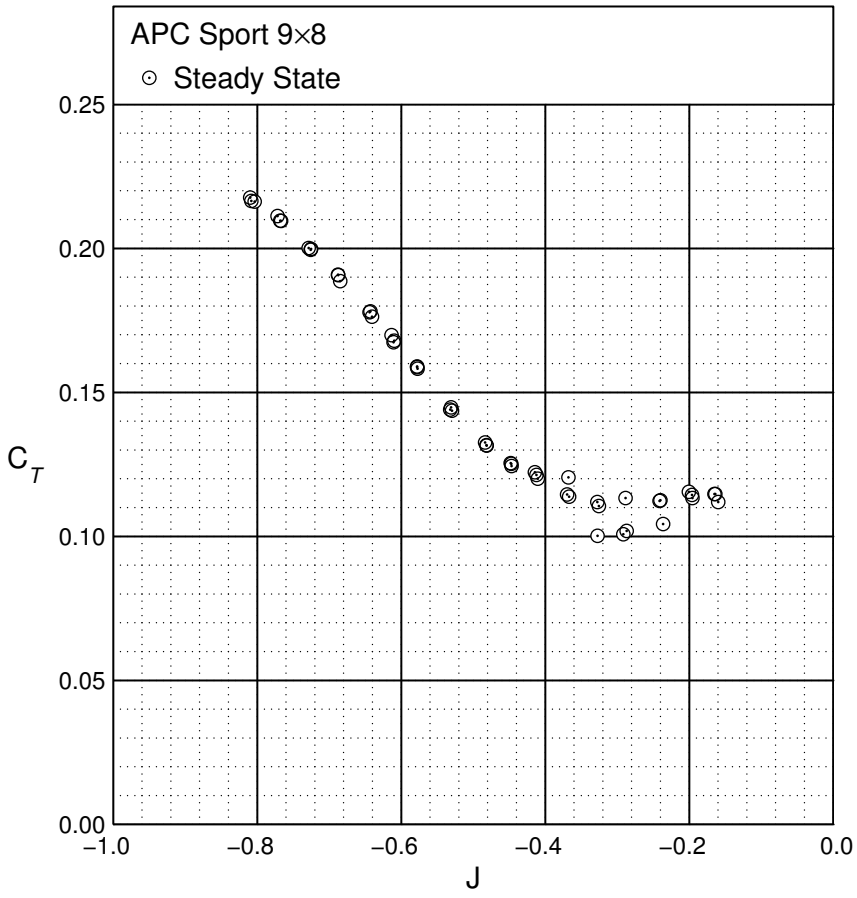

Fig. 4.31: Steady state thrust coefficient data for the APC Sport 9×8.

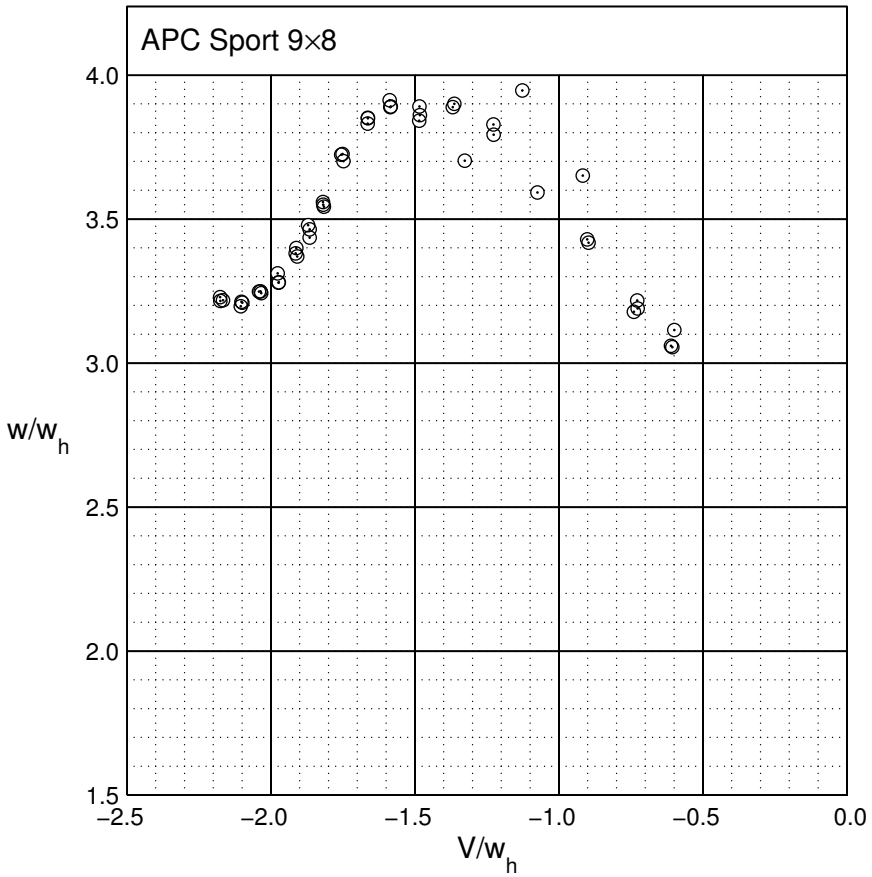

Fig. 4.32: Induced velocity data for the APC Sport 9×8.

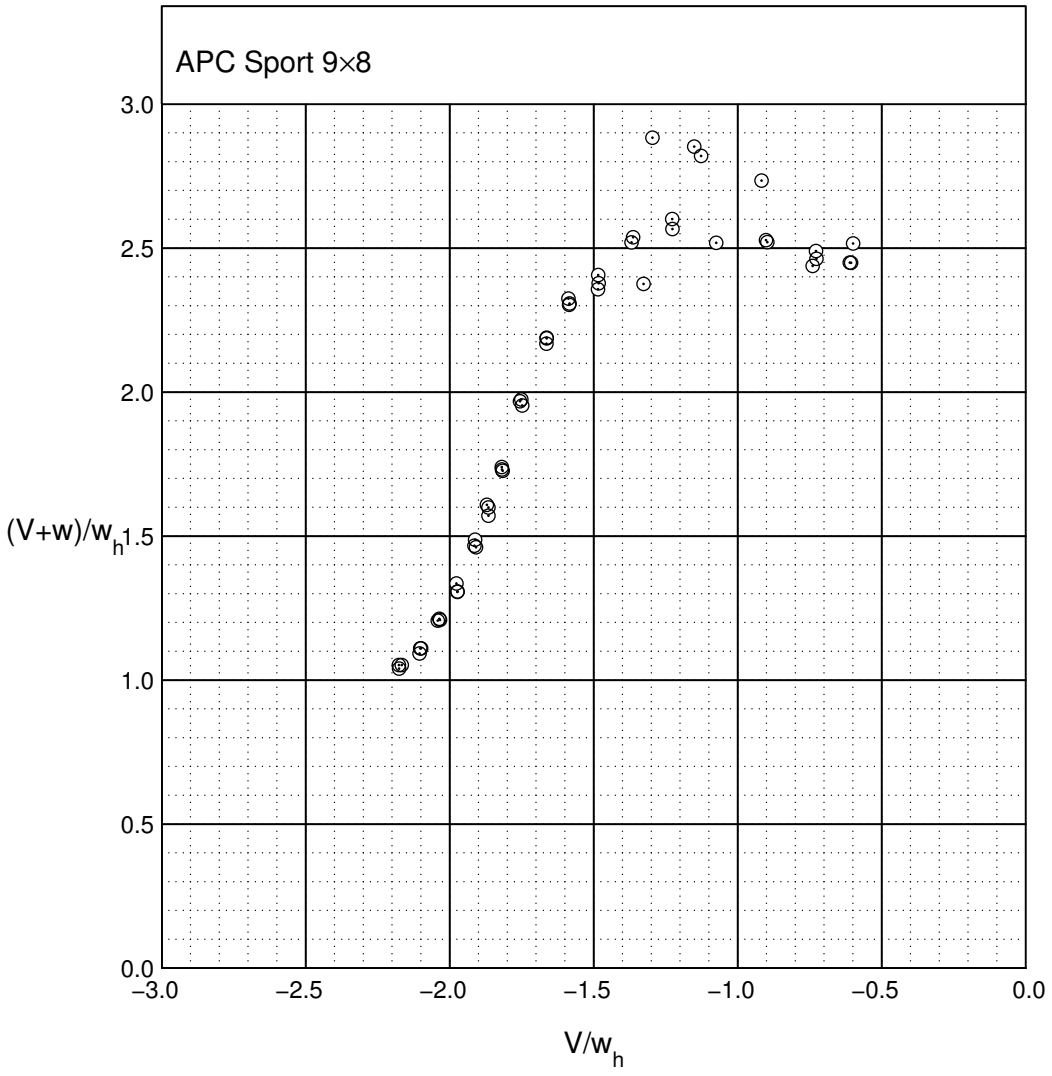

Fig. 4.33: Net inflow data for the APC Sport 9×8.

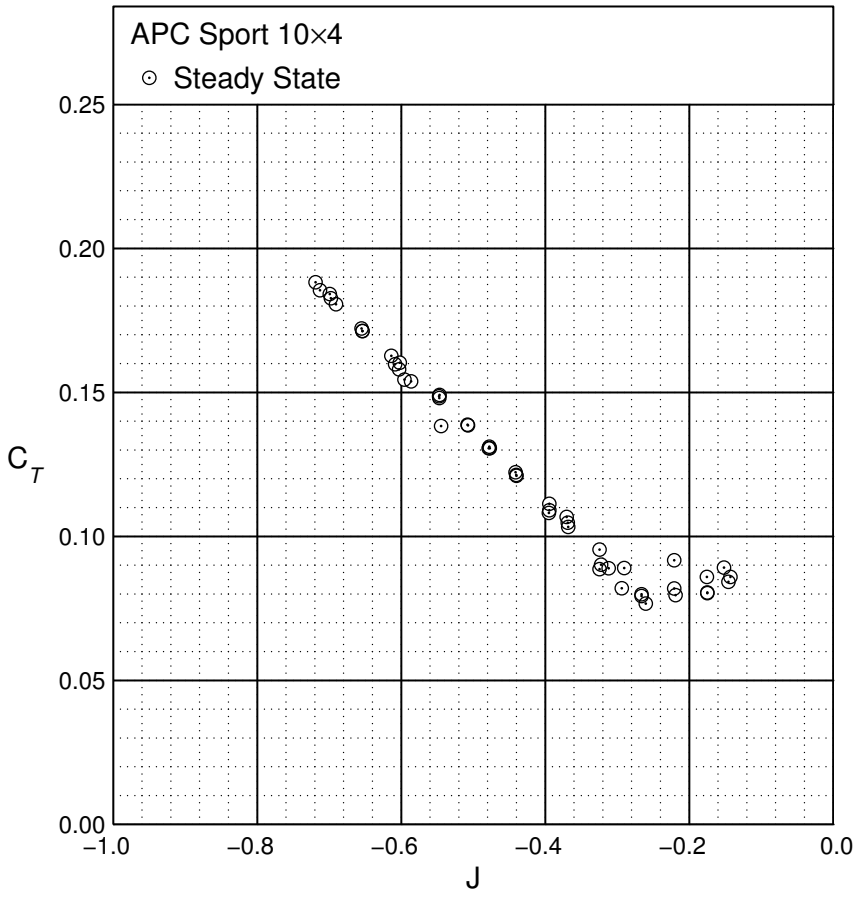

Fig. 4.34: Steady state thrust coefficient data for the APC Sport 10×4.

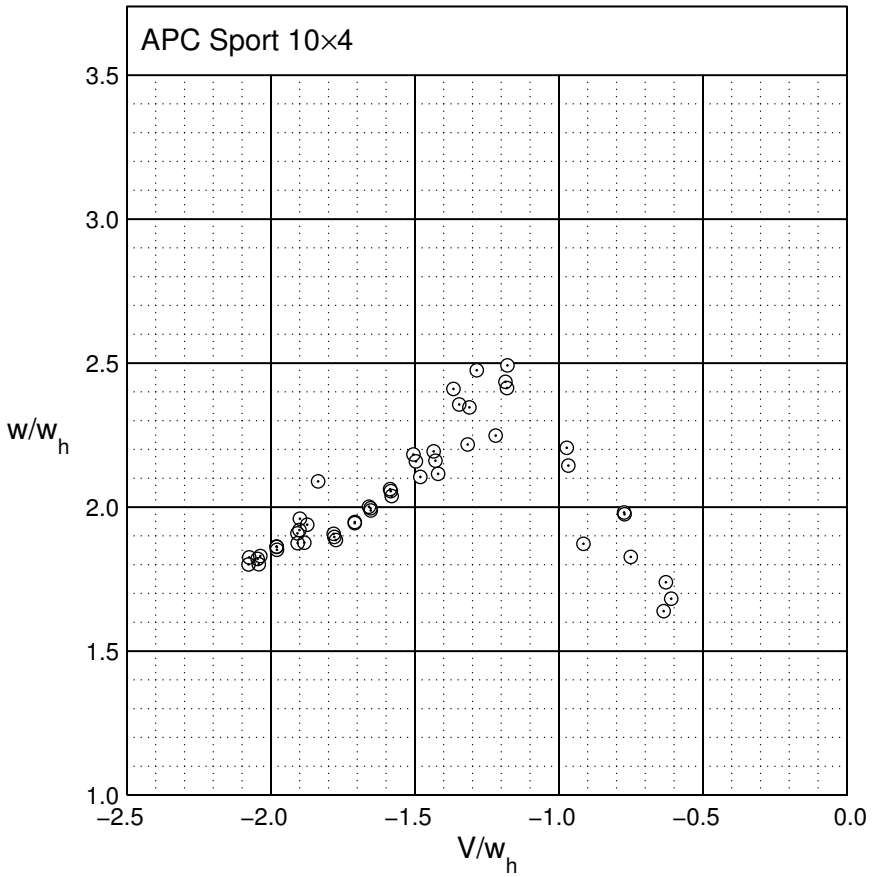

Fig. 4.35: Induced velocity data for the APC Sport 10×4.

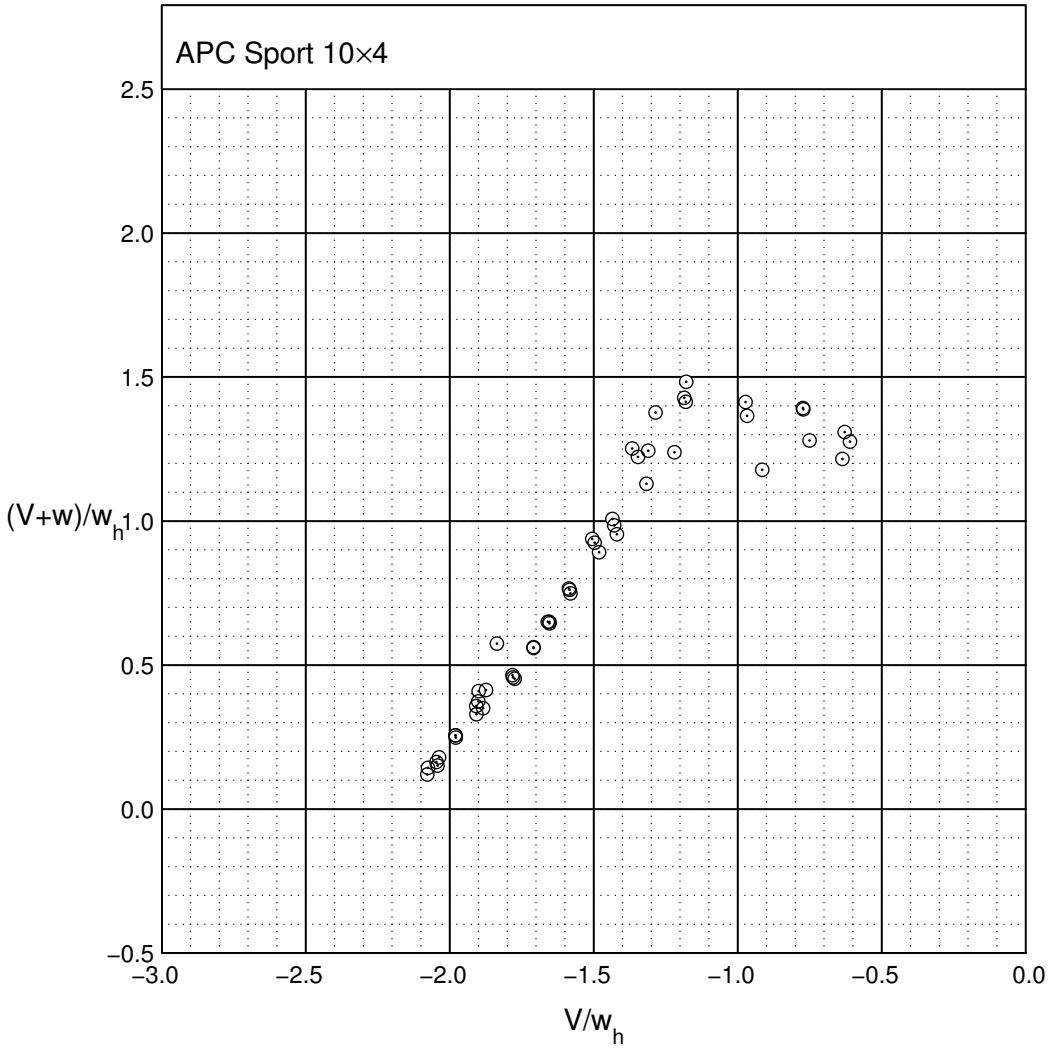

Fig. 4.36: Net inflow data for the APC Sport 10×4.

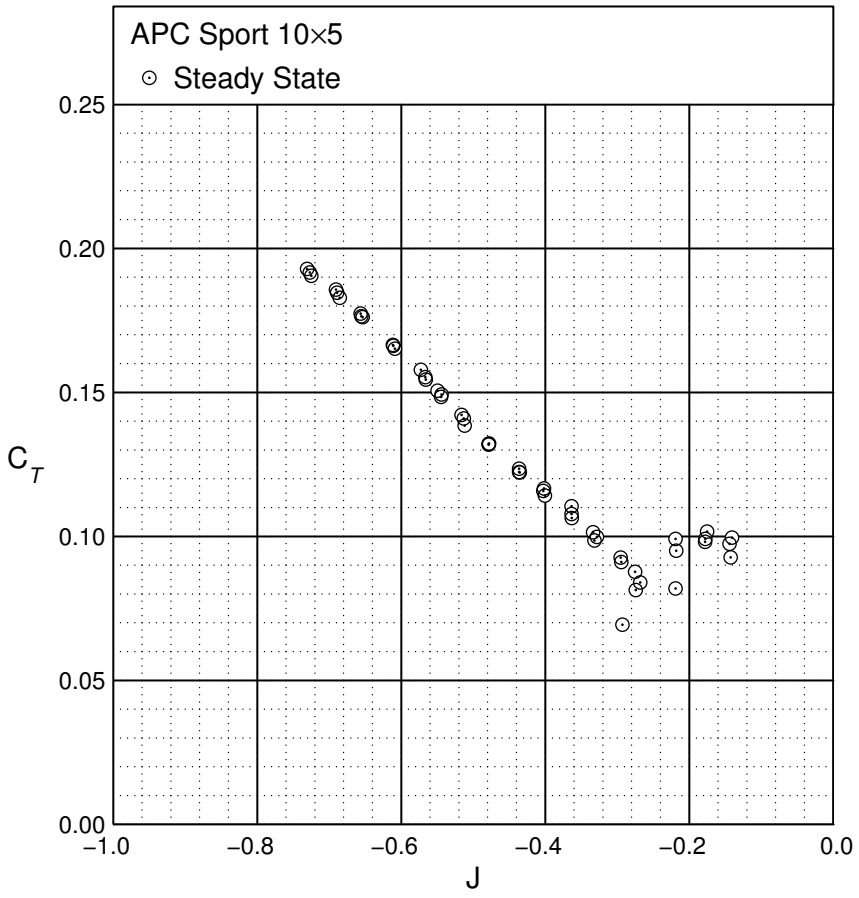

Fig. 4.37: Steady state thrust coefficient data for the APC Sport 10×5.

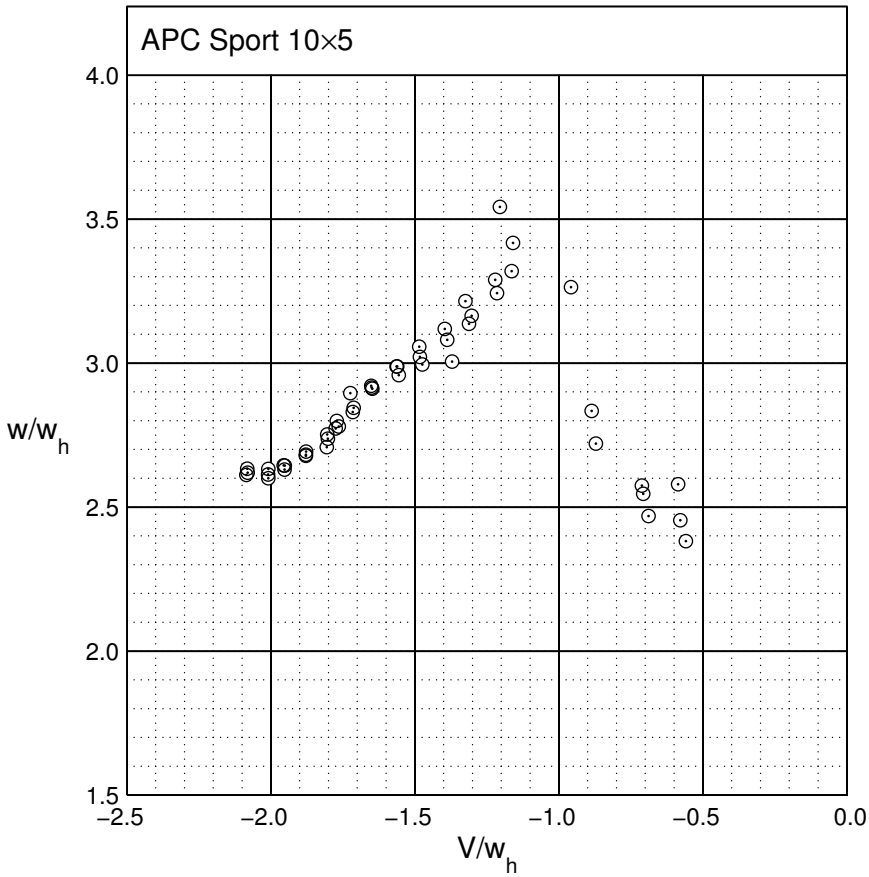

Fig. 4.38: Induced velocity data for the APC Sport 10×5.

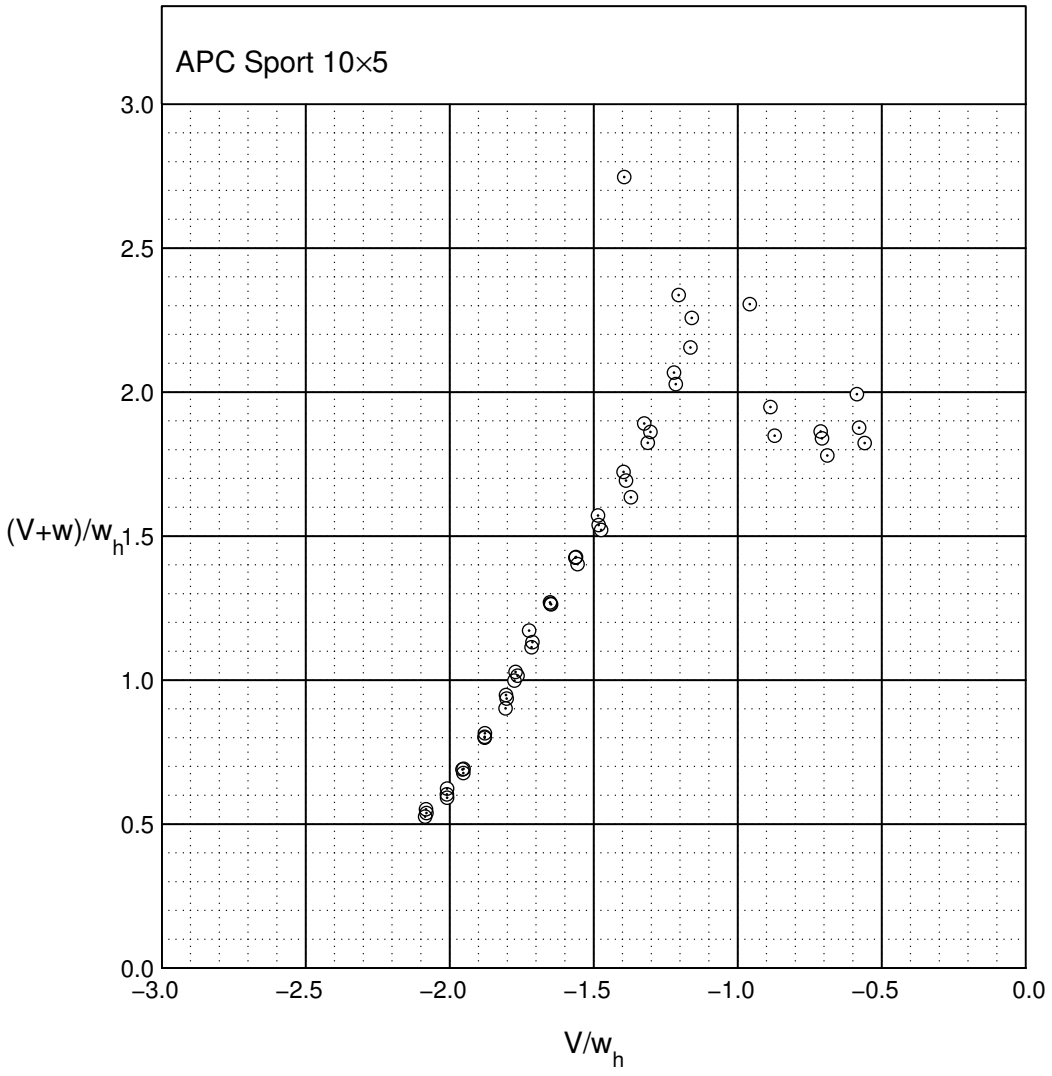

Fig. 4.39: Net inflow data for the APC Sport 10×5.

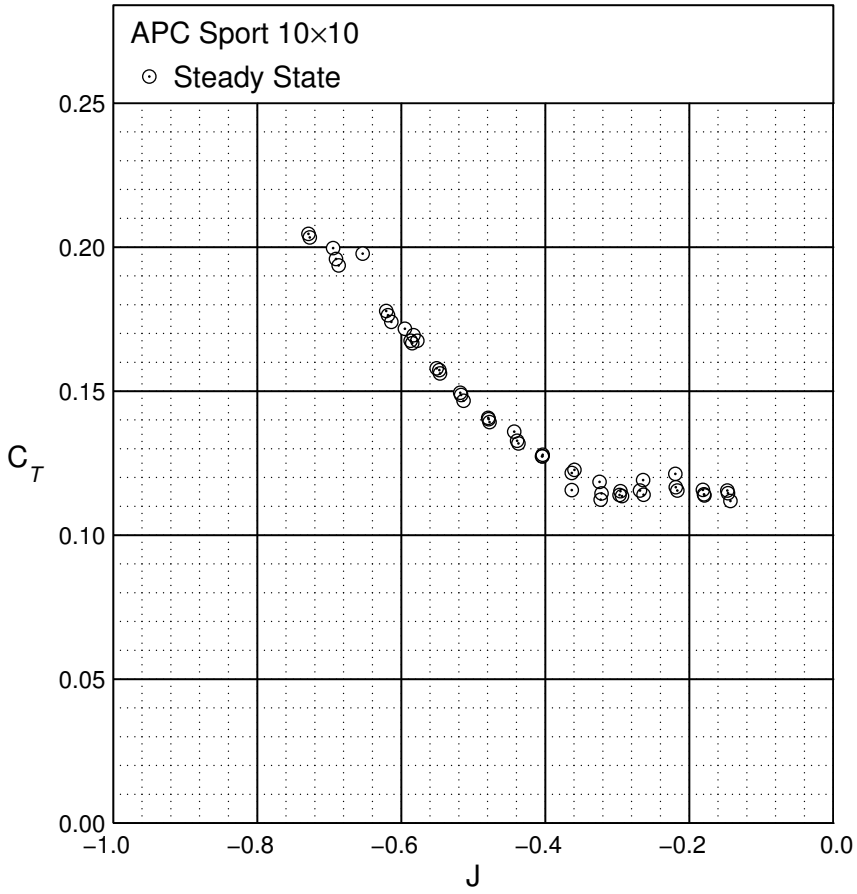

Fig. 4.40: Steady state thrust coefficient data for the APC Sport 10×10.

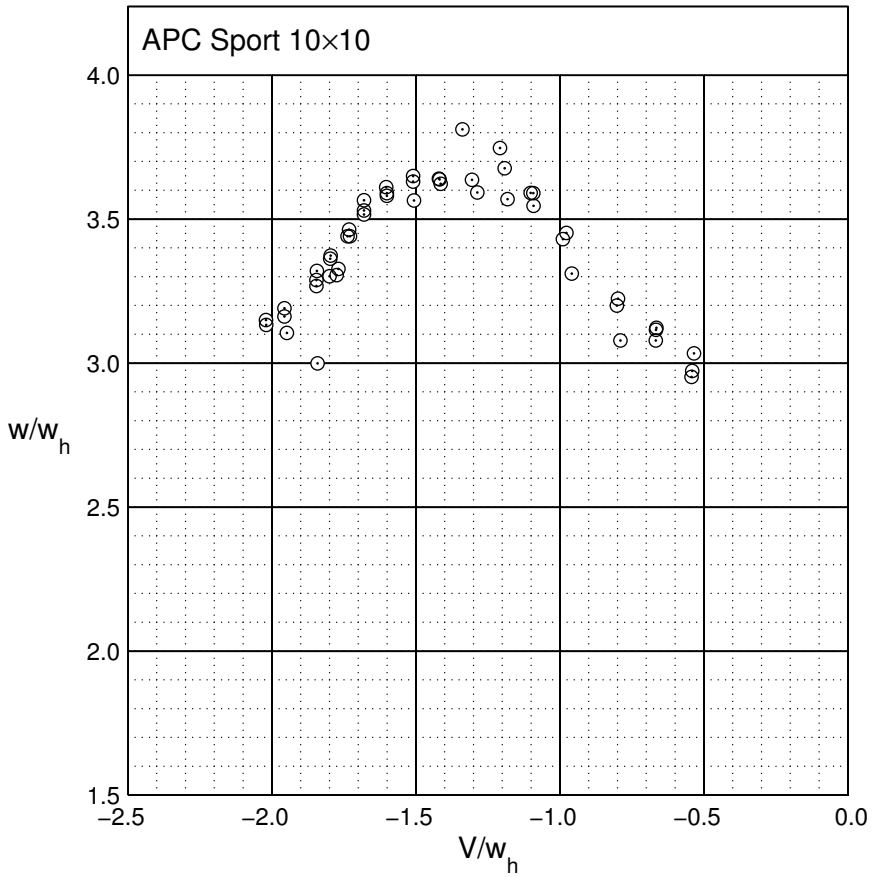

Fig. 4.41: Induced velocity data for the APC Sport 10×10.

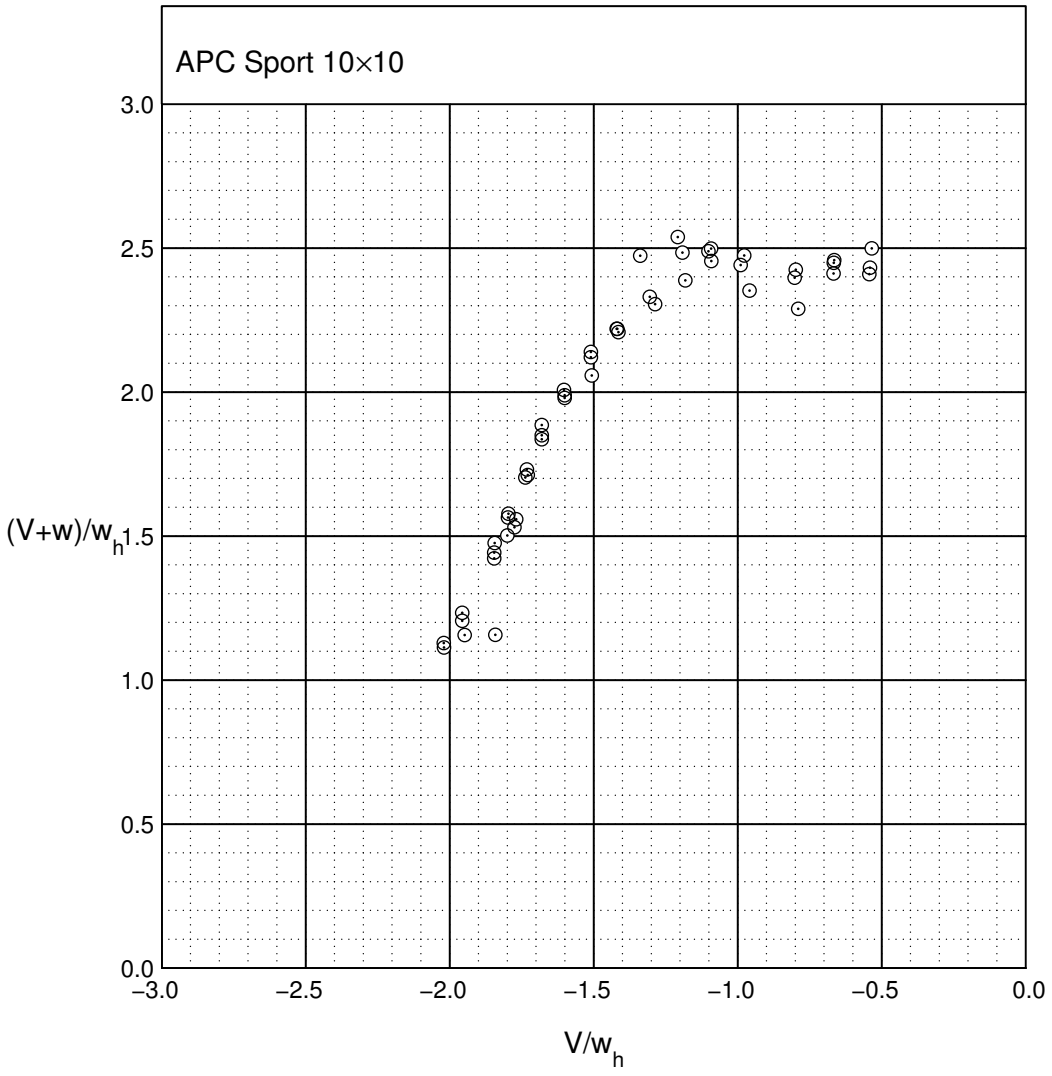

Fig. 4.42: Net inflow data for the APC Sport 10×10.

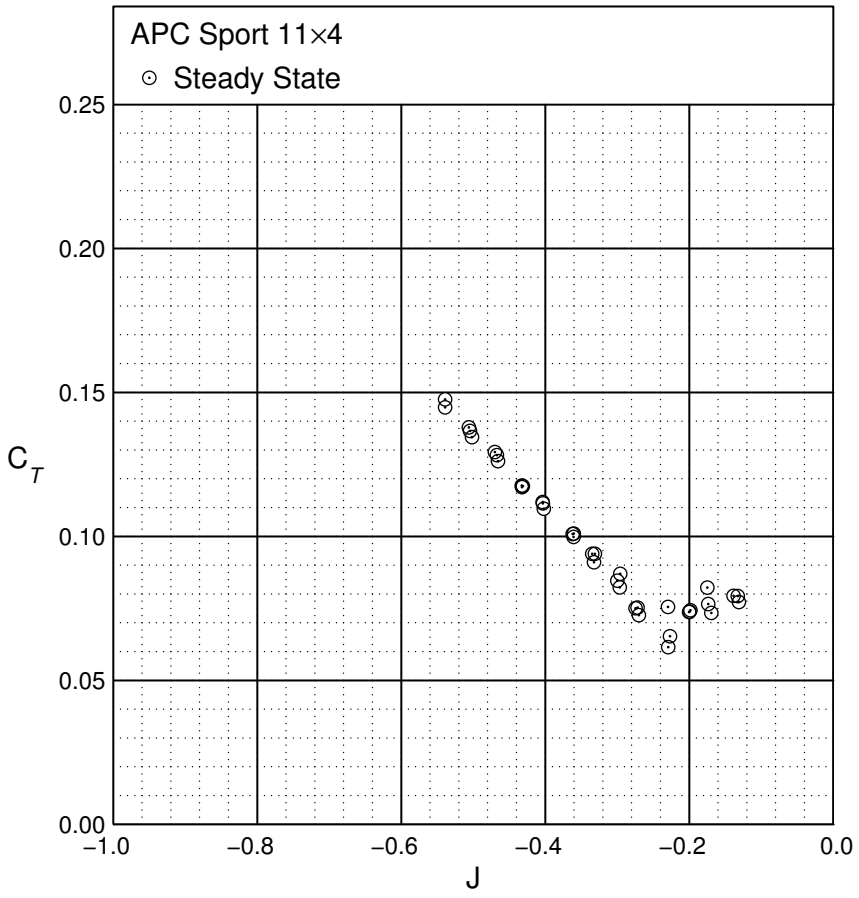

Fig. 4.43: Steady state thrust coefficient data for the APC Sport 11×4.

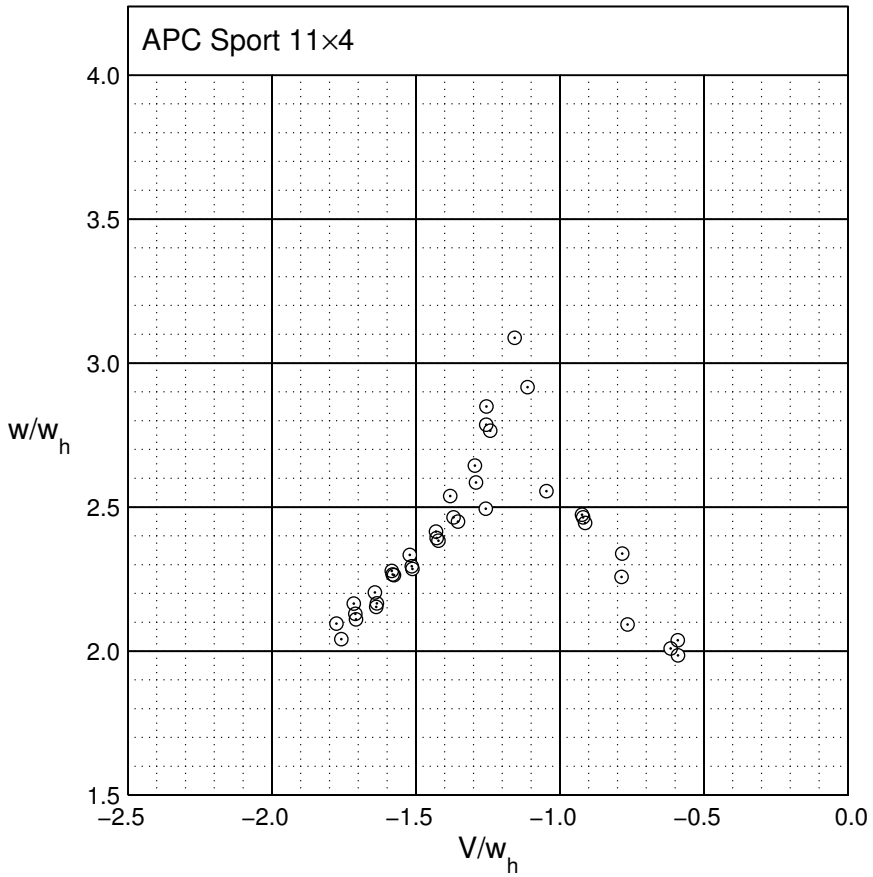

Fig. 4.44: Induced velocity data for the APC Sport 11×4.

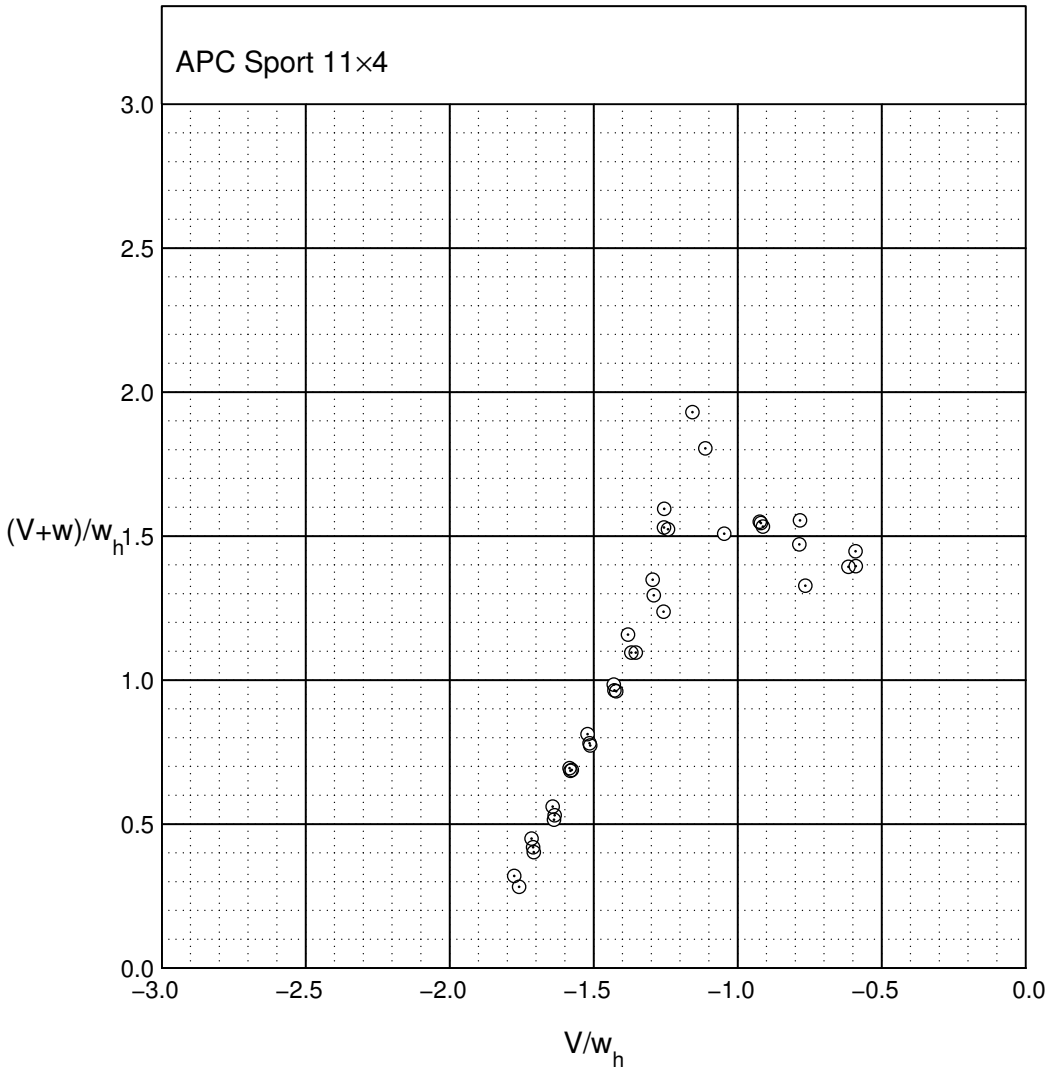

Fig. 4.45: Net inflow data for the APC Sport 11×4.

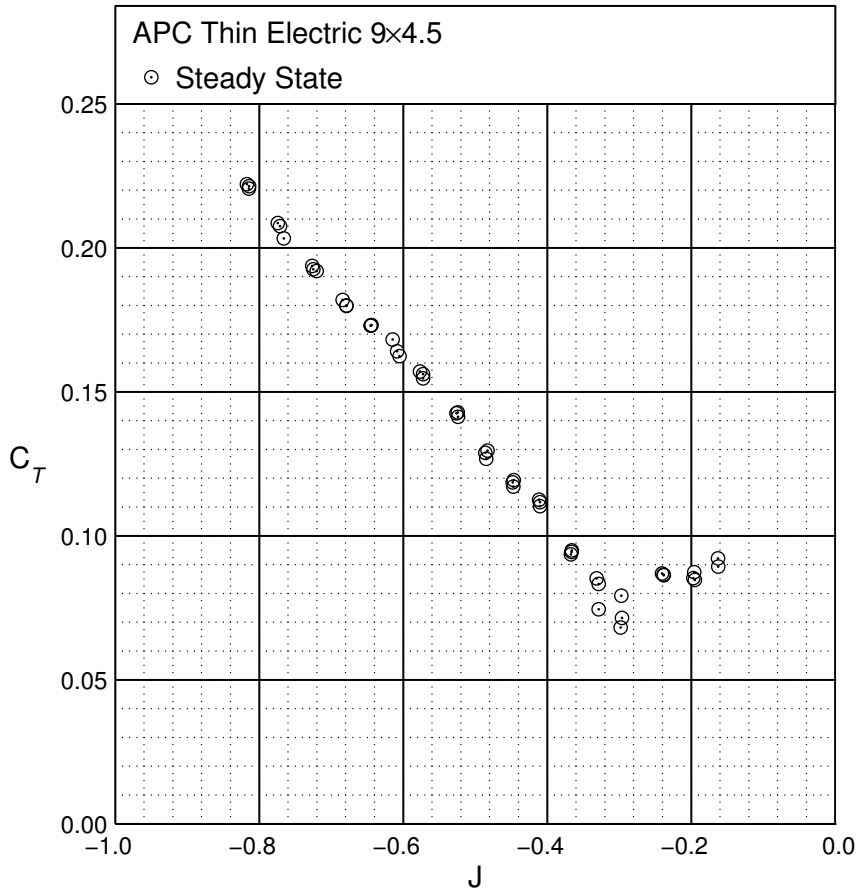

Fig. 4.46: Steady state thrust coefficient data for the APC Thin Electric 9×4.5.

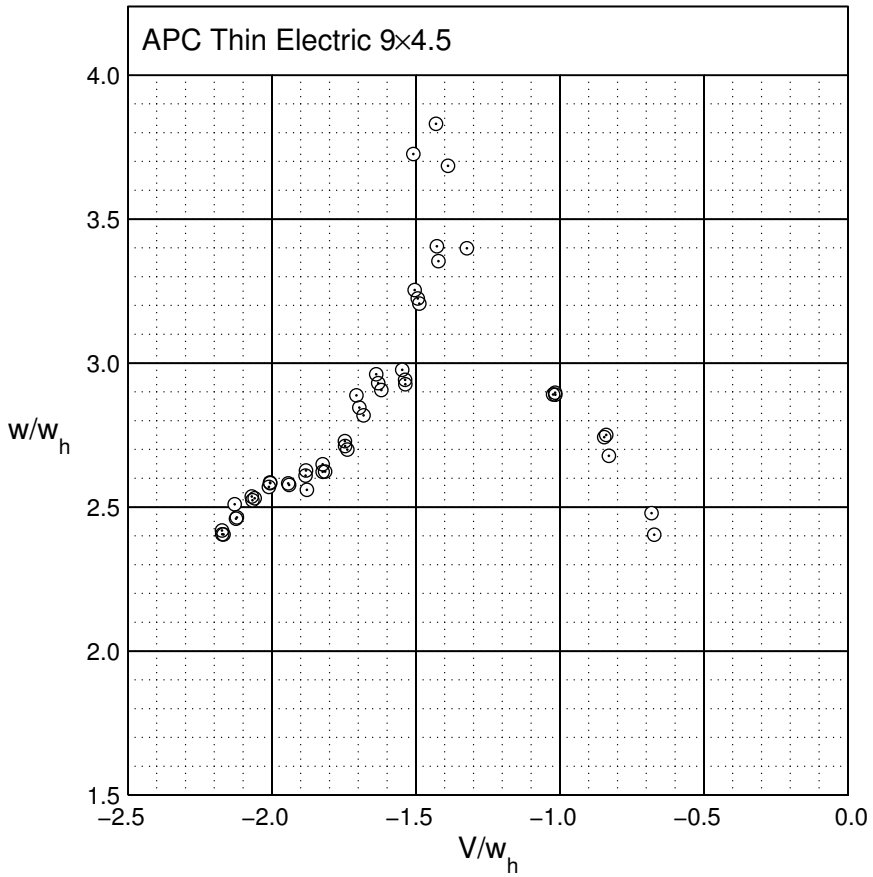

Fig. 4.47: Induced velocity data for the APC Thin Electric 9×4.5.

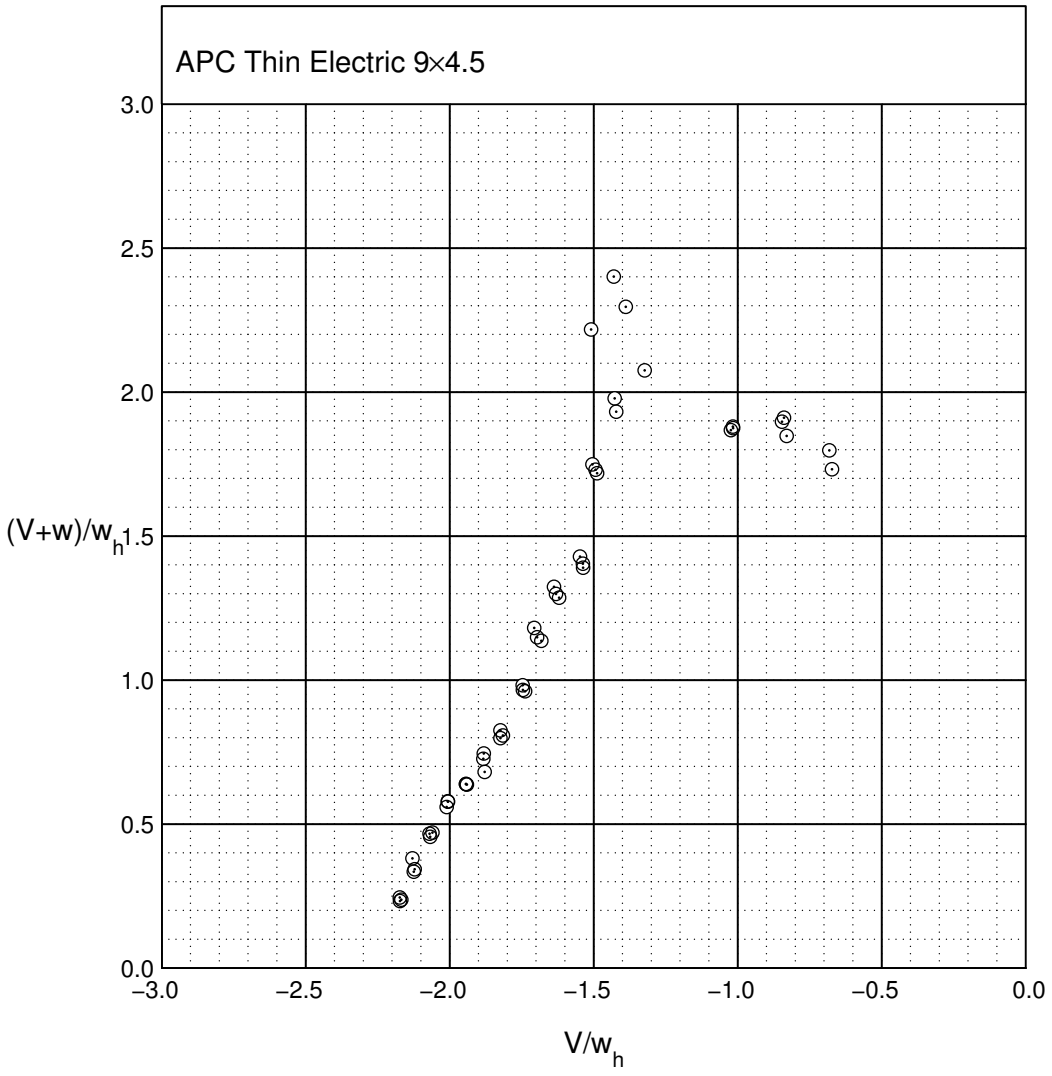

Fig. 4.48: Net inflow data for the APC Thin Electric 9×4.5.

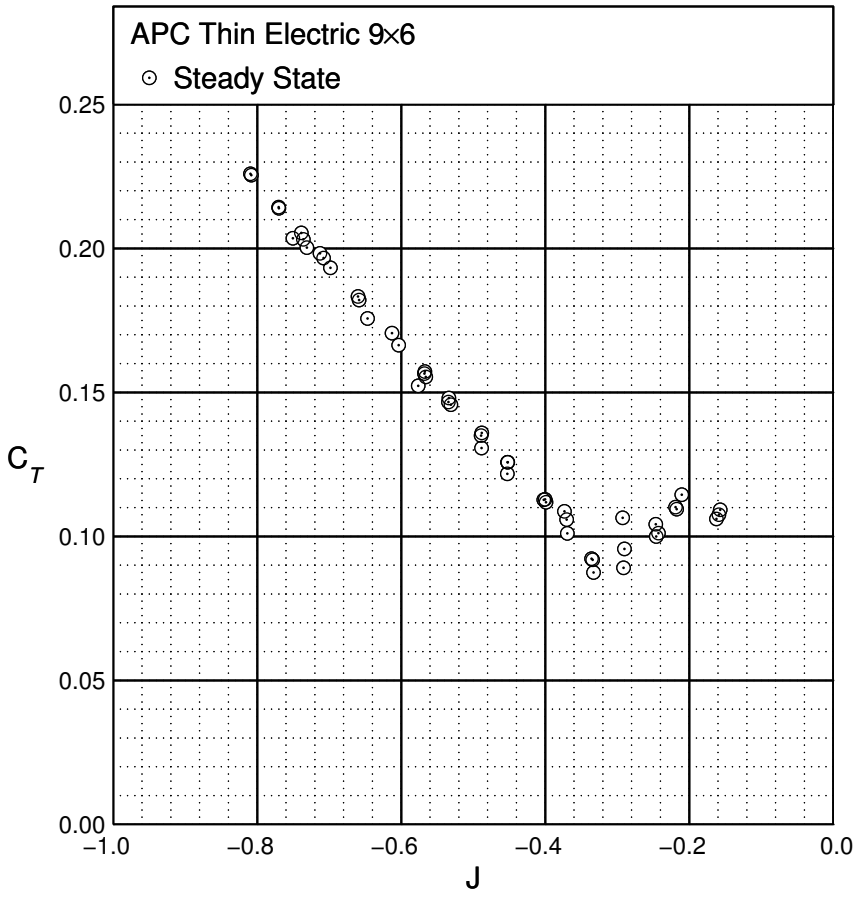

Fig. 4.49: Steady state thrust coefficient data for the APC Thin Electric 9×6.

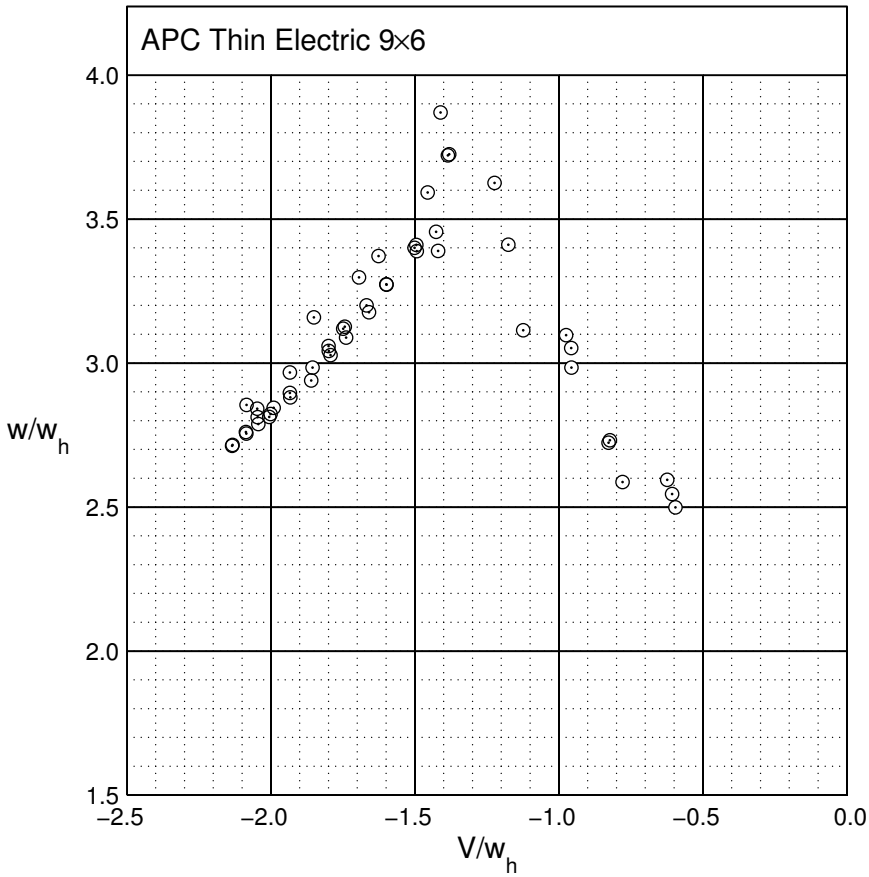

Fig. 4.50: Induced velocity data for the APC Thin Electric 9×6.

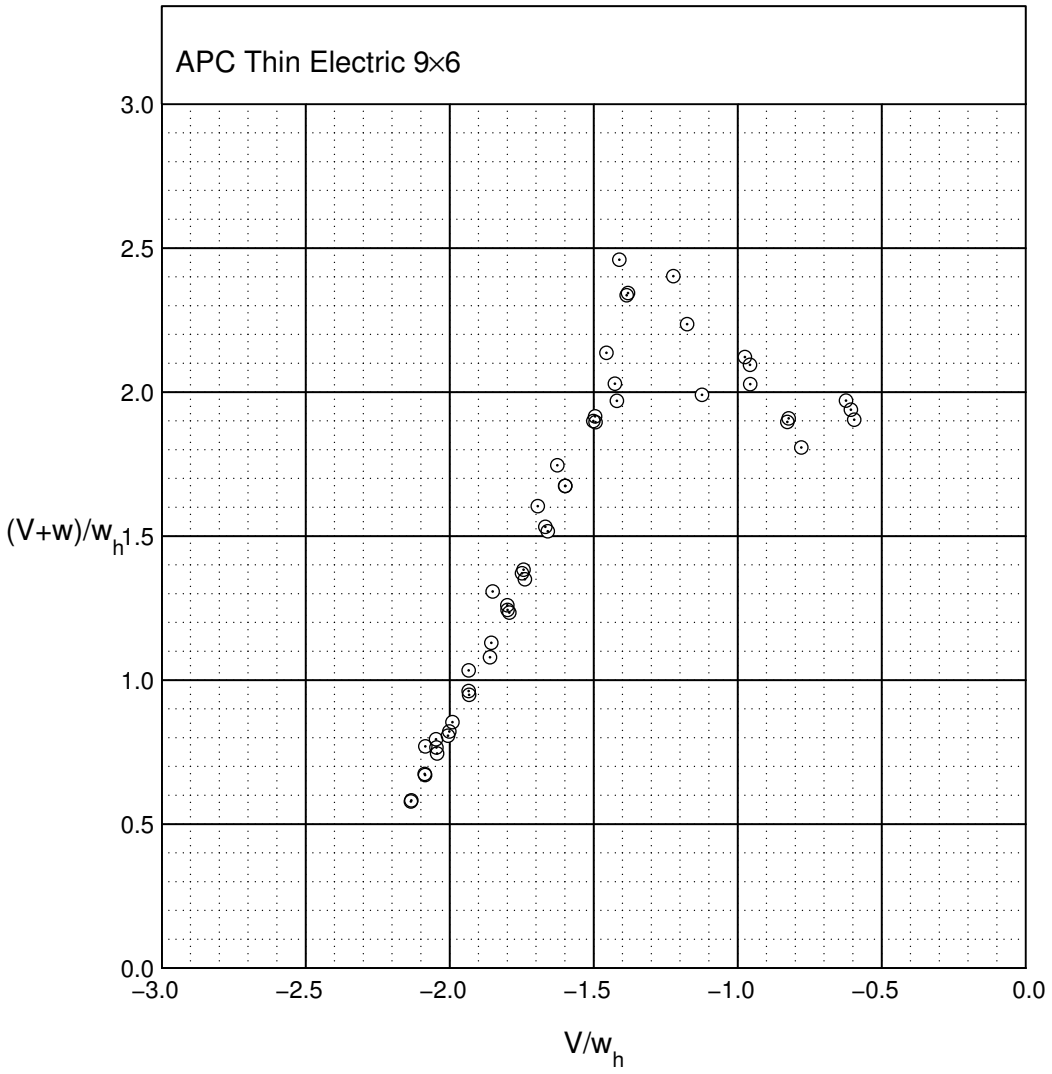

Fig. 4.51: Net inflow data for the APC Thin Electric 9×6.

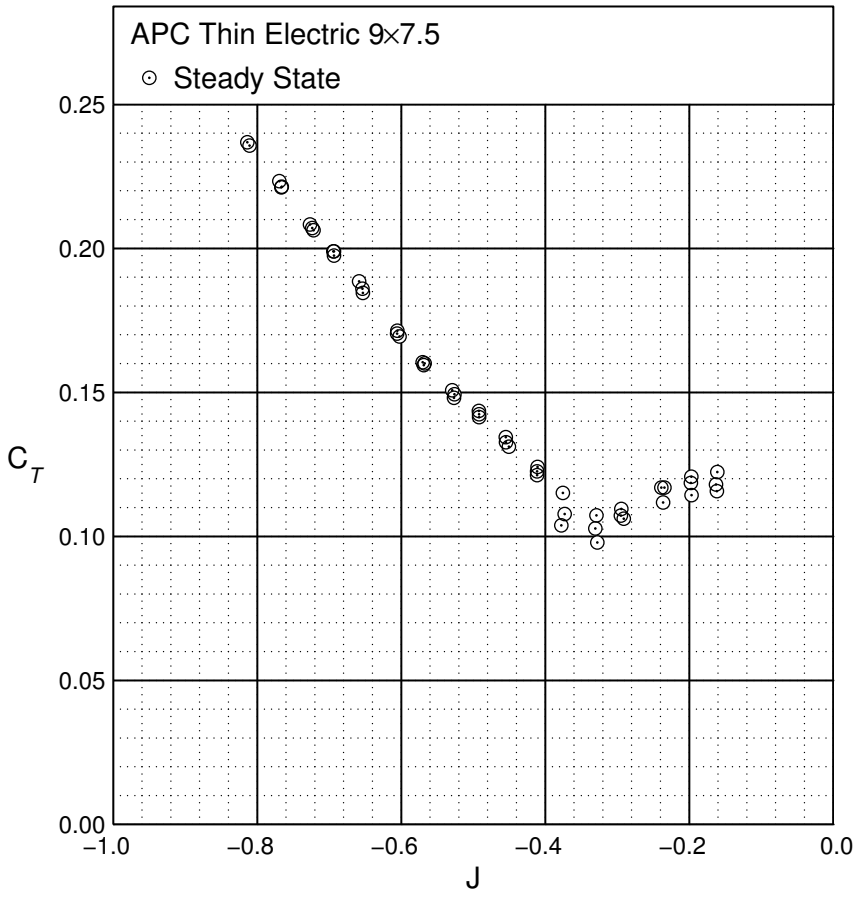

Fig. 4.52: Steady state thrust coefficient data for the APC Thin Electric 9×7.5.

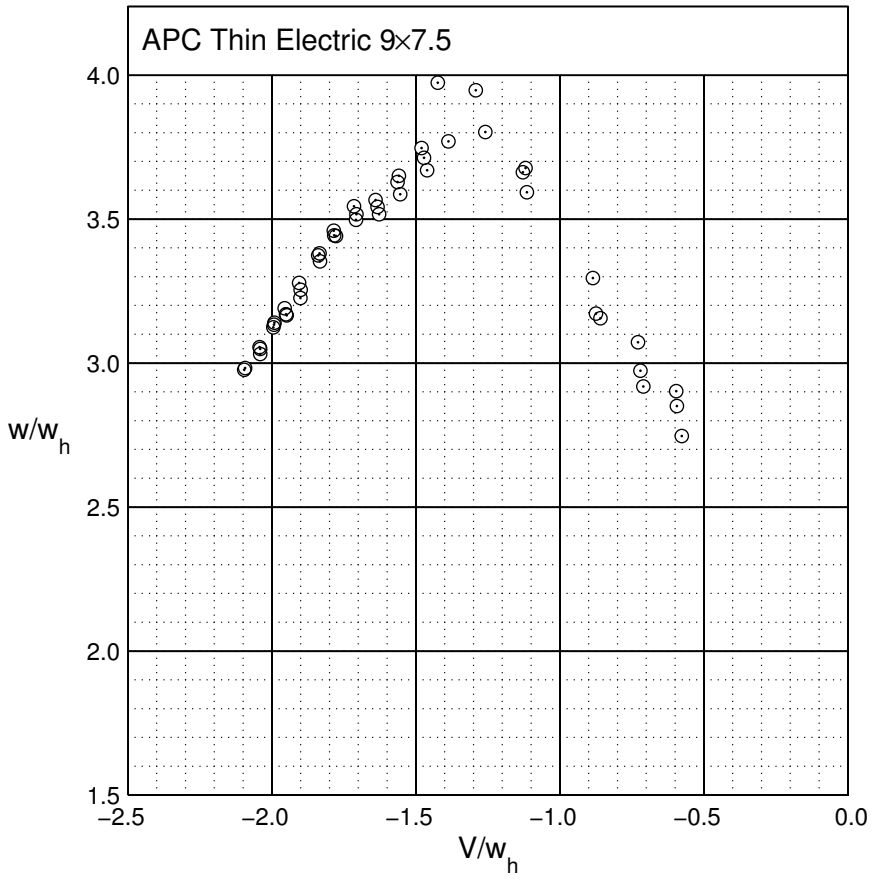

Fig. 4.53: Induced velocity data for the APC Thin Electric 9×7.5.

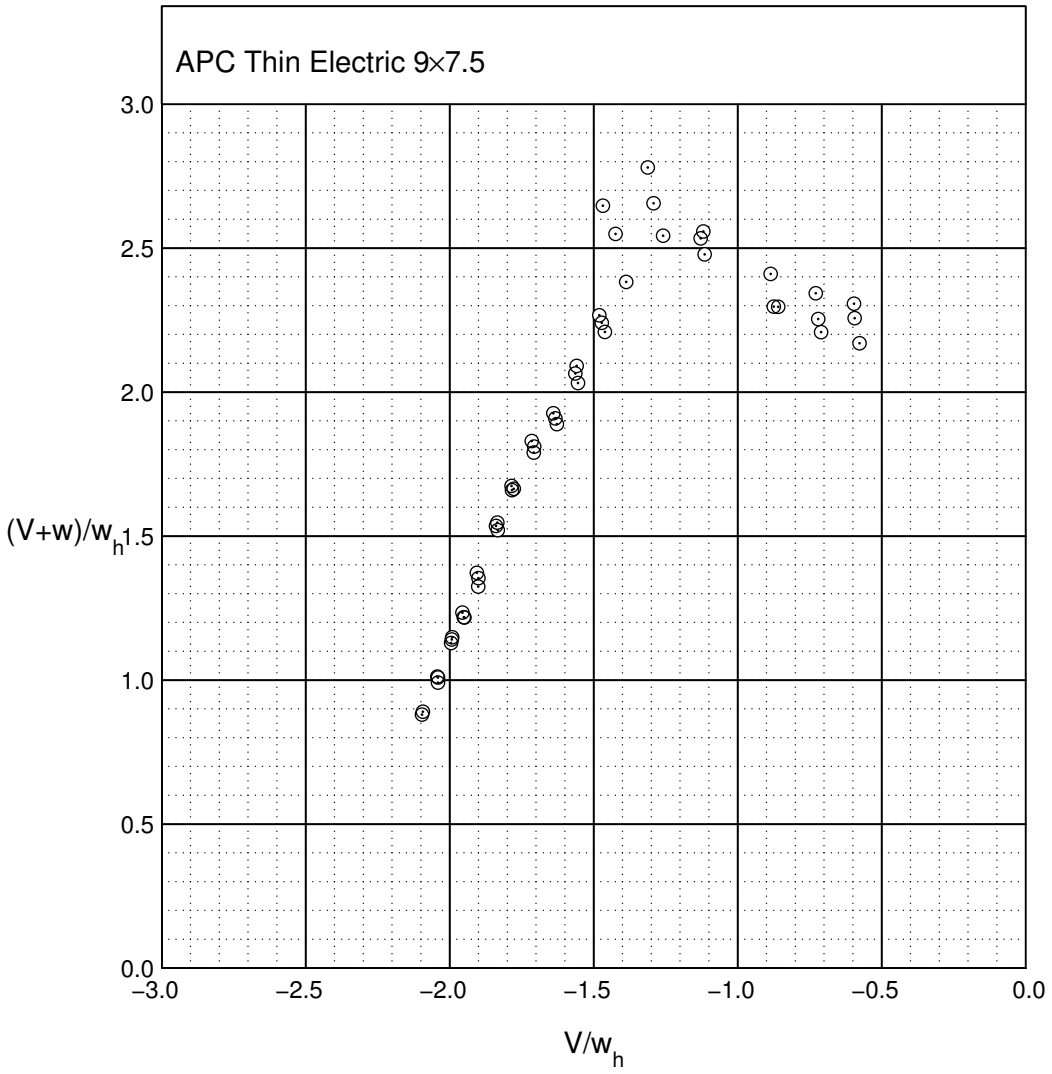

Fig. 4.54: Net inflow data for the APC Thin Electric 9×7.5.

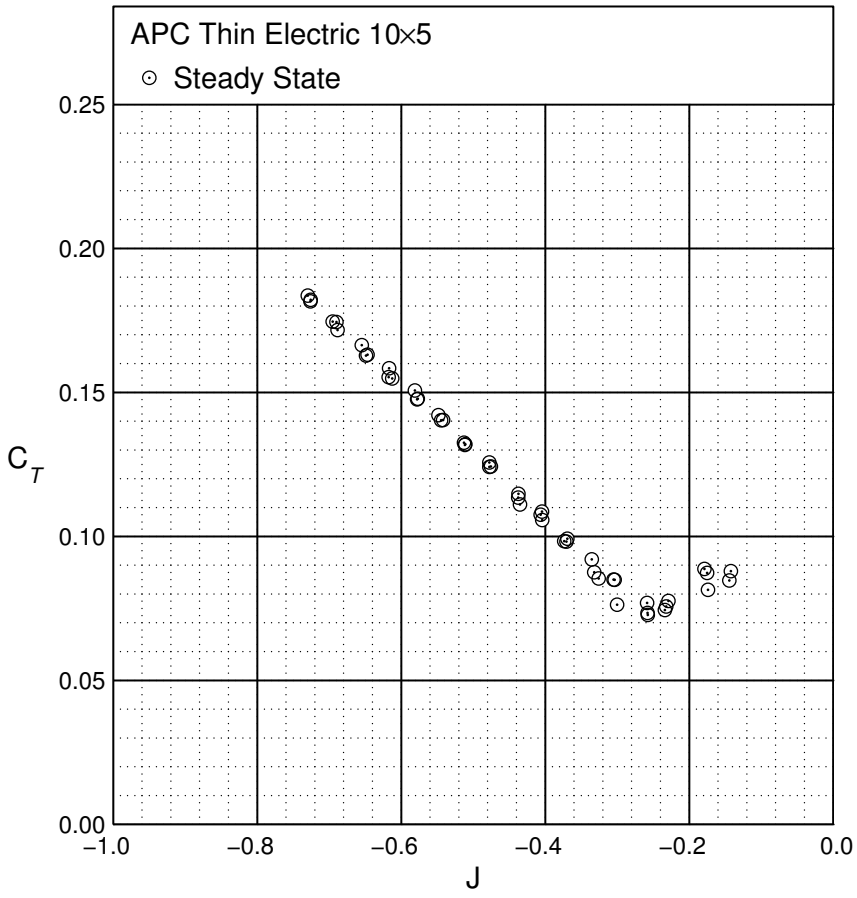

Fig. 4.55: Steady state thrust coefficient data for the APC Thin Electric 10×5.

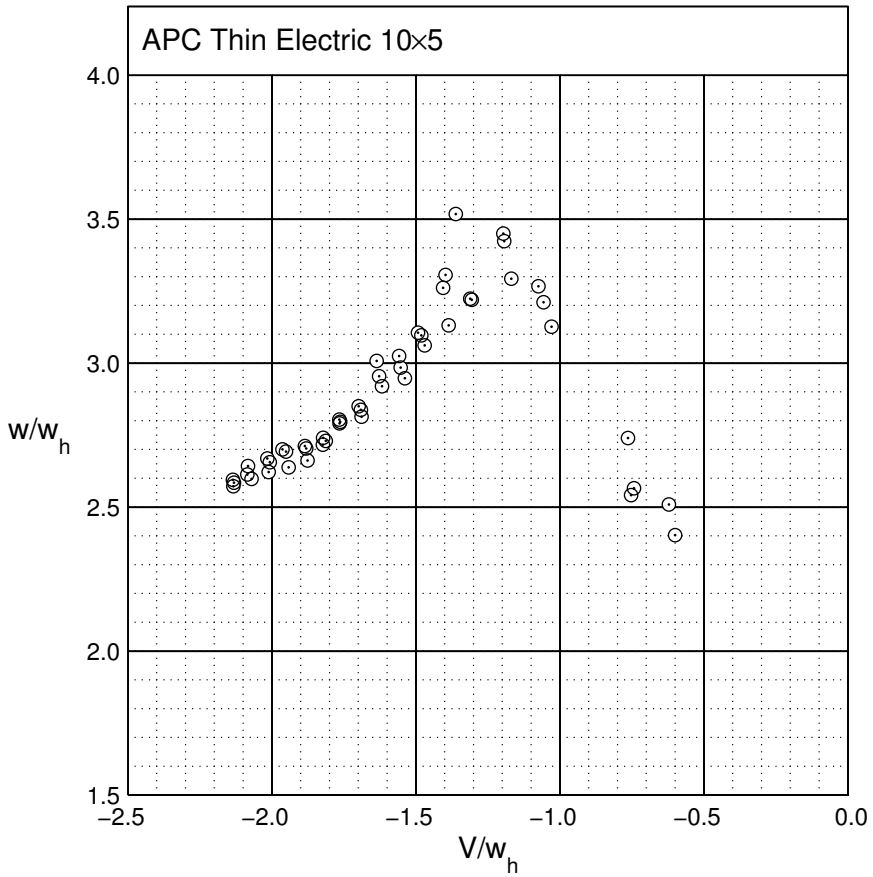

Fig. 4.56: Induced velocity data for the APC Thin Electric 10×5.

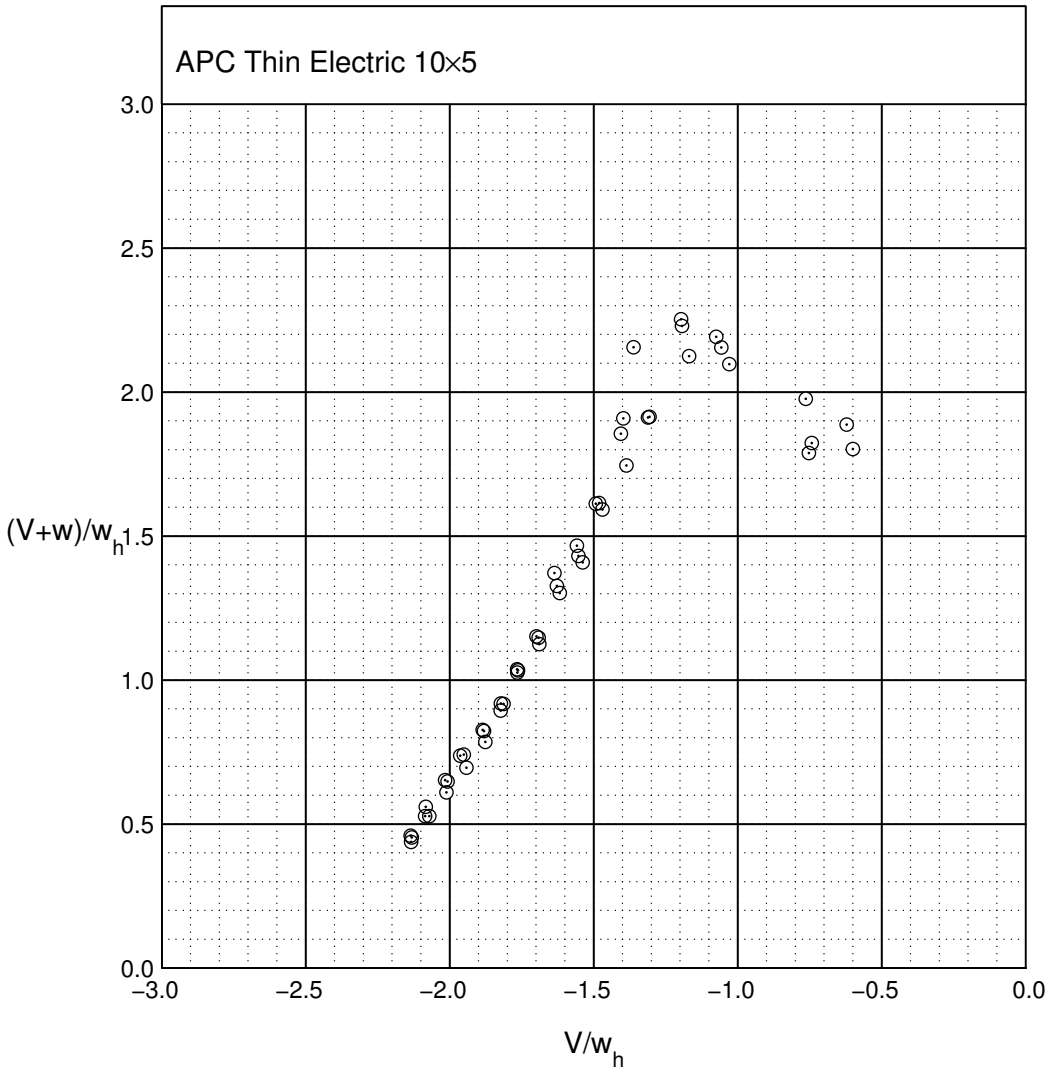

Fig. 4.57: Net inflow data for the APC Thin Electric 10×5.

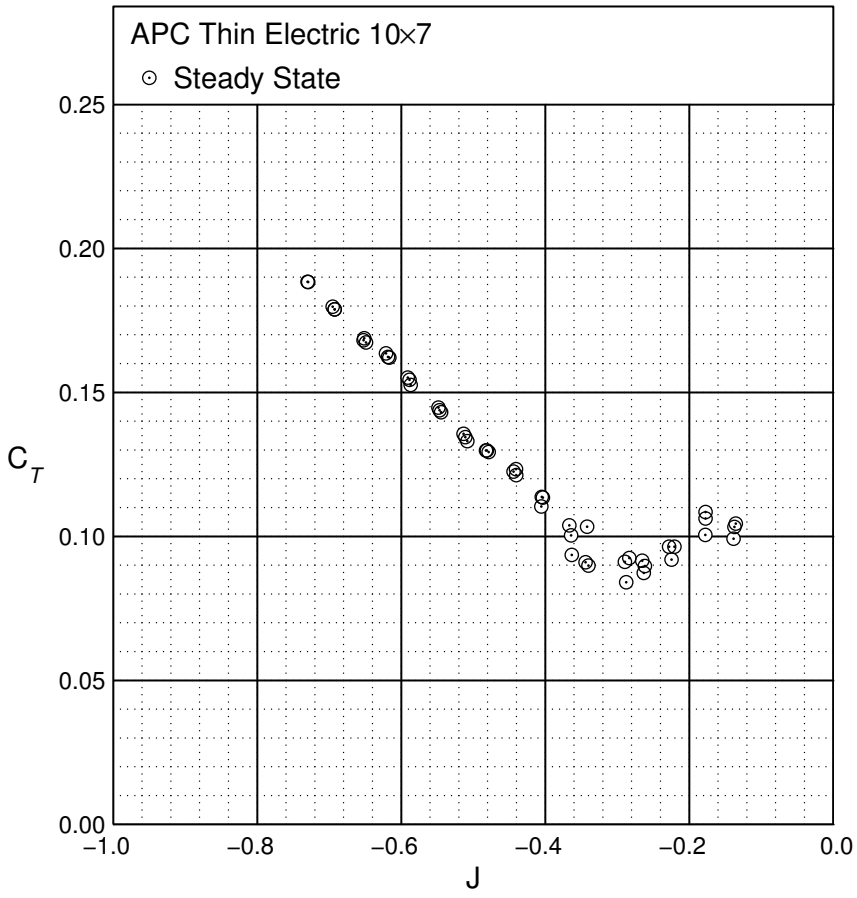

Fig. 4.58: Steady state thrust coefficient data for the APC Thin Electric 10×7.

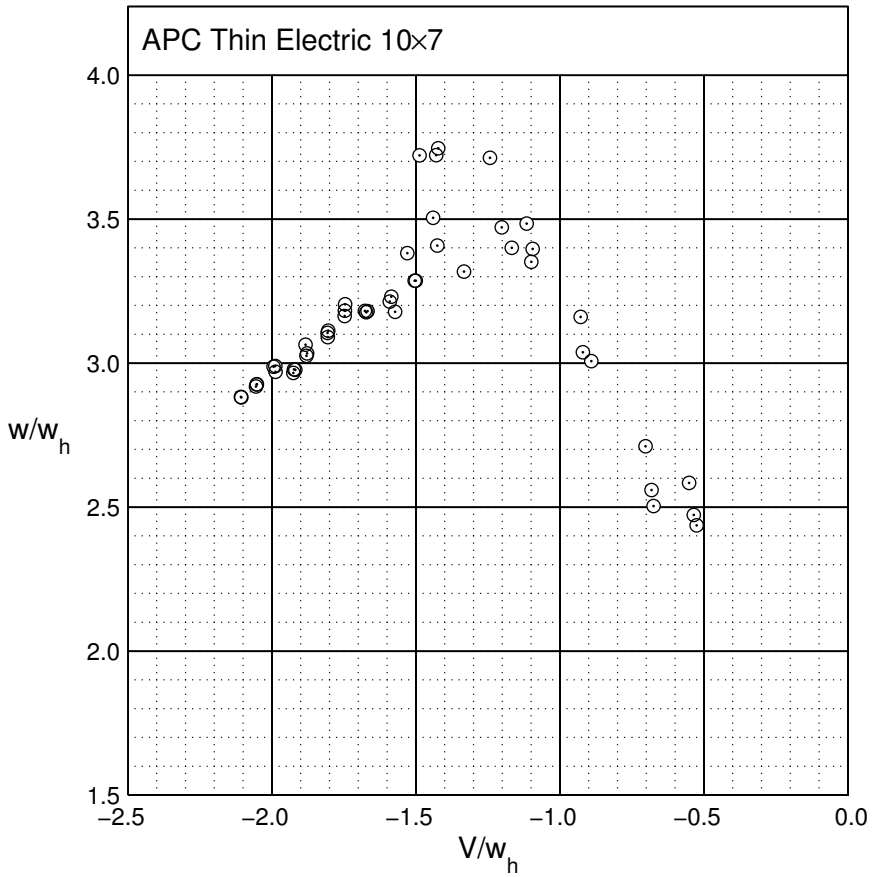

Fig. 4.59: Induced velocity data for the APC Thin Electric 10×7.

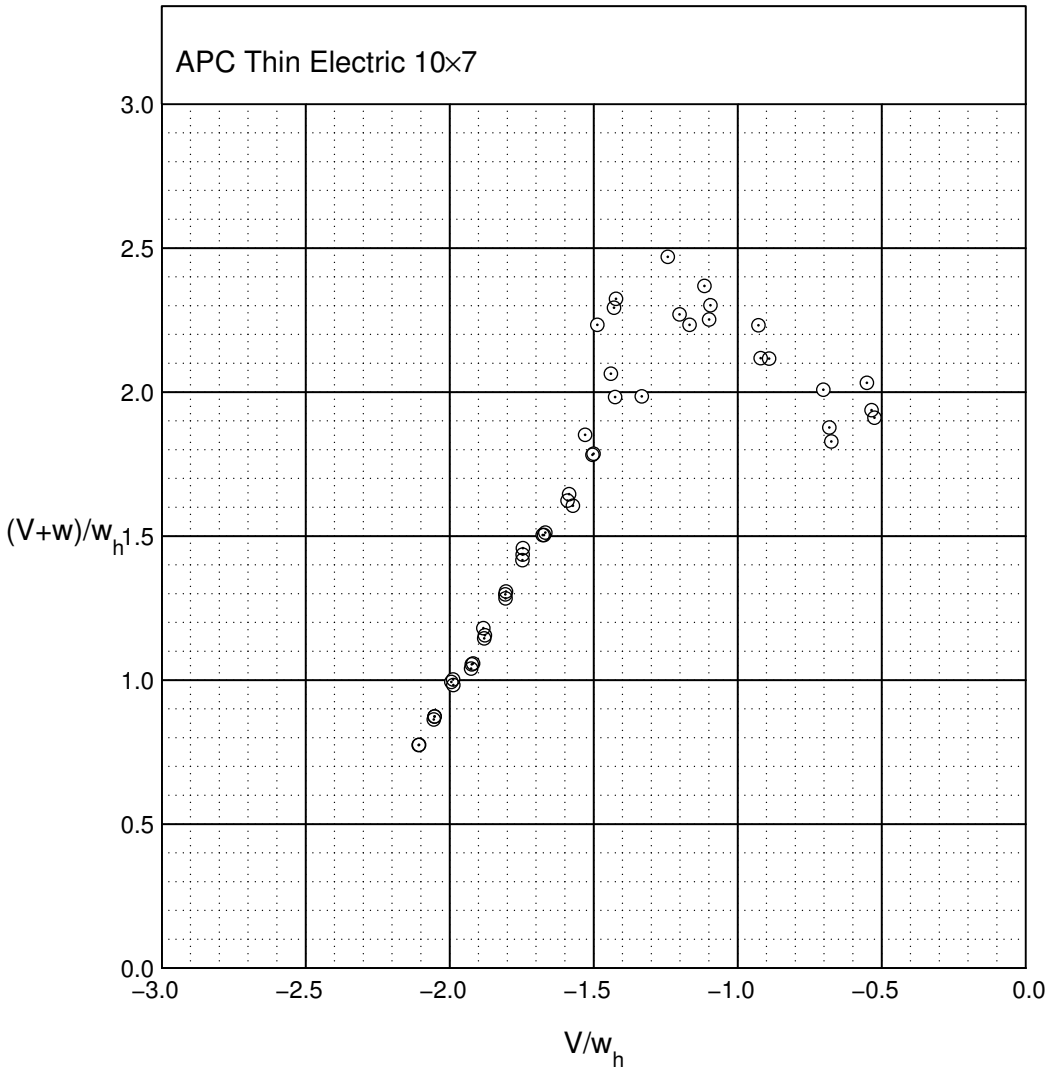

Fig. 4.60: Net inflow data for the APC Thin Electric 10×7.

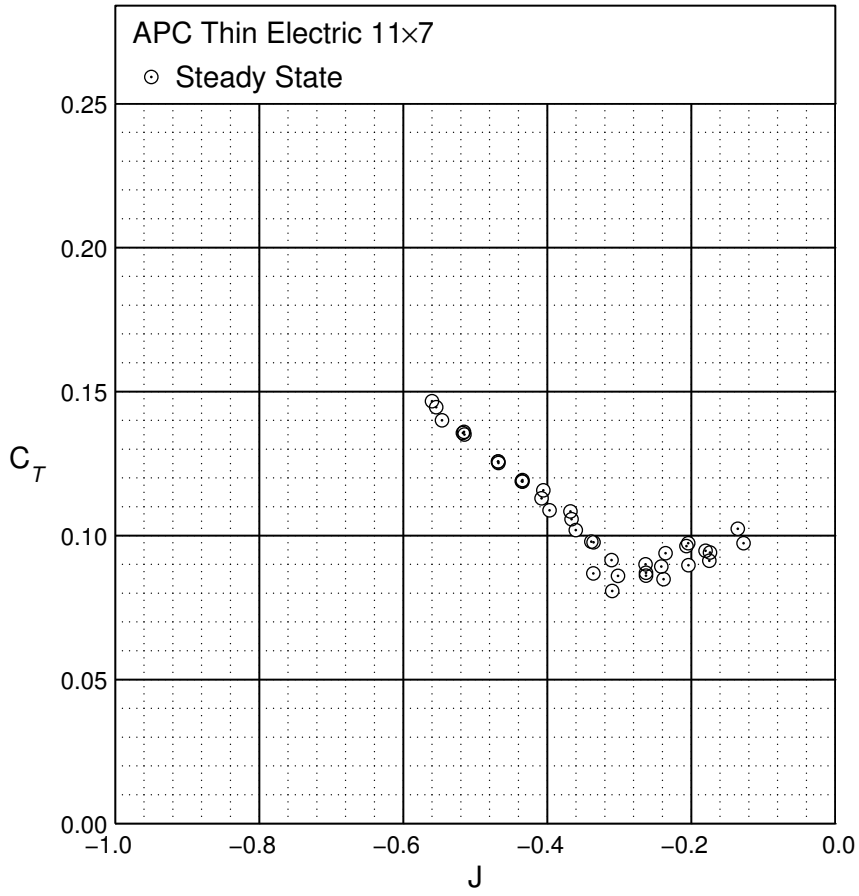

Fig. 4.61: Steady state thrust coefficient data for the APC Thin Electric 11×7.

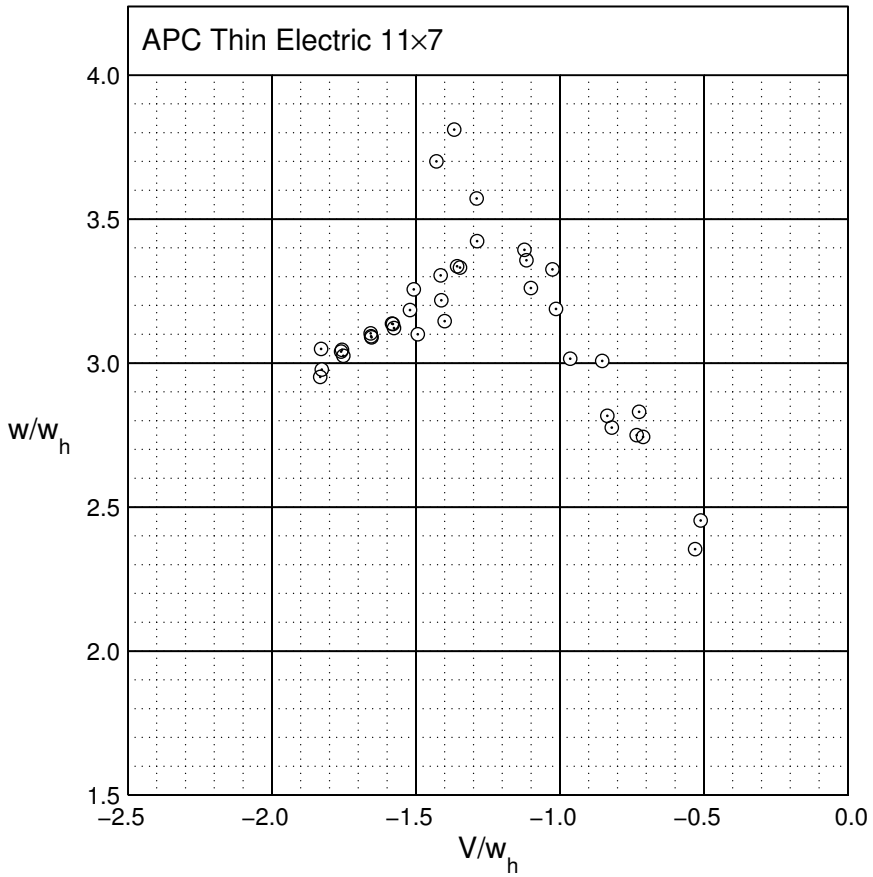

Fig. 4.62: Induced velocity data for the APC Thin Electric 11×7.

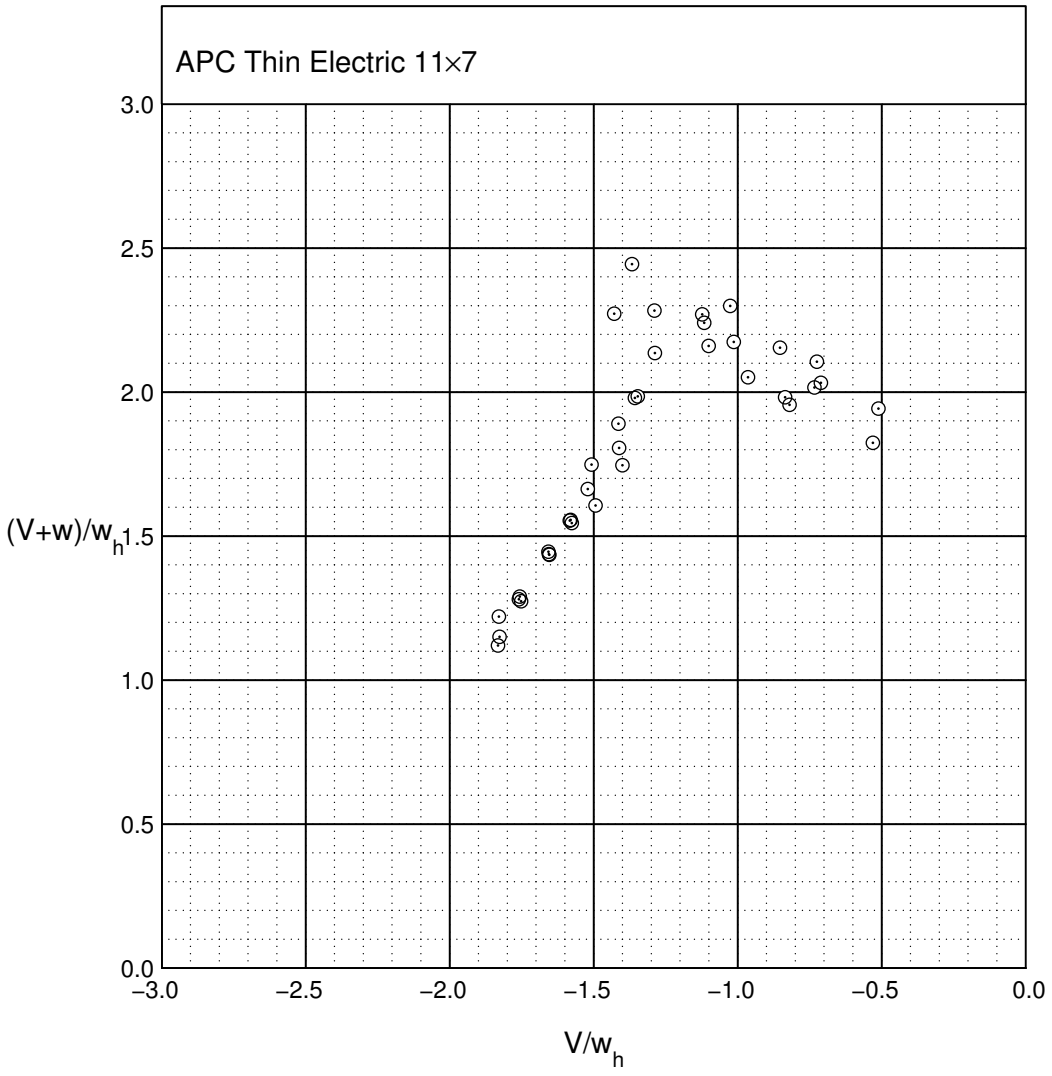

Fig. 4.63: Net inflow data for the APC Thin Electric 11×7.

4.2 Time History Data

The following figures represent the thrust time history recorded for 10 propellers. The data is represented in terms of the thrust coefficient, lb thrust and the raw thrust data recorded in volts. It is to be noted that here zero volts represents zero lb of thrust generated by the propeller. Although the time history data was recorded at nine values of advance ratio, this report only includes data plots for four advance ratios per propeller so as to avoid redundancy. Also, the plots represent the data recorded over the first 5 sec instead of the entire 90 sec.

The general trend observed is that the thrust and hence the recorded time history remains rather steady at the hover condition and at higher descent velocities. A large amount of fluctuation can be observed at the intermediate descent velocities with a peak at the advance ratio corresponding to the minimum thrust on the steady state data. This trend is further verified from Figs 4.181–4.219 which represent the histograms of the thrust as a function of the ratio of actual thrust to the mean thrust. The vertical bold lines denote the mean thrust and $\pm 3\sigma$ limits for the time history recorded. In general, these plots illustrate the extent of thrust fluctuations observed as the propeller transitions from hover to the windmill brake state passing through the turbulent VRS state.

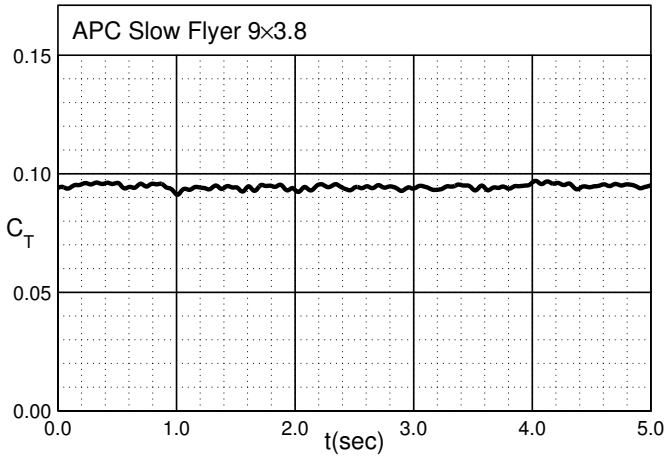

Fig. 4.64: Thrust coefficient time history for the APC Slow Flyer 9×3.8 in hover.

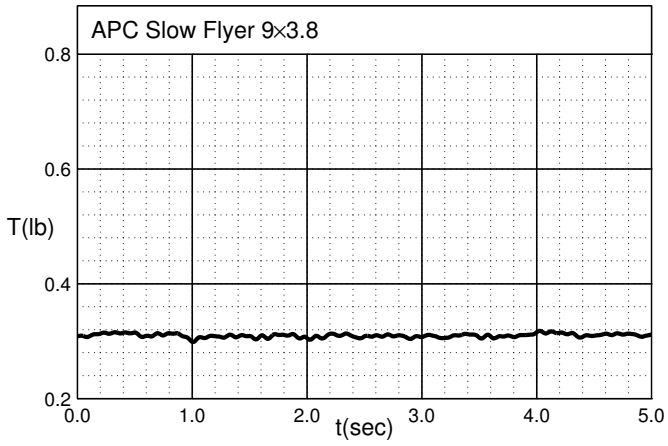

Fig. 4.65: Thrust (lb) time history for the APC Slow Flyer 9×3.8 in hover.

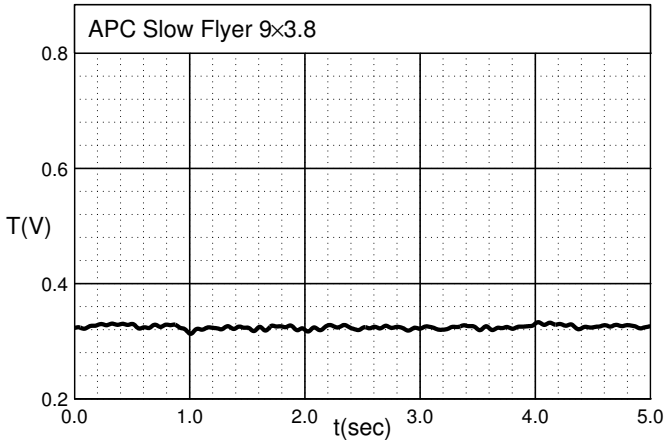

Fig. 4.66: Thrust (V) time history for the APC Slow Flyer 9×3.8 in hover.

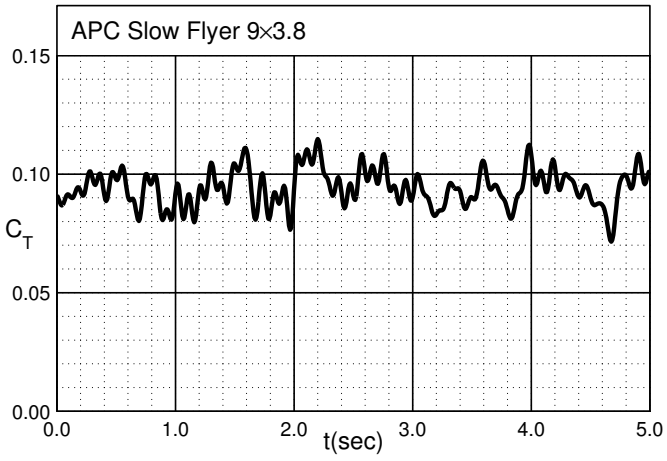

Fig. 4.67: Thrust coefficient time history for the APC Slow Flyer 9×3.8 at $J = -0.21$.

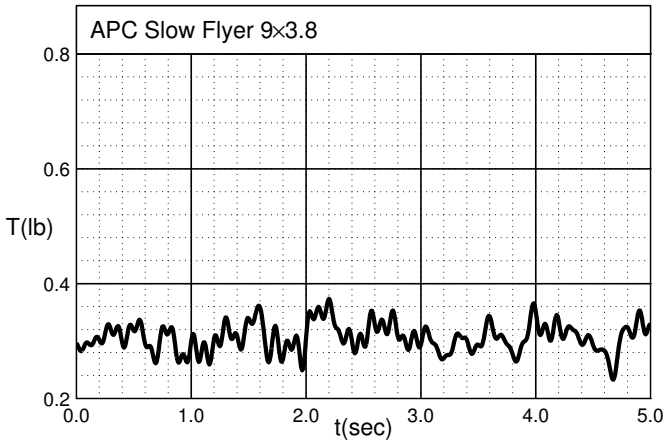

Fig. 4.68: Thrust (lb) time history for the APC Slow Flyer 9×3.8 at $J = -0.21$.

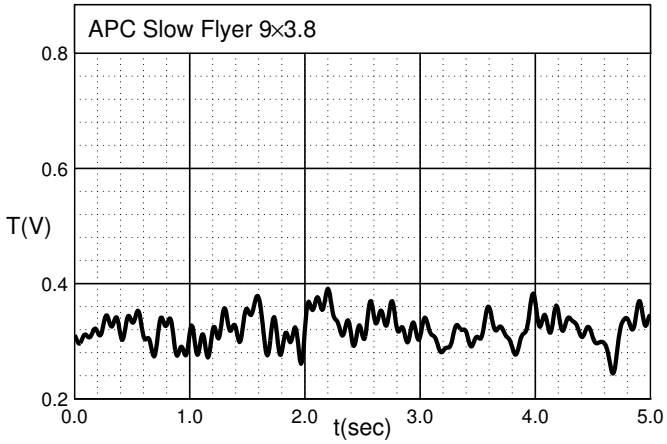

Fig. 4.69: Thrust (V) time history for the APC Slow Flyer 9×3.8 at $J = -0.21$.

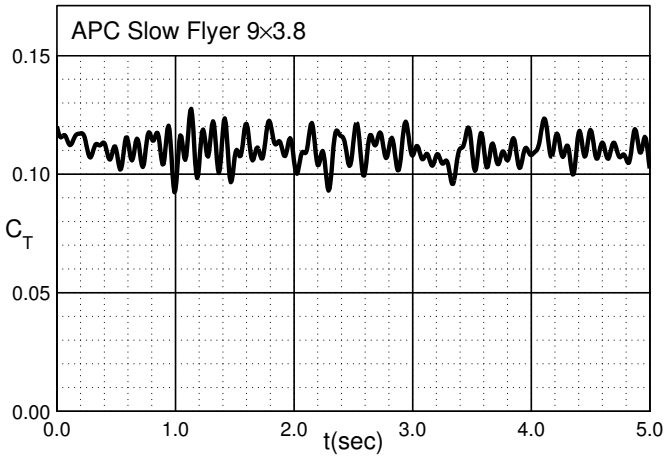

Fig. 4.70: Thrust coefficient time history for the APC Slow Flyer 9×3.8 at $J = -0.40$.

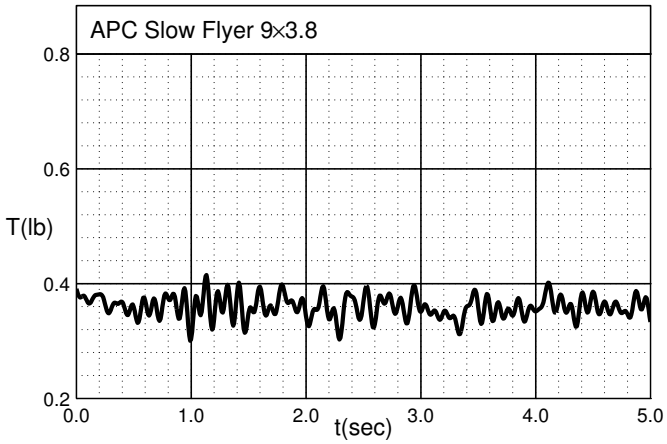

Fig. 4.71: Thrust (lb) time history for the APC Slow Flyer 9×3.8 at $J = -0.40$.

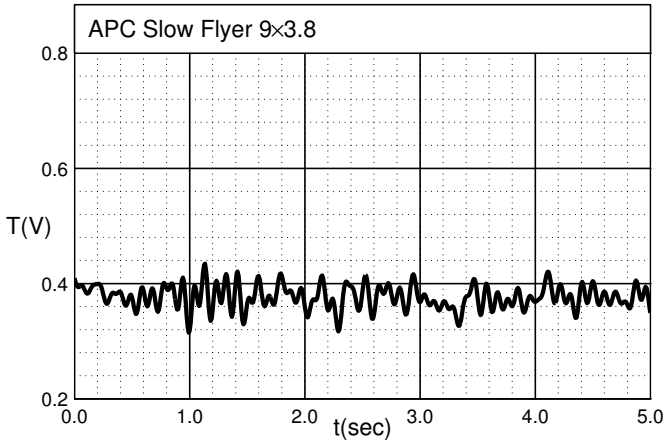

Fig. 4.72: Thrust (V) time history for the APC Slow Flyer 9×3.8 at $J = -0.40$.

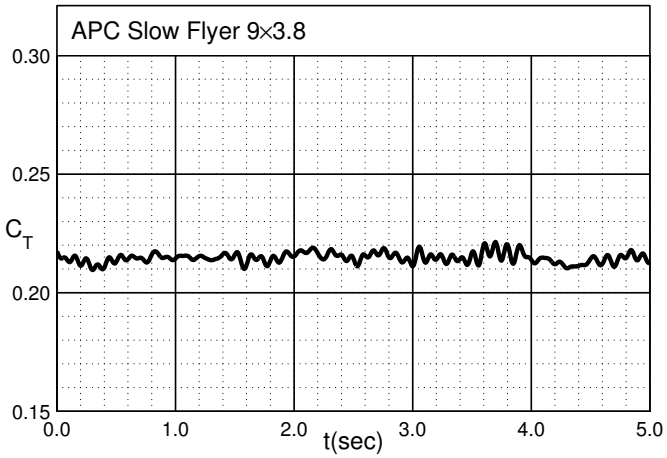

Fig. 4.73: Thrust coefficient time history for the APC Slow Flyer 9×3.8 at $J = -0.68$.

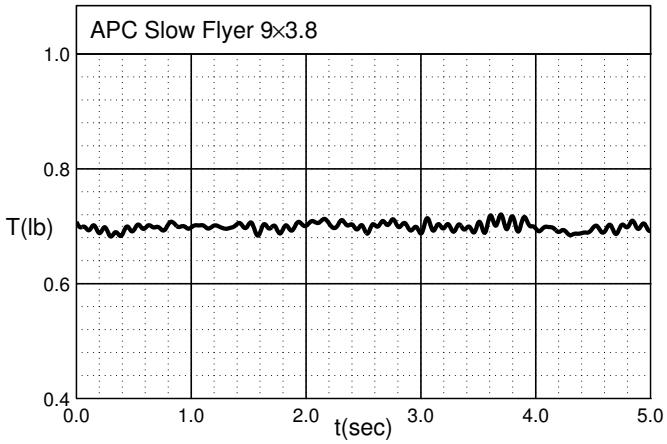

Fig. 4.74: Thrust (lb) time history for the APC Slow Flyer 9×3.8 at $J = -0.68$.

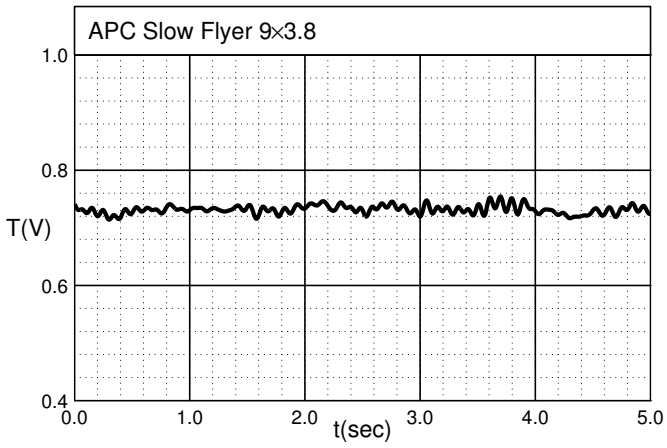

Fig. 4.75: Thrust (V) time history for the APC Slow Flyer 9×3.8 at $J = -0.68$.

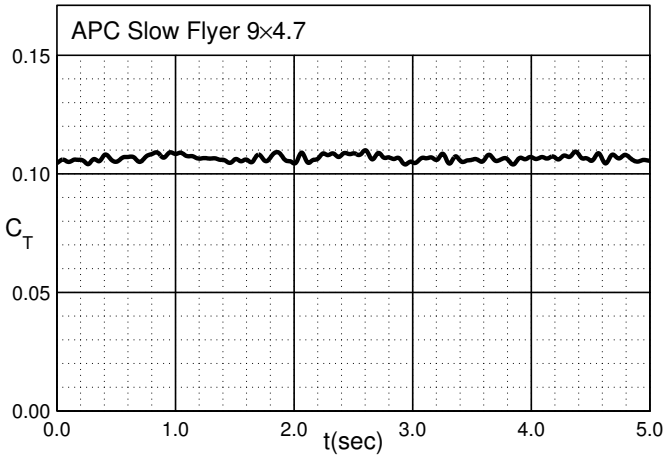

Fig. 4.76: Thrust coefficient time history for the APC Slow Flyer 9×4.7 in hover.

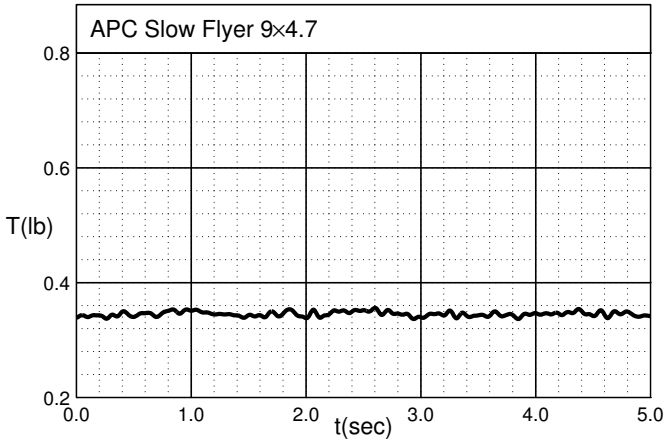

Fig. 4.77: Thrust (lb) time history for the APC Slow Flyer 9×4.7 in hover.

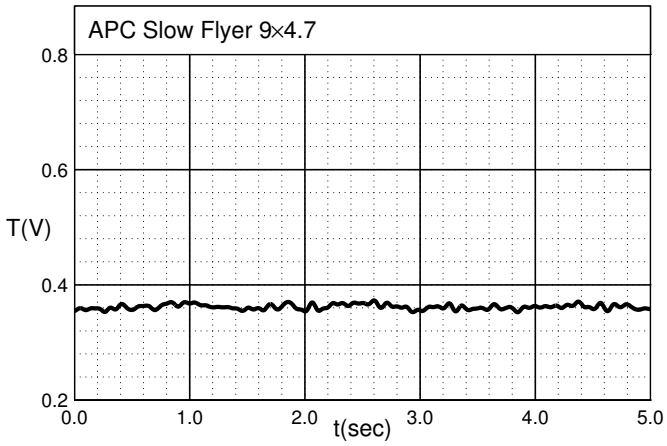

Fig. 4.78: Thrust (V) time history for the APC Slow Flyer 9×4.7 in hover.

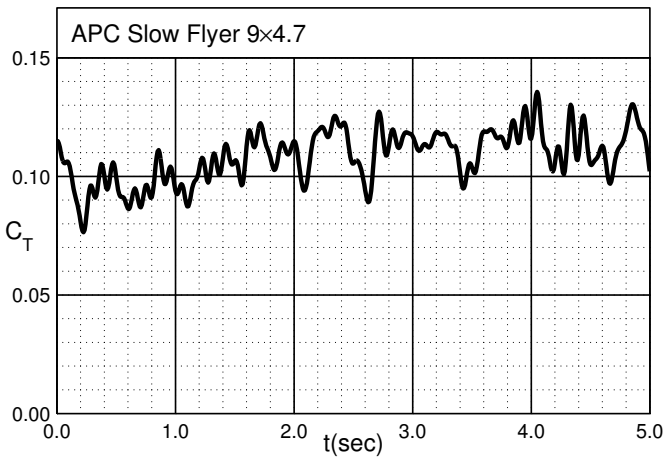

Fig. 4.79: Thrust coefficient time history for the APC Slow Flyer 9×4.7 at $J = -0.21$.

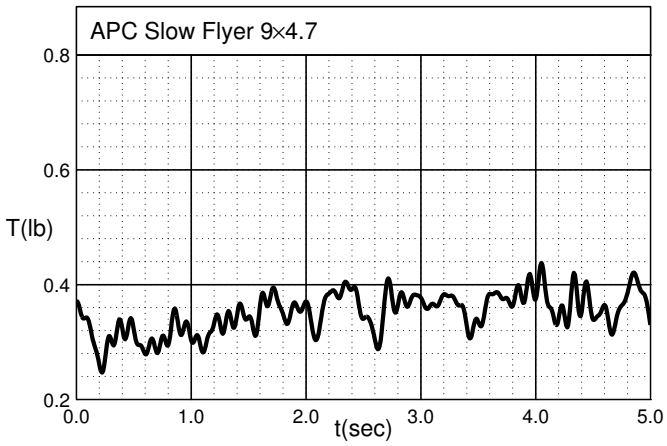

Fig. 4.80: Thrust (lb) time history for the APC Slow Flyer 9×4.7 at $J = -0.21$.

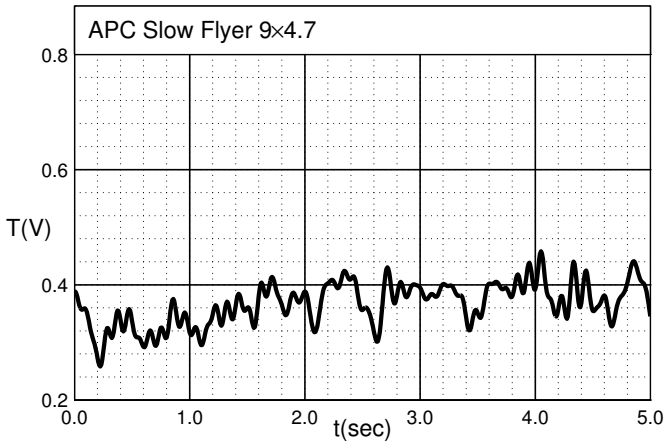

Fig. 4.81: Thrust (V) time history for the APC Slow Flyer 9×4.7 at $J = -0.21$.

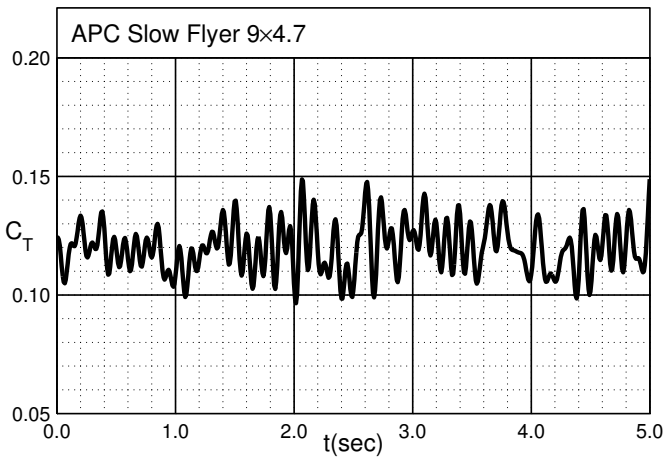

Fig. 4.82: Thrust coefficient time history for the APC Slow Flyer 9×4.7 at $J = -0.40$.

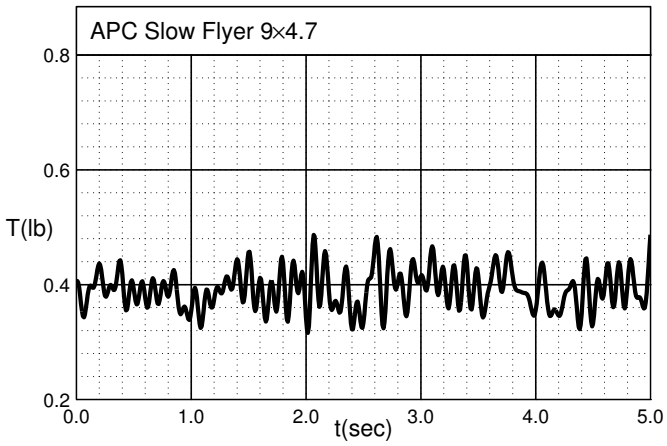

Fig. 4.83: Thrust (lb) time history for the APC Slow Flyer 9×4.7 at $J = -0.40$.

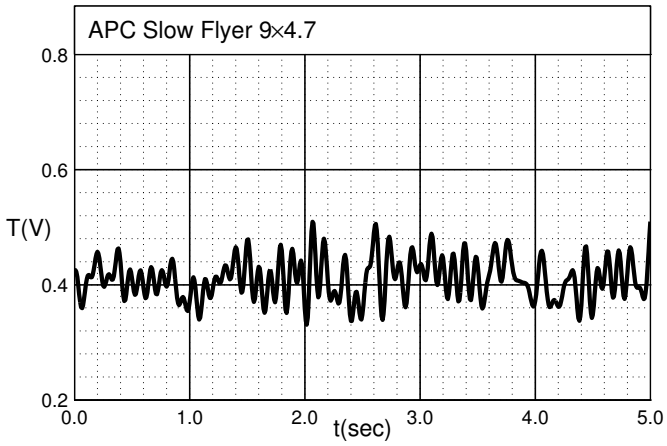

Fig. 4.84: Thrust (V) time history for the APC Slow Flyer 9×4.7 at $J = -0.40$.

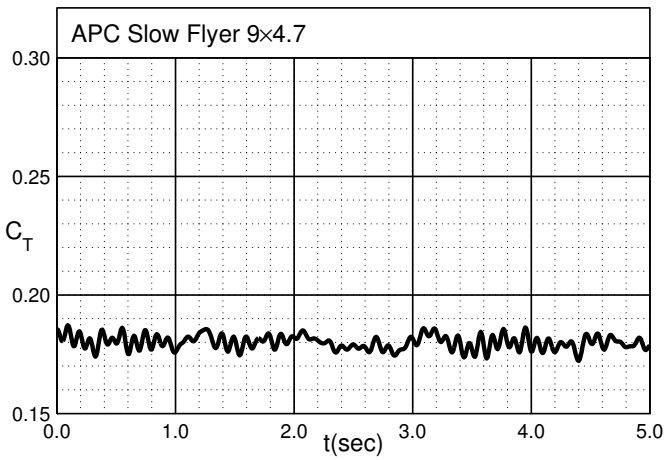

Fig. 4.85: Thrust coefficient time history for the APC Slow Flyer 9×4.7 at $J = -0.68$.

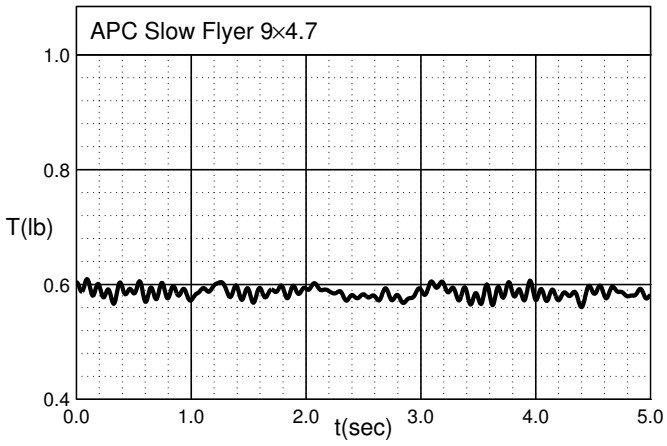

Fig. 4.86: Thrust (lb) time history for the APC Slow Flyer 9×4.7 at $J = -0.68$.

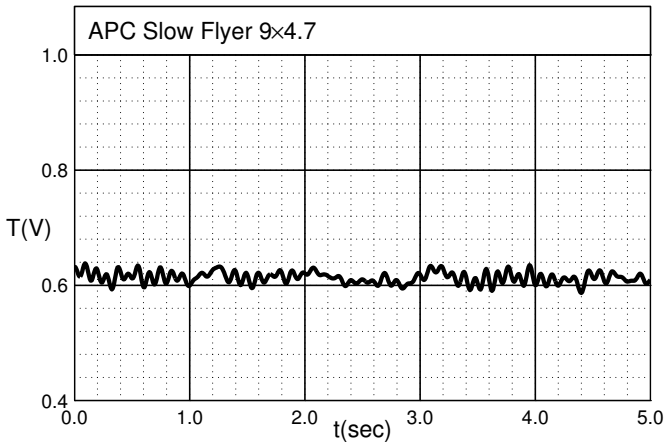

Fig. 4.87: Thrust (V) time history for the APC Slow Flyer 9×4.7 at $J = -0.68$.

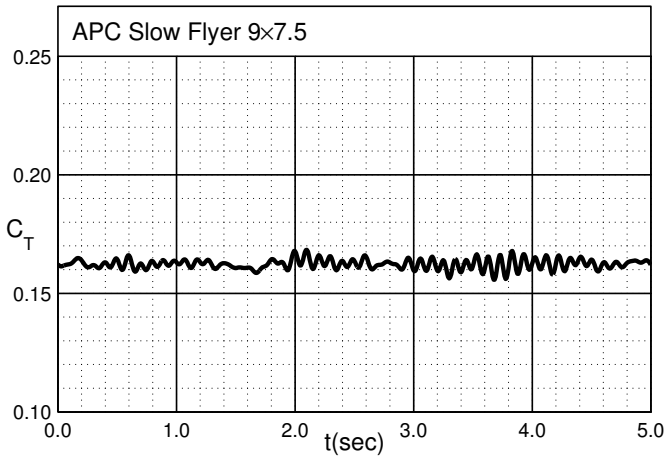

Fig. 4.88: Thrust coefficient time history for the APC Slow Flyer 9×7.5 in hover.

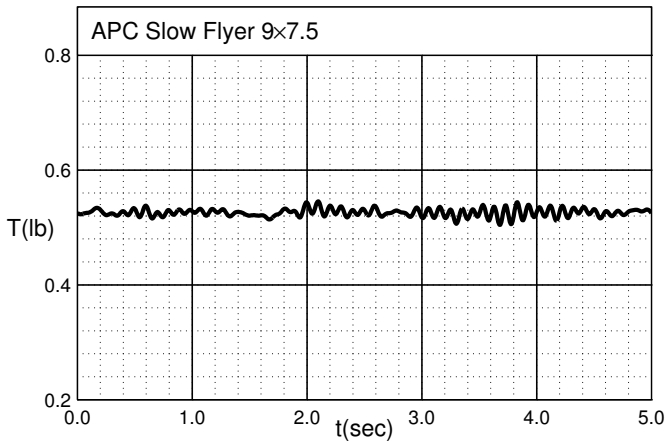

Fig. 4.89: Thrust (lb) time history for the APC Slow Flyer 9×7.5 in hover.

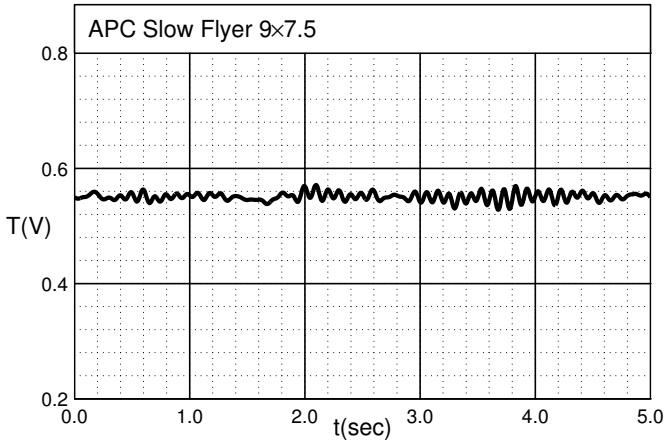

Fig. 4.90: Thrust (V) time history for the APC Slow Flyer 9×7.5 in hover.

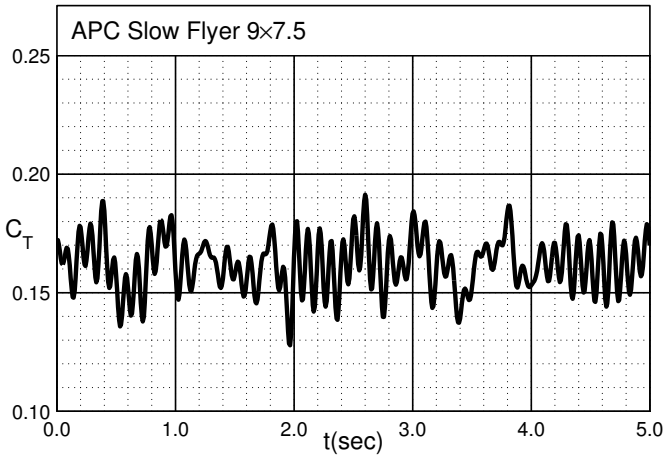

Fig. 4.91: Thrust coefficient time history for the APC Slow Flyer 9×7.5 at $J = -0.21$.

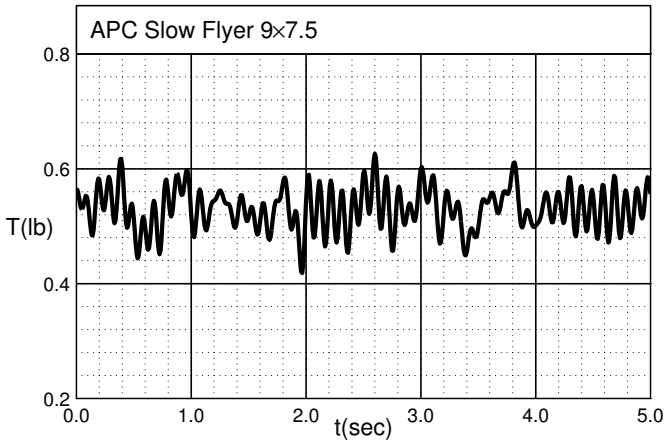

Fig. 4.92: Thrust (lb) time history for the APC Slow Flyer 9×7.5 at $J = -0.21$.

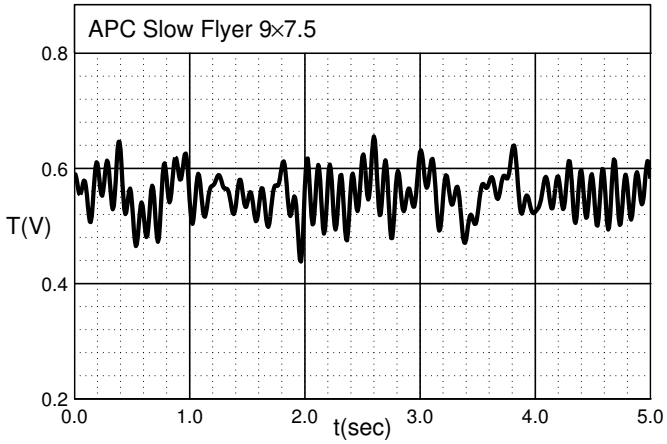

Fig. 4.93: Thrust (V) time history for the APC Slow Flyer 9×7.5 at $J = -0.21$.

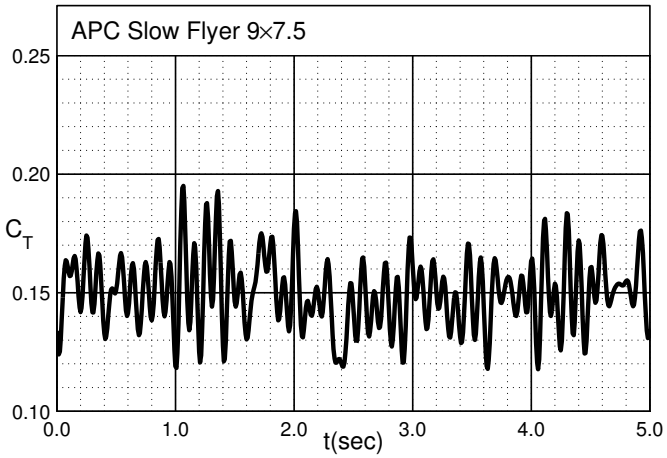

Fig. 4.94: Thrust coefficient time history for the APC Slow Flyer 9×7.5 at $J = -0.40$.

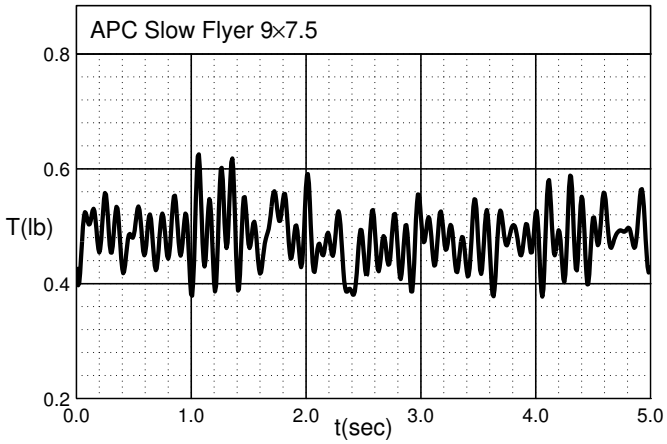

Fig. 4.95: Thrust (lb) time history for the APC Slow Flyer 9×7.5 at $J = -0.40$.

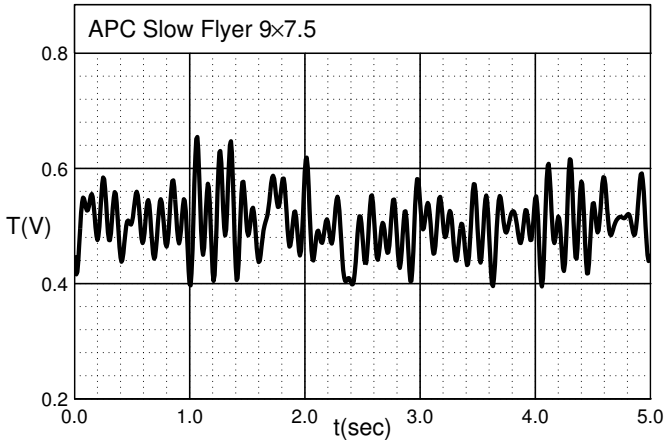

Fig. 4.96: Thrust (V) time history for the APC Slow Flyer 9×7.5 at $J = -0.40$.

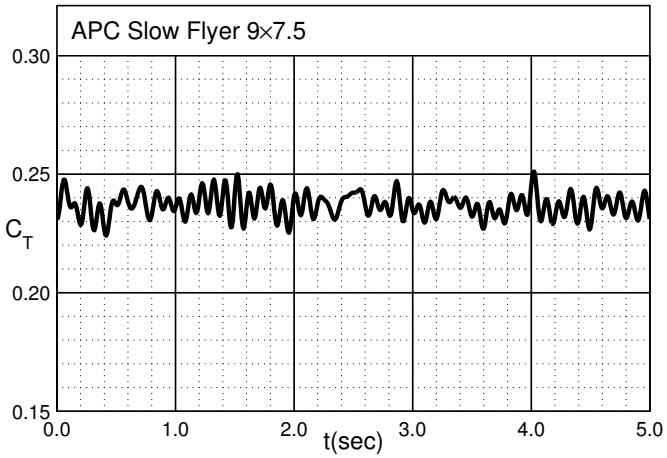

Fig. 4.97: Thrust coefficient time history for the APC Slow Flyer 9×7.5 at $J = -0.68$.

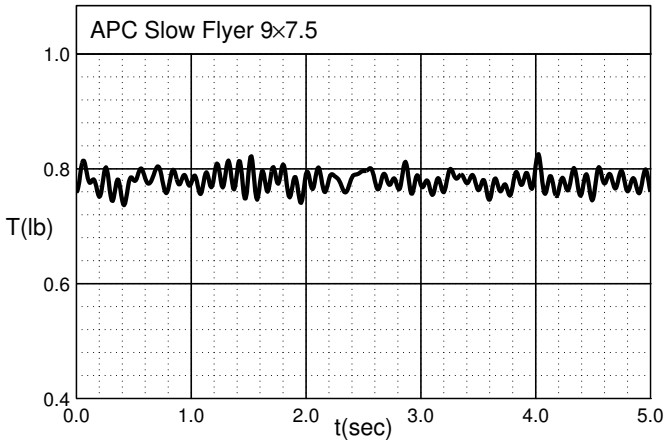

Fig. 4.98: Thrust (lb) time history for the APC Slow Flyer 9×7.5 at $J = -0.68$.

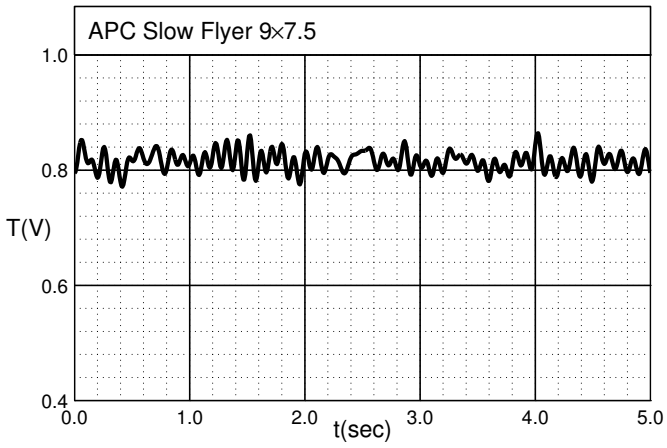

Fig. 4.99: Thrust (V) time history for the APC Slow Flyer 9×7.5 at $J = -0.68$.

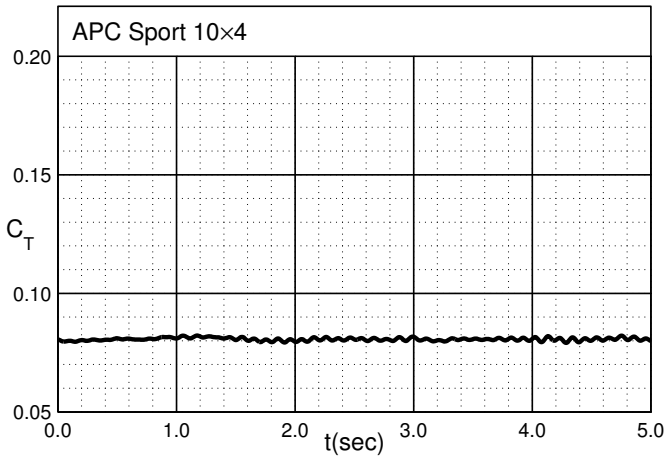

Fig. 4.100: Thrust coefficient time history for the APC Sport 10×4 in hover.

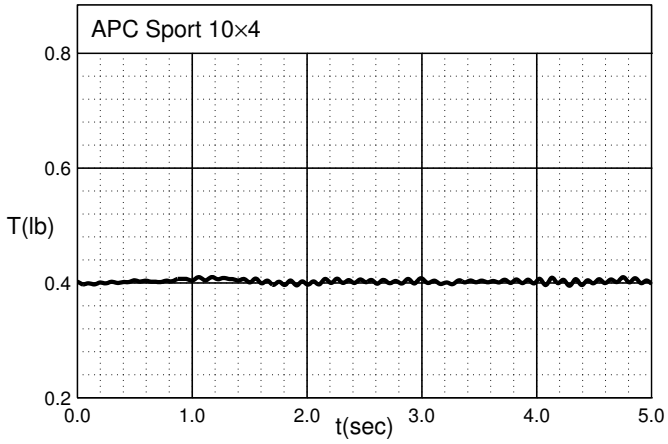

Fig. 4.101: Thrust (lb) time history for the APC Sport 10×4 in hover.

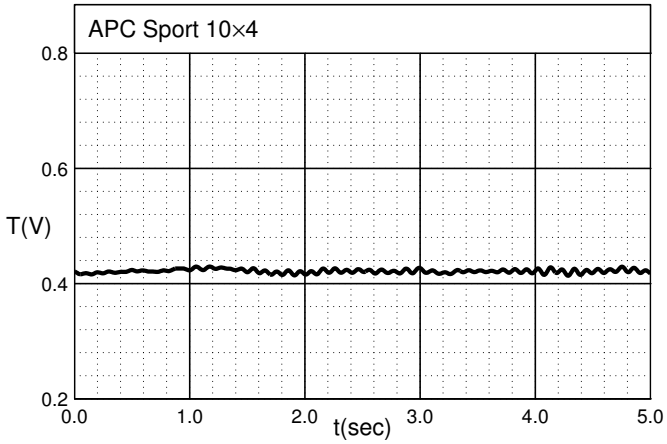

Fig. 4.102: Thrust (V) time history for the APC Sport 10×4 in hover.

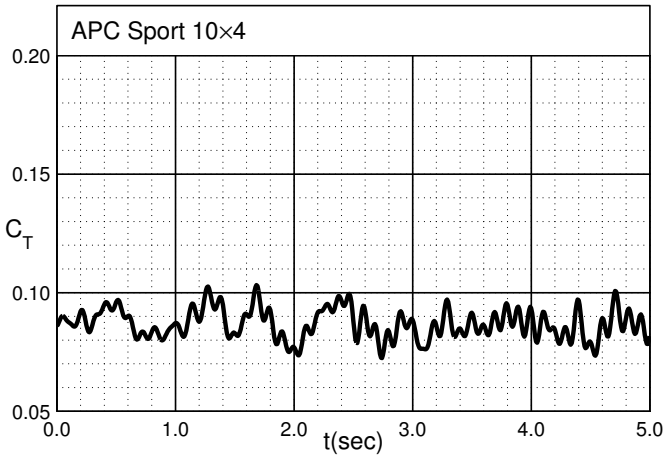

Fig. 4.103: Thrust coefficient time history for the APC Sport 10×4 at $J = -0.19$.

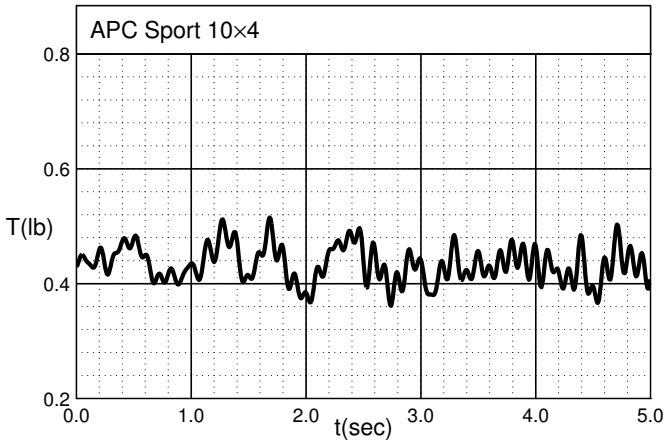

Fig. 4.104: Thrust (lb) time history for the APC Sport 10×4 at $J = -0.19$.

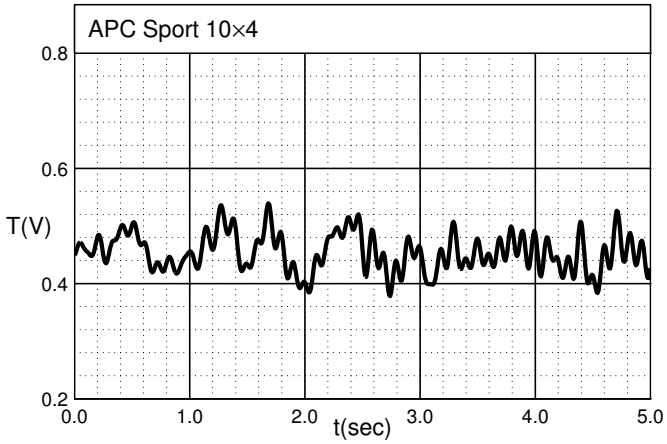

Fig. 4.105: Thrust (V) time history for the APC Sport 10×4 at $J = -0.19$.

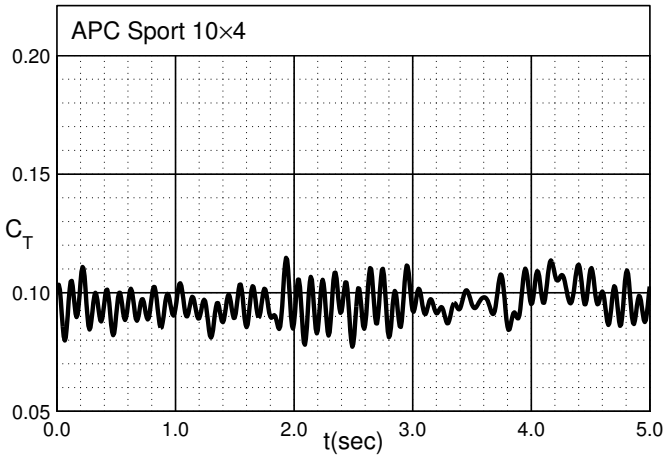

Fig. 4.106: Thrust coefficient time history for the APC Sport 10×4 at $J = -0.36$.

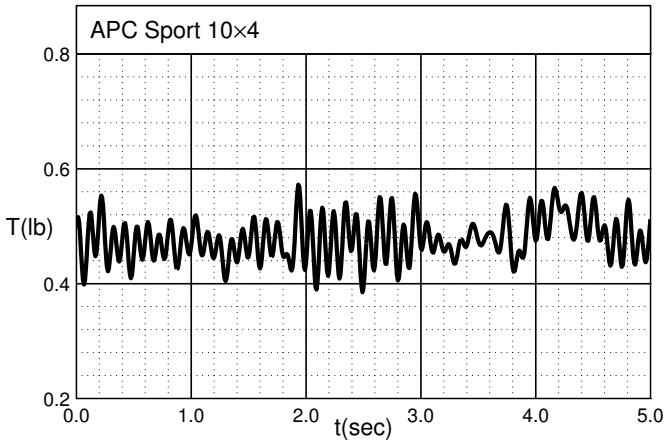

Fig. 4.107: Thrust (lb) time history for the APC Sport 10×4 at $J = -0.36$.

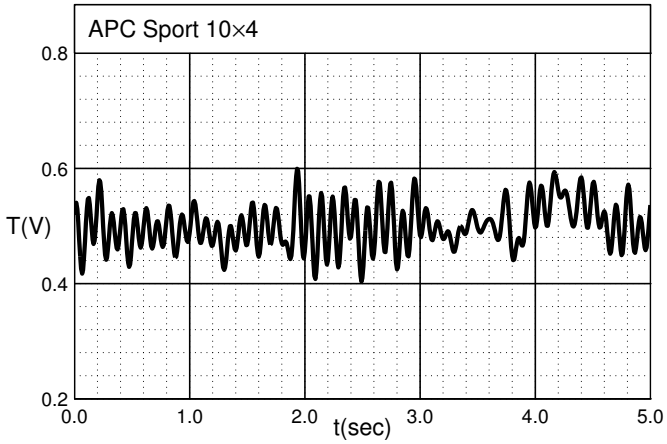

Fig. 4.108: Thrust (V) time history for the APC Sport 10×4 at $J = -0.36$.

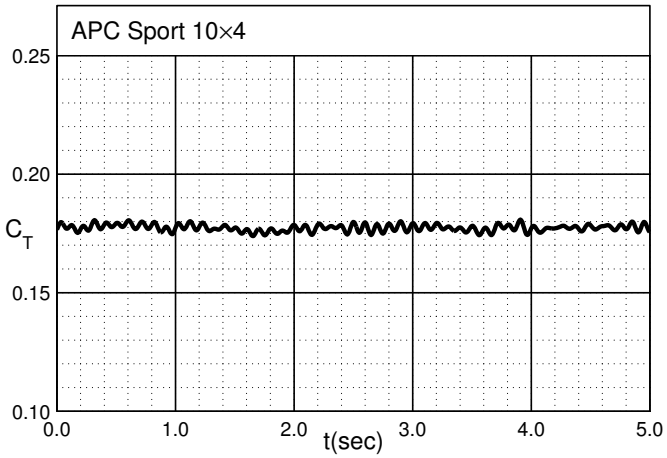

Fig. 4.109: Thrust coefficient time history for the APC Sport 10×4 at $J = -0.62$.

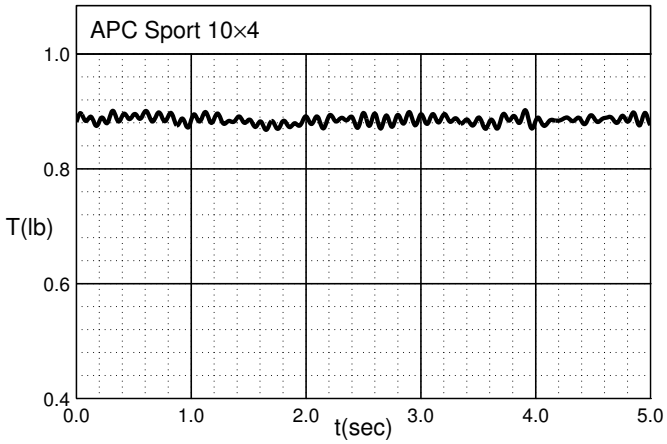

Fig. 4.110: Thrust (lb) time history for the APC Sport 10×4 at $J = -0.62$.

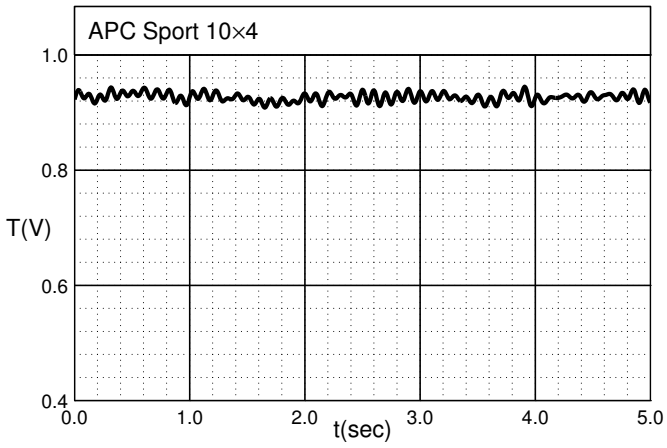

Fig. 4.111: Thrust (V) time history for the APC Sport 10×4 at $J = -0.62$.

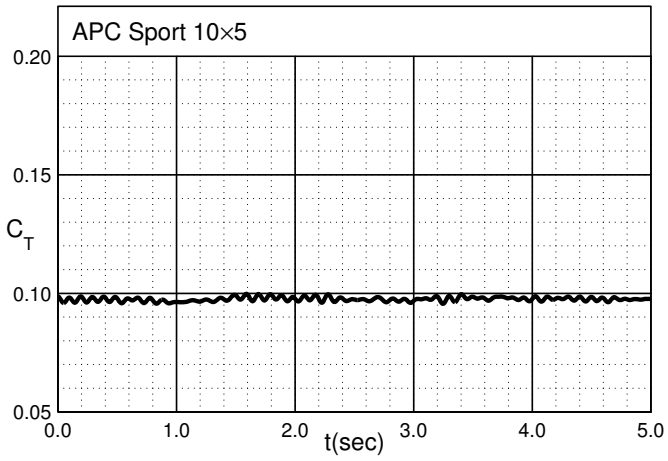

Fig. 4.112: Thrust coefficient time history for the APC Sport 10×5 in hover.

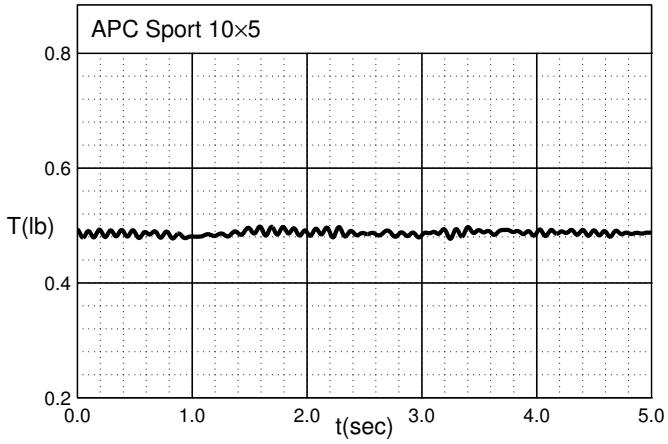

Fig. 4.113: Thrust (lb) time history for the APC Sport 10×5 in hover.

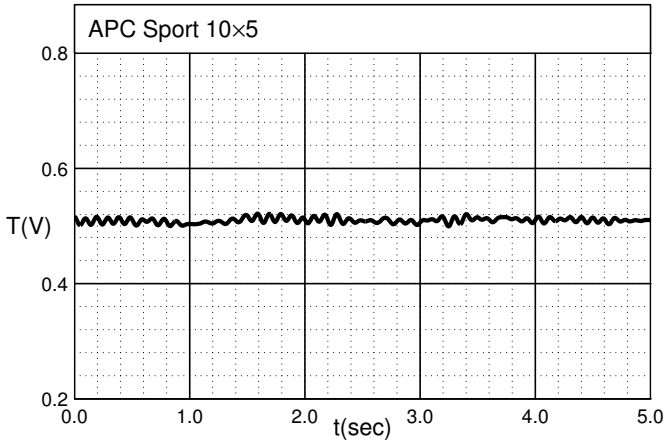

Fig. 4.114: Thrust (V) time history for the APC Sport 10×5 in hover.

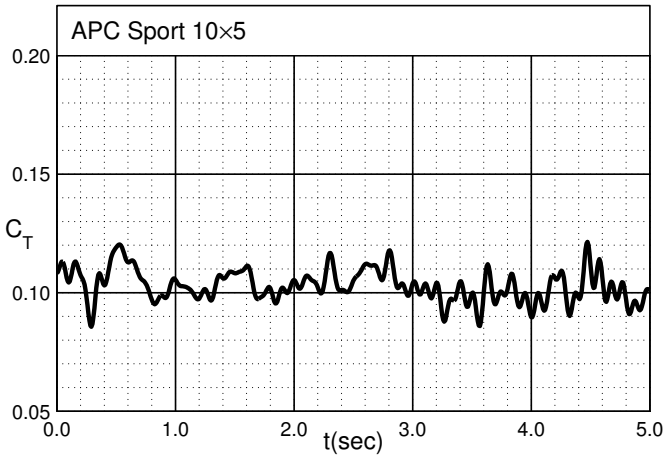

Fig. 4.115: Thrust coefficient time history for the APC Sport 10×5 at $J = -0.19$.

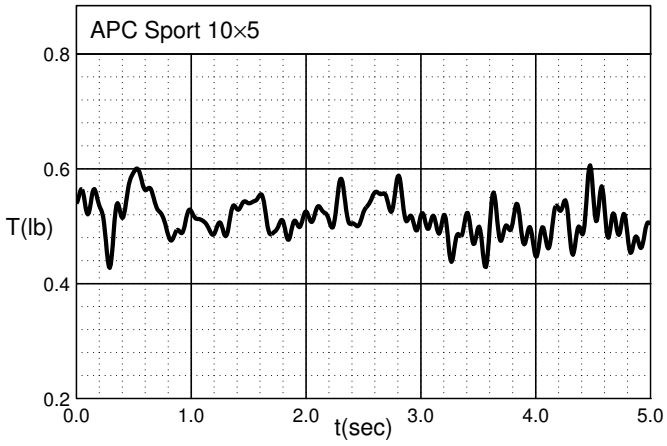

Fig. 4.116: Thrust (lb) time history for the APC Sport 10×5 at $J = -0.19$.

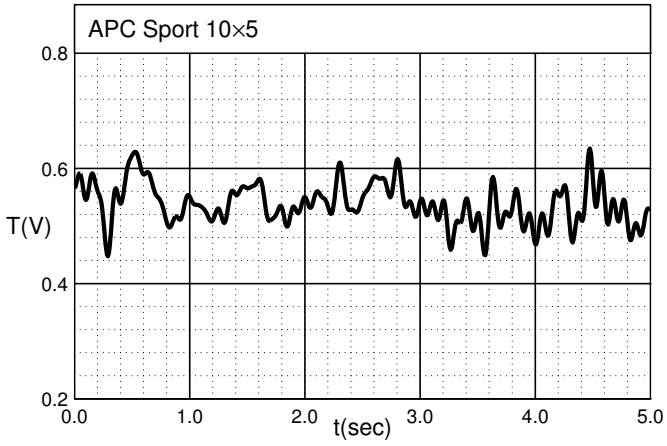

Fig. 4.117: Thrust (V) time history for the APC Sport 10×5 at $J = -0.19$.

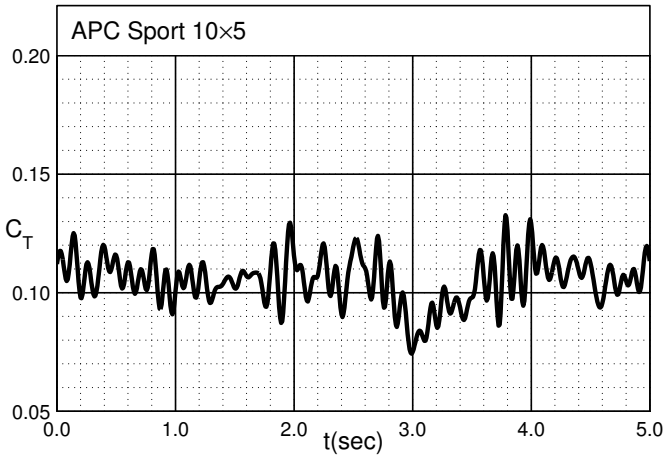

Fig. 4.118: Thrust coefficient time history for the APC Sport 10×5 at $J = -0.36$.

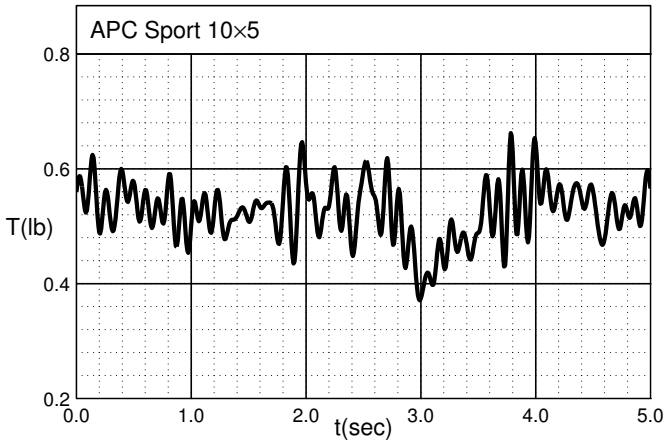

Fig. 4.119: Thrust (lb) time history for the APC Sport 10×5 at $J = -0.36$.

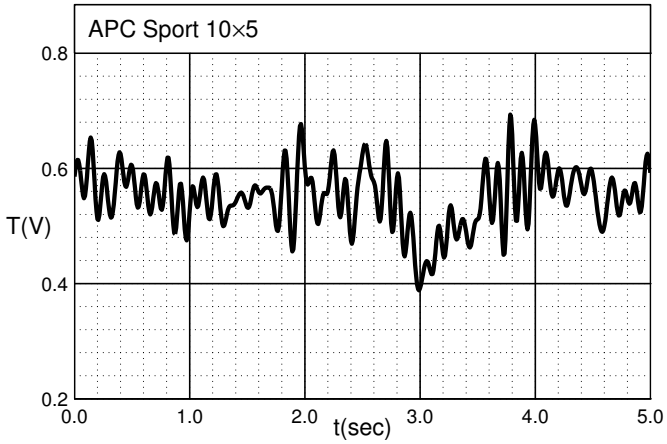

Fig. 4.120: Thrust (V) time history for the APC Sport 10×5 at $J = -0.36$.

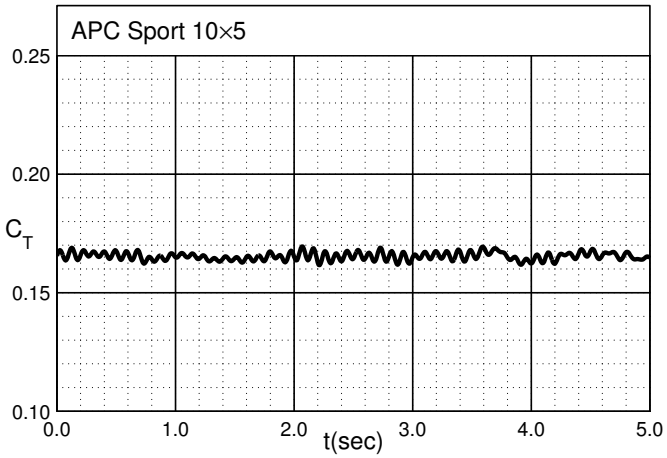

Fig. 4.121: Thrust coefficient time history for the APC Sport 10×5 at $J = -0.62$.

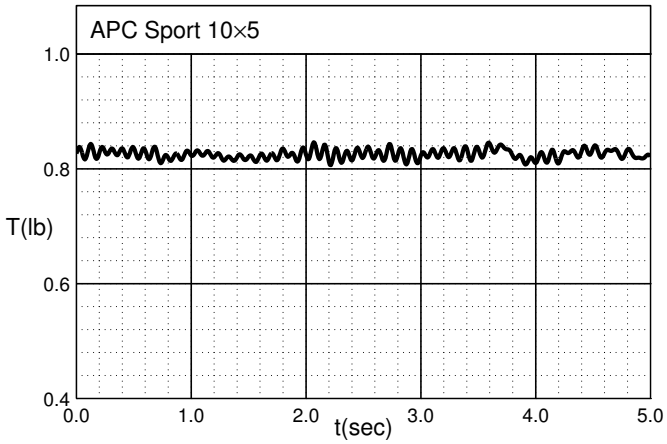

Fig. 4.122: Thrust (lb) time history for the APC Sport 10×5 at $J = -0.62$.

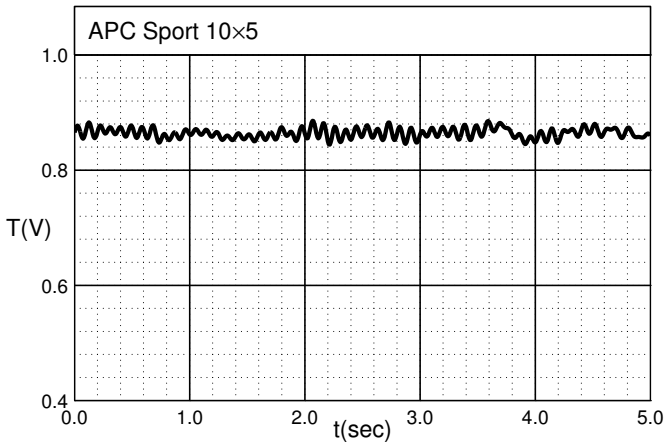

Fig. 4.123: Thrust (V) time history for the APC Sport 10×5 at $J = -0.62$.

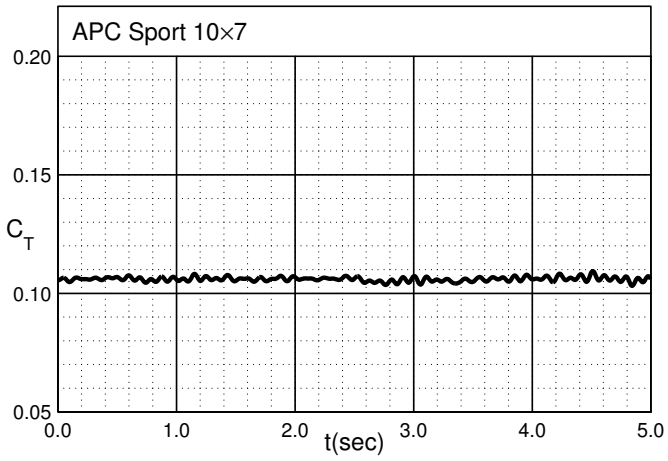

Fig. 4.124: Thrust coefficient time history for the APC Sport 10×7 in hover.

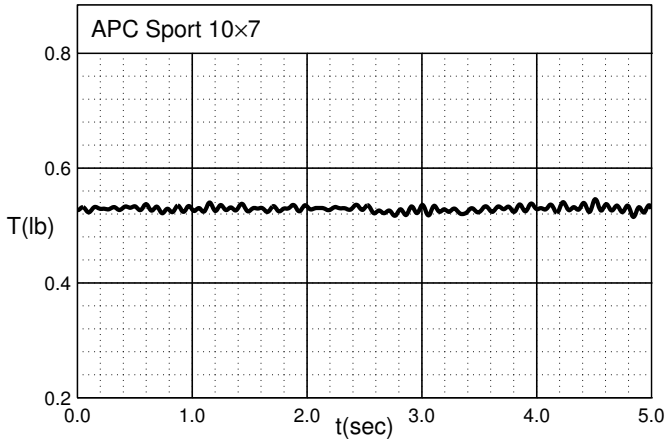

Fig. 4.125: Thrust (lb) time history for the APC Sport 10×7 in hover.

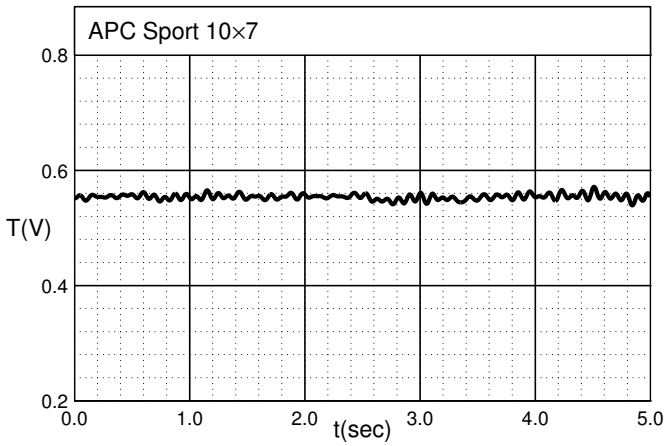

Fig. 4.126: Thrust (V) time history for the APC Sport 10×7 in hover.

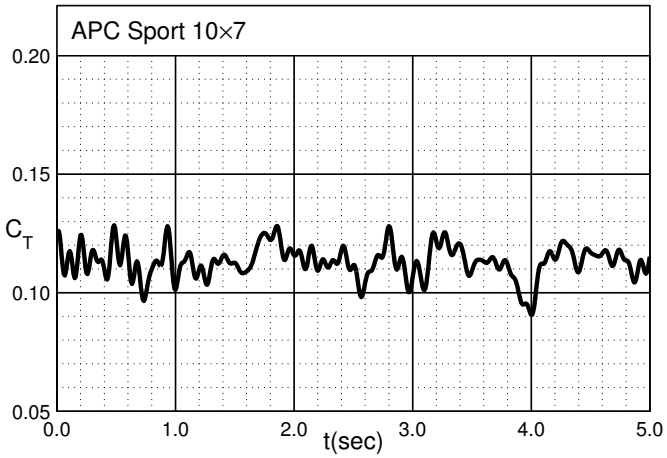

Fig. 4.127: Thrust coefficient time history for the APC Sport 10×7 at $J = -0.19$.

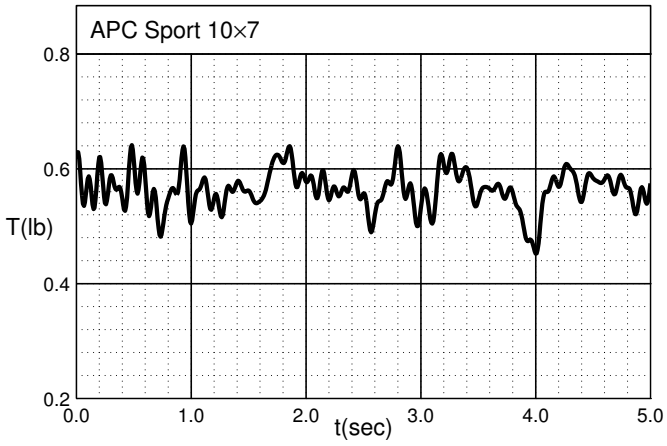

Fig. 4.128: Thrust (lb) time history for the APC Sport 10×7 at $J = -0.19$.

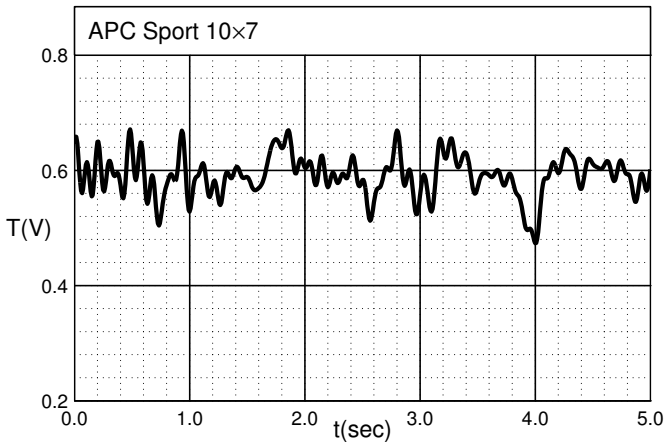

Fig. 4.129: Thrust (V) time history for the APC Sport 10×7 at $J = -0.19$.

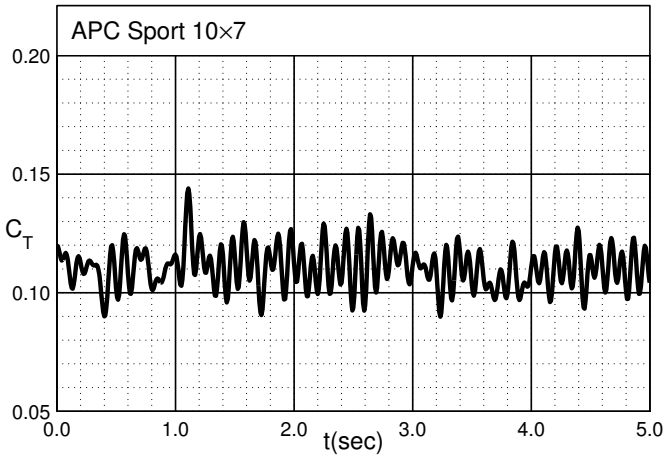

Fig. 4.130: Thrust coefficient time history for the APC Sport 10×7 at $J = -0.36$.

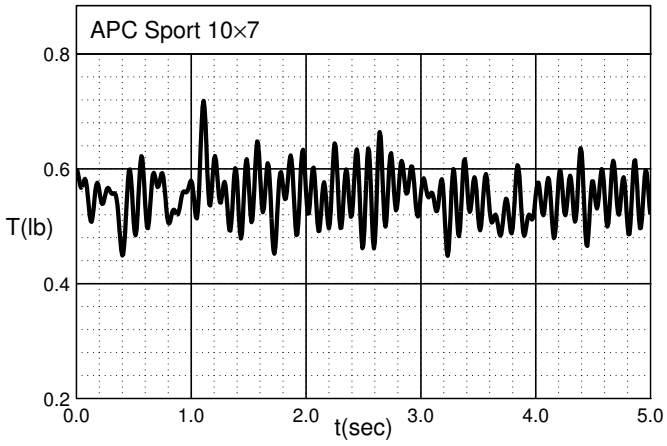

Fig. 4.131: Thrust (lb) time history for the APC Sport 10×7 at $J = -0.36$.

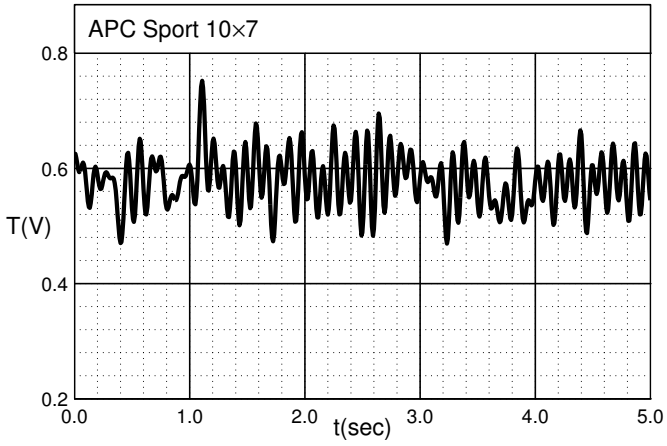

Fig. 4.132: Thrust (V) time history for the APC Sport 10×7 at $J = -0.36$.

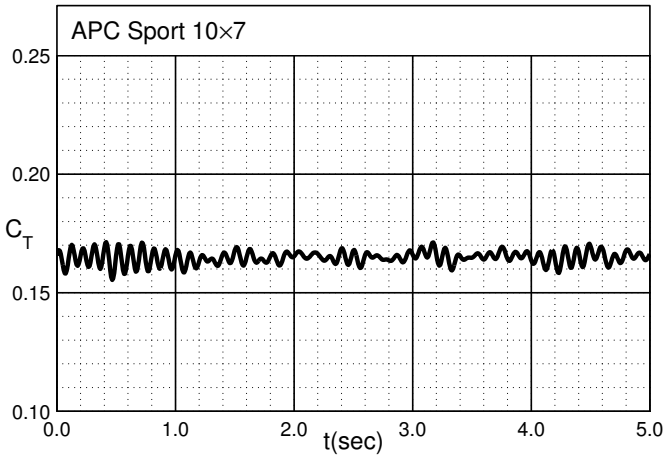

Fig. 4.133: Thrust coefficient time history for the APC Sport 10×7 at $J = -0.62$.

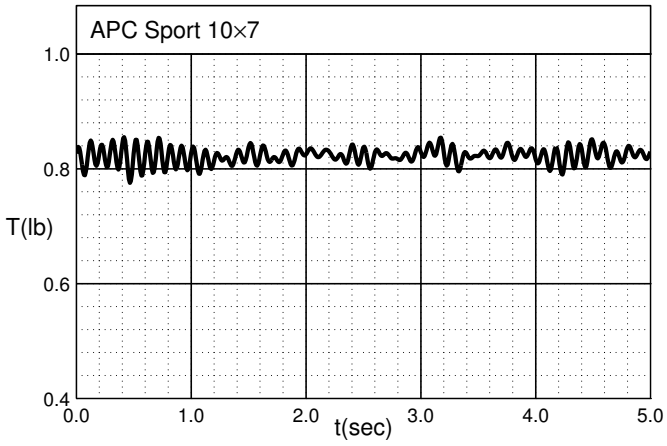

Fig. 4.134: Thrust (lb) time history for the APC Sport 10×7 at $J = -0.62$.

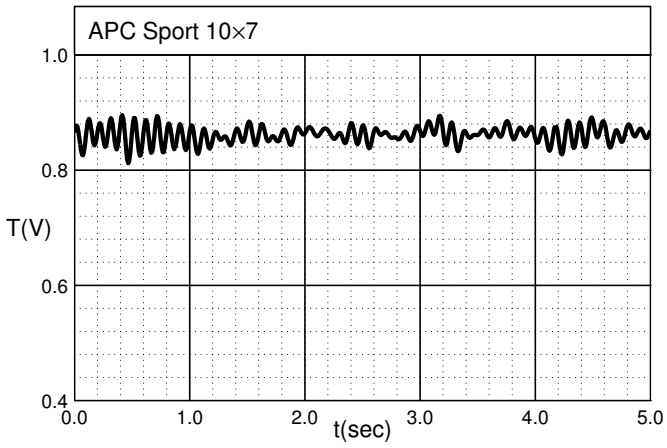

Fig. 4.135: Thrust (V) time history for the APC Sport 10×7 at $J = -0.62$.

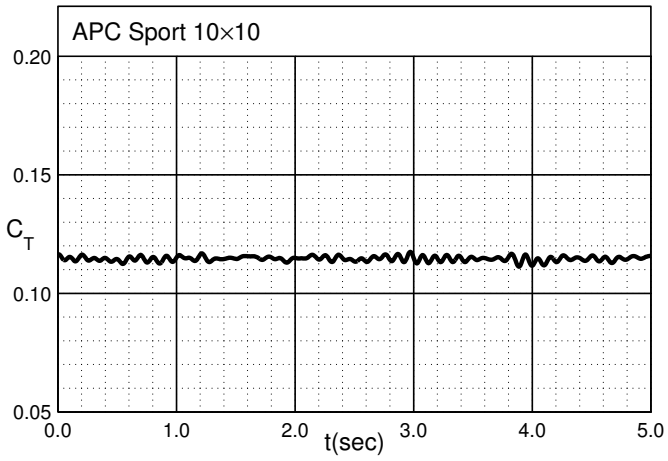

Fig. 4.136: Thrust coefficient time history for the APC Sport 10×10 in hover.

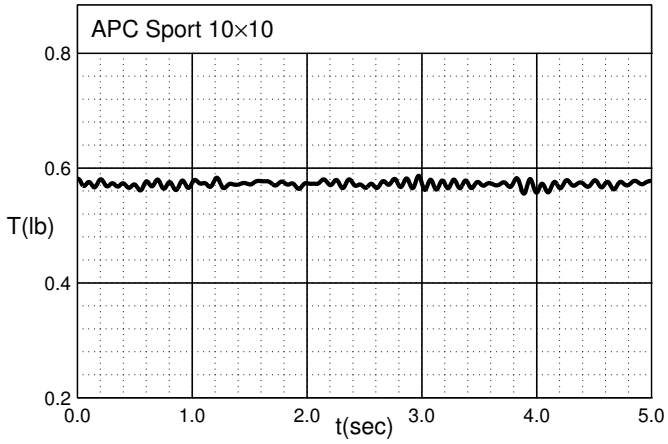

Fig. 4.137: Thrust (lb) time history for the APC Sport 10×10 in hover.

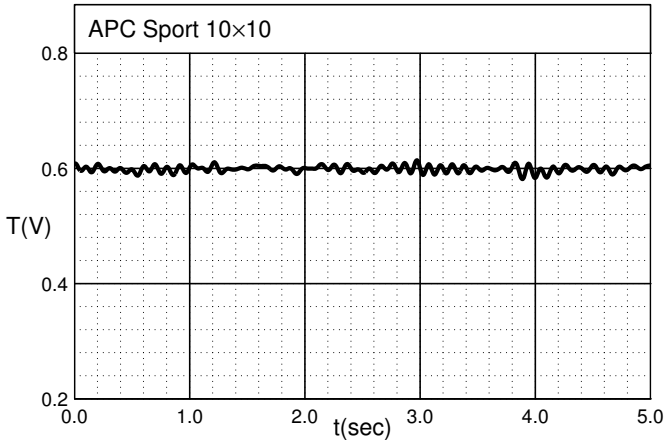

Fig. 4.138: Thrust (V) time history for the APC Sport 10×10 in hover.

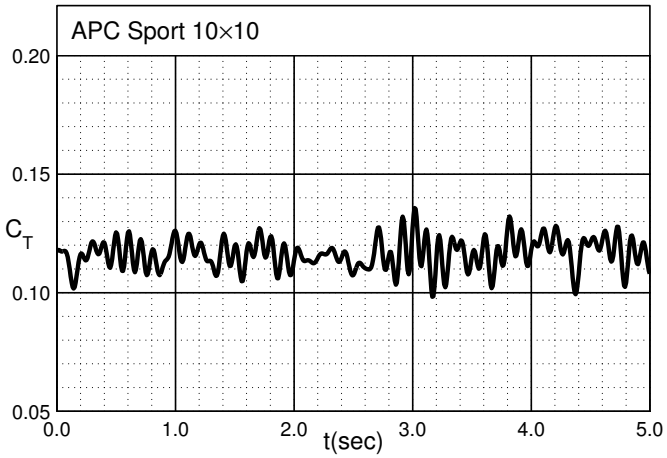

Fig. 4.139: Thrust coefficient time history for the APC Sport 10×10 at $J = -0.19$.

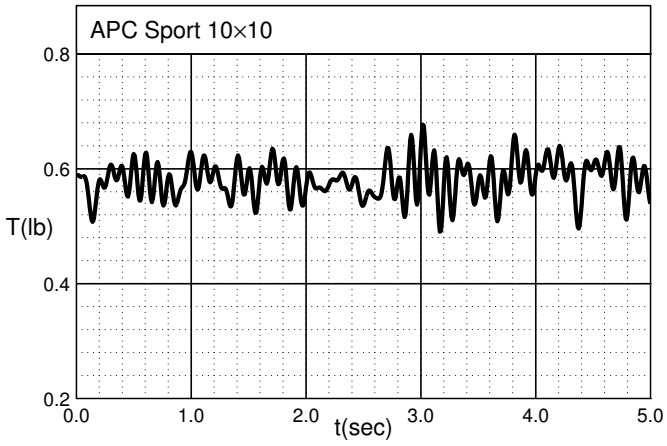

Fig. 4.140: Thrust (lb) time history for the APC Sport 10×10 at $J = -0.19$.

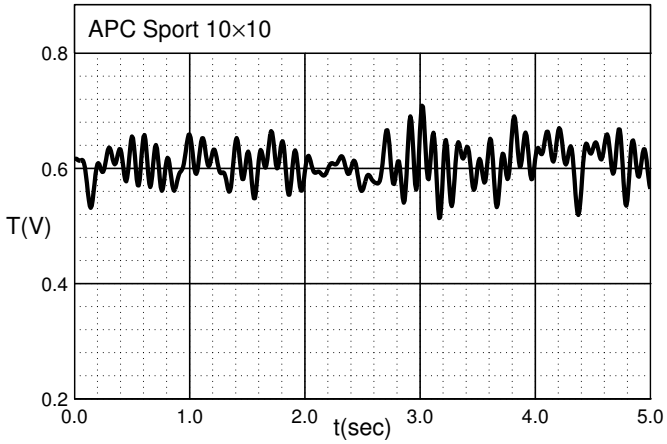

Fig. 4.141: Thrust (V) time history for the APC Sport 10×10 at $J = -0.19$.

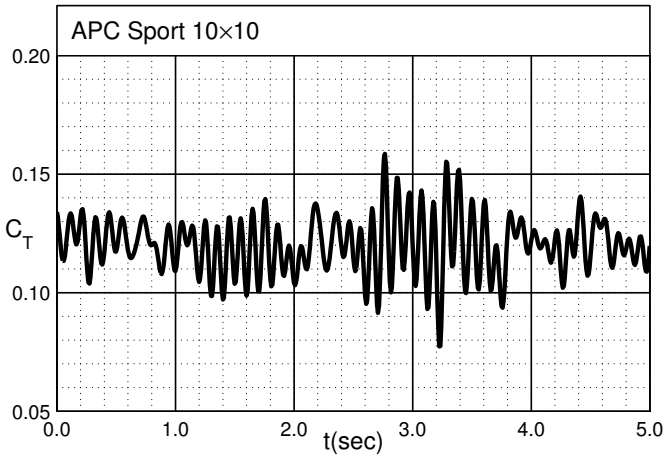

Fig. 4.142: Thrust coefficient time history for the APC Sport 10×10 at $J = -0.36$.

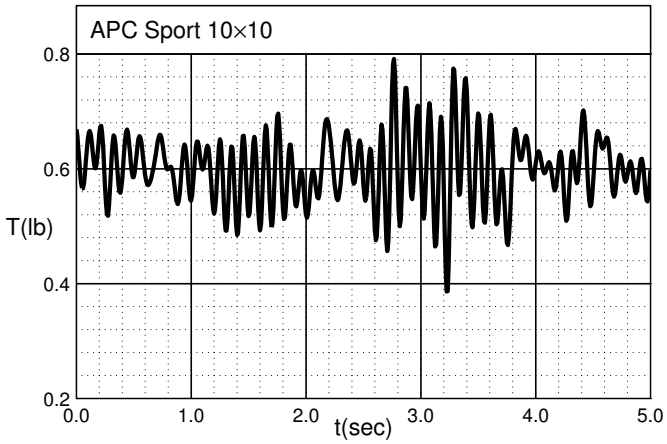

Fig. 4.143: Thrust (lb) time history for the APC Sport 10×10 at $J = -0.36$.

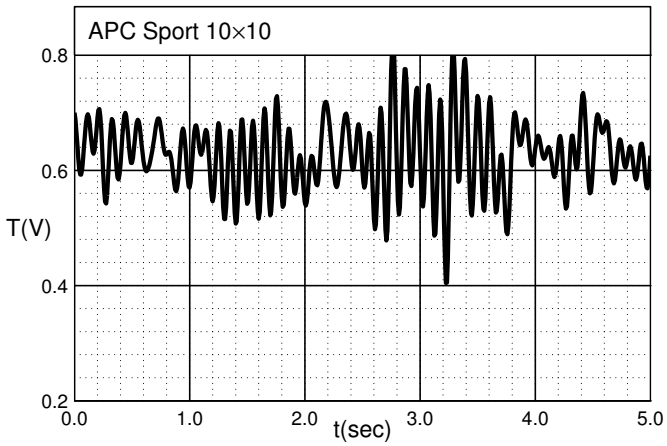

Fig. 4.144: Thrust (V) time history for the APC Sport 10×10 at $J = -0.36$.

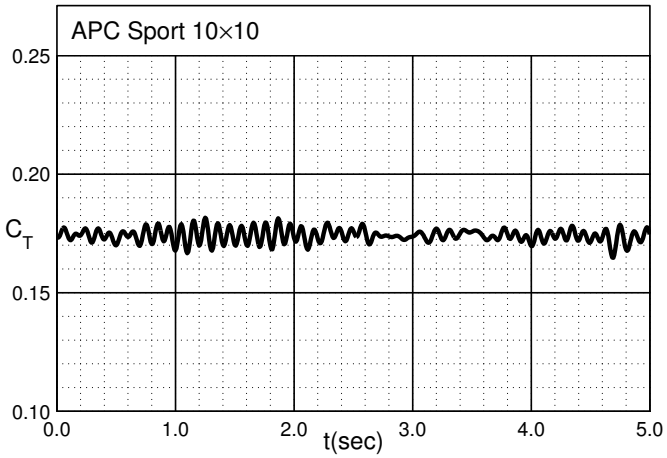

Fig. 4.145: Thrust coefficient time history for the APC Sport 10×10 at $J = -0.62$.

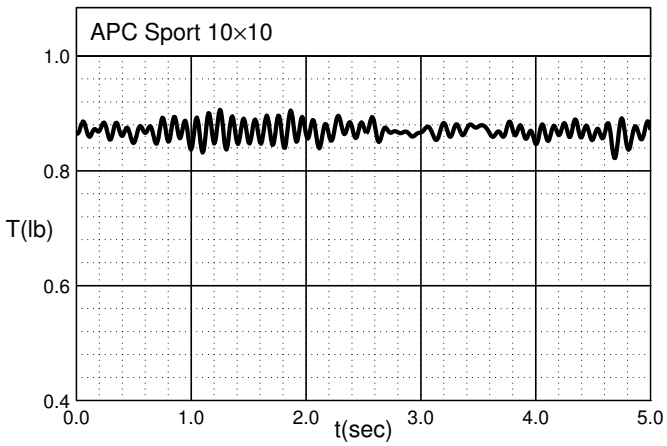

Fig. 4.146: Thrust (lb) time history for the APC Sport 10×10 at $J = -0.62$.

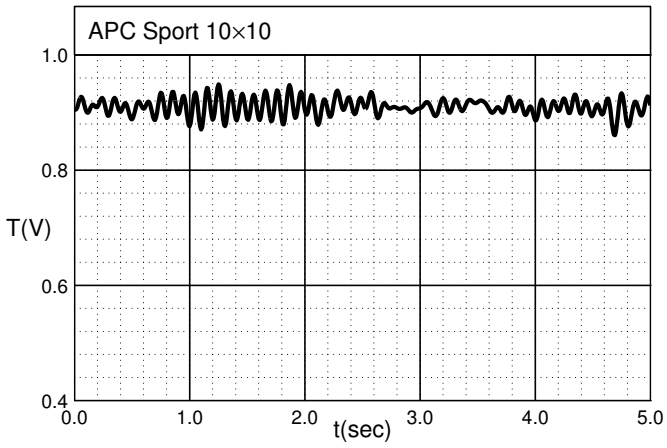

Fig. 4.147: Thrust (V) time history for the APC Sport 10×10 at $J = -0.62$.

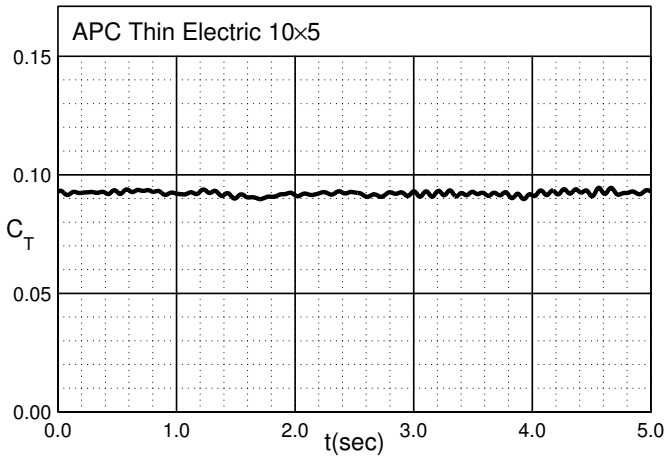

Fig. 4.148: Thrust coefficient time history for the APC Thin Electric 10×5 in hover.

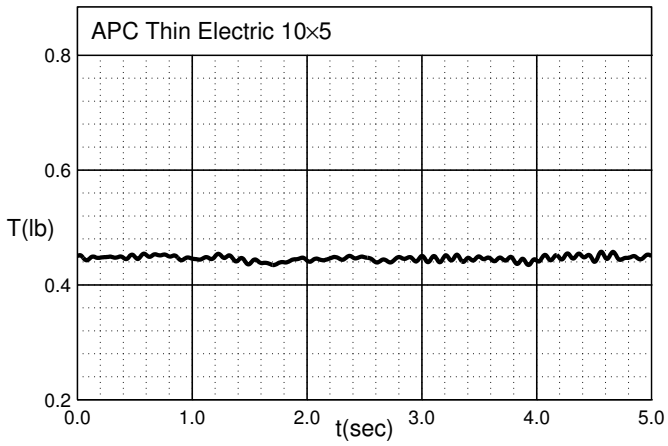

Fig. 4.149: Thrust (lb) time history for the APC Thin Electric 10×5 in hover.

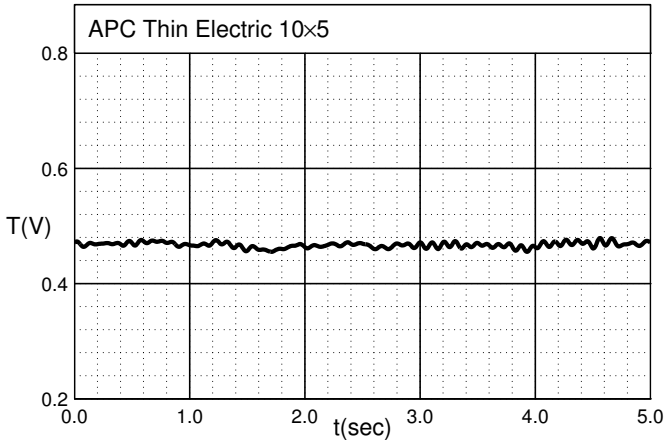

Fig. 4.150: Thrust (V) time history for the APC Thin Electric 10×5 in hover.

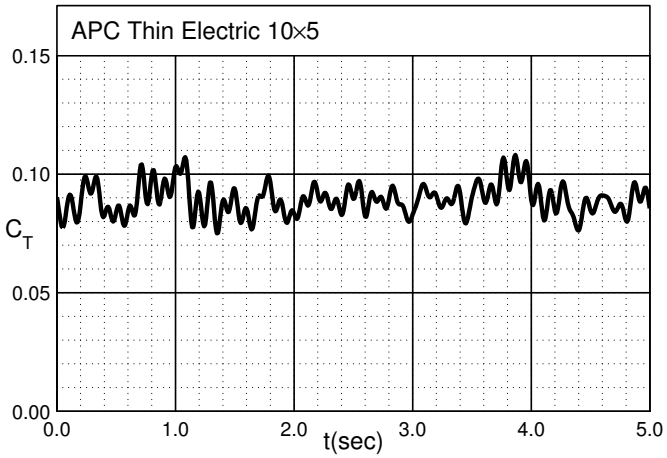

Fig. 4.151: Thrust coefficient time history for the APC Thin Electric 10×5 at $J = -0.19$.

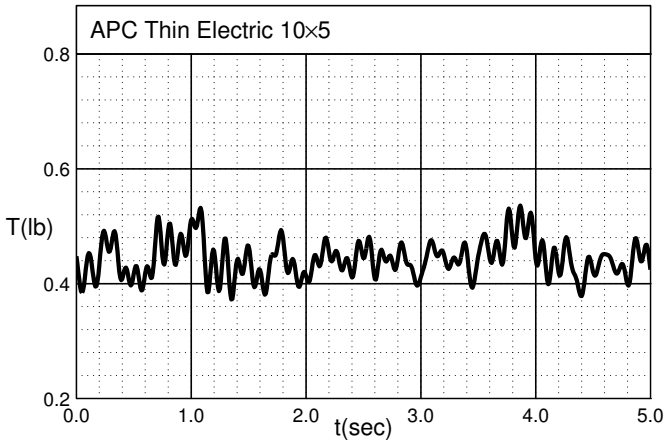

Fig. 4.152: Thrust (lb) time history for the APC Thin Electric 10×5 at $J = -0.19$.

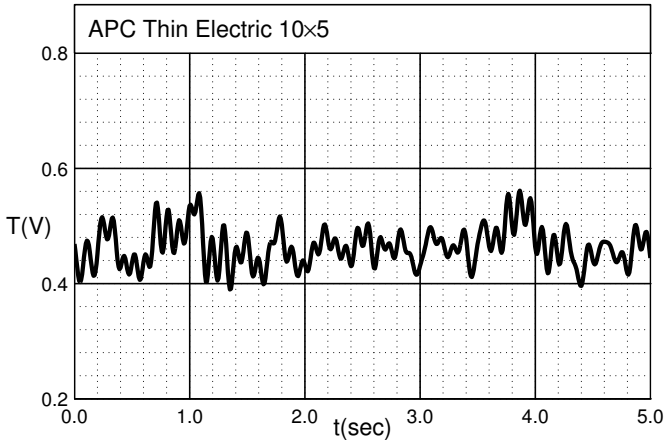

Fig. 4.153: Thrust (V) time history for the APC Thin Electric 10×5 at $J = -0.19$.

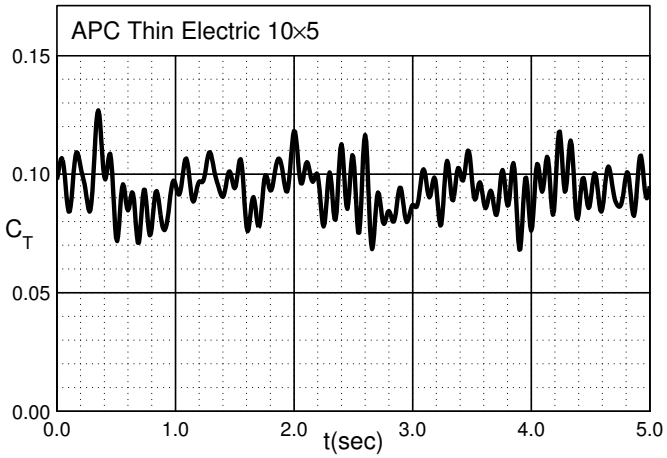

Fig. 4.154: Thrust coefficient time history for the APC Thin Electric 10×5 at $J = -0.36$.

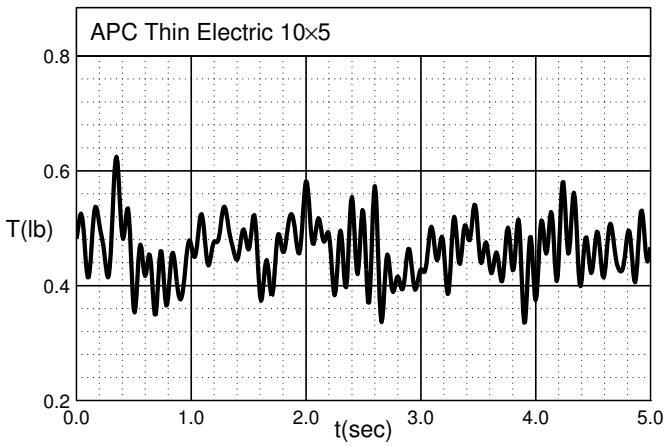

Fig. 4.155: Thrust (lb) time history for the APC Thin Electric 10×5 at $J = -0.36$.

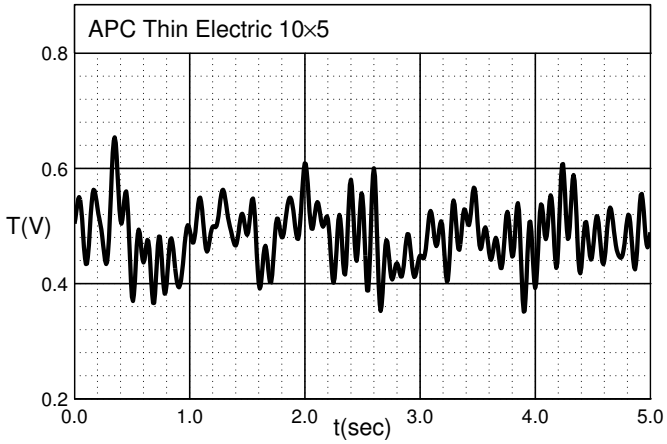

Fig. 4.156: Thrust (V) time history for the APC Thin Electric 10×5 at $J = -0.36$.

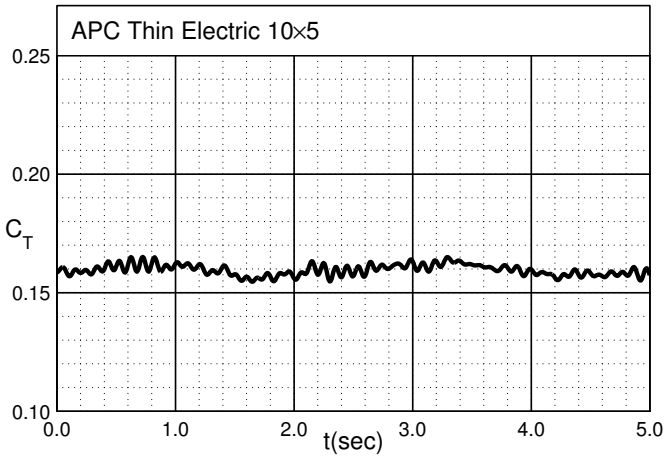

Fig. 4.157: Thrust coefficient time history for the APC Thin Electric 10×5 at $J = -0.62$.

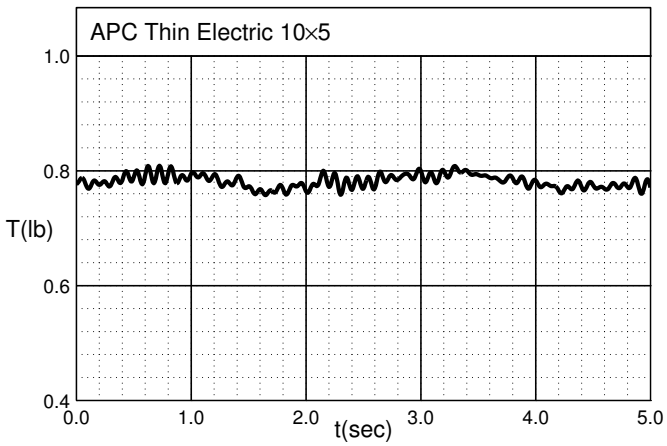

Fig. 4.158: Thrust (lb) time history for the APC Thin Electric 10×5 at $J = -0.62$.

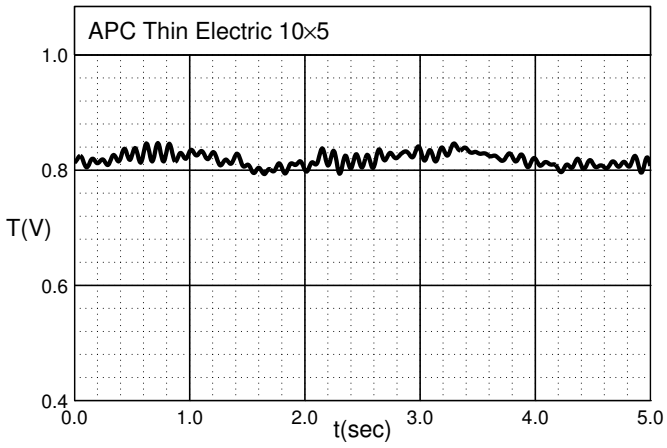

Fig. 4.159: Thrust (V) time history for the APC Thin Electric 10×5 at $J = -0.62$.

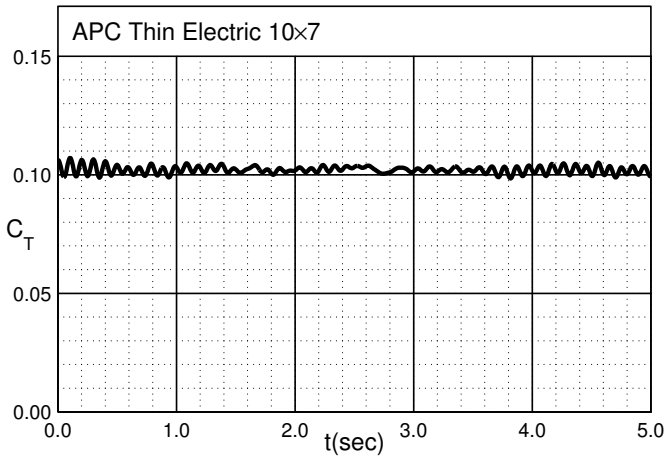

Fig. 4.160: Thrust coefficient time history for the APC Thin Electric 10×7 in hover.

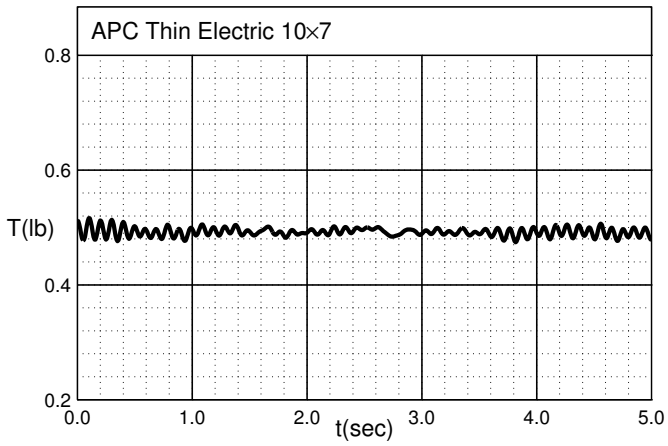

Fig. 4.161: Thrust (lb) time history for the APC Thin Electric 10×7 in hover.

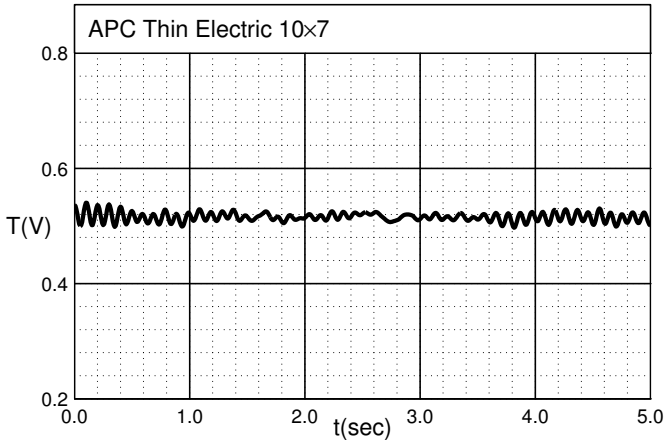

Fig. 4.162: Thrust (V) time history for the APC Thin Electric 10×7 in hover.

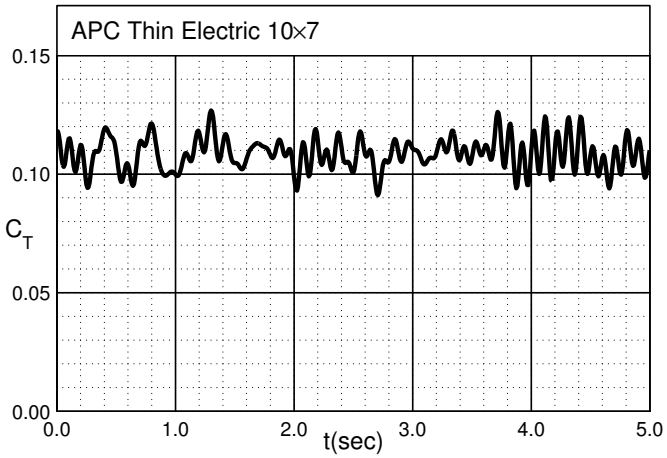

Fig. 4.163: Thrust coefficient time history for the APC Thin Electric 10×7 at $J = -0.19$.

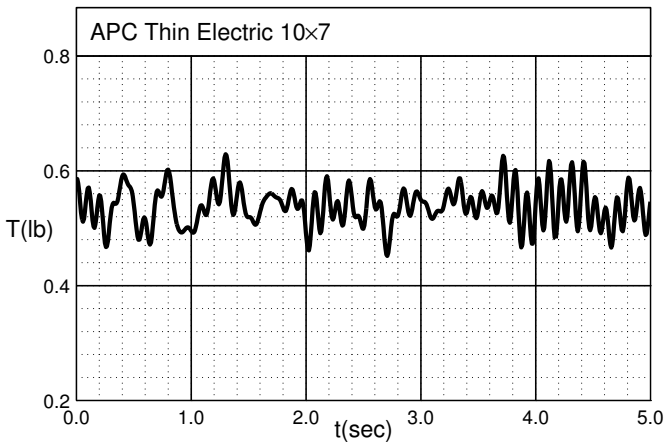

Fig. 4.164: Thrust (lb) time history for the APC Thin Electric 10×7 at $J = -0.19$.

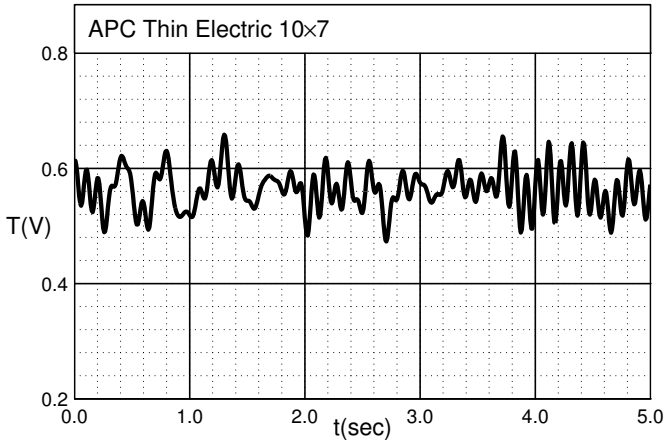

Fig. 4.165: Thrust (V) time history for the APC Thin Electric 10×7 at $J = -0.19$.

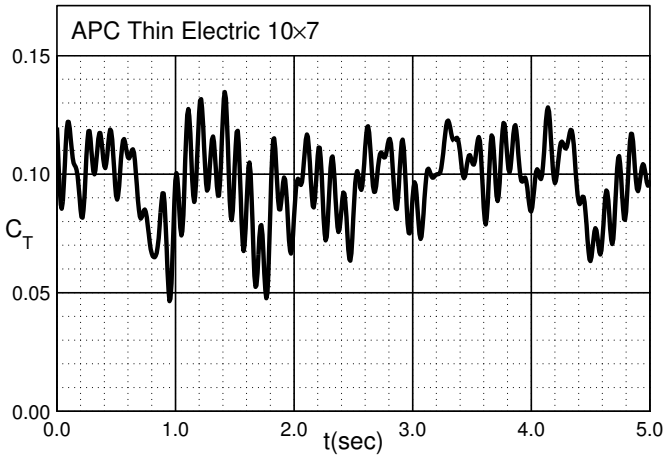

Fig. 4.166: Thrust coefficient time history for the APC Thin Electric 10×7 at $J = -0.36$.

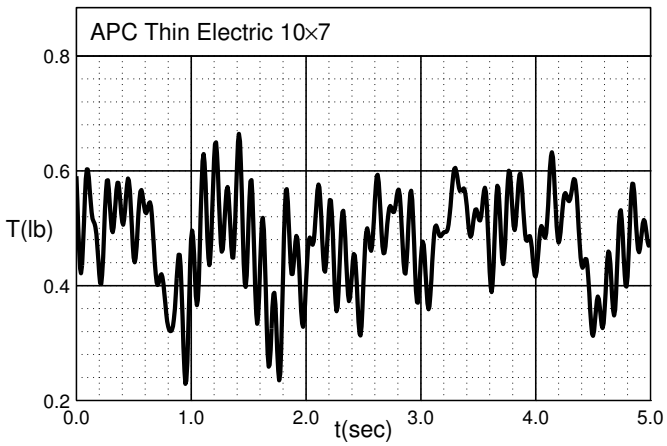

Fig. 4.167: Thrust (lb) time history for the APC Thin Electric 10×7 at $J = -0.36$.

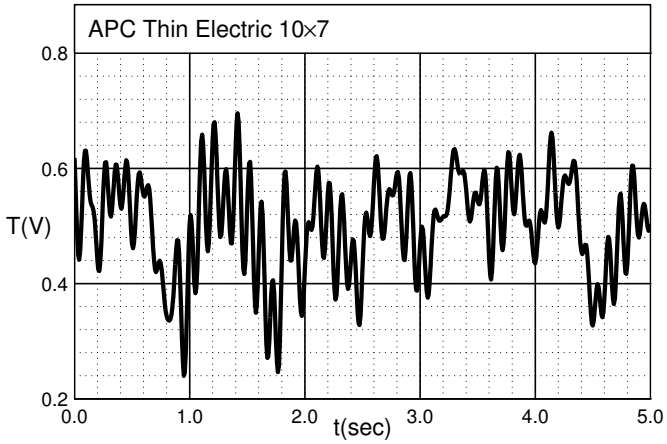

Fig. 4.168: Thrust (V) time history for the APC Thin Electric 10×7 at $J = -0.36$.

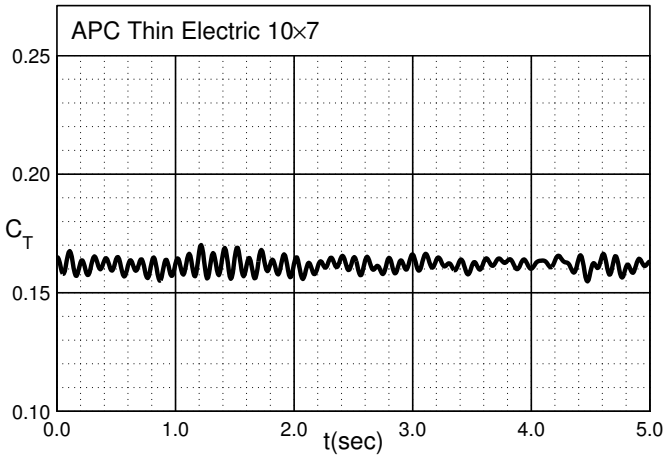

Fig. 4.169: Thrust coefficient time history for the APC Thin Electric 10×7 at $J = -0.62$.

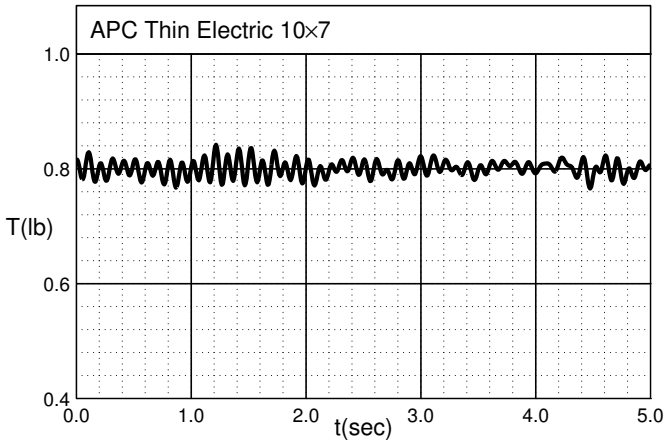

Fig. 4.170: Thrust (lb) time history for the APC Thin Electric 10×7 at $J = -0.62$.

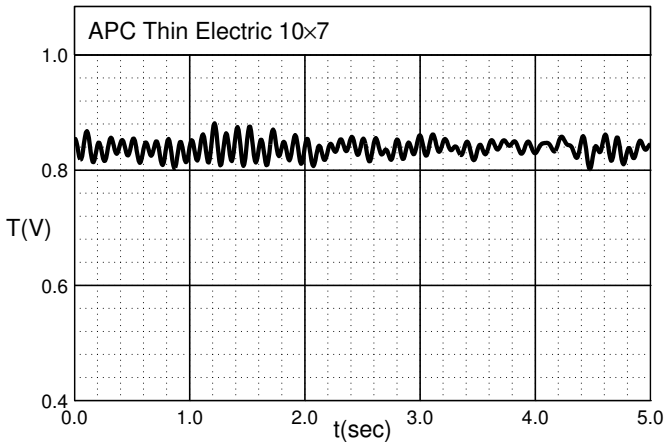

Fig. 4.171: Thrust (V) time history for the APC Thin Electric 10×7 at $J = -0.62$.

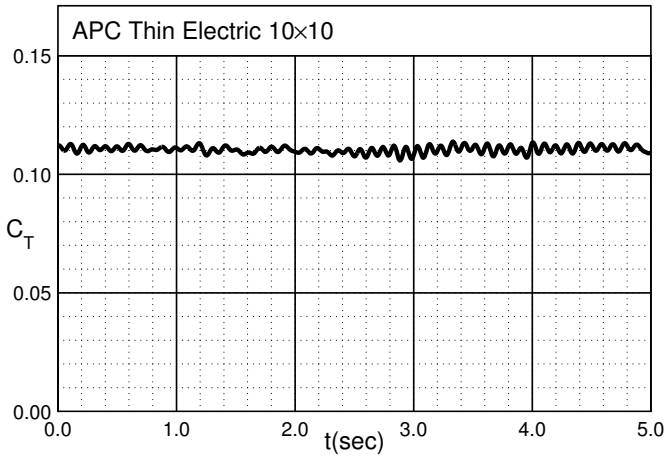

Fig. 4.172: Thrust coefficient time history for the APC Thin Electric 10×10 in hover.

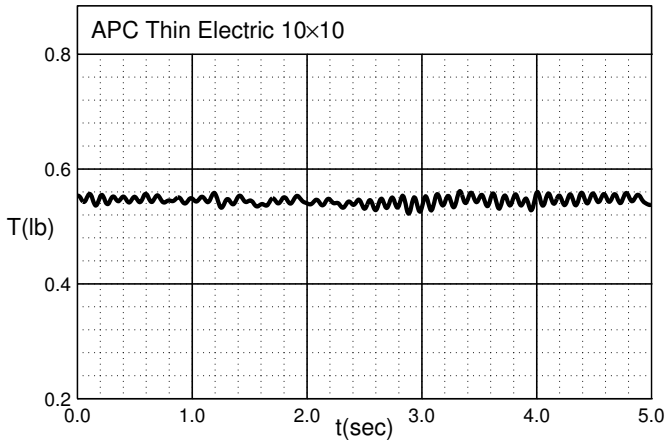

Fig. 4.173: Thrust (lb) time history for the APC Thin Electric 10×10 in hover.

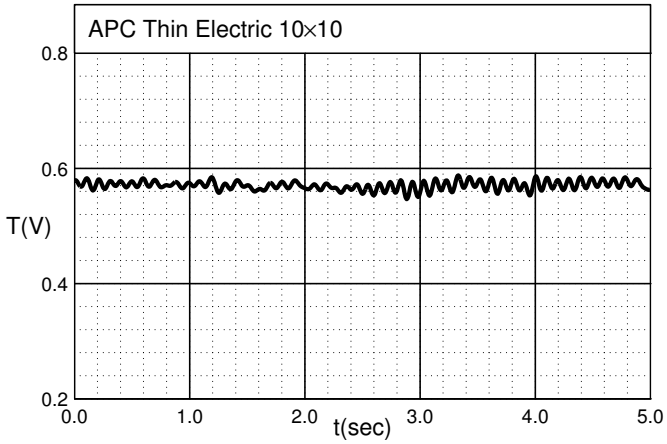

Fig. 4.174: Thrust (V) time history for the APC Thin Electric 10×10 in hover.

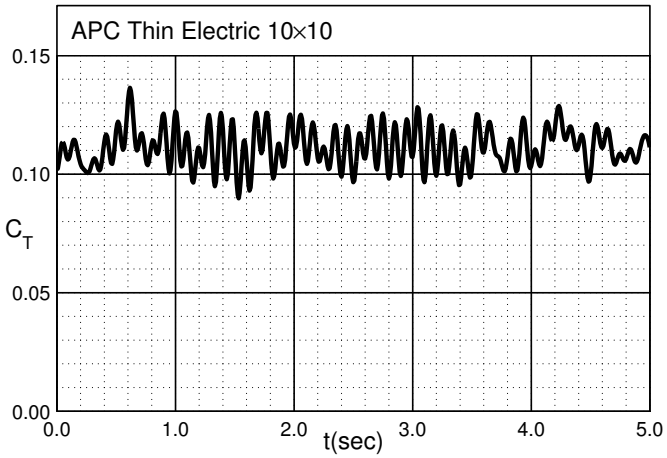

Fig. 4.175: Thrust coefficient time history for the APC Thin Electric 10×10 at $J = -0.19$.

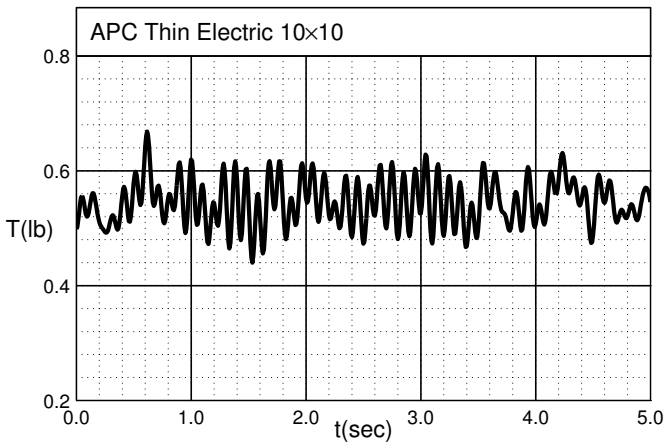

Fig. 4.176: Thrust (lb) time history for the APC Thin Electric 10×10 at $J = -0.19$.

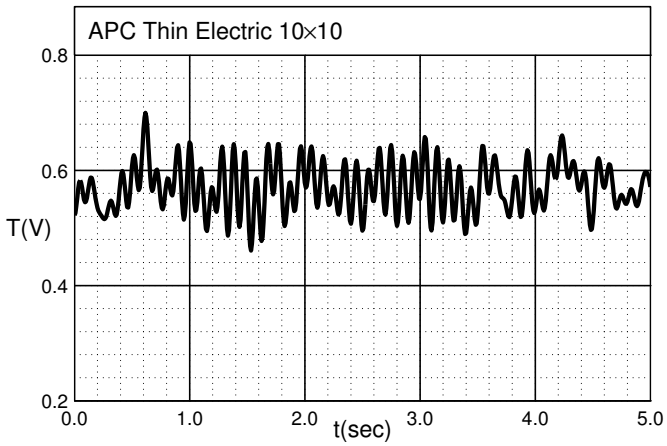

Fig. 4.177: Thrust (V) time history for the APC Thin Electric 10×10 at $J = -0.19$.

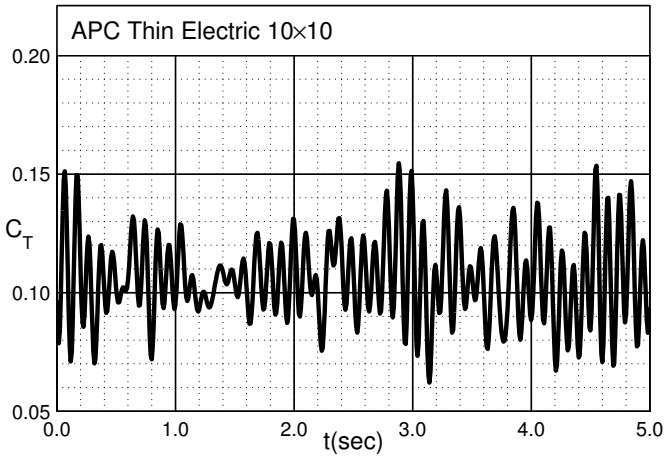

Fig. 4.178: Thrust coefficient time history for the APC Thin Electric 10×10 at $J = -0.36$.

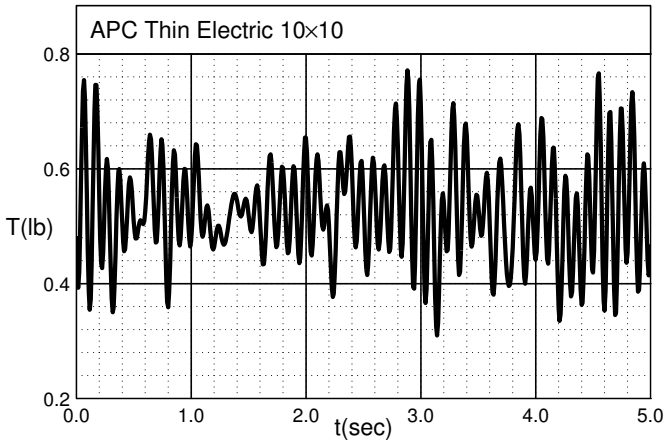

Fig. 4.179: Thrust (lb) time history for the APC Thin Electric 10×10 at $J = -0.36$.

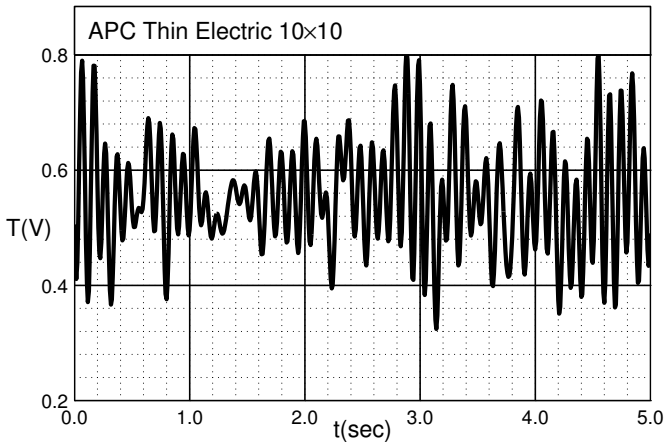

Fig. 4.180: Thrust (V) time history for the APC Thin Electric 10×10 at $J = -0.36$.

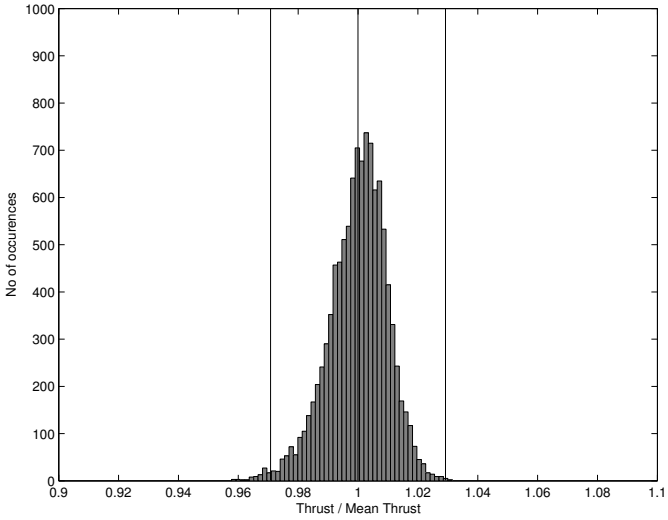

Fig. 4.181: Thrust data histogram for the APC Slow Flyer 9×3.8 in hover.

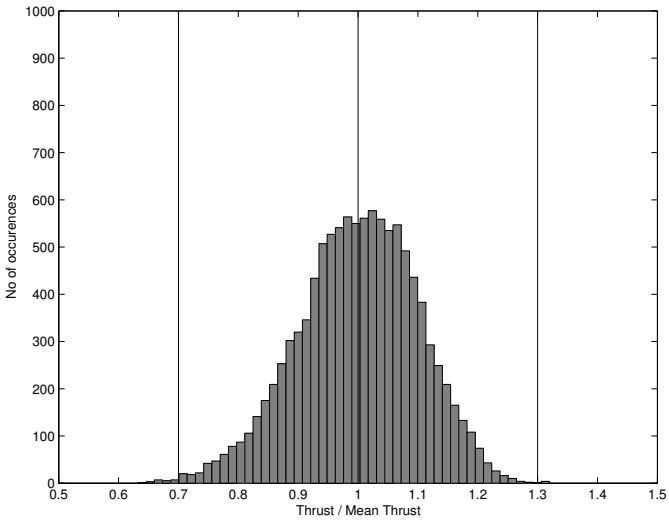

Fig. 4.182: Thrust data histogram for the APC Slow Flyer 9×3.8 at $J = -0.21$.

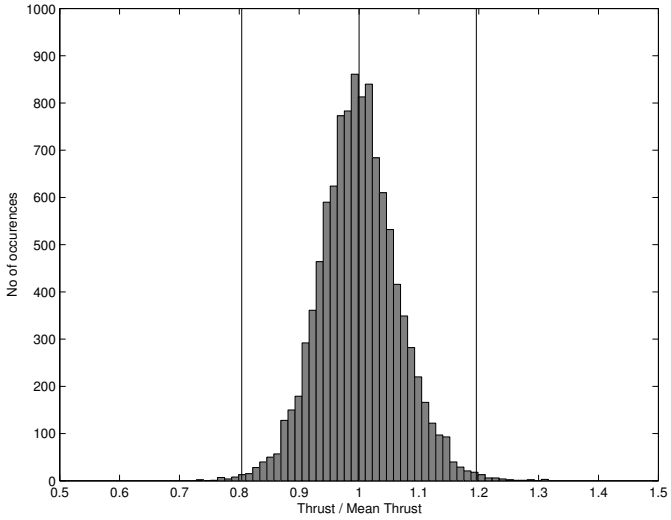

Fig. 4.183: Thrust data histogram for the APC Slow Flyer 9×3.8 at $J = -0.40$.

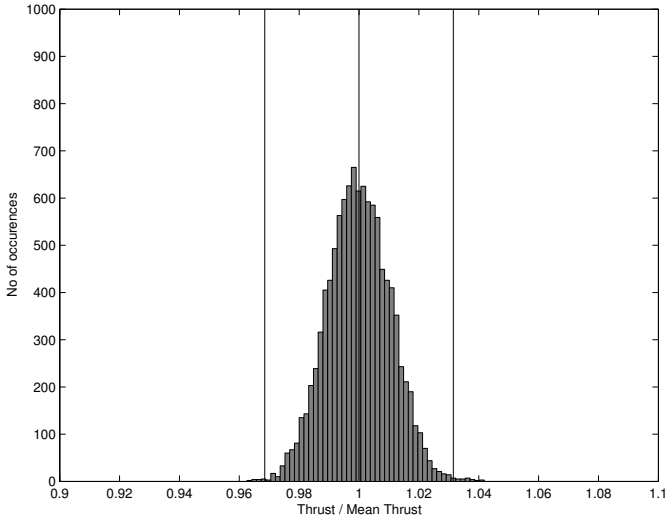

Fig. 4.184: Thrust data histogram for the APC Slow Flyer 9×3.8 at $J = -0.68$.

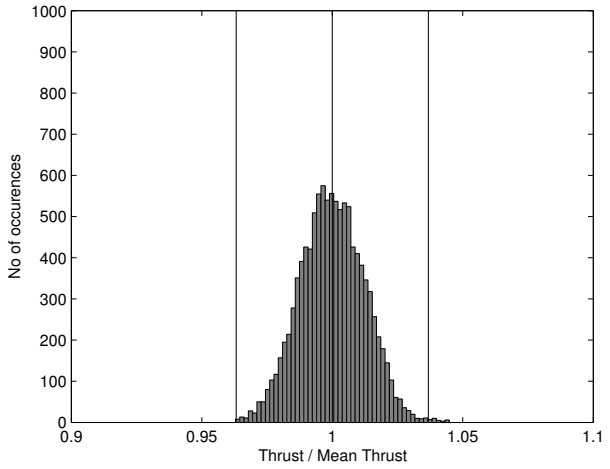

Fig. 4.185: Thrust data histogram for the APC Slow Flyer 9×4.7 in hover.

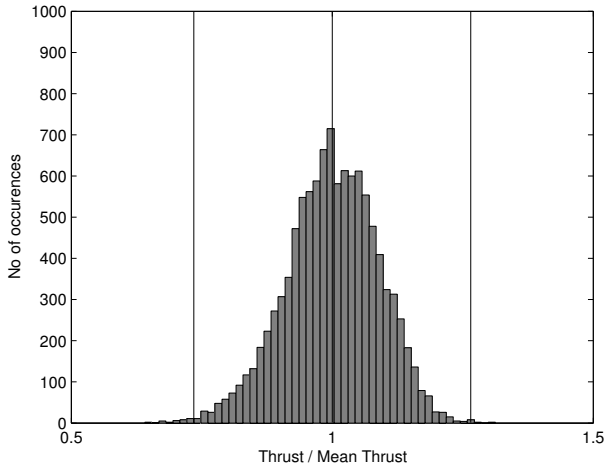

Fig. 4.186: Thrust data histogram for the APC Slow Flyer 9×4.7 at $J = -0.21$.

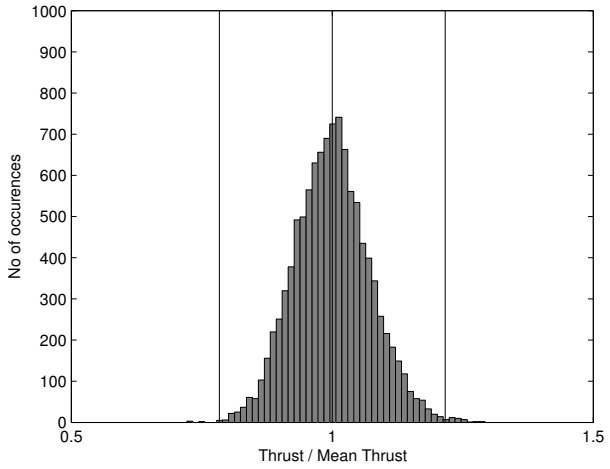

Fig. 4.187: Thrust data histogram for the APC Slow Flyer 9×4.7 at $J = -0.40$.

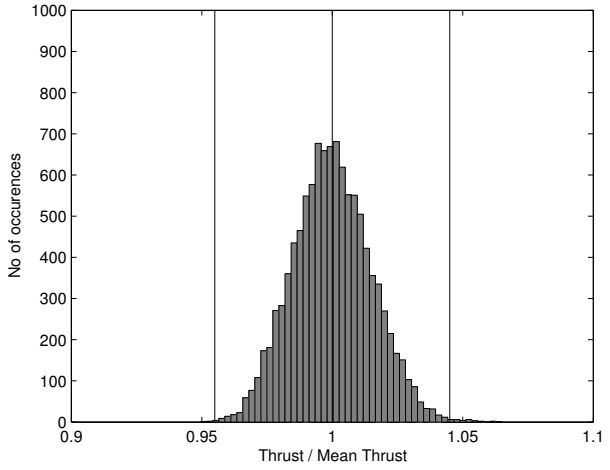

Fig. 4.188: Thrust data histogram for the APC Slow Flyer 9×4.7 at $J = -0.68$.

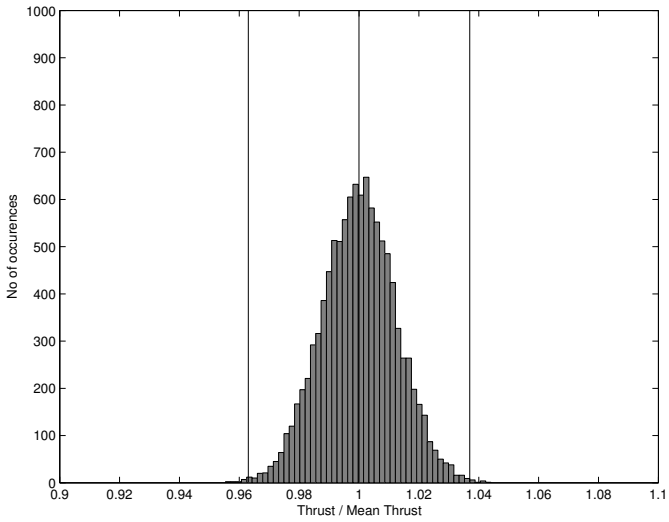

Fig. 4.189: Thrust data histogram for the APC Slow Flyer 9×7.5 in hover.

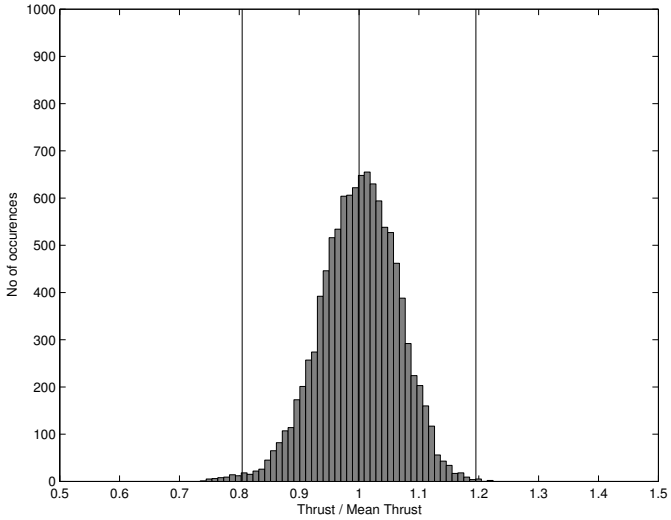

Fig. 4.190: Thrust data histogram for the APC Slow Flyer 9×7.5 at $J = -0.21$.

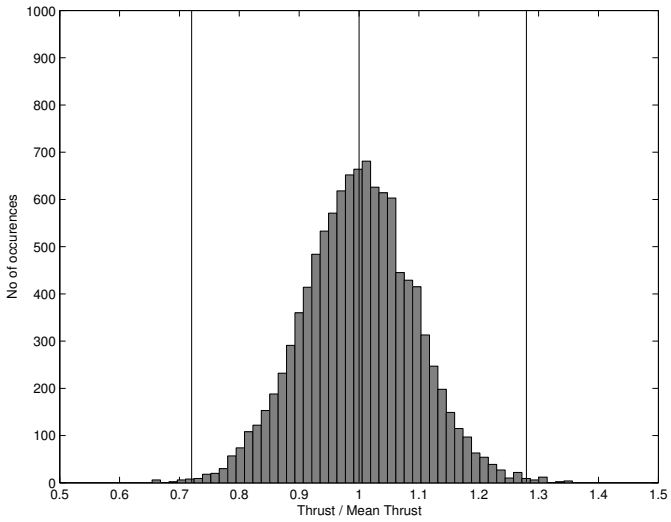

Fig. 4.191: Thrust data histogram for the APC Slow Flyer 9×7.5 at $J = -0.40$.

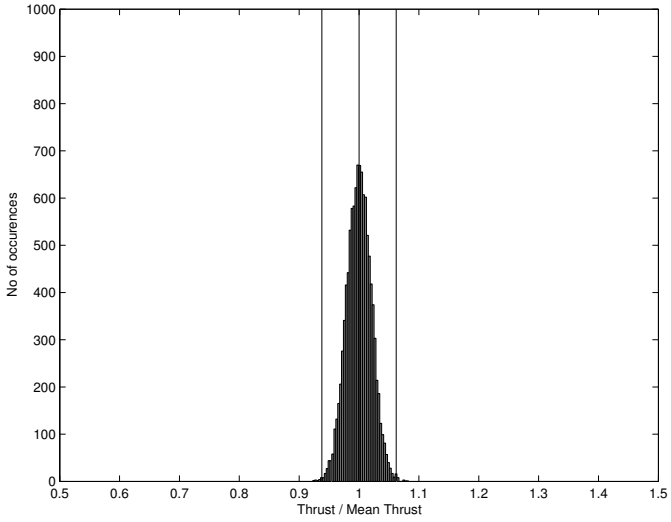

Fig. 4.192: Thrust data histogram for the APC Slow Flyer 9×7.5 at $J = -0.68$.

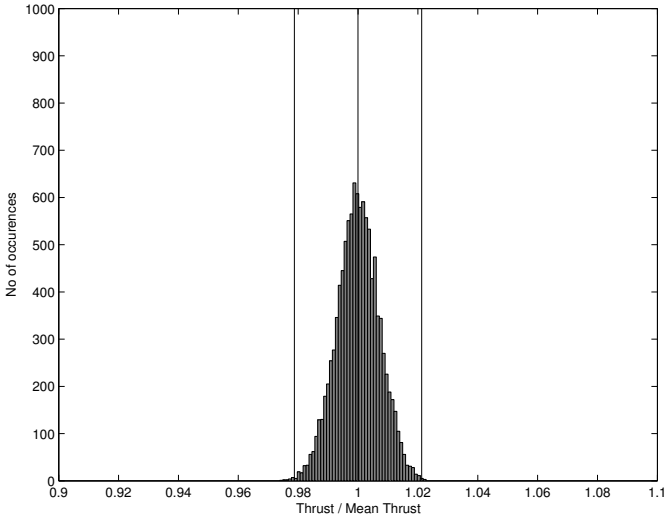

Fig. 4.193: Thrust data histogram for the APC Sport 10×4 in hover.

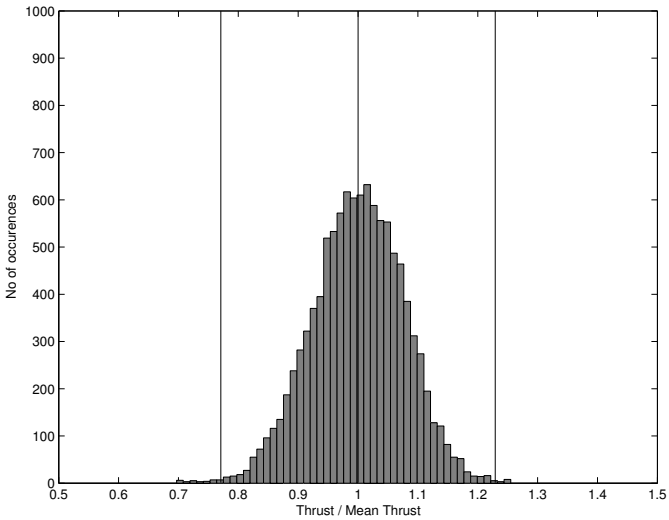

Fig. 4.194: Thrust data histogram for the APC Sport 10×4 at $J = -0.19$.

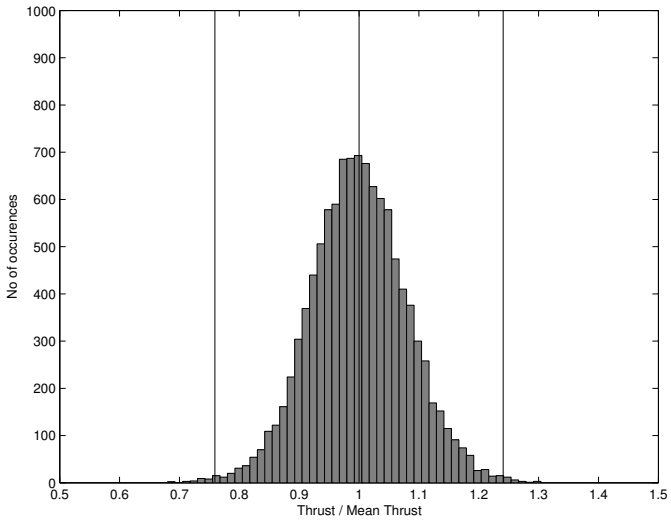

Fig. 4.195: Thrust data histogram for the APC Sport 10×4 at $J = -0.36$.

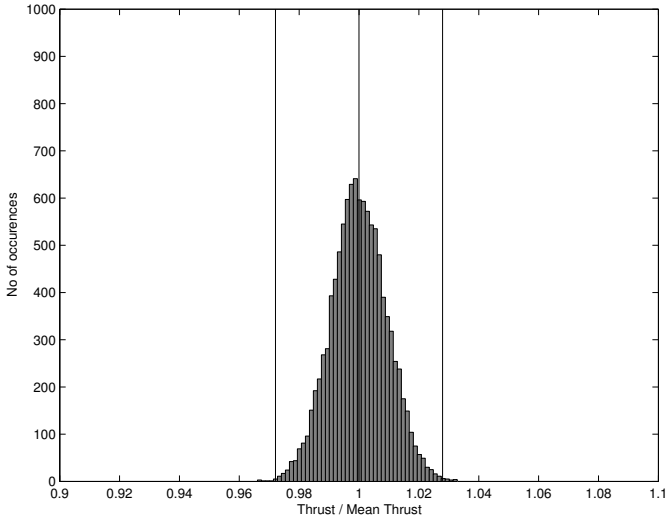

Fig. 4.196: Thrust data histogram for the APC Sport 10×4 at $J = -0.62$.

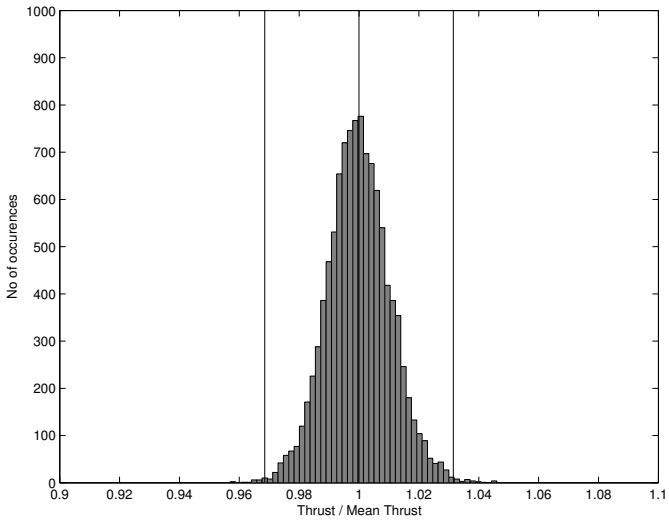

Fig. 4.197: Thrust data histogram for the APC Sport 10×5 in hover.

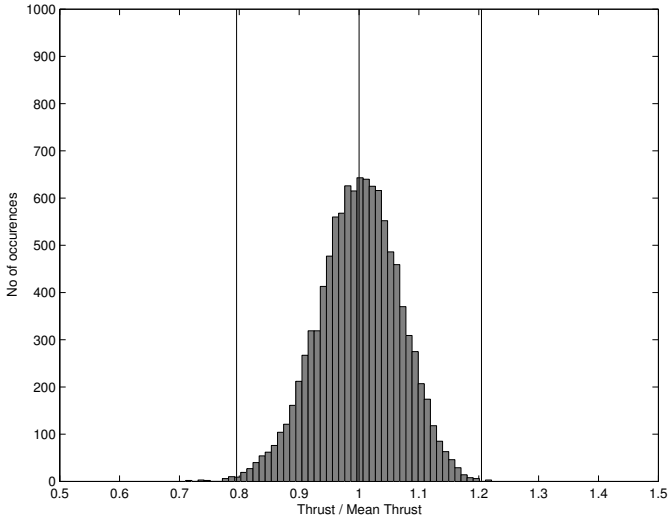

Fig. 4.198: Thrust data histogram for the APC Sport 10×5 at $J = -0.19$.

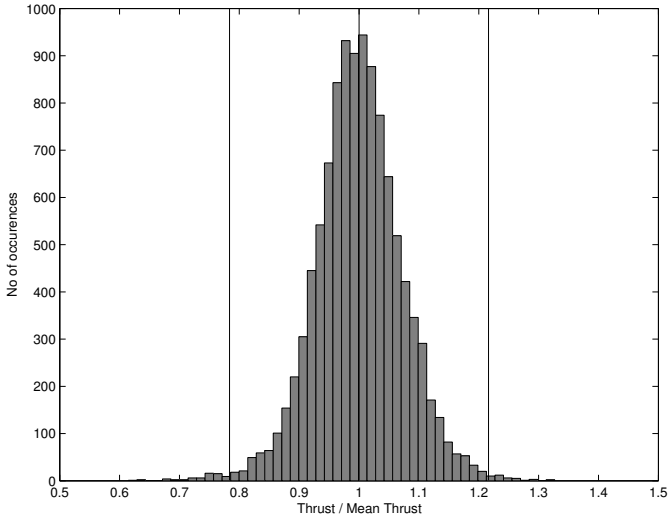

Fig. 4.199: Thrust data histogram for the APC Sport 10×5 at $J = -0.36$.

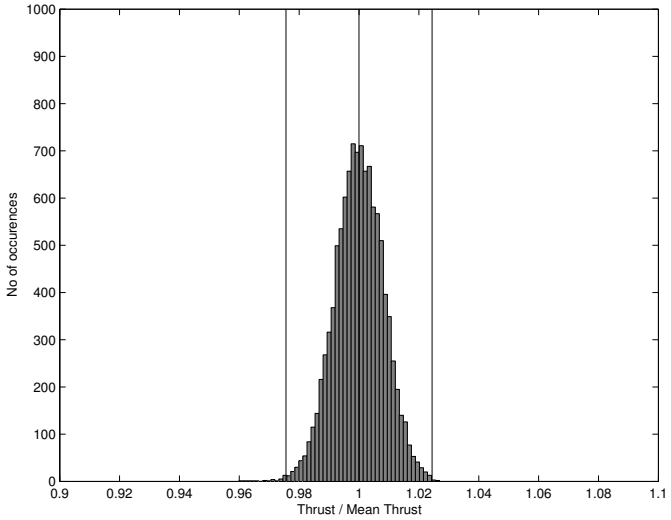

Fig. 4.200: Thrust data histogram for the APC Sport 10×5 at $J = -0.62$.

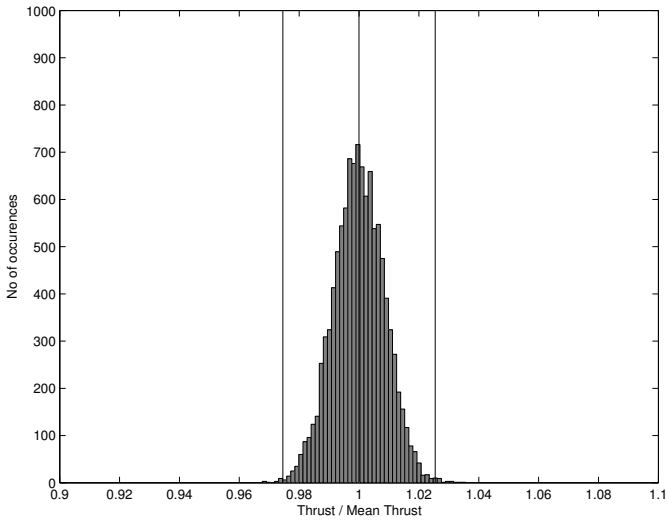

Fig. 4.201: Thrust data histogram for the APC Sport 10×7 in hover.

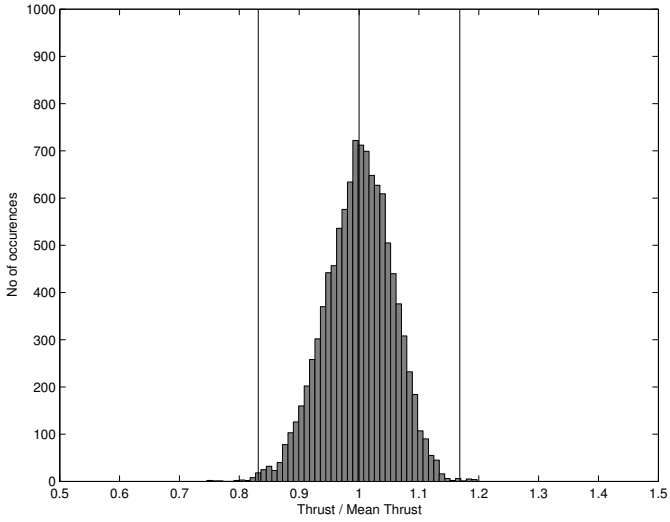

Fig. 4.202: Thrust data histogram for the APC Sport 10×7 at $J = -0.19$.

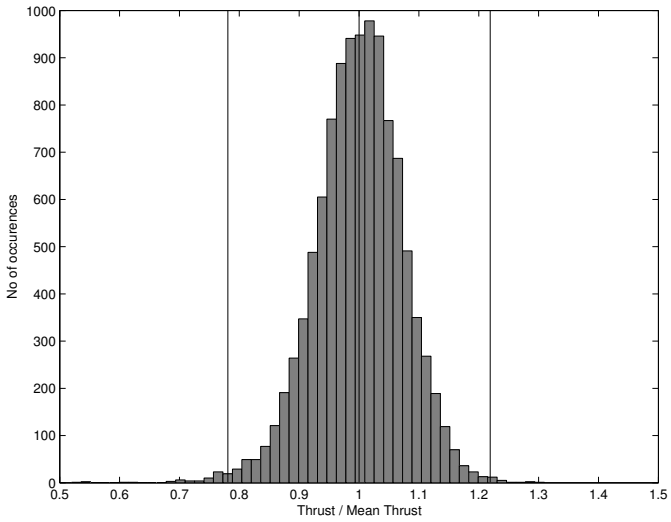

Fig. 4.203: Thrust data histogram for the APC Sport 10×7 at $J = -0.36$.

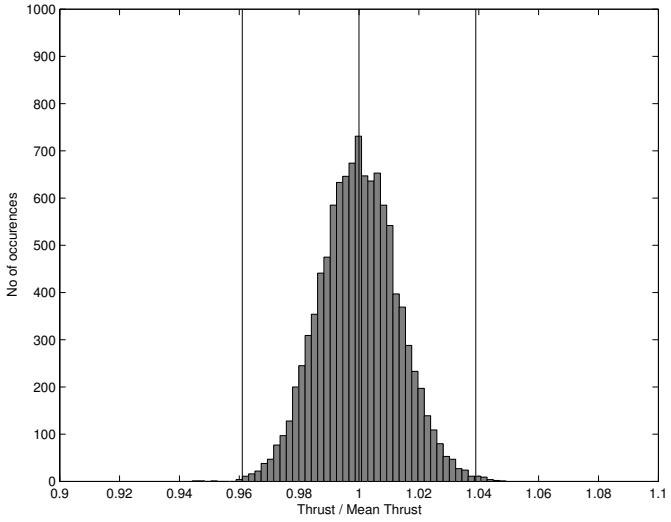

Fig. 4.204: Thrust data histogram for the APC Sport 10×7 at $J = -0.62$.

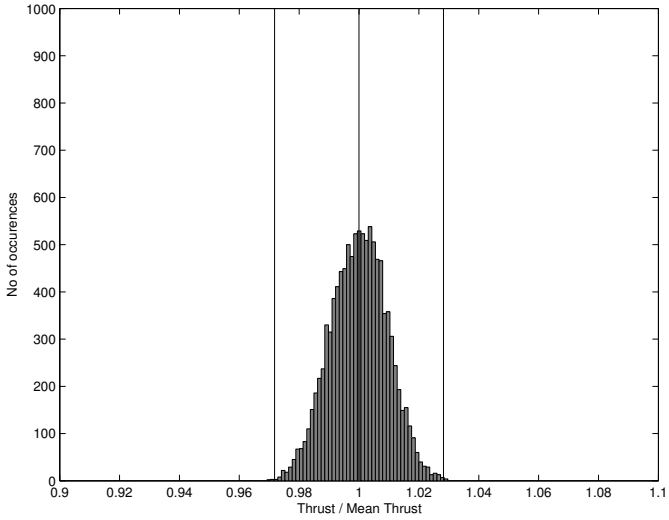

Fig. 4.205: Thrust data histogram for the APC Sport 10×10 in hover.

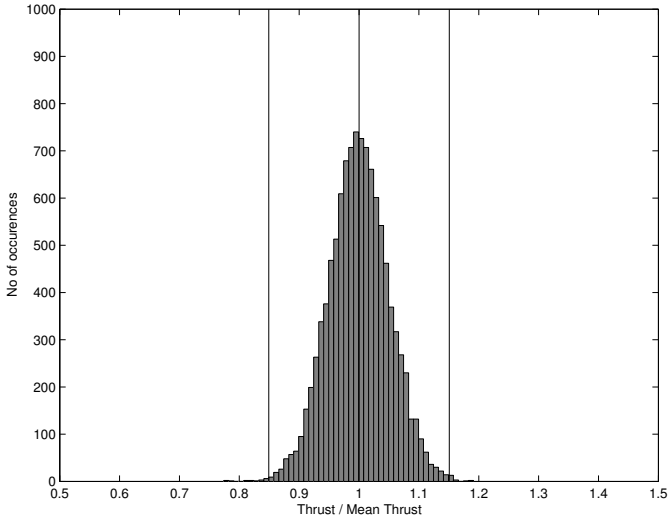

Fig. 4.206: Thrust data histogram for the APC Sport 10×10 at $J = -0.19$.

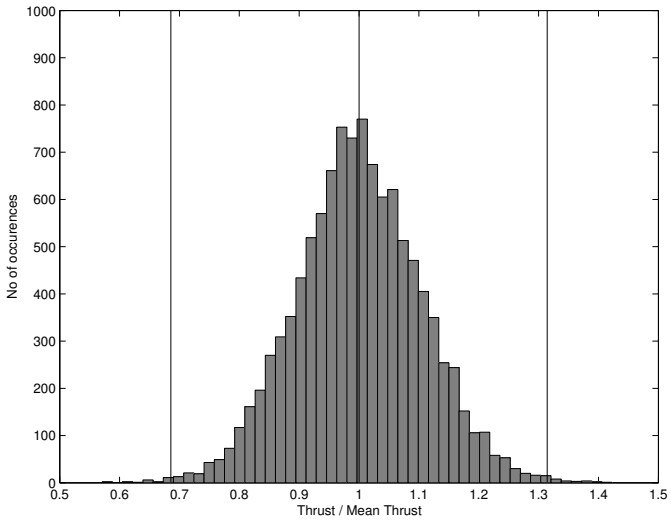

Fig. 4.207: Thrust data histogram for the APC Sport 10×10 at $J = -0.36$.

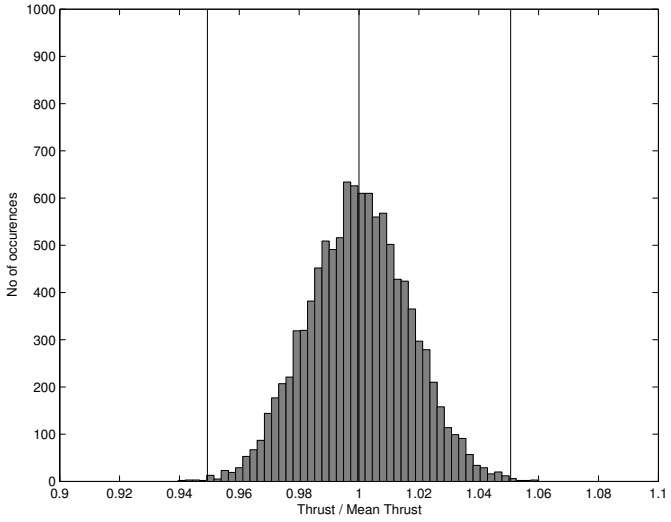

Fig. 4.208: Thrust data histogram for the APC Sport 10×10 at $J = -0.62$.

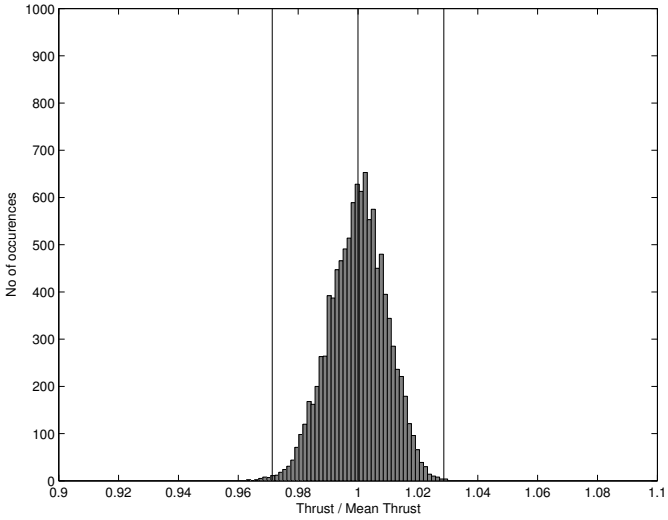

Fig. 4.209: Thrust data histogram for the APC Thin Electric 10×5 in hover.

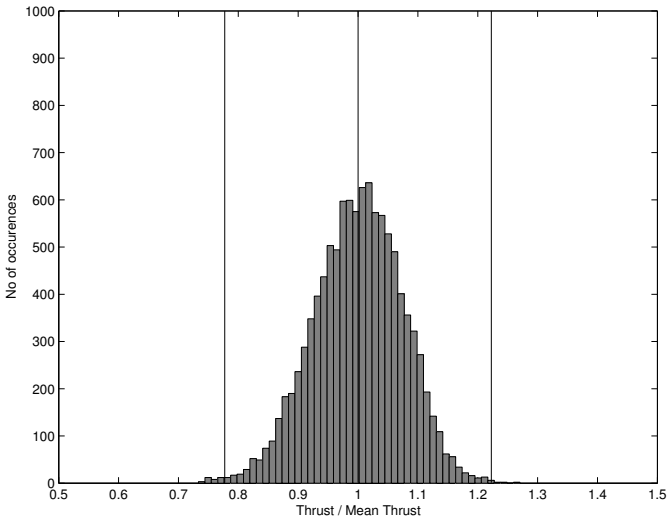

Fig. 4.210: Thrust data histogram for the APC Thin Electric 10×5 at $J = -0.19$.

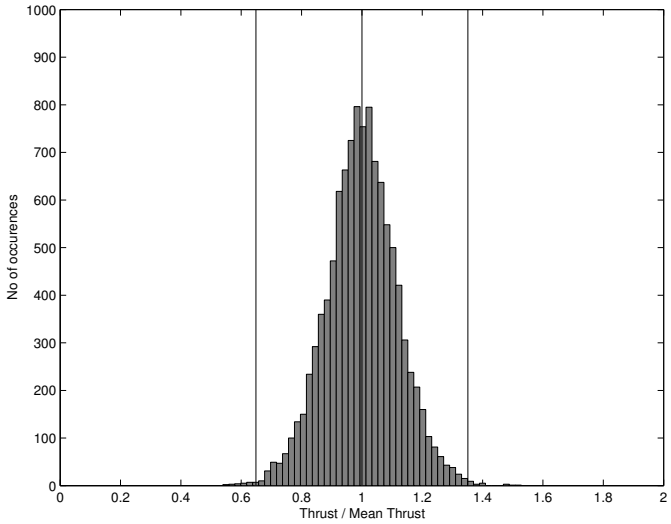

Fig. 4.211: Thrust data histogram for the APC Thin Electric 10×5 at $J = -0.36$.

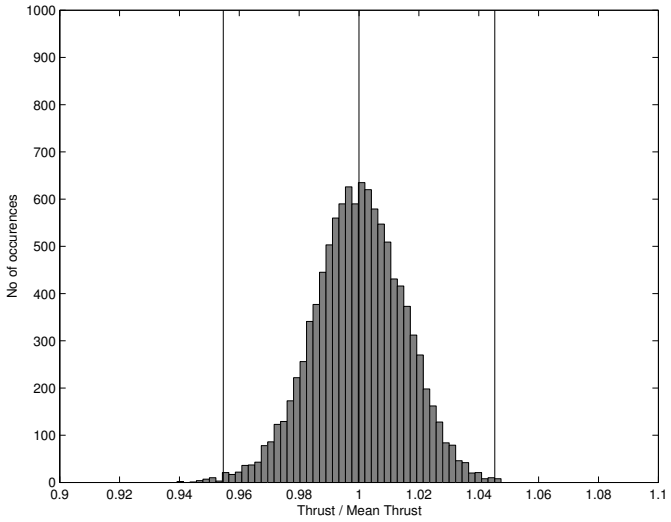

Fig. 4.212: Thrust data histogram for the APC Thin Electric 10×5 at $J = -0.62$.

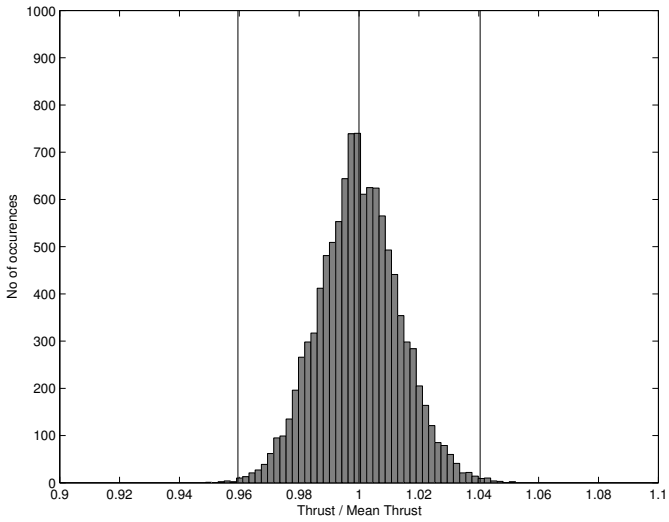

Fig. 4.213: Thrust data histogram for the APC Thin Electric 10×7 in hover.

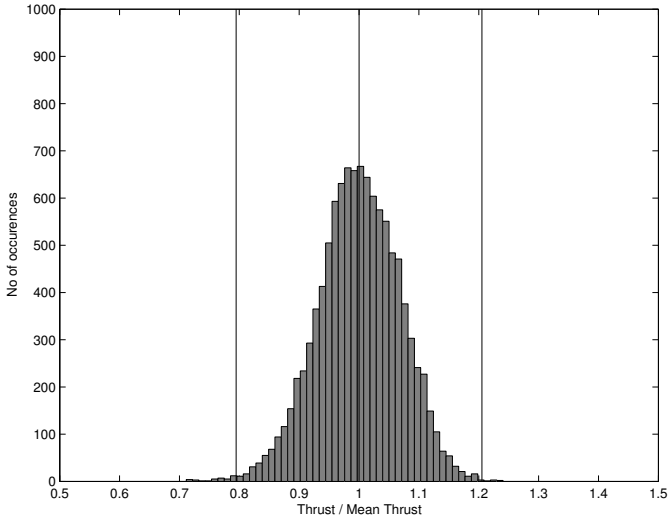

Fig. 4.214: Thrust data histogram for the APC Thin Electric 10×7 at $J = -0.19$.

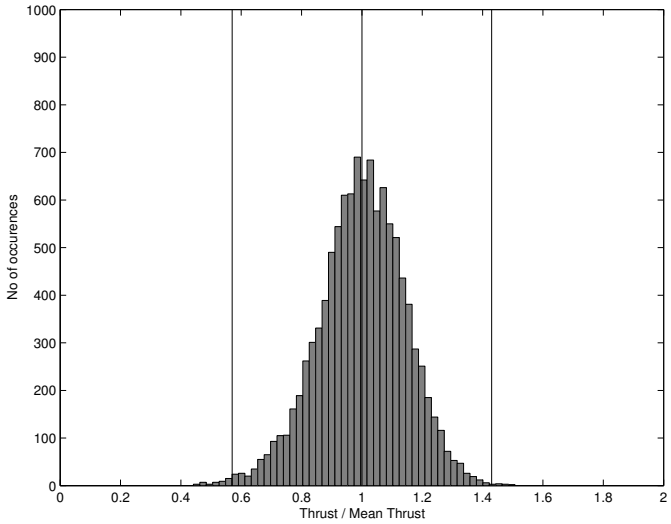

Fig. 4.215: Thrust data histogram for the APC Thin Electric 10×7 at $J = -0.36$.

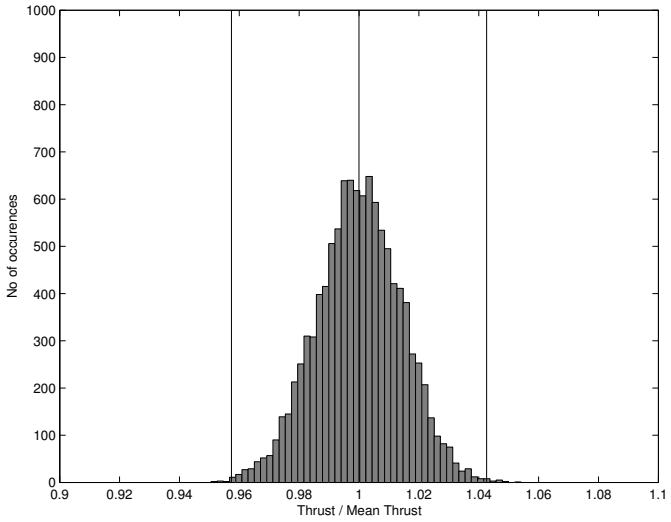

Fig. 4.216: Thrust data histogram for the APC Thin Electric 10×7 at $J = -0.62$.

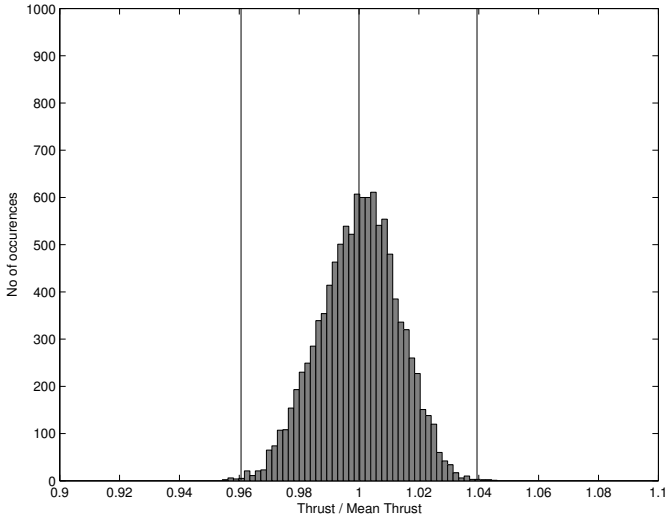

Fig. 4.217: Thrust data histogram for the APC Thin Electric 10×10 in hover.

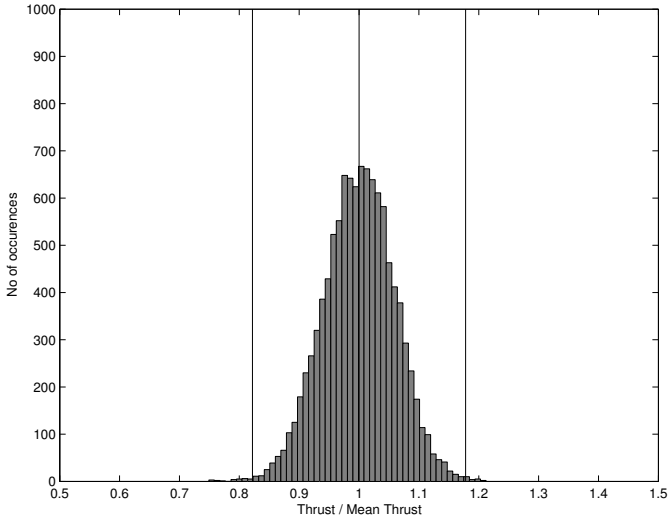

Fig. 4.218: Thrust data histogram for the APC Thin Electric 10×10 at $J = -0.19$.

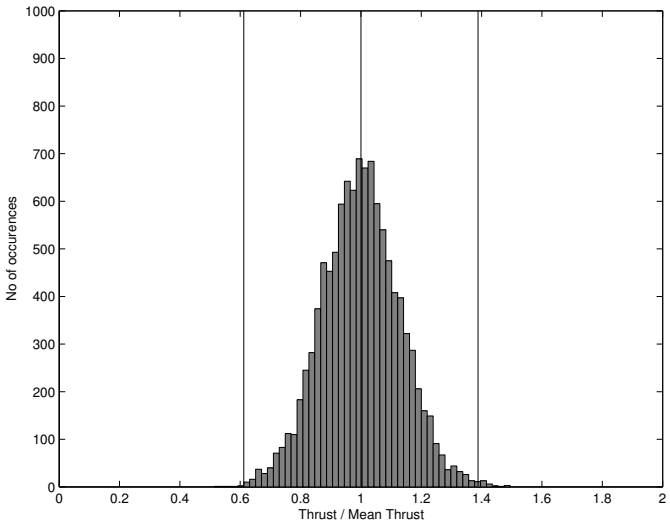

Fig. 4.219: Thrust data histogram for the APC Thin Electric 10×10 at $J = -0.36$.

Chapter 5

Summary of performance

In this chapter, the data from the wind tunnel experiments is studied and the resultant trends are discussed. The performance data is analyzed with respect to the propeller geometry based on factors such as the pitch of the propeller and the activity factor. The activity factor is calculated using the propeller geometry with the equation:[20]

$$AF = \frac{10^5}{16} \int_{0.15R}^{1.0R} \left(\frac{c}{D}\right) x^3 dx \tag{5.1}$$

Also, the time history data is analyzed and the thrust fluctuations are plotted with the steady state thrust coefficients for the respective propellers. The fluctuations are represented by the actual measured maximum and minimum values and by a $\pm 3\sigma$ limit, where the σ is the standard deviation for the thrust calculated for each set of time history data.

Along with the differences in the recorded data, there were also differences in the way the propellers behave during the wind tunnel tests. In general, as the advance ratio approaches the value corresponding to the minimum thrust, vibrations set in at the propeller which are transferred through the motor to the post. At this point, propeller tip oscillations are also observed. The amplitude of these oscillations varies based on the style of propeller being tested. In general, the Slow Flyer propellers exhibit greater amplitudes of oscillation as compared to the other two propeller styles. This higher oscillation is attributed to the sharp leading edge and low thickness to chord ratios, characteristic of Slow Flyer propellers. Also, as mentioned earlier, for certain propellers typically with a greater pitch, it becomes difficult to maintain the constant RPM at higher descent velocities.

As seen in the previous section, the thrust characteristics follow a specific trend. This curve represents the transition, starting from the hover condition through the turbulent working state and finally for the most cases culminating at the windmill state. The thrust

coefficient represented as a function of advance ratio clearly illustrates the loss in thrust experienced in the VRS. This trend is similar to results obtained in comparative studies. However, the current study differs from them on quite a few accounts. To begin with, the diameters of the propellers tested in previous studies are traditional a few feet in order of magnitude. In comparison, the biggest propellers tested in the current study are 11 inches in diameter. Also, most of the propellers tested tended to have constant chord blades with a linear twist. As shown in previous figures, the propellers used for this study are markedly different in those aspects. As a result of these differences, it is expected that the specific values observed in the results will be different from the references. However, the general trends are observed to be similar for the most part.

5.1 Pitch Comparison

In general, as the descent velocity is increased (advance ratio decreases), the thrust generated by the propeller reduces until reaching a particular value of the advance ratio, where the minimum thrust is observed. It is observed that this behavior of propellers in descent is highly dependent on the value of the pitch. Hence Figs 5.1–5.3 show a comparison of the steady state thrust coefficient of propellers when the pitch is varied. The pitch angle at the 75% radial station is indicated in parantheses for each of the propellers in the figures. It is to be noted that in each case, the propellers belong to the same style of design which means that the planform for each of the propellers is very similar. It can be seen that as the pitch of the propeller is increased, the minimum thrust is obtained at a lower value of advance ratio. Also, the value of this minimum thrust increases with an increase in the pitch of the propeller to the point that for propellers with a pitch angle of greater than about 16 deg, instead of a drop, the thrust coefficient remains nearly steady until a certain value of advance ratio, beyond which point the thrust coefficient increases with an increase in advance ratio.

These trends are similar to those observed in the data plotted by Washizu.[4] It might seem suggestive based on this trend that increasing the pitch of the propeller would be a solution to avoid the drop in the thrust experienced in the VRS. However the data plotted is

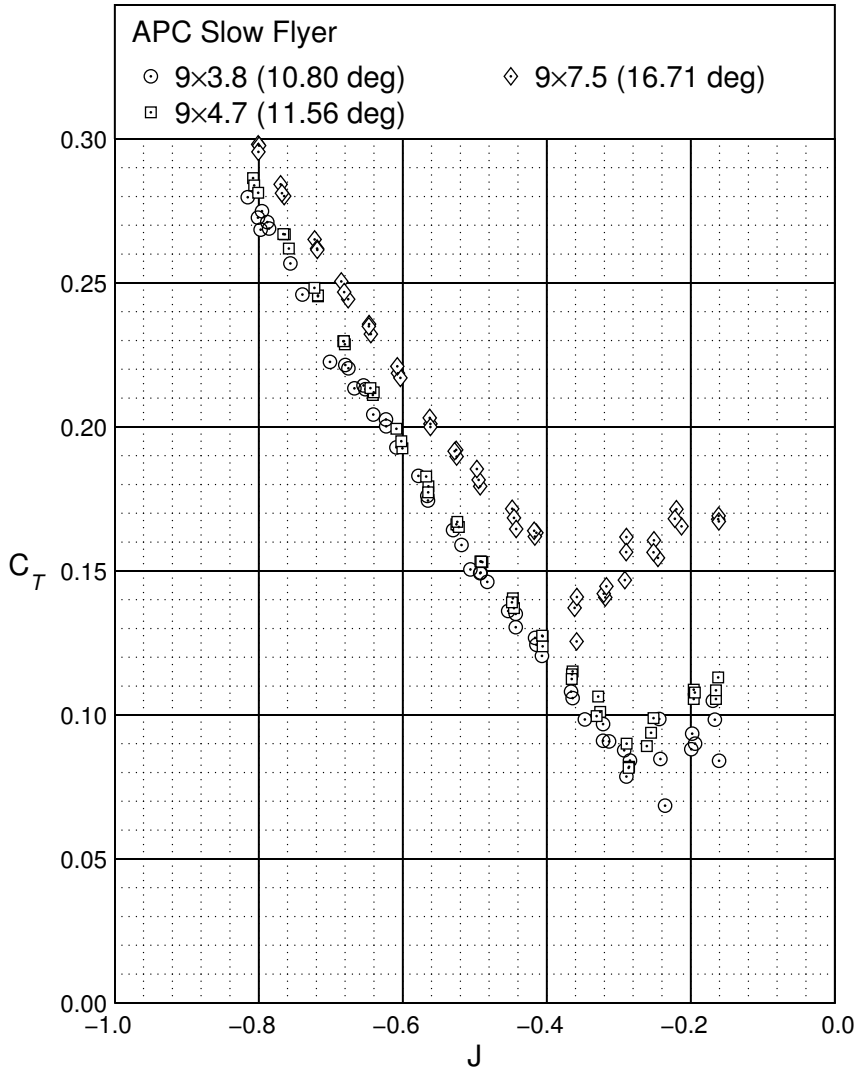

Fig. 5.1: Thrust characteristics for APC Slow Flyer propellers with diameter 9 in. The value of β is given in parantheses corresponding to each propeller.

the steady state data and does not take the instability and hence the thrust fluctuations into consideration. Also, at a higher value of pitch, it becomes difficult to maintain the constant RPM. In fact an FAA advisory states that in case of a VRS condition, the collective pitch of the rotor should be reduced and a forward velocity be imparted so that the vortices are convected away from the rotor plane.

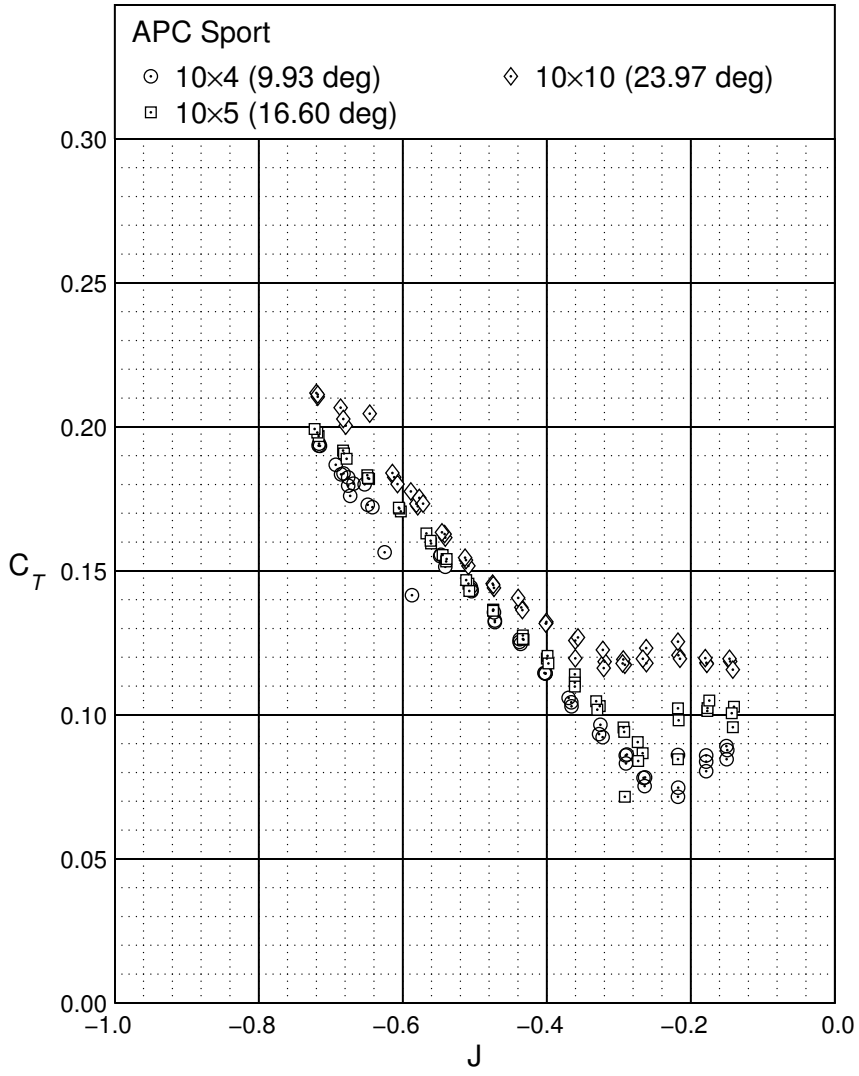

Fig. 5.2: Thrust characteristics for APC Sport propellers with diameter 10 in. The value of β is given in parantheses corresponding to each propeller.

5.2 Planform Comparison

As discussed in the earlier chapters, the propellers tested are either APC Slow Flyers, APC Sport or APC Thin Electric propellers. There are significant differences in the geometry for each of the different types of propellers. The Slow Flyer and Thin Electric propellers are designed for use only with electric motors; whereas, the Sport propellers are compatible with

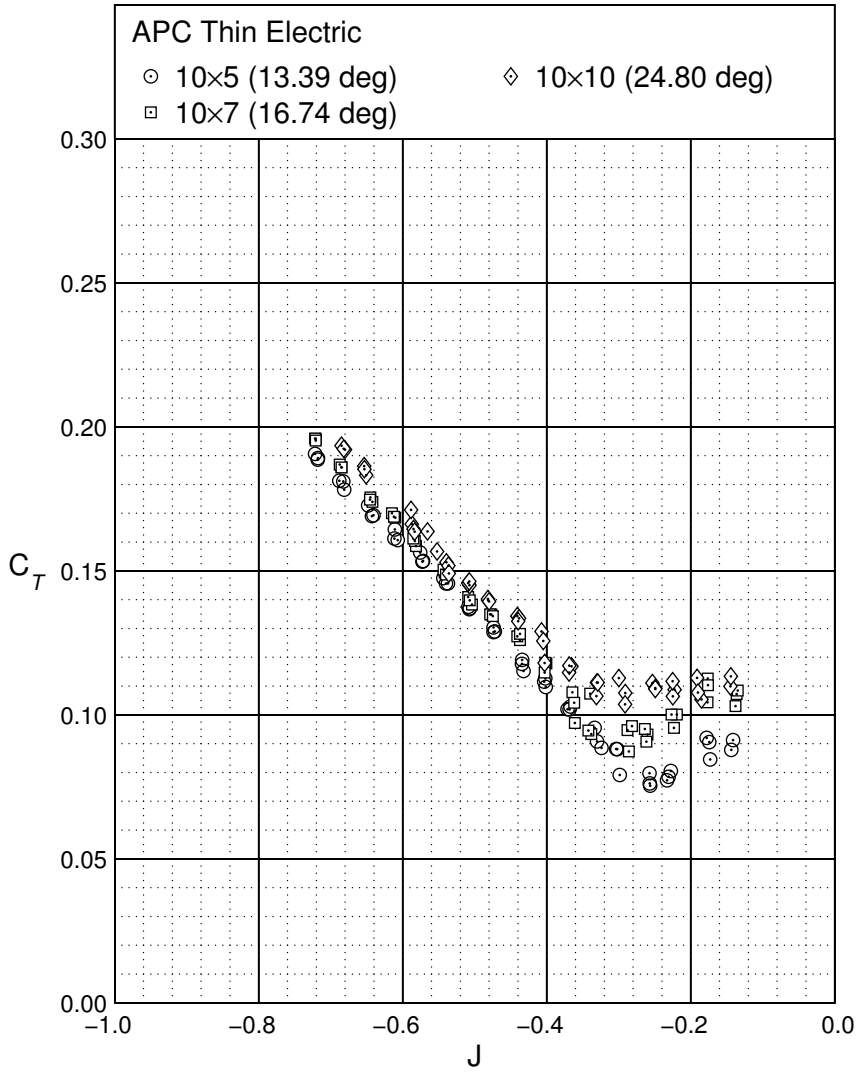

Fig. 5.3: Thrust characteristics for APC Thin Electric propellers with diameter 10 in. The value of β is given in parantheses corresponding to each propeller.

gas engines as well. The Slow Flyer propellers have thinner airfoil sections with sharper leading edges whereas the other two have comparatively thicker sections with rounded leading edges. Also, in general, the Slow Flyer propellers tend to have thicker chord lengths along the radial stations as compared to the Sport and Thin Electric propellers. As a result of these geometric differences, Slow Flyers exhibit a greater degree of physical vibrations

while operating in the VRS as compared to the other propellers. The difference in the chord distribution is reflected in the value of the activity factor, the equation for which was earlier in the chapter.

In contrast to the previous section, propellers having a similar pitch but with a different planform are compared. The activity factor, listed in Table 4.1, is used as a measure to compare the planforms. Among the three styles of propellers tested, in general the Slow Flyers exhibited the highest values of activity factor. Figure 5.4 shows the comparison of the steady state thrust coefficients of three propellers with a diameter of 9 in and a pitch of about 5 in/rev. Since all three propellers have a similar diameter and pitch, the minimum thrust point is achieved at a similar value of advance ratio. However, beyond this point as the descent velocity increases, the thrust increases at a different rate for each of the propellers. The APC Slow Flyer 9×4.7 (AF = 122.65) exhibits the highest slope, followed by the APC Thin Electric 9×4.5 (AF = 98.20) and the APC Sport (AF = 83.97) has the lowest slope.

Similarly Fig 5.5 gives a comparison of three APC propellers with a diameter of 10 in and a pitch of approximately 5 in/rev. Again the Slow Flyer 10×4.7 (AF = 118.33) shows the highest thrust slope beyond the minimum thrust point. However, in this case the Sport 10×5 (AF = 90.37) has a higher slope than the Thin Electric 10×5 (AF = 83.96).

Figures 5.4–5.7 reveal a strong dependence of the thrust characteristics of the propeller on the value of the activity factor. It is concluded based on these plots that higher the activity factor of the propeller, higher is the rate at which the thrust increases as a function of the advance ratio and the easier it becomes to recover from the VRS. This is understandable as a higher value of the activity factor implies a thicker chord distribution, thereby leading to a greater value of the generated thrust.

5.3 Thrust Fluctuations

Figures 5.8–5.16 represent the thrust fluctuations along with the steady state thrust coefficient data. The extent of the thrust fluctuation varies with a variation in the advance ratio. The fluctuations are at a minimum when the propeller is in hover. As the descent velocity is

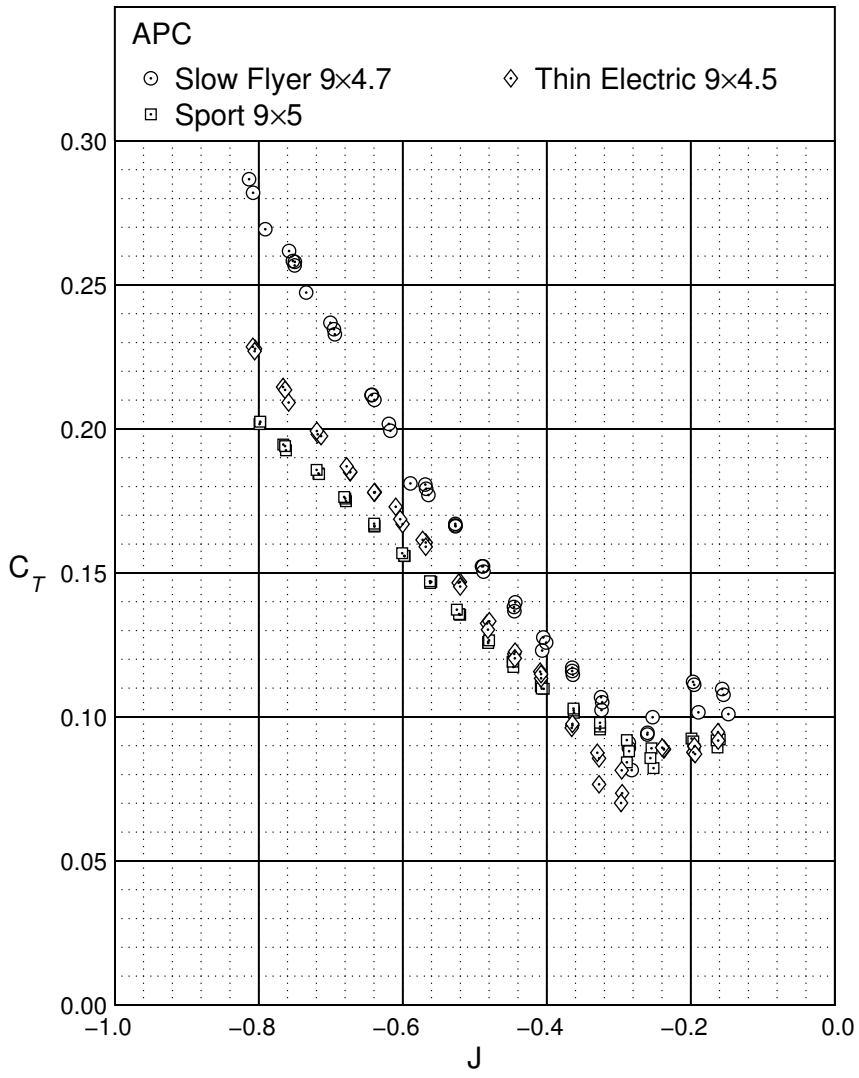

Fig. 5.4: Thrust characteristics for APC Slow Flyer, Sport and Thin Electric propellers with diameter 9 in and pitch 5 in.

increased, the extent of fluctuations increases as well, reaching a maximum at the advance ratio where the minimum thrust is observed. Beyond this point, the fluctuations decrease as the descent velocity increases.

These set of tests as well, display a correlation between the thrust characteristics and the pitch of the propeller. Figures 5.8–5.10 show the steady state and the fluctuating

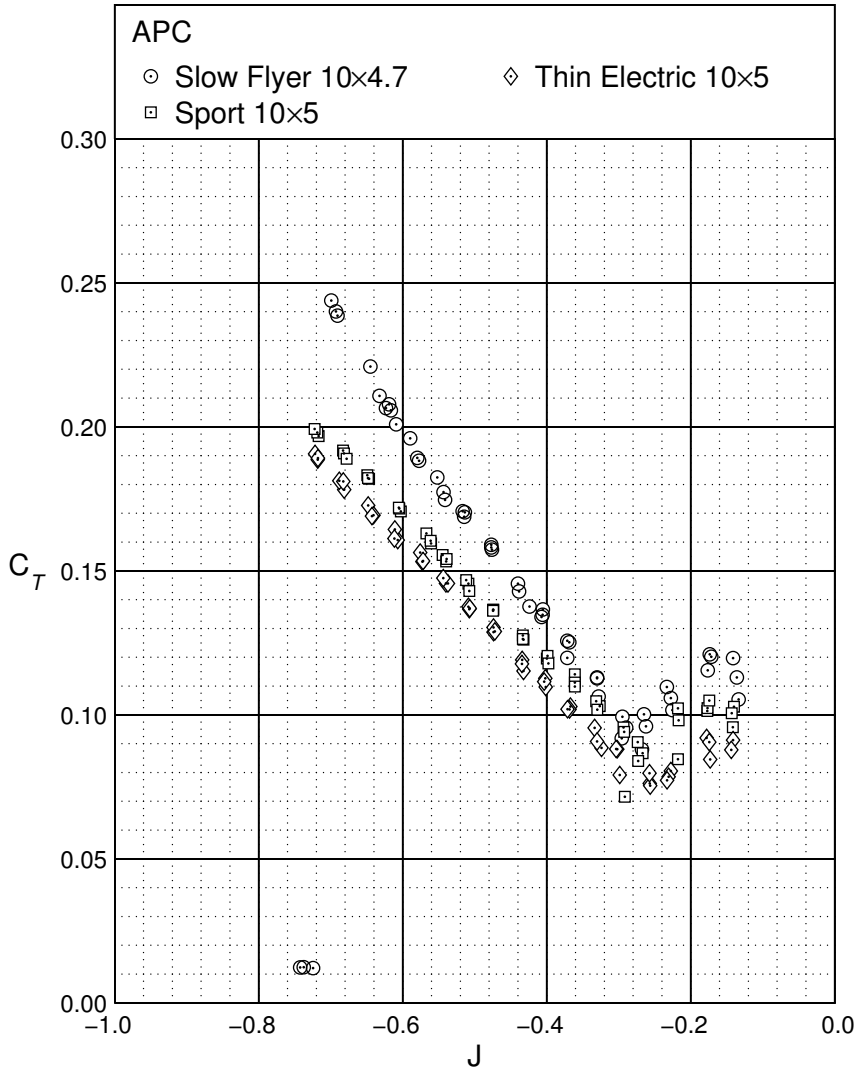

Fig. 5.5: Thrust characteristics for APC Slow Flyer, Sport and Thin Electric propellers with diameter 10 in and pitch 5 in.

thrust coefficient range for the APC Slow Flyer 9 in diameter propellers. The magnitude of fluctuations increases with an increase in the propeller pitch. Also, it is observed that for lower values of the pitch, the fluctuations dissipate within a shorter range of advance ratios. The higher pitch propellers tend to exhibit thrust oscillations for a greater range of descent velocities, dying down only at the end of the velocity range tested. The APC

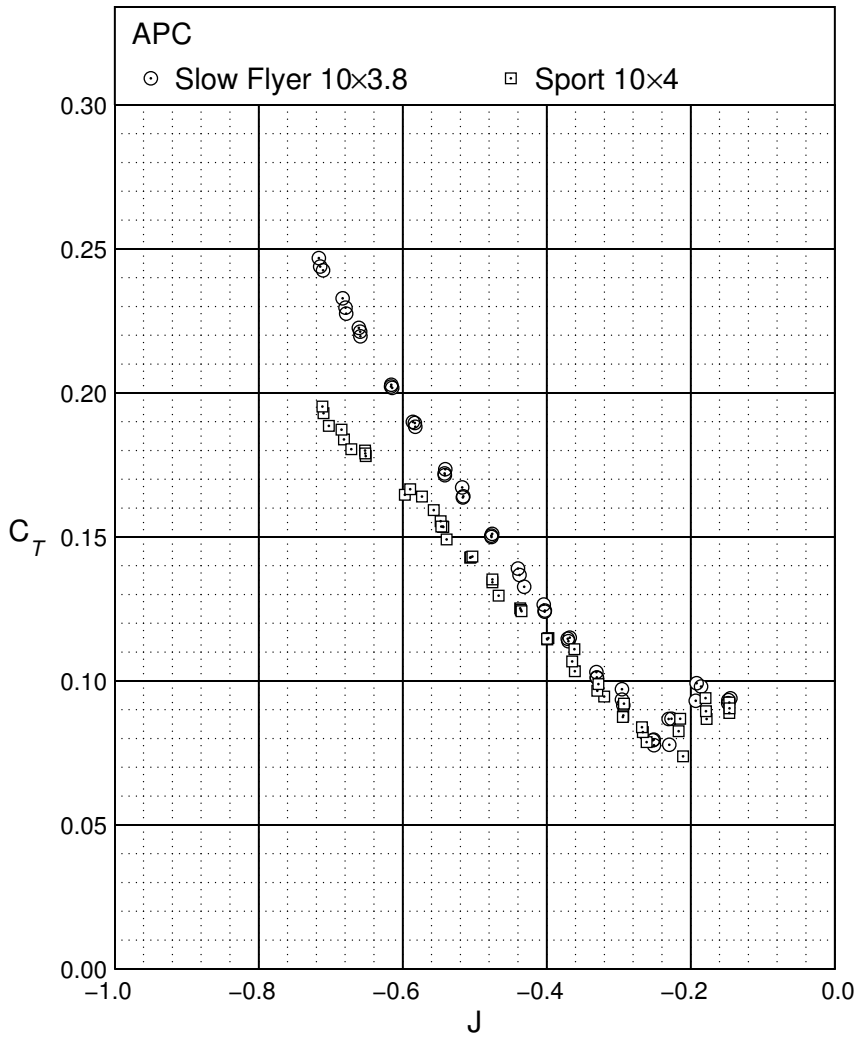

Fig. 5.6: Thrust characteristics for APC Slow Flyer and Sport propellers with diameter 10 in and pitch 4 in.

Sport and Thin Electric propellers exhibit similar trends as is seen in the subsequent figures. This data is similar to what was observed in a few earlier studies including Washizu[4]and Yaggy and Mort[5] among others. This relation of thrust oscillations with the pitch would be another reason why it is more advisable to reduce the collective pitch of a rotor or propeller when experiencing vortex ring conditions. Yaggy and Mort discuss the relation between

the disc loading and the thrust oscillations observed in the VRS and state that for a given descent velocity, the extent of the thrust oscillations decreases with an increase in the disc loading until the point of maximum oscillations. However, Figs 4.181–4.219 in the previous section suggest the contrary. These figures that represent the thrust fluctuations recorded as percentages of the mean thrust. As the pitch of the propeller increases, the mean thrust coefficient increases until the point of maximum fluctuations as discussed earlier. For a constant descent velocity (and hence a constant advance ratio), the percentage fluctuations are of a similar order of magnitude. Also, Washizu[4]and Betzina[6] among others discuss the presence of a characteristic frequency observed in the thrust oscillations. However, for the present study the presence of noise in the signal made it difficult to effectively isolate the frequency component associated with the thrust fluctuations. It is recommended that more comprehensive tests be carried out in order to analyze the observed unsteadiness.

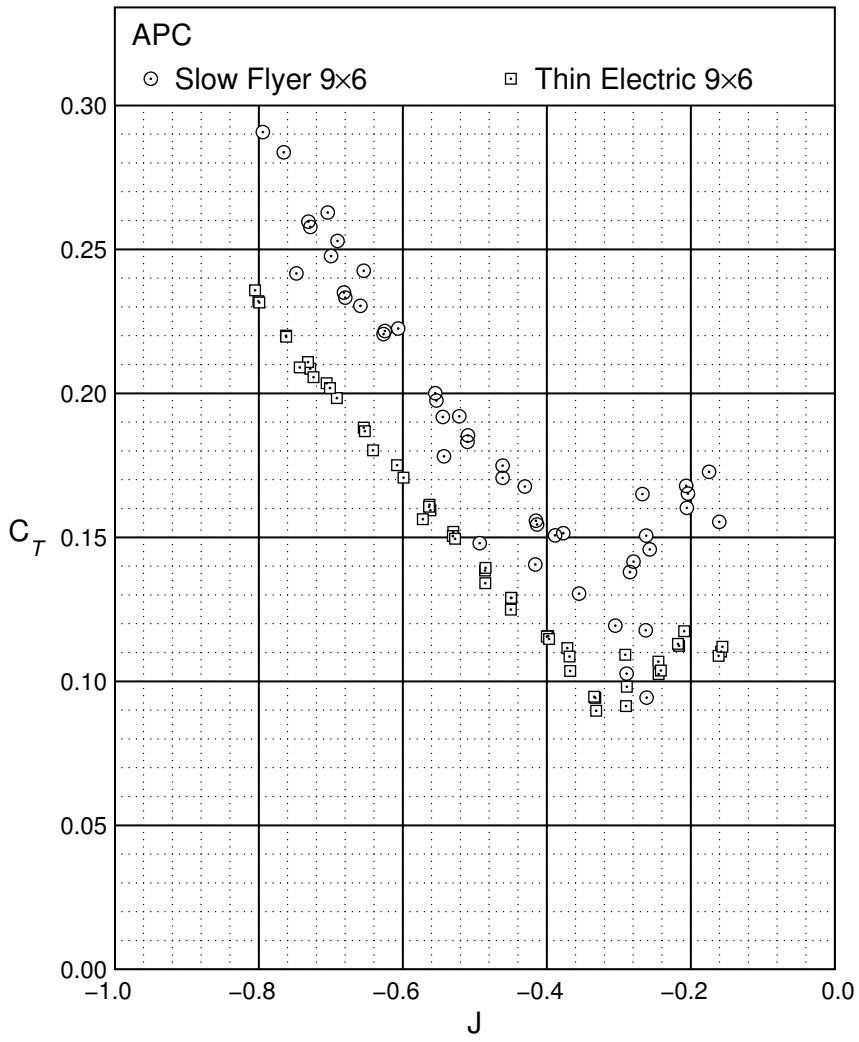

Fig. 5.7: Thrust characteristics for APC Slow Flyer and Thin Electric propellers with diameter 9 in and pitch 6 in.

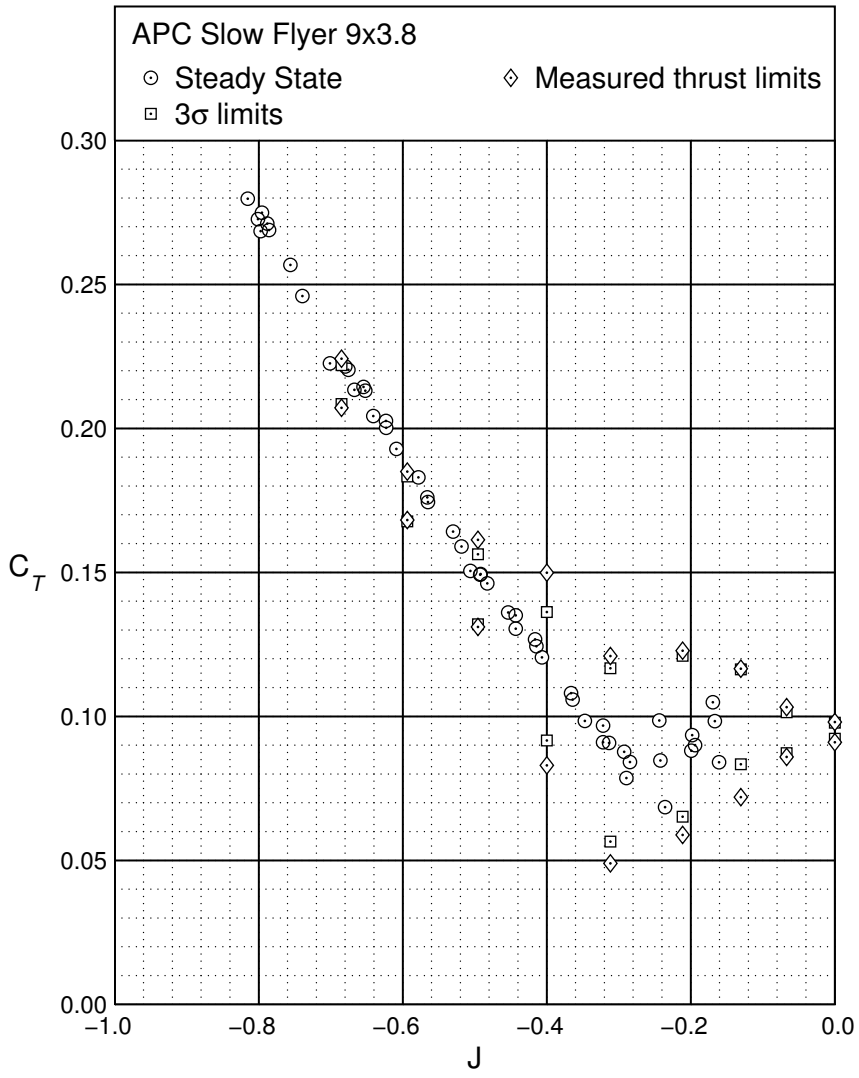

Fig. 5.8: Steady state and fluctuating thrust coefficient for the APC Slow Flyer 9×3.8.

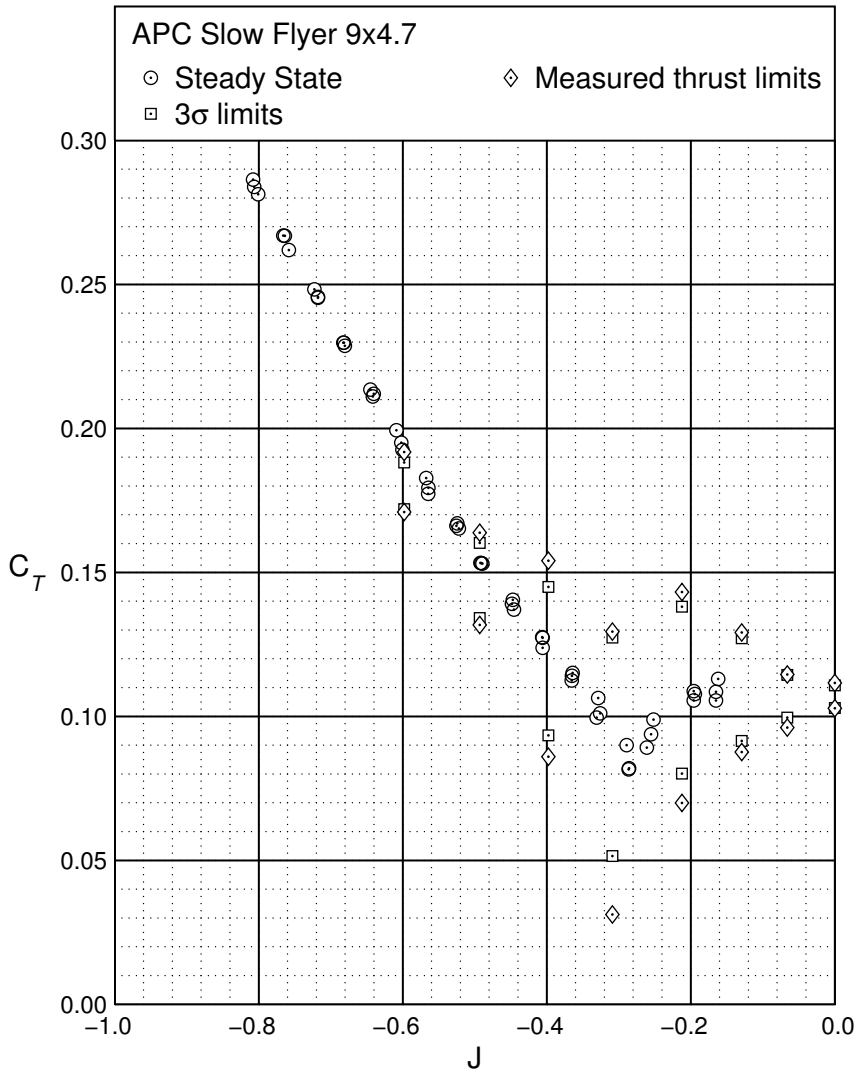

Fig. 5.9: Steady state and fluctuating thrust coefficient for the APC Slow Flyer 9×4.7.

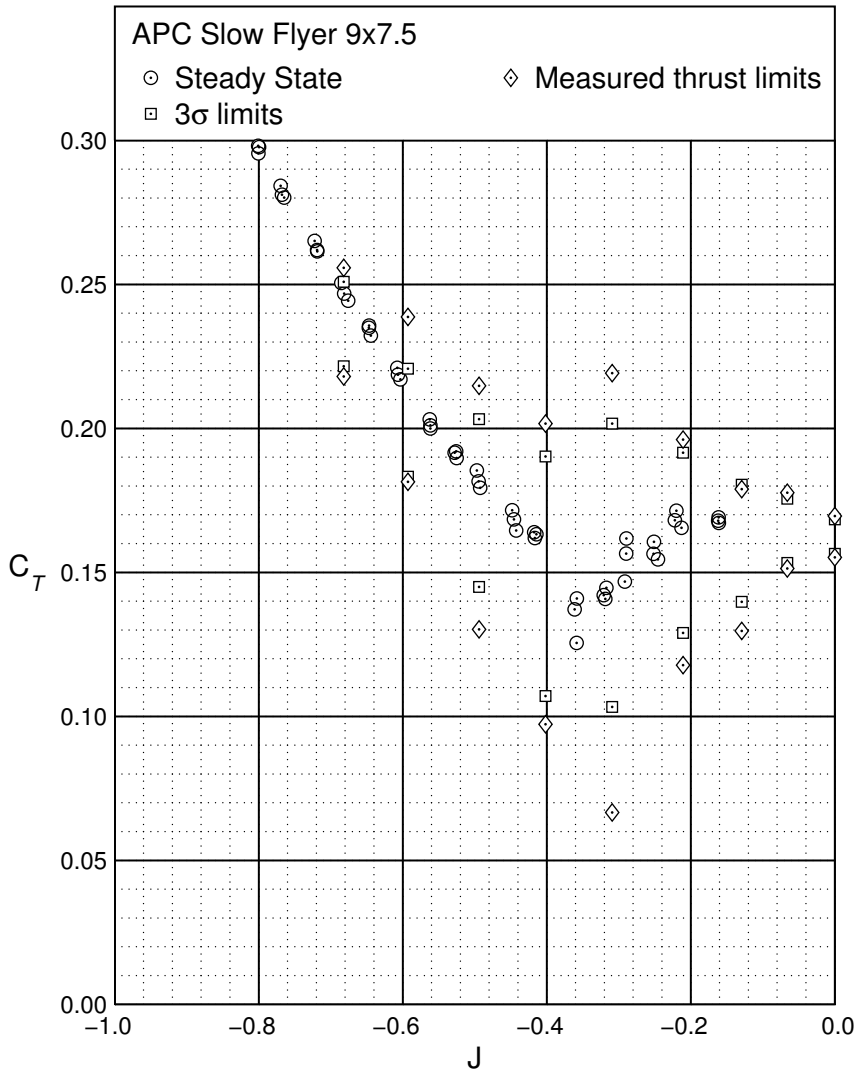

Fig. 5.10: Steady state and fluctuating thrust coefficient for the APC Slow Flyer 9×7.5.

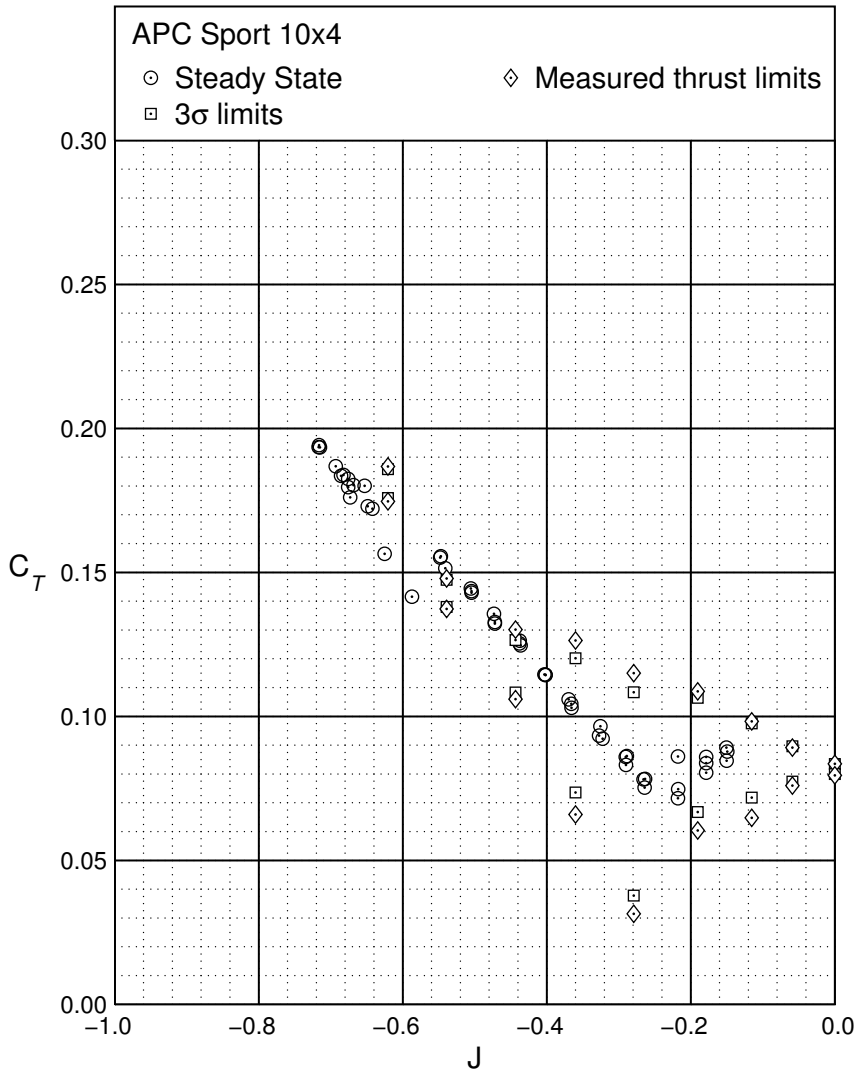

Fig. 5.11: Steady state and fluctuating thrust coefficient for the APC Sport 10×4.

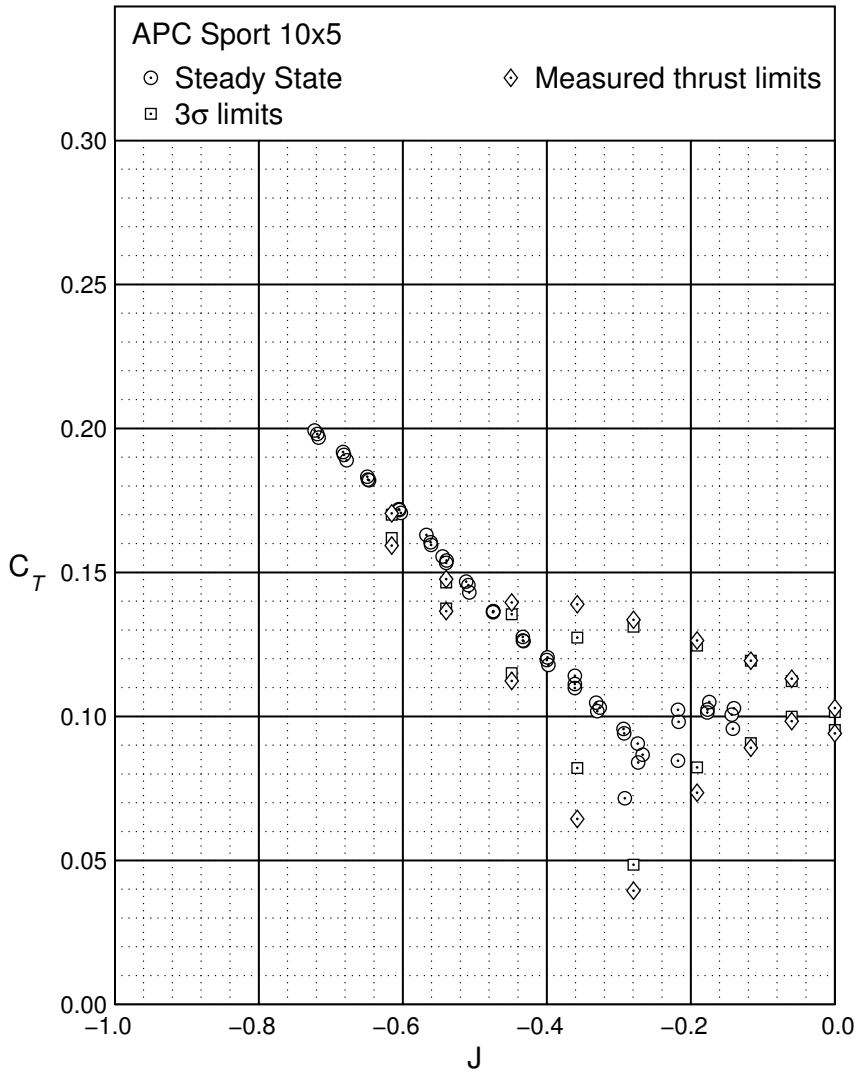

Fig. 5.12: Steady state and fluctuating thrust coefficient for the APC Sport 10×5.

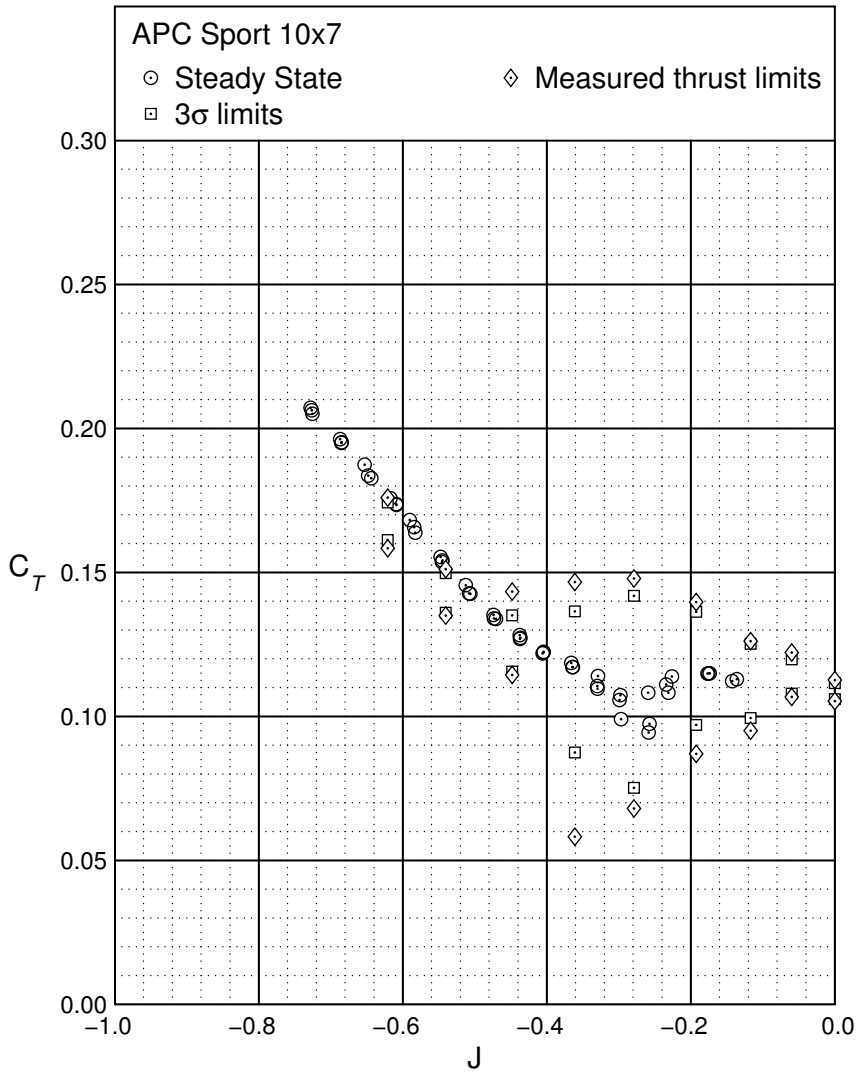

Fig. 5.13: Steady state and fluctuating thrust coefficient for the APC Sport 10×7.

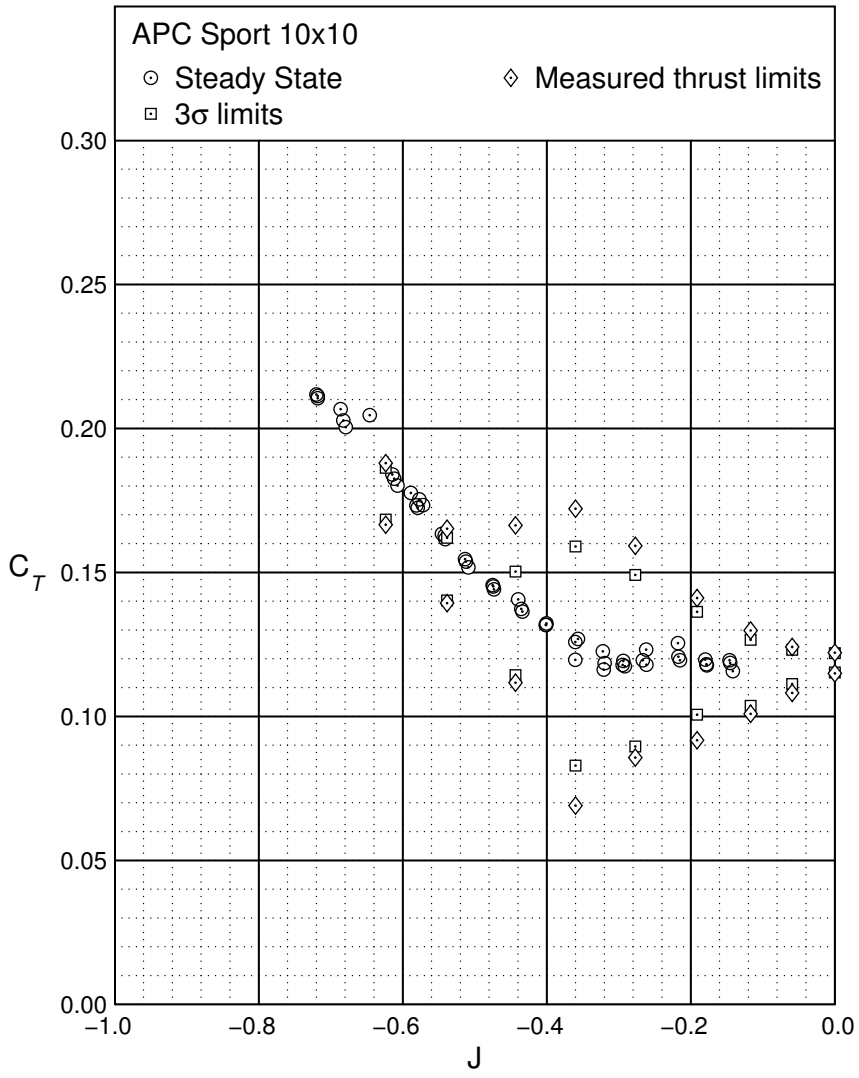

Fig. 5.14: Steady state and fluctuating thrust coefficient for the APC Sport 10×10.

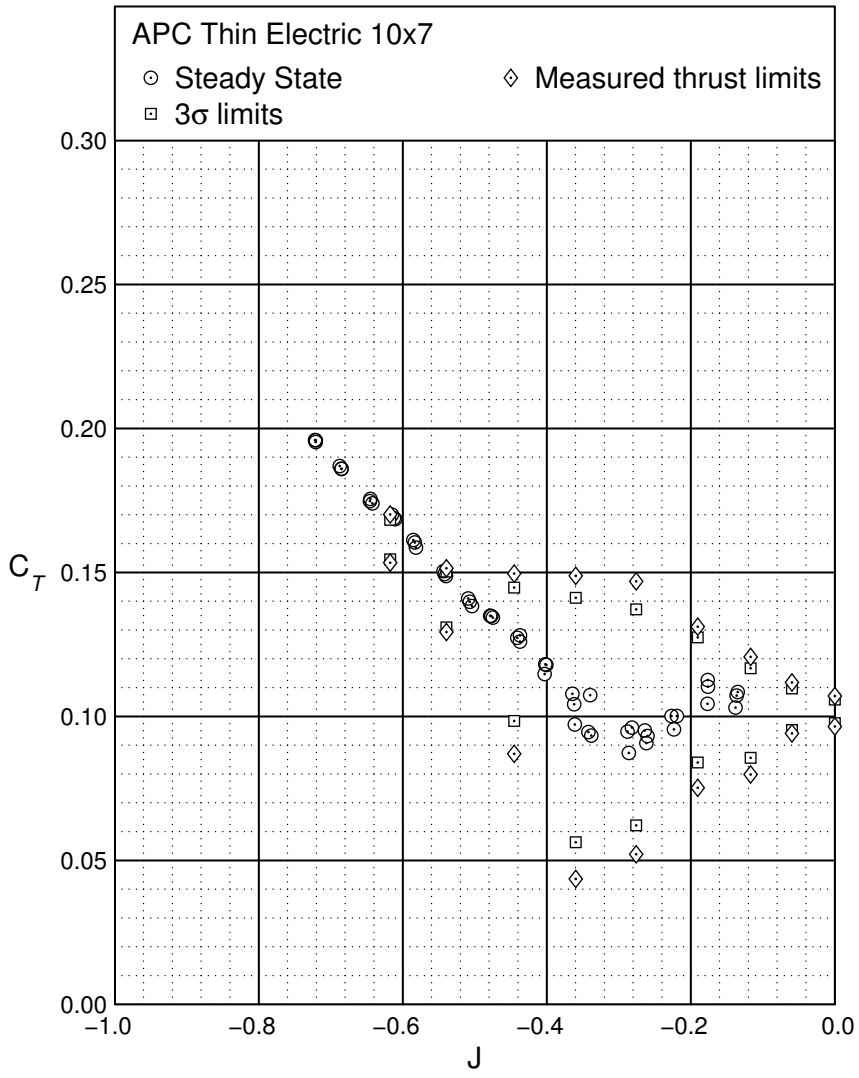

Fig. 5.15: Steady state and fluctuating thrust coefficient for the APC Thin Electric 10×7.

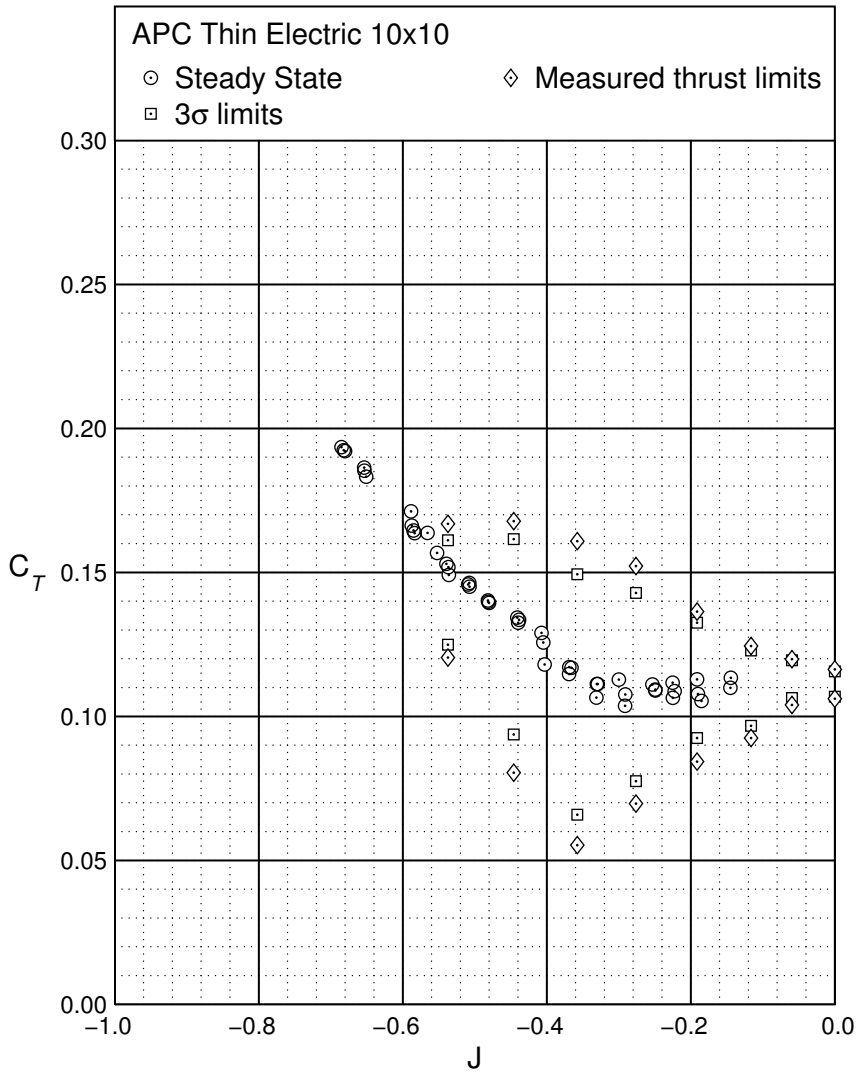

Fig. 5.16: Steady state and fluctuating thrust coefficient for the APC Thin Electric 10×10.

Chapter 6

Conclusion

The significance of the VRS to flight safety and the lack of sufficiently accurate theoretical predictions have made studies on the VRS extremely relevant. The set of experiments associated with this study revealed a number of trends some of which were consistent with prior research including Washizu[4]and Yaggy and Mort[5] among others. These data illustrate hitherto unknown information.

Propeller behavior in the VRS was largely dictated by the propeller geometry and flow conditions. For the purpose of this study, only axial descent was considered at a constant rotational speed of 4,000 RPM. In general, a propeller experienced a drop in thrust as it entered the Vortex Ring State. The amplitude of this thrust drop, depended largely on the pitch of the propellers. Similarly, the descent velocity at which the maximum drop in thrust depended on pitch as well. A propeller with a higher value of pitch experienced the least drop in thrust. Also, this drop was observed at a higher descent velocity. This general behavior is independent of other geometric characteristics. The recovery of thrust beyond this descent velocity depended on the chord distribution of the propeller, which for the purpose of this study was quantified by the activity factor. A higher value of activity factor represented in general a thicker chord distribution. It was concluded that a propeller with a higher activity factor generates a greater amount of thrust at the same descent velocity as compared to one with a lower activity factor. This characteristic would be useful in order to design rotors and propellers that can recover faster from the VRS. Another aspect that was studied was the thrust time history data and the effect of propeller geometry on it. As described in prior research, propellers in the VRS exhibit fluctuations in thrust. The maximum amplitude of these fluctuations was observed to be $\pm 30\%$ in the current study. The amplitude of these fluctuations increased with an increase in pitch and the maximum

fluctuations were observed at the descent velocity that corresponded to the minimum thrust for the particular propeller.

6.1 Recommendation for Future Research

Although, a substantial amount of time averaged thrust data was acquired and analyzed in this report, there is still scope to acquire more time history data and analyze in further detail the instabilities observed in the VRS. The measurement of the thrust time history was impacted to a large extent by the presence of the 10 Hz frequency. For subsequent studies on propellers in descent, replacing the existing setup with an alternative that resolves this issue may yield better data. Also, it is suggested that a more robust torque transducer that is capable of withstanding the vibrations generated in the VRS be identified and procured. Acquiring the torque data along with the thrust would lead to a better understanding of the phenomenon.

Prior researchers describe the presence of a characteristic period in the thrust oscillations. Further reducing the noise content in the existing setup would enable more accurate time history data to be recorded. It would thus be possible to analyze this frequency content of the thrust fluctuations in detail.

The current study was limited since only axial descent conditions were tested. Prior researchers including Tehrani[11] have modified the current setup in order to test propellers in yaw, albeit in the normal working state. It is suggested that tests be carried out for propellers in non-axial descent. These results could be then compared with the data discussed in this thesis.

References

[1] A. R. S. Bramwell. *Helicopter Dynamics*. John Wiley and Sons, New York, 1976.

[2] H. Glauert. The Analysis of Experimental Results in the Windmill Brake and Vortex Ring States of an Airscrew. Reports and Memoranda 1026, British A.R.C, 1926.

[3] W. Castles and R.B. Gray. Empirical Relation between Induced Velocity, Thrust and Rate of Descent of a Helicopter as Determined by Wind-Tunnel Tests on Four Model Rotors. NACA TN 2474, 1951.

[4] K. Washizu, A. Azuma, J. Koo, and T. Oka. Experiments on a Model Helicopter Rotor Operating in the Vortex Ring State. *Journal of Aircraft*, 3(3):225–230, 1966.

[5] P. F. Yaggy and K. W. Mort. Wind-Tunnel Tests of Two VTOL Propellers in Descent. NACA TN D-1766, 1963.

[6] M. D. Betzina. Tiltrotor Descent Aerodynamics: A Small-Scale Experimental Investigation of Vortex Ring State. American Helicopter Society 57th Annual Forum, Washington, D. C., May 2001.

[7] J. G. Leishman, M. J. Bhagwat, and S. Ananthan. Free-Vortex Wake Predictions of the Vortex Ring State for Single-Rotor and Multi-Rotor Configurations. American Helicopter Society 58th Annual Forum, Montreal, Canada, June 2002.

[8] C. Chen and J. V. R. Prasad. Simplified Rotor Inflow Model for Descent Flight. *Journal of Aircraft*, 44(3):936–944, 2007.

[9] Federal Aviation Administration. *Rotorcraft Flying Handbook*. Skyhorse Publishing, New York, 2007.

[10] J. Brandt. Small-Scale Propeller Performance at Low Speeds. Master's thesis, University of Illinois at Urbana-Champaign, Department of Aerospace Engineering, Urbana, IL, 2005.

[11] K. Tehrani. Propellers in Yawed Flow at Low Speeds. Master's thesis, University of Illinois at Urbana-Champaign, Department of Aerospace Engineering, Urbana, IL, 2006.

[12] D. Uhlig. Post Stall Behavior at Low Reynolds Numbers. Master's thesis, University of Illinois at Urbana-Champaign, Department of Aerospace Engineering, Urbana, IL, 2007.

[13] Landing Products. *APC Propellers*. http://www.apcprop.com/v/index.html.

[14] J. B. Barlow, W. H. Rae, and A. Pope. *Low-Speed Wind Tunnel Testing, Third Ed.* John Wiley and Sons, New York, 1984.

[15] E. C. Maskell. A Theory of the Blockage Effects on Bluff Bodies and Stalled Wings in a Closed Wind Tunnel. Reports and Memoranda 3400, British A.R.C, 1963.

[16] B. W. McCormick. *Aerodynamics Aeronautics and Flight Mechanics, Second Ed.* John Wiley & Sons, New York, 1995.

[17] W. Johnson. Model for Vortex Ring State Influence on Rotorcraft Flight Dynamics. NASA TP-2005-213477, December 2005.

[18] M. Hepperle. *PropellerScanner Manual*. MH AeroTools, www.mh-aerotools.de, 2003.

[19] M. Drela and H. Youngren. *XFOIL 6.9 User Primer*. Massachusetts Institute of Technology, Boston, MA, 2001.

[20] J. Roskam and C. E. Lan. *Airplane Aerodynamics and Performance*. DAR Corporation, Lawrence, KS, 1997.

[21] W. Johnson. *Helicopter Theory*. Dover Publications, New York, 1994.

Appendix A

Tabulated Geometry

In this appendix, the geometry of the propellers tested was provided in tabular form. The numerical values for the chord distribution and the pitch angle are given for each of the 18 radial stations. This data is calculated using PropellerScanner.[18]

APC
Slow Flyer
9×3.8

r/R	c/R	β
0.15	0.121	32.40
0.20	0.143	29.90
0.25	0.164	26.30
0.30	0.182	23.60
0.35	0.196	21.10
0.40	0.208	19.00
0.45	0.217	17.10
0.50	0.223	15.50
0.55	0.226	14.20
0.60	0.225	13.20
0.65	0.220	12.20
0.70	0.213	11.40
0.75	0.201	10.80
0.80	0.185	10.40
0.85	0.165	9.98
0.90	0.141	9.46
0.95	0.097	8.00
1.00	0.012	5.68

APC
Slow Flyer
9×6

r/R	c/R	β
0.15	0.122	37.73
0.20	0.133	39.74
0.25	0.156	36.96
0.30	0.176	33.71
0.35	0.193	30.82
0.40	0.207	28.05
0.45	0.218	25.25
0.50	0.225	22.79
0.55	0.227	20.71
0.60	0.227	18.88
0.65	0.222	17.24
0.70	0.214	15.79
0.75	0.201	14.54
0.80	0.183	13.40
0.85	0.162	12.30
0.90	0.136	11.40
0.95	0.097	10.33
1.00	0.056	9.26

APC
Slow Flyer
10×3.8

r/R	c/R	β
0.15	0.112	35.54
0.20	0.134	34.08
0.25	0.157	28.78
0.30	0.177	24.16
0.35	0.194	20.85
0.40	0.208	18.28
0.45	0.218	16.34
0.50	0.225	14.79
0.55	0.228	13.45
0.60	0.227	12.34
0.65	0.222	11.26
0.70	0.214	10.18
0.75	0.201	9.24
0.80	0.184	8.33
0.85	0.163	7.35
0.90	0.138	6.53
0.95	0.098	6.03
1.00	0.056	5.55

APC
Slow Flyer
9×4.7

r/R	c/R	β
0.15	0.127	27.54
0.20	0.135	25.28
0.25	0.158	26.08
0.30	0.178	25.47
0.35	0.195	24.07
0.40	0.209	22.18
0.45	0.219	20.00
0.50	0.225	18.18
0.55	0.227	16.38
0.60	0.226	14.83
0.65	0.221	13.63
0.70	0.212	12.56
0.75	0.199	11.56
0.80	0.182	10.65
0.85	0.161	9.68
0.90	0.135	8.51
0.95	0.097	6.72
1.00	0.058	4.89

APC
Slow Flyer
9×7.5

r/R	c/R	β
0.15	0.106	38.09
0.20	0.125	41.29
0.25	0.147	39.68
0.30	0.167	36.99
0.35	0.184	34.20
0.40	0.198	31.38
0.45	0.208	28.52
0.50	0.215	25.88
0.55	0.217	23.61
0.60	0.216	21.58
0.65	0.210	19.78
0.70	0.203	18.16
0.75	0.191	16.71
0.80	0.176	15.42
0.85	0.156	14.52
0.90	0.128	13.40
0.95	0.086	13.02
1.00	0.044	12.67

APC
Slow Flyer
10×4.7

r/R	c/R	β
0.15	0.109	21.11
0.20	0.132	23.90
0.25	0.156	24.65
0.30	0.176	24.11
0.35	0.193	22.78
0.40	0.206	21.01
0.45	0.216	19.00
0.50	0.223	17.06
0.55	0.226	15.33
0.60	0.225	13.82
0.65	0.219	12.51
0.70	0.210	11.36
0.75	0.197	10.27
0.80	0.179	9.32
0.85	0.157	8.36
0.90	0.130	7.27
0.95	0.087	6.15
1.00	0.042	5.04

APC
Slow Flyer
11×3.8

r/R	c/R	β
0.15	0.112	33.43
0.20	0.135	31.77
0.25	0.157	26.41
0.30	0.177	21.94
0.35	0.194	18.66
0.40	0.208	16.16
0.45	0.218	14.19
0.50	0.225	12.62
0.55	0.228	11.31
0.60	0.227	10.19
0.65	0.222	9.23
0.70	0.214	8.30
0.75	0.202	7.43
0.80	0.185	6.65
0.85	0.165	6.11
0.90	0.140	5.65
0.95	0.100	5.47
1.00	0.060	5.31

APC
Sport Propeller
9×5

r/R	c/R	β
0.15	0.160	31.68
0.20	0.146	34.45
0.25	0.144	35.93
0.30	0.143	33.33
0.35	0.143	29.42
0.40	0.146	26.25
0.45	0.151	23.67
0.50	0.155	21.65
0.55	0.158	20.02
0.60	0.160	18.49
0.65	0.159	17.06
0.70	0.155	15.95
0.75	0.146	14.87
0.80	0.133	13.82
0.85	0.114	12.77
0.90	0.089	11.47
0.95	0.056	10.15
1.00	0.022	8.82

APC
Sport Propeller
9×8

r/R	c/R	β
0.15	0.157	39.36
0.20	0.155	44.66
0.25	0.156	46.76
0.30	0.156	44.83
0.35	0.155	41.55
0.40	0.156	38.59
0.45	0.159	35.79
0.50	0.163	33.19
0.55	0.165	30.95
0.60	0.165	28.89
0.65	0.163	27.07
0.70	0.158	25.43
0.75	0.150	23.82
0.80	0.138	22.40
0.85	0.121	21.01
0.90	0.098	19.61
0.95	0.063	15.90
1.00	0.005	NA

APC
Slow Flyer
11×4.7

r/R	c/R	β
0.15	0.112	19.64
0.20	0.137	21.81
0.25	0.160	22.45
0.30	0.181	21.88
0.35	0.198	20.73
0.40	0.211	19.14
0.45	0.221	17.30
0.50	0.227	15.58
0.55	0.230	14.06
0.60	0.228	12.71
0.65	0.222	11.53
0.70	0.213	10.47
0.75	0.199	9.53
0.80	0.181	8.63
0.85	0.158	7.71
0.90	0.132	6.61
0.95	0.084	5.28
1.00	0.035	3.93

APC
Sport Propeller
9×7

r/R	c/R	β
0.15	0.180	35.61
0.20	0.158	39.44
0.25	0.157	42.45
0.30	0.156	41.18
0.35	0.154	37.35
0.40	0.155	33.74
0.45	0.157	30.77
0.50	0.160	27.98
0.55	0.162	25.54
0.60	0.162	23.41
0.65	0.161	21.87
0.70	0.156	20.17
0.75	0.147	18.87
0.80	0.134	17.76
0.85	0.115	16.05
0.90	0.091	14.17
0.95	0.057	12.29
1.00	0.024	10.41

APC
Sport Propeller
10×5

r/R	c/R	β
0.15	0.164	30.97
0.20	0.157	34.26
0.25	0.153	34.39
0.30	0.151	31.93
0.35	0.151	29.31
0.40	0.153	26.84
0.45	0.157	24.56
0.50	0.160	22.71
0.55	0.163	21.21
0.60	0.165	19.94
0.65	0.165	18.78
0.70	0.163	17.64
0.75	0.156	16.61
0.80	0.144	15.80
0.85	0.126	15.15
0.90	0.102	14.65
0.95	0.066	16.05
1.00	0.004	18.37

APC
Sport Propeller
10×10

r/R	c/R	β
0.15	0.163	39.21
0.20	0.155	46.33
0.25	0.152	50.28
0.30	0.149	49.16
0.35	0.147	46.00
0.40	0.146	41.58
0.45	0.148	37.45
0.50	0.152	34.41
0.55	0.156	31.75
0.60	0.158	29.41
0.65	0.158	27.63
0.70	0.155	25.75
0.75	0.148	23.97
0.80	0.137	22.16
0.85	0.120	20.50
0.90	0.098	18.86
0.95	0.066	17.17
1.00	0.034	15.48

APC
Sport Propellers
11×5

r/R	c/R	β
0.15	0.167	27.64
0.20	0.165	30.17
0.25	0.165	31.50
0.30	0.162	29.54
0.35	0.160	26.43
0.40	0.160	23.57
0.45	0.161	21.03
0.50	0.162	18.92
0.55	0.162	17.14
0.60	0.161	15.69
0.65	0.158	14.44
0.70	0.152	13.29
0.75	0.142	12.44
0.80	0.128	11.32
0.85	0.109	10.27
0.90	0.083	9.07
0.95	0.050	7.28
1.00	0.015	5.42

APC
Thin Electric
9×6

r/R	c/R	β
0.15	0.141	31.67
0.20	0.147	37.59
0.25	0.183	38.78
0.30	0.207	35.90
0.35	0.218	32.07
0.40	0.223	28.50
0.45	0.222	25.81
0.50	0.217	23.58
0.55	0.209	21.66
0.60	0.197	19.99
0.65	0.183	18.58
0.70	0.167	17.29
0.75	0.150	16.37
0.80	0.132	15.46
0.85	0.114	14.30
0.90	0.098	13.40
0.95	0.075	12.02
1.00	0.051	10.61

APC
Sport Propeller
11×4

r/R	c/R	β
0.15	0.170	28.19
0.20	0.169	30.01
0.25	0.168	30.46
0.30	0.164	27.59
0.35	0.162	23.97
0.40	0.161	21.02
0.45	0.162	18.63
0.50	0.163	16.77
0.55	0.163	15.23
0.60	0.161	13.88
0.65	0.158	12.74
0.70	0.153	11.63
0.75	0.143	10.69
0.80	0.129	9.80
0.85	0.109	8.69
0.85	0.096	14.64
0.90	0.084	7.32
0.95	0.051	6.29
1.00	0.017	5.29

APC
Thin Electric
9×4.5

r/R	c/R	β
0.15	0.157	34.80
0.20	0.163	36.50
0.25	0.187	34.26
0.30	0.206	29.64
0.35	0.217	25.62
0.40	0.222	22.53
0.45	0.222	20.25
0.50	0.217	18.37
0.55	0.209	16.83
0.60	0.197	15.51
0.65	0.183	14.38
0.70	0.167	13.45
0.75	0.150	12.56
0.80	0.133	12.09
0.85	0.116	11.25
0.90	0.099	10.46
0.95	0.074	9.68
1.00	0.049	8.90

APC
Thin Electric
9×7.5

r/R	c/R	β
0.15	0.152	46.70
0.20	0.171	51.36
0.25	0.192	47.89
0.30	0.206	42.29
0.35	0.215	37.66
0.40	0.218	34.07
0.45	0.218	31.03
0.50	0.213	28.43
0.55	0.204	26.28
0.60	0.193	24.48
0.65	0.180	22.86
0.70	0.165	21.48
0.75	0.149	20.39
0.80	0.132	19.36
0.85	0.116	18.24
0.90	0.101	17.05
0.95	0.070	21.13
1.00	0.002	31.71

APC
Thin Electric
10×5

r/R	c/R	β
0.15	0.130	32.76
0.20	0.149	37.19
0.25	0.173	33.54
0.30	0.189	29.25
0.35	0.197	25.64
0.40	0.201	22.54
0.45	0.200	20.27
0.50	0.194	18.46
0.55	0.186	17.05
0.60	0.174	15.97
0.65	0.160	14.87
0.70	0.145	14.09
0.75	0.128	13.39
0.80	0.112	12.84
0.85	0.096	12.25
0.90	0.081	11.37
0.95	0.061	10.19
1.00	0.041	8.99

APC
Thin Electric
10×10

r/R	c/R	β
0.15	0.134	48.95
0.20	0.154	55.79
0.25	0.174	53.16
0.30	0.187	47.70
0.35	0.194	42.94
0.40	0.197	39.13
0.45	0.196	36.08
0.50	0.191	33.57
0.55	0.183	31.37
0.60	0.172	29.49
0.65	0.159	27.83
0.70	0.145	26.23
0.75	0.130	24.75
0.80	0.115	23.49
0.85	0.100	22.38
0.90	0.086	21.24
0.95	0.061	18.98
1.00	0.004	22.24

APC
Thin Electric
10×7

r/R	c/R	β
0.15	0.138	37.86
0.20	0.154	45.82
0.25	0.175	44.19
0.30	0.190	38.35
0.35	0.198	33.64
0.40	0.202	29.90
0.45	0.200	27.02
0.50	0.195	24.67
0.55	0.186	22.62
0.60	0.174	20.88
0.65	0.161	19.36
0.70	0.145	17.98
0.75	0.129	16.74
0.80	0.112	15.79
0.85	0.096	14.64
0.90	0.081	13.86
0.95	0.061	12.72
1.00	0.040	11.53

APC
Thin Electric
11×7

r/R	c/R	β
0.15	0.131	41.81
0.20	0.145	45.76
0.25	0.161	41.73
0.30	0.176	36.13
0.35	0.185	31.59
0.40	0.189	28.07
0.45	0.189	25.32
0.50	0.185	23.02
0.55	0.177	21.04
0.60	0.167	19.62
0.65	0.154	18.47
0.70	0.140	17.38
0.75	0.125	16.28
0.80	0.110	15.33
0.85	0.095	14.58
0.90	0.081	13.77
0.95	0.062	13.05
1.00	0.043	12.34

Appendix B

Tabulated Performance Data

Appendix B contains the performance data for all propellers tested that were plotted in the previous chapters. The thrust coefficient data for the APC propellers is listed over the range of advance ratios.

APC
Slow Flyer
9×3.8
Run: 3061os
Average RPM: 3955

J	C_T
-0.161	0.0931
-0.202	0.0941
-0.254	0.0691
-0.280	0.0844
-0.328	0.0932
-0.367	0.1121
-0.408	0.1242
-0.450	0.1353
-0.492	0.1484
-0.525	0.1618
-0.570	0.1779
-0.609	0.1937
-0.641	0.2078
-0.678	0.2246
-0.720	0.2428
-0.759	0.2606
-0.798	0.2771

APC
Slow Flyer
9×4.7
Run: 3122os
Average RPM: 4000

J	C_T
-0.164	0.1090
-0.195	0.1073
-0.256	0.0940
-0.287	0.0845
-0.328	0.1023
-0.365	0.1139
-0.406	0.1262
-0.447	0.1389
-0.491	0.1532
-0.524	0.1661
-0.565	0.1798
-0.604	0.1957
-0.642	0.2122
-0.681	0.2294
-0.719	0.2464
-0.763	0.2652
-0.805	0.2838

APC
Slow Flyer
9×6
Run: 3058os
Average RPM: 3960

J	C_T
-0.168	0.1491
-0.215	0.1406
-0.251	0.1377
-0.291	0.1316
-0.331	0.1221
-0.367	0.1336
-0.413	0.1506
-0.446	0.1583
-0.480	0.1663
-0.526	0.1844
-0.583	0.2024
-0.630	0.2223
-0.648	0.2301
-0.692	0.2472
-0.725	0.2621
-0.772	0.2814
-0.832	0.3079

APC
Slow Flyer
9×7.5
Run: 3123os
Average RPM: 3987

J	C_T
-0.161	0.1681
-0.218	0.1683
-0.249	0.1572
-0.290	0.1550
-0.319	0.1425
-0.359	0.1345
-0.416	0.1630
-0.445	0.1682
-0.495	0.1821
-0.526	0.1911
-0.562	0.2014
-0.606	0.2189
-0.646	0.2343
-0.681	0.2472
-0.720	0.2628
-0.767	0.2818
-0.800	0.2971

APC
Slow Flyer
10×3.8
Run: 3070os
Average RPM: 3986

J	C_T
-0.147	0.0932
-0.190	0.0968
-0.229	0.0838
-0.252	0.0789
-0.295	0.0940
-0.331	0.1018
-0.370	0.1145
-0.403	0.1250
-0.436	0.1362
-0.477	0.1505
-0.517	0.1650
-0.541	0.1723
-0.584	0.1892
-0.616	0.2022
-0.660	0.2211
-0.681	0.2300
-0.714	0.2444

APC
Slow Flyer
10×4.7
Run: 3071os
Average RPM: 3999

J	C_T
-0.137	0.1127
-0.174	0.1189
-0.229	0.1057
-0.265	0.0947
-0.293	0.0956
-0.329	0.1107
-0.371	0.1236
-0.406	0.1351
-0.434	0.1420
-0.477	0.1582
-0.515	0.1699
-0.546	0.1782
-0.582	0.1912
-0.615	0.2048
-0.633	0.2128
-0.694	0.2409
-0.735	0.0122

APC
Slow Flyer
11×3.8
Run: 3072os
Average RPM: 3984

J	C_T
-0.131	0.1073
-0.177	0.1076
-0.193	0.1115
-0.218	0.1097
-0.262	0.0955
-0.301	0.1091
-0.335	0.1217
-0.369	0.1311
-0.399	0.1365
-0.433	0.1494
-0.465	0.1601
-0.501	0.1718
-0.537	0.1843
-0.563	0.1901
-0.595	0.2059
-0.629	0.2210
-0.662	0.2326

APC
Slow Flyer
11×4.7
Run: 3073os
Average RPM: 4003

J	C_T
-0.127	0.0803
-0.180	0.0754
-0.200	0.0761
-0.233	0.0687
-0.274	0.0808
-0.295	0.0876
-0.333	0.0974
-0.357	0.1059
-0.390	0.1161
-0.430	0.1307
-0.467	0.1416
-0.498	0.1548
-0.516	0.1595
-0.543	0.1672
-0.604	0.1922
-0.630	0.2041
-0.653	0.2148

APC
Sport Propeller
9×4
Run: 3063os
Average RPM: 4013

J	C_T
-0.162	0.0905
-0.197	0.0867
-0.234	0.0785
-0.290	0.0821
-0.323	0.0907
-0.363	0.1022
-0.407	0.1121
-0.441	0.1228
-0.486	0.1330
-0.527	0.1441
-0.550	0.1506
-0.581	0.1556
-0.638	0.1679
-0.674	0.1754
-0.720	0.1881
-0.766	0.2014
-0.806	0.2137

APC
Sport Propeller
9×5
Run: 3064os
Average RPM: 4020)

J	C_T
-0.160	0.0952
-0.193	0.0966
-0.235	0.0887
-0.288	0.0898
-0.322	0.0979
-0.360	0.1031
-0.407	0.1126
-0.448	0.1206
-0.493	0.1309
-0.525	0.1398
-0.562	0.1502
-0.600	0.1592
-0.635	0.1679
-0.682	0.1788
-0.720	0.1881
-0.757	0.1964
-0.799	0.2061

APC
Sport Propeller
9×7
Run: 3115os
Average RPM: 4011

J	C_T
-0.162	0.1113
-0.213	0.1114
-0.244	0.1066
-0.275	0.1018
-0.329	0.1065
-0.360	0.1126
-0.407	0.1190
-0.449	0.1264
-0.484	0.1333
-0.522	0.1433
-0.561	0.1554
-0.596	0.1651
-0.647	0.1782
-0.680	0.1886
-0.719	0.1995
-0.758	0.2086
-0.798	0.2192

APC
Sport Propeller
9×8
Run: 3116os
Average RPM: 4004

J	C_T
-0.162	0.1174
-0.196	0.1181
-0.238	0.1132
-0.287	0.1087
-0.325	0.1110
-0.366	0.1200
-0.410	0.1251
-0.445	0.1291
-0.479	0.1362
-0.527	0.1488
-0.573	0.1638
-0.606	0.1739
-0.637	0.1833
-0.680	0.1964
-0.719	0.2064
-0.761	0.2171
-0.799	0.2240

APC
Sport Propeller
9×10
Run: 3117os
Average RPM: 4004

J	C_T
-0.161	0.1106
-0.194	0.1123
-0.250	0.1098
-0.288	0.1064
-0.329	0.1112
-0.368	0.1181
-0.409	0.1253
-0.446	0.1309
-0.485	0.1390
-0.525	0.1487
-0.566	0.1605
-0.605	0.1722
-0.645	0.1826
-0.685	0.1922
-0.727	0.2035
-0.760	0.2113
-0.802	0.2205

APC
Sport Propeller
10×4
Run: 3127os
Average RPM: 3959

J	C_T
-0.150	0.0872
-0.179	0.0834
-0.218	0.0775
-0.264	0.0772
-0.290	0.0851
-0.325	0.0940
-0.367	0.1044
-0.402	0.1144
-0.437	0.1254
-0.472	0.1335
-0.505	0.1436
-0.545	0.1541
-0.645	0.1657
-0.668	0.1756
-0.648	0.1751
-0.676	0.1822
-0.716	0.1937

APC
Sport Propeller
10×5
Run: 3124os
Average RPM: 4010

J	C_T
-0.141	0.0997
-0.176	0.1029
-0.217	0.0950
-0.271	0.0871
-0.293	0.0871
-0.329	0.1032
-0.361	0.1117
-0.399	0.1193
-0.433	0.1267
-0.475	0.1364
-0.509	0.1451
-0.541	0.1543
-0.563	0.1610
-0.604	0.1714
-0.648	0.1825
-0.681	0.1905
-0.719	0.1980

APC
Sport Propeller
10×7
Run: 3125os
Average RPM: 3995

J	C_T
-0.139	0.1128
-0.175	0.1149
-0.230	0.1111
-0.258	0.1000
-0.298	0.1040
-0.329	0.1114
-0.365	0.1176
-0.405	0.1222
-0.437	0.1275
-0.473	0.1344
-0.509	0.1436
-0.546	0.1543
-0.586	0.1659
-0.612	0.1743
-0.648	0.1846
-0.686	0.1955
-0.727	0.2062

APC
Sport Propeller
10×10
Run: 3126os
Average RPM: 4020

J	C_T
-0.144	0.1179
-0.179	0.1185
-0.217	0.1219
-0.263	0.1202
-0.293	0.1182
-0.321	0.1191
-0.359	0.1241
-0.401	0.1319
-0.436	0.1381
-0.474	0.1449
-0.512	0.1534
-0.543	0.1626
-0.583	0.1744
-0.611	0.1822
-0.598	0.1844
-0.683	0.2033
-0.719	0.2112

APC
Sport Prop
11×5
Run: 3086os
Average RPM: 4014

J	C_T
-0.131	0.0954
-0.169	0.0959
-0.207	0.0896
-0.230	0.0911
-0.257	0.0818
-0.295	0.0963
-0.329	0.1052
-0.359	0.1113
-0.400	0.1207
-0.424	0.1245
-0.459	0.1337
-0.498	0.1439
-0.525	0.1503
-0.544	0.1527
-0.589	0.1621
-0.617	0.1671
-0.656	0.1787

APC
Thin Electric
9×4.5
Run: 3111os
Average RPM: 4005

J	C_T
-0.157	0.0935
-0.198	0.0888
-0.240	0.0853
-0.290	0.0739
-0.323	0.0857
-0.367	0.0985
-0.405	0.1107
-0.441	0.1195
-0.482	0.1343
-0.522	0.1459
-0.568	0.1594
-0.608	0.1701
-0.639	0.1780
-0.678	0.1874
-0.719	0.1996
-0.761	0.2131
-0.801	0.2262

APC
Thin Electric
9×6
Run: 3090os
Average RPM: 3995

J	C_T
-0.158	0.1104
-0.214	0.1142
-0.244	0.1044
-0.290	0.0996
-0.333	0.0929
-0.369	0.1079
-0.398	0.1153
-0.450	0.1276
-0.485	0.1373
-0.529	0.1506
-0.563	0.1604
-0.593	0.1673
-0.649	0.1850
-0.700	0.2012
-0.728	0.2083
-0.756	0.2162
-0.802	0.2331

APC
Thin Electric
9×7.5
Run: 3089os
Average RPM: 4003

J	C_T
-0.157	0.1186
-0.193	0.1194
-0.254	0.1168
-0.286	0.1108
-0.332	0.1054
-0.362	0.1116
-0.409	0.1259
-0.442	0.1343
-0.493	0.1444
-0.525	0.1529
-0.562	0.1649
-0.599	0.1761
-0.648	0.1911
-0.690	0.2050
-0.719	0.2138
-0.765	0.2294
-0.788	0.2363

APC
Thin Electric
10×5
Run: 3118os
Average RPM: 4002

J	C_T
-0.142	0.0902
-0.175	0.0890
-0.230	0.0787
-0.257	0.0771
-0.301	0.0851
-0.329	0.0916
-0.369	0.1023
-0.402	0.1113
-0.434	0.1173
-0.473	0.1293
-0.508	0.1371
-0.540	0.1462
-0.573	0.1543
-0.610	0.1621
-0.644	0.1703
-0.684	0.1802
-0.719	0.1895

APC
Thin Electric
10×7
Run: 3119os
Average RPM: 4003

J	C_T
-0.136	0.1062
-0.176	0.1091
-0.223	0.0986
-0.262	0.0930
-0.285	0.0927
-0.340	0.0984
-0.362	0.1031
-0.402	0.1169
-0.438	0.1271
-0.477	0.1347
-0.507	0.1397
-0.542	0.1495
-0.583	0.1601
-0.613	0.1691
-0.644	0.1747
-0.686	0.1863
-0.721	0.1957

APC
Thin Electric
10×10
Run: 3120os
Average RPM: 4021

J	C_T
-0.144	0.1118
-0.189	0.1087
-0.224	0.1090
-0.251	0.1098
-0.294	0.1080
-0.330	0.1097
-0.368	0.1162
-0.405	0.1242
-0.440	0.1335
-0.481	0.1398
-0.508	0.1457
-0.537	0.1513
-0.585	0.1648
-0.569	0.1639
-0.653	0.1849
-0.682	0.1927